Quasi-Particle Simulations of Skyrmion Dynamics with Applications in Unconventional Computing

Dissertation
zur Erlangung des Grades
„Doktor
der Naturwissenschaften"
am Fachbereich Physik, Mathematik und Informatik
der Johannes Gutenberg-Universität
in Mainz

Maarten Alexander Brems

geb. in Worms

Mainz, den 29.08.2025

Gutachter:

[redacted]

[redacted]

Tag der Prüfung: [redacted]

Licensing and Third-Party Material

Data Privacy

Parts of this thesis have been removed or censored due to data privacy.

Abstract

Magnetic skyrmions are effectively two-dimensional, topologically stabilized whirls of magnetization that exhibit particle-like behavior and can perform thermal random motion akin to Brownian dynamics. These properties, alongside a variety of external movement-inducing mechanisms, such as current-induced spin torques, make skyrmions promising candidates for applications in data storage and unconventional computing. Computer simulations are a valuable tool for in-silico device development and optimization. However, conventional atomistic and micromagnetic simulation approaches exhibit prohibitive computational costs at large experimentally relevant length and time scales. Here, we focus on the coarse-grained quasi-particle description of skyrmions. In the so-called Thiele framework, these limitations with respect to time and length scales are overcome by representing skyrmions as soft disks without explicitly modeling their internal magnetic structure. In this thesis, statistical physics methods are employed to determine the key parameters for quantitative quasi-particle simulations of skyrmions directly from experimental trajectories. Consequently, these methods do not rely on any assumptions about the underlying magnetic interactions or the skyrmion's internal structure, while automatically averaging over thermal fluctuations of the latter.

Two methods are developed to ascertain the skyrmion damping parameter and the force acting on a skyrmion in response to an applied current density. The skyrmion damping sets the time scale of the system's dynamics. Accounting for the interaction with local variations of the magnetic properties is crucial for the time scale conversion between simulation and experiment. These "pinning effects" are unavoidable in state-of-the-art skyrmion systems and act to slow down skyrmion dynamics significantly. Modeling skyrmion pinning via a spatially inhomogeneous energy landscape enables us to isolate its effects from the intrinsic skyrmion damping. Moreover, the current-induced force acting on a skyrmion is determined based on the bias it inflicts on the thermal diffusion and the resulting effective energy landscape. Thereby, this method reveals even the effects of ultra-low current densities and allows us to ascertain the linear relation between the applied current density and the acting force. Furthermore, a strong dependence of pinning effects on the skyrmion size is revealed and explained by going beyond the quasi-particle picture. We exploit this size-dependence to develop a diffusion enhancement mechanism based on periodically changing the skyrmion size via an oscillating magnetic field. This deterministic excitation is shown to drastically increase the skyrmions' random motion even at a constant temperature, which can be particularly valuable for Brownian computing devices.

Unconventional computers within the Brownian computing paradigm leverage (thermal) randomness for the benefit of a specific computer architecture. Here, a skyrmion-based Brownian reservoir computer is developed. Our concept device exploits the complex non-linear behavior of a confined skyrmion performing thermal diffusion, which arises due to a competition of different interactions at similar scales. This design ensures fast learning at a low computational cost and mitigates the obstructive effects of pinning. In addition, access to the skyrmion's trajectory during operation allows for the interpretation of the trained parameters and the role of thermal activity.

Zusammenfassung

Magnetische Skyrmionen sind effektiv zweidimensionale, topologisch stabilisierte Magnetisierungswirbel, die sich wie Teilchen verhalten und thermische Zufallsbewegungen ähnlich der Brownschen Molekularbewegung ausführen können. Diese Eigenschaften, in Verbindung mit einer Vielzahl externer Bewegungsmechanismen, wie z.B. strominduzierter Bewegung, machen Skyrmionen zu vielversprechenden Kandidaten für Anwendungen in Datenspeichern und unkonventionellen Computern. Computersimulationen sind ein wertvolles Werkzeug für die In-Silico-Entwicklung und -Optimierung solcher Geräte. Herkömmliche atomistische und mikromagnetische Simulationsansätze sind jedoch auf großen, experimentell relevanten Längen- und Zeitskalen mit unterbindend hohen Rechenkosten verbunden. Stattdessen konzentrieren wir uns hier auf die stark vergröberte Quasiteilchenbeschreibung von Skyrmionen. Im sogenannten Thiele-Modell werden die Einschränkungen bezüglich der Längen- und Zeitskalen überwunden, indem Skyrmionen als weiche Scheiben dargestellt werden, ohne ihre interne magnetische Struktur explizit zu modellieren. In dieser Arbeit werden Methoden der Statistischen Physik eingesetzt, um die Schlüsselparameter für quantitative Quasiteilchensimulationen von Skyrmionen direkt aus experimentellen Trajektorien zu bestimmen. Folglich benötigen diese Methoden weder Annahmen über die zugrunde liegenden magnetischen Wechselwirkungen noch über die innere Struktur der Skyrmionen, während sie zudem automatisch über thermische Fluktuationen der Struktur mitteln.

In dieser Arbeit wurden zwei Methoden entwickelt, um die Skyrmion-Dämpfung, sowie die strominduzierte Kraft als Funktion der angelegten Stromdichte, zu bestimmen. Die Skyrmion-Dämpfung bestimmt die Zeitskala der Dynamik des Systems. Die Berücksichtigung der Wechselwirkung mit lokalen Variationen der magnetischen Eigenschaften ist essenziell für die Zeitskalenumrechnung zwischen Simulation und Experiment. Diese „Pinning-Effekte" sind selbst in modernen Skyrmion-Systemen unvermeidbar und verlangsamen die Skyrmion-Dynamik erheblich. Die Modellierung des Skyrmion-Pinnings über eine räumlich inhomogene Energielandschaft ermöglicht es uns, dessen Auswirkungen von der intrinsischen Skyrmion-Dämpfung zu isolieren. Zudem wird die auf ein Skyrmion wirkende strominduzierte Kraft über den Bias bestimmt, den diese auf die thermische Diffusion und damit auf die effektive Energielandschaft ausübt. Auf diese Weise lässt sich sogar die Wirkung extrem niedriger Stromdichten nachweisen und die lineare Beziehung zwischen der angelegten Stromdichte und der wirkenden Kraft ermitteln. Darüber hinaus wird eine starke Abhängigkeit des Pinning-Effekts von der Skyrmiongröße aufgezeigt und durch Analysen über das Quasiteilchenbild hinaus erklärt. Wir nutzen diese Größenabhängigkeit, um einen Mechanismus zur Diffusionserhöhung zu entwickeln, der auf einer periodischen Veränderung der Skyrmiongröße also Folge eines oszillierenden Magnetfeldes basiert. Es zeigt sich, dass diese deterministische Anregung die Zufallsbewegung der Skyrmionen selbst bei konstanter Temperatur drastisch erhöht, was für Brownsche Computer besonders wertvoll sein kann.

Unkonventionelle Computer innerhalb des Brownian-Computing-Paradigmas nutzen (thermische) Zufälligkeit zum Vorteil einer Computerarchitektur. In dieser Arbeit wird ein Skyrmion-basierender Brownscher Reservoir-Computer entwickelt. Unser Konzept nutzt das komplexe nichtlineare Verhalten eines thermisch diffundierenden, eingeschlossenen Skyrmions, welches aufgrund der Konkurrenz verschiedener Wechselwirkungen auf ähnlichen Skalen entsteht. Dieses Design gewährleistet schnelles Lernen bei geringen Rechenkosten und überwindet die hinderlichen Auswirkungen des Pinnings. Darüber hinaus ermöglicht der Zugriff auf die Trajektorie des Skyrmions während des Betriebs die Interpretation der trainierten Parameter und der Rolle der thermischen Aktivität.

Contents

1. Introduction

The recent widespread adoption of artificial intelligence (AI) has ignited a technological race among major firms such as Microsoft, Google, and others. Driven in part by market valuations that already assume continued breakthroughs [1], these companies are estimated to spend tens of millions of dollars for training a new frontier AI model, with amortized training costs more than doubling each year since 2016 [2]. The resulting need for high-performance hardware further fuels the ongoing miniaturization of computing devices. For four decades, the advancement in chip fabrication technology has been surprisingly well-described by Moore's Law, with the number of transistors on integrated circuits roughly doubling every two years [3–5]. Recently, however, the pace of advancement has slowed down in accordance with expected physical limitations. As the devices are scaled down, the relevant energy scale for computing becomes comparable to the one of thermal fluctuation at operating temperature [5], such that deterministic behavior can no longer be guaranteed. These challenges motivate the exploration of alternative, unconventional computing architectures that could potentially circumvent these limitations. Research in unconventional computing often goes hand in hand with the study of physical systems that may offer unique computational advantages.

Magnetic skyrmions are nanometer- to micrometer-sized magnetic textures with quasiparticle properties [6–10]. They are spatially localized, can move as a whole, typically interact repulsively with each other and with the boundaries of the magnetic material [11–15], and can perform thermal diffusion [16, 17]. Moreover, there exists a variety of mechanisms for the external manipulation of skyrmion dynamics, for instance via electrical currents [18–20] or magnetic field gradients [21]. Combined with electrical detection methods such as tunnel magnetoresistance [22], these mechanisms make skyrmions promising for various applications in data storage [9, 23, 24] and unconventional computing [25–32].

Beyond that, the aforementioned properties make skyrmions in many ways similar to colloidal systems [31, 33, 34]. However, unlike colloids, multiple methods exist for the controlled creation and annihilation of skyrmions [16, 35]. Their size is also adjustable on-the-fly via an applied magnetic field [36, 37]. Here, we predominantly consider micrometer-sized skyrmions in thin film multilayer systems, where the ferromagnetic layer is only a few nanometers thick. Consequently, these skyrmions are, in excellent approximation, two-dimensional. These properties make skyrmions valuable for fundamental statistical mechanics research questions, for instance, the study of two-dimensional phase behavior [33, 34], flow properties [38], or diffusive dynamics [16, 17, 39].

For both fundamental and application-oriented research, computer simulations can be an extremely valuable tool, e.g., for the parallel screening and parameter optimization of planned experimental setups and devices. However, conventional atomistic and micromagnetic simulations typically cannot capture skyrmion dynamics at experimentally relevant, large length and time scales due to their high computational cost. Quasi-particle simulations employing the Thiele model [40] overcome this limitation by representing skyrmions as two-dimensional particles without explicitly modeling their internal magnetic structure. The resulting Thiele equation of motion in terms of the skyrmion center position is very reminiscent of the overdamped Langevin equation [41], further corroborating the similarity to colloidal systems. The parameters of the Thiele equation can, in principle, be determined via a bottom-up coarse-graining approach starting from the internal skyrmion structure and the magnetic properties of the skyrmion-hosting material [40]. However, the details of the skyrmion's internal structure are usually experimentally inaccessible. Furthermore, thermal fluctuations of the skyrmion structure should be taken into account for the determination of reliable effective parameters. Central to this thesis is, therefore, a top-down approach for determining the parameters of a quantitative quasi-particle skyrmion model. Effectively, all parameters are determined directly from experimental observables, i.e., the skyrmion trajectory. Therein, the experiments are performed by my experimental collaborators. My contributions, stated at the outset of each chapter, involve method development, computer simulation, experiment conceptualization, analysis, and interpretation. The presented top-down approach does, by design, not rely on any assumptions about the underlying magnetic interactions or the internal structure of the skyrmion. It, furthermore, automatically provides effective parameters that account for thermal fluctuations of the internal skyrmion structure.

This thesis is organized into one background chapter and four results chapters, presenting published and unpublished research results. Chapter 2 provides background information regarding the studied systems and employed methods, including an overview over relevant magnetism concepts. It also contains an extended section on magnetic skyrmions and their quasi-particle modeling. The chapter concludes with an introduction to the relevant unconventional computing approaches and a brief overview of the required experimental methods. The latter is aimed at theoreticians working with the resulting data.

While Thiele model simulations have been very successful in quantitatively describing the statics of large experimental skyrmion systems [15, 33, 42, 43], the study of skyrmion dynamics has so far been limited to qualitative results only [38, 42, 43]. In chapter 3, we overcome this limitation by developing methods to ascertain two key missing parameters for a quantitative quasi-particle modeling of dynamics. This chapter is primarily based on our publication

- Maarten A. Brems, Tobias Sparmann, Simon M. Fröhlich, Leonie-C. Dany, Jan Rothörl, Fabian Kammerbauer, Elizabeth M. Jefremovas, Oded Farago, Mathias Kläui, and Peter Virnau, "Realizing Quantitative Quasiparticle Modeling of Skyrmion Dynamics in Arbitrary Potentials", *Physical Review Letters* **134**, 046701 (2025) (Ref. [39]).

with some further results currently planned to be published as

- Simon M. Fröhlich, Tobias Sparmann, Maarten A. Brems, Jan Rothörl, Fabian Kammerbauer, Klaus Raab, Sachin Krishnia, Mathias Kläui, and Peter Virnau, ”Real-Time Simulation of Skyrmion Dynamics in 2D Spatially-Dependent Pinning Potential Landscapes”, *in preparation* (2025) (Ref. [44])

and employing a few results from our publication

- Klaus Raab, Maurice Schmitt, Maarten A. Brems, Jan Rothörl, Fabian Kammerbauer, Sachin Krishnia, Mathias Kläui, and Peter Virnau, ”Skyrmion flow in periodically modulated channels”, *Physical Review E* **110**, L042601 (2024) (Ref. [38]).

The presented analysis reveals that the interaction with local variations of the magnetic properties, “pinning effects”, are crucial for skyrmion dynamics in real systems. In chapter 4, pinning is studied within the quasi-particle picture and beyond, based on our publication

- Raphael Gruber, Jakub Zázvorka, Maarten A. Brems, Davi R. Rodrigues, Takaaki Dohi, Nico Kerber, Boris Seng, Mehran Vafaee, Karin Everschor-Sitte, Peter Virnau, Mathias Kläui, “Skyrmion pinning energetics in thin film systems”, *Nature Communications* **13**, 3144 (2022) (Ref. [36])

to reveal and explain a strong dependence of pinning on the skyrmion size. In chapter 5 this size-dependence is then exploited to develop a diffusion enhancement mechanism, which works at constant temperature. The chapter is primarily based on our publication

- Raphael Gruber, Maarten A. Brems, Jan Rothörl, Tobias Sparmann, Maurice Schmitt, Iryna Kononenko, Fabian Kammerbauer, Maria-Andromach Syskaki, Oded Farago, Peter Virnau, and Mathias Kläui, ”300-Times-Increased Diffusive Skyrmion Dynamics and Effective Pinning Reduction by Periodic Field Excitation”, *Advanced Materials* **35**, 2208922 (2023) (Ref. [37]).

The chapter also contains an outlook on the application of the method in Brownian token-based computing and in the study of the melting of skyrmion lattices based on our publications

- Maarten A. Brems, Mathias Kläui and Peter Virnau, ”Circuits and excitations to enable Brownian token-based computing with skyrmions”, *Applied Physics Letters* **119**, 132405 (2021) (Ref. [29])

and

- Raphael Gruber, Jan Rothörl, Simon M. Fröhlich, Maarten A. Brems, Fabian Kammerbauer, Maria-A. Syskaki, Elizabeth M. Jefremovas, Sachin Krishnia, Asle Sudbø, Peter Virnau, and Mathias Kläui, ”Real-time observation of topological defect dynamics mediating two-dimensional skyrmion lattice melting”, *Nature Nanotechnology*, in press (2025) (Ref. [34]),

respectively. Chapter 6 is entirely dedicated to skyrmion-based unconventional computing. Reservoir computing is a computing paradigm that leverages the complex non-linear behavior of a physical system to map a complicated problem to a much simpler linear problem [45–49]. It provides fast learning at low computational costs. Several theoretical concepts for skyrmion-based reservoir computing have been proposed [25–28, 50]. However, experimental realizations had previously remained elusive. We combine the reservoir and Brownian computing [28–30, 51, 52] paradigms, exploiting the skyrmions' thermal random motion. We develop and experimentally demonstrate a skyrmion-based Brownian reservoir computer. Chapter 6 is mainly based on our publication

- Klaus Raab, Maarten A. Brems, Grischa Beneke, Takaaki Dohi, Jan Rothörl, Fabian Kammerbauer, Johan H. Mentik, M. Kläui, "Brownian reservoir computing realized using geometrically confined skyrmion dynamics", *Nature Communications* **13**, 6982 (2022) (Ref. [31])

with the introduction to reservoir and Brownian computing for the comparison of the general operating principles to our device design based on our review/perspective publication

- Oscar Lee, Robin Msiska, Maarten A. Brems, Mathias Kläui, Hidekazu Kurebayashi, Karin Everschor-Sitte, "Perspective on unconventional computing using magnetic skyrmions", *Applied Physics Letters* **122**, 260501 (2023) (Ref. [28]),

and our scientific outreach publication

- Maarten A. Brems, Klaus Raab, Peter Virnau, Mathias Kläui, "Brownscher Reservoir-Computer mit Skyrmionen", *Physik in unserer Zeit* **54**, 60-61 (2023) (Ref. [53]).

The discussion on the advantages of employing diffusion enhancement mechanisms in this kind of devices is based on our international patent disclosure

- Maarten A. Brems, Mathias Kläui, Peter Virnau, "Information Processing Apparatus", *International Patent disclosure*, WO2022200504A1 (2022) (Ref. [30]),

and the outlook on the use of time-dependent inputs is based on our publication

- Grischa Beneke, Thomas B. Winkler, Klaus Raab, Maarten A. Brems, Fabian Kammerbauer, Pascal Gerhards, Klaus Knobloch, Sachin Krishnia, Johan H. Mentink, Mathias Kläui, "Gesture recognition with Brownian reservoir computing using geometrically confined skyrmion dynamics", *Nature Communications* **15**, 8103 (2024) (Ref. [32]).

Chapter 7 revisits and discusses the results presented in this thesis, and provides an outlook on possible future research directions. The appendix chapter A contains detailed contribution statements for each chapter. It also includes additional information and results organized by the associated main chapters. Finally, the appendix also briefly discusses side projects in the field of biophysics, on which I worked during the time of my PhD, but which are unrelated to my research on skyrmions. The associated publications are

- Maarten A. Brems, Robert Runkel, Todd O. Yeates, Peter Virnau, „AlphaFold predicts the most complex protein knot and composite protein knots", *Protein Science* **31**, (8):e4380 (2022) (Ref. [54]),

- Jan Rothörl, Maarten A. Brems, Tim J. Stevens, Peter Virnau, "Reconstructing diploid 3D chromatin structures from single cell Hi-C data with a polymer-based approach", *Frontiers in Bioinformatics* **3**, 1284484 (2023) (Ref. [55]).

2. Background

While the subsequent chapters of this thesis aim to provide sufficient context for understanding the presented research results, this chapter contains additional background information regarding the studied systems and employed methods. Even though this thesis is about magnetic skyrmions, I would associate the presented research closely with fundamental statistical mechanics and additionally with the field of magnetism. Still, this chapter starts with a brief overview of the magnetic effects relevant for the stabilization and dynamics of skyrmions. The purpose of this overview is to provide an intuitive understanding of these underlying magnetic effects. Then, we turn to the quasi-particle description of skyrmions, which is central to this thesis. After comparing the simulation methods associated with the micromagnetic and quasi-particle descriptions of skyrmions, two unconventional computing paradigms are discussed, which are relevant for the device development part of this thesis. While my contributions to the results presented in this thesis are of a theoretical nature, the research was conducted in close collaboration with several experimental physicists from the group of [redacted]. Therefore, the final section of this chapter provides a brief introduction to some relevant experimental concepts.

2.1 Magnetism Overview

This magnetism overview is structured as follows: First, the origin of magnetic moments and the energy terms associated with different magnetic interactions are introduced. These fundamental topics are well-covered in literature and the brief corresponding sections are mainly based on different textbooks pointed out at the beginning of the section. After summarizing the interpretations of the magnetic energy terms, we turn to the magnetization dynamics, motivate the Landau-Lifshitz-Gilbert equation, and discuss its numerical solution via micromagnetic simulations. As the majority of the simulations performed in this thesis are quasi-particle Thiele model simulations (section 2.2.2) and micromagnetic simulations are a vast topic extensively covered in literature, the discussion here focuses specifically on aspects of micromagnetic simulations relevant for the simulation of skyrmions (subject to thermal fluctuation).

2.1.1 Microscopic Origin of Magnetism

We start with a brief introduction of electron magnetic moments as the microscopic origin of magnetism based on the textbook by J. M. D. Coey (Ref. [56]). The macroscopic magnetism of solids originates from the interacting electronic magnetic moments on a microscopic lenght scale. In general, microscopic magnetism is closely tied to angular momentum, in particular to the electron's intrinsic spin angular momentum. The connection between magnetism and angular momentum was experimentally demonstrated via the Einstein-de Haas effect [57]: A suspended ferromagnetic rod starts turning when its magnetization direction is reversed. Electrons, protons, and neutrons possess an intrinsic angular momentum, spin, of $1/2\,\hbar$, where $\hbar$ is the reduced Planck constant. Moreover, the electron's orbital motion around the nucleus is an additional source of angular momentum. Because of the nucleons drastically larger mass, nuclear spin creates much smaller magnetic moments compared to electric spin and is therefore often neglected. In the following, the electric orbital and spin magnetic moments are discussed.

The orbital magnetic moment μ expressed via the electron charge $-e$, mass m_e and orbital angular momentum ℓ given by

$$\mu = -\frac{e}{2m_e}\ell \tag{2.1}$$

can be rationalized in the context of the Bohr model of the atom in which the electrons revolve around the nucleus in circular orbits. The equivalent current of the orbital motion is $I = -e/\tau$, where the period τ depends on the orbit radius r and absolute electron velocity v via $\tau = 2\pi r/v$. The magnetic moment of a current loop with area A is $\mu = IA$ which can be rewritten using the aforementioned relations as $\mu = -\frac{1}{2}erv$. Comparing this expression with the angular momentum in the Bohr model $\ell = m_e rv$ gives Eqn. (2.1). The quantization of the orbital angular momentum in units of $\hbar$ translates into a quantization of the magnetic moment in a particular direction, conventionally chosen as the z-direction,

$$\mu_z = -\frac{e}{2m_e}m_\ell\hbar, \tag{2.2}$$

where $m_\ell = 0, \pm1, \pm2, \ldots$ is the orbital magnetic quantum number. The direction of the magnetic moment opposes the direction of the orbital angular momentum because of the negative electron charge. The Bohr magneton

$$\mu_\mathrm{B} \coloneqq \frac{e\hbar}{2m_e} \tag{2.3}$$

acts as the natural unit for magnetic moments which allows to express the ratio between the magnitude of the magnetic moment and the responsible angular momentum in terms of a dimensionless factor

$$g \coloneqq \frac{(|\mu|/\mu_\mathrm{B})}{(|\ell|/\hbar)}, \tag{2.4}$$

called the g-factor, which is 1 for orbital angular momentum. This factor is useful, for instance, for comparing sources of magnetic moments. In addition to the orbital angular momentum, the electron possesses an intrinsic spin angular momentum. The latter cannot be rationalized via any orbital motion and instead arises as a consequence of relativistic quantum mechanics. Still, it creates an associated intrinsic magnetic moment which exhibits a g-factor of around 2. So, spin angular momentum is about twice as effective at creating a magnetic moment than orbital angular momentum. Electron spin and its eigenvalues are further discussed in section 2.1.2.2.

Beyond this basic introduction, a few thing should be kept in mind: For atoms and ions, one must consider the total angular momentum of the many-electron state. Moreover, spin and orbital angular momentum may couple through spin-orbit interaction to form the total angular momentum, which determines the electronic magnetic moment. This coupling originates from relativistic corrections to the electron's motion. Still, it is conventional when discussing magnetic interactions to talk in terms of spin and employ the letter S. This convention is rooted in the fact that the orbital contribution is often negligible in equilibrium, in particular in the 3d metal systems commonly studied in textbooks.

2.1.2 Magnetic Energy Terms

2.1.2.1 Micromagnetic Description of Magnetism

While the atomistic description of magnetism models individual atomic magnetic moments, the coarse-grained micromagnetic model acts in the continuum approximation. The underlying atomistic structure is averaged away to represent the magnetization $\vec{M}(\vec{r})$ as a smoothly varying vector field of constant magnitude that is generally assumed to be slowly varying in both space and time [56]. Often, the reduced magnetization $\vec{m}(\vec{r})$ of unit magnitude is considered, which is related to the magnetization via

$$\vec{M}(\vec{r}) = M_{\mathrm{s}}\vec{m}(\vec{r}), \tag{2.5}$$

where M_{s} is the saturation magnetization. From a simulation point of view, the key advantage of the micromagnetic model is the reduced computational cost that arises when a suitable discretization of the magnetization requires significantly fewer cells than the number of magnetic moments in the corresponding atomistic model. Micromagnetic simulations are discussed in section 2.1.4. For the description of skyrmions, Thiele model [40] simulations offer an even more drastic reduction in computational cost by treating skyrmions as particles without explicitly modeling their internal structure. Micromagnetic and Thiele model simulations are compared in section 2.2.9.

While this thesis predominantly employs Thiele model simulations, some micromagnetic simulations, and no atomistic simulations, it is often helpful to begin the explanation of the magnetic energy terms with an atomistic description. Several competing conventions exist for expressing the energy terms. Here, the primary objective is to gain an intuitive understanding of how the various energetic contributions affect the system, which is then summarized in section 2.1.2.6. Still, to maintain consistency, the micromagnetic energy terms are formulated following the conventions used in the publication ”The design and verification of MuMax3” (Ref. [58]) since MuMax3 is the micromagnetic simulation software employed in this thesis.

2.1.2.2 Exchange Interaction

For many magnetic materials, exchange interactions are the dominant effect responsible for magnetic order. The following explanations of the exchange interaction, the Heisenberg model, and the micromagnetic description of the exchange interaction are based on the textbook by Stephen Blundell (Ref. [59]). As the starting point, the concept of exchange interaction is introduced via a simple two-electron model. At the origin of the exchange interaction is the fact that electrons are indistinguishable fermions with half-integer spin. The spin-statistics theorem [60] therefore dictates that the quantum mechanical total wave function of any system of identical electrons must be antisymmetric under exchange of any two electrons. This is related to the Pauli exclusion principle [61], which states that two electrons cannot be in the same quantum state, as the only wave function antisymmetric under exchange of two electrons with identical quantum states is zero everywhere. In the following, we assume that the spin and spatial degrees of freedom are separate in the sense that the total wave function $\Psi_{\text{Spin}}\left(\vec{r}_1, \vec{r}_2\right)$ can be expressed as the product of a spatial wave function ψ and a spin wave function χ_{Spin}, i.e.,

$$\Psi_{\text{Spin}}\left(\vec{r}_1, \vec{r}_2\right) = \psi\left(\vec{r}_1, \vec{r}_2\right) \cdot \chi_{\text{Spin}}, \tag{2.6}$$

where $\vec{r}_i$ is the position of electron i. Thus if χ_{Spin} is symmetric then ψ must be antisymmetric and vice versa. Combining two spin-1/2 particles results in a joint state with spin quantum number either $S = 0$ (antisymmetric) or $S = 1$ (symmetric), which are referred to as singlet (S) and triplet (T) states due to their respective degeneracy. We are now interested in finding an effective Hamiltonian $\hat{\mathcal{H}}$ to obtain the energies of the two states

$$\begin{aligned} E_{\text{S}} &= \int \Psi_{\text{S}}^* \hat{\mathcal{H}} \Psi_{\text{S}} \mathrm{d}\vec{r}_1 \mathrm{d}\vec{r}_2 \\ E_{\text{T}} &= \int \Psi_{\text{T}}^* \hat{\mathcal{H}} \Psi_{\text{T}} \mathrm{d}\vec{r}_1 \mathrm{d}\vec{r}_2. \end{aligned} \tag{2.7}$$

For this, we exploit that the total spin operator's expectation value takes the form

$$\left\langle \vec{S}^2 \right\rangle = \left\langle \left(\vec{s}_1 + \vec{s}_2\right)^2 \right\rangle = \left\langle \vec{s}_1^{\,2} \right\rangle + \left\langle \vec{s}_2^{\,2} \right\rangle + 2\left\langle \vec{s}_1 \cdot \vec{s}_2 \right\rangle = \frac{3}{2} + 2\left\langle \vec{s}_1 \cdot \vec{s}_2 \right\rangle. \tag{2.8}$$

The spin eigenvalue (using spin angular momenta normalized by $\hbar$) is given [59] by $\left\langle \vec{s}^{\,2} \right\rangle = s(s+1)$ and we can therefore conclude from the above equation

$$\left\langle \vec{s}_1 \cdot \vec{s}_2 \right\rangle = \begin{cases} \frac{1}{4} & \text{if} \quad S = 1 \\ -\frac{3}{4} & \text{if} \quad S = 0 \end{cases} \tag{2.9}$$

The effective Hamiltonian can therefore be expressed as

$$\hat{\mathcal{H}} = \frac{1}{4}\left(E_{\text{S}} + 3E_{\text{T}}\right) - \left(E_{\text{S}} - E_{\text{T}}\right)\left\langle \vec{s}_1 \cdot \vec{s}_2 \right\rangle, \tag{2.10}$$

where the constant first term is neglected due to gauge invariance. The prefactor can be determined by constructing the total wave functions to be antisymmetric in both cases as discussed above

$$\begin{aligned} \Psi_{\text{S}} &= \frac{1}{\sqrt{2}}\left[\psi_a\left(\vec{r}_1\right)\psi_b\left(\vec{r}_2\right) + \psi_a\left(\vec{r}_2\right)\psi_b\left(\vec{r}_1\right)\right]\chi_{\text{S}} \\ \Psi_{\text{T}} &= \frac{1}{\sqrt{2}}\left[\psi_a\left(\vec{r}_1\right)\psi_b\left(\vec{r}_2\right) - \psi_a\left(\vec{r}_2\right)\psi_b\left(\vec{r}_1\right)\right]\chi_{\text{T}}, \end{aligned} \tag{2.11}$$

resulting in

$$\hat{\mathcal{H}} = -J\left\langle \vec{s}_1 \cdot \vec{s}_2 \right\rangle \tag{2.12}$$

with the exchange constant

$$J := E_{\text{S}} - E_{\text{T}} = \int \psi_a^*\left(\vec{r}_1\right)\psi_b^*\left(\vec{r}_2\right)\hat{\mathcal{H}}\psi_a\left(\vec{r}_2\right)\psi_b\left(\vec{r}_1\right)\mathrm{d}\vec{r}_1 \ \mathrm{d}\vec{r}_2. \tag{2.13}$$

So, for $J > 0$ the triplet state $S = 1$ is favored and for $J < 0$ the singlet state $S = 0$ is preferred. Eqn. (2.12) motivates the atomistic Heisenberg model [62]

$$E_{\mathrm{ex}} = -\sum_{i>j} \mathrm{J}_{ij} \vec{S}_i \cdot \vec{S}_j, \tag{2.14}$$

where $\vec{S}_i$ represents the semi-classical spin of atom i and the sum goes over all pairs of particles without double counting. The exchange constants J_{ij} are specific for each pair of spins, but often only nearest neighbor interactions in the crystal lattice are considered with the same exchange constant J for each pair. Fig. 2.1 schematically illustrates preferred arrangements for positive and negative nearest neighbor exchange constants associated with ferromagnetic and antiferromagnetic ordering, respectively.

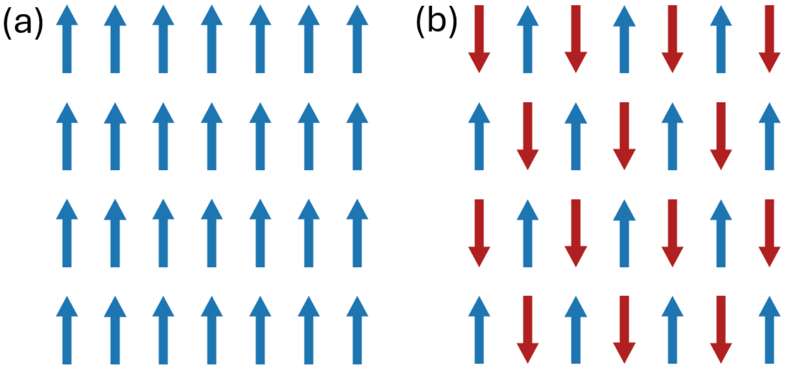

Figure 2.1: Schematic illustration of preferred arrangements of magnetic moments (same orientation highlighted by matching color) interacting via nearest neighbor exchange interaction with a positive exchange constant (a, ferromagnetic) and a negative exchange constant (b, antiferromagnetic).

To represent the nearest neighbor Heisenberg model in the micromagnetic continuum approximation, we express the nearest neighbor variant of Eqn. (2.14) in terms of the angle between neighboring spins ϕ_{ij}. The latter is assumed to be sufficiently small such that Taylor expansion to second order is a valid approximation of the cosine in

$$E_{\mathrm{ex}} = -JS^2 \sum_{<ij>} \cos\phi_{ij} = \text{ constant } + \frac{JS^2}{2} \sum_{<ij>} \phi_{ij}^2. \tag{2.15}$$

Here, $< ij >$ refers to pairs of neighboring spins and $S =| \vec{S}_i | \, \forall i$. Expressed in terms of the reduced magnetization $\vec{m}$ (Eqn. (2.5)) evaluated at two lattice points separated by $\vec{r}_{ij}$, one can approximate

$$|\phi_{ij}| \approx |\vec{m}_i - \vec{m}_j| \approx |(\vec{r}_{ij} \cdot \nabla)\, \vec{m}| \,. \tag{2.16}$$

In the continuum limit the exchange energy can therefore be expressed in the form

$$E_{\mathrm{ex}} = A_{\mathrm{ex}} \int_V \left[(\nabla m_x)^2 + (\nabla m_y)^2 + (\nabla m_z)^2 \right] \mathrm{d}^3 r, \tag{2.17}$$

where A_{ex} is the micromagnetic exchange constant.

2.1.2.3 Dzyaloshinskii-Moriya interaction

The Dzyaloshinskii-Moriya interaction (DMI) [63, 64], also referred to as antisymmetric exchange, favors chiral canting of spins instead of the alignment preferred by the (symmetric) exchange interaction discussed above. Therefore, it can stabilize complex magnetic structures. The following brief introduction of DMI and its micromagnetic continuum description is based on the publication Ref. [65] by Robert E. Camley and Karen L. Livesey. DMI arises in systems with broken inversion symmetry and strong spin-orbit-coupling. Here, we focus on the case where the inversion symmetry is broken by an interface between a ferromagnetic material and a material with strong spin-orbit-coupling such as a heavy metal (Fig. 2.2). Such configurations occur in the thin film multilayer stacks relevant for this thesis (section 2.4.1). The DMI energy has the form

$$E_{\mathrm{DMI}} = \vec{D}_{ij}\left(\vec{S}_i \times \vec{S}_j\right), \tag{2.18}$$

where $\vec{D}_{ij}$ is the DMI vector, which, for interfacial DMI, is perpendicular to both the symmetry-breaking out-of-plane direction and the vector connecting sites i and j as illustrated in Fig. 2.2. Due to the cross-product, the sign changes if $\vec{S}_i$ and $\vec{S}_j$ are swapped in contrast to the Heisenberg exchange energy in Eqn. (2.14). This property motivates the name ”antisymmetric exchange”.

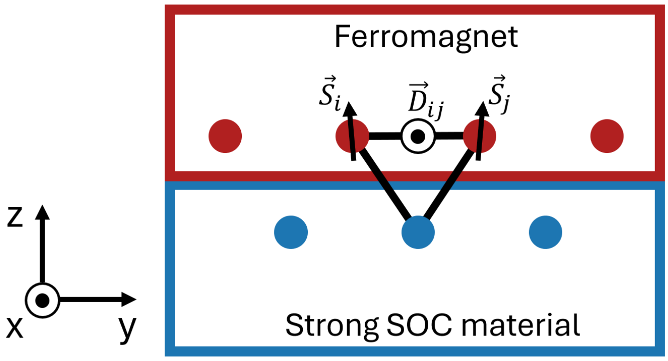

Figure 2.2: Schematic illustration of a system exhibiting interfacial DMI, where a ferromagnetic layer is on top of a layer with strong spin-orbit-coupling (SOC). Vectors going out of the plane are represented by a dot inside a circle. The DMI vector is indicated for a particular pair of spins. Bold dots represent atoms. This figure is inspired by Ref. [23] but with a perspective chosen to also aid in the derivation of the DMI energy’s continuum approximation.

To derive the micromagnetic continuum approximation of the DMI energy, we consider a simplified system consisting of a chain of semi-classical spins arranged along the y-direction with a nearest neighbor distance a. So, each site i has two neighbor sites $i-1$ and $i+1$. The DMI vector is assumed to be the same for all site pairs and oriented in the x-direction as in Fig. 2.2, consequently with only one non-zero component D_{ij}. Based on Eqn. (2.18), the DMI energy associated with site i is then

$$\begin{aligned} E_{\mathrm{DMI}} &= D_{ij}\left(S^z_{i-1}S^y_i - S^y_{i-1}S^z_i\right) + D_{ij}\left(S^z_i S^y_{i+1} - S^y_i S^z_{i+1}\right) \\ &= 2D_{ij}a\left(S^z_i\left(\frac{S^y_{i+1}-S^y_{i-1}}{2a}\right) - S^y_i\left(\frac{S^z_{i+1}-S^z_{i-1}}{2a}\right)\right) \\ &\approx 2D_{ij}a\left(S^z_i\frac{\partial S^y}{\partial y_i} - S^y_i\frac{\partial S^z}{\partial y_i}\right), \end{aligned} \tag{2.19}$$

where the final step assumes the spin direction varies slowly enough such that the finite difference approximation for the derivative evaluated at site i is valid. Expressed in terms of the reduced magnetization, the DMI energy is

$$E_{\mathrm{DMI}} = D\int_V \left(m_z\frac{\partial m_y}{\partial y} - m_y\frac{\partial m_z}{\partial y}\right)\mathrm{d}^3r, \tag{2.20}$$

where the micromagnetic DMI constant D depends on the underlying atomic structure. For instance assuming a simple cubic lattice where the volume occupied by one spin site is a^3, $D = 2D_{ij}/a^2$. Generalized forms of Eqn. (2.20) exist [58, 65]. Importantly, Eqn. (2.20) shows that there is a prefered chirality in the system: if there is a gradient in the magnetization, the energy depends on whether the magnetization component is increasing to left or right direction. Therefore, DMI can act to stabilize chiral structures such as skyrmions (section 2.2.1).

2.1.2.4 Zeeman and Stray Field Energy

Magnetostatic effects, i.e. the interaction with an external magnetic field (Zeeman interaction) or the field created by the magnetic body itself (stray field), are typically weak compared to the close-range exchange interaction. However, they are often crucial for the system's domain structure due to the long-ranged nature of the dipole-dipole interaction. Here, the Zeeman and stray field energy are introduced based on the textbook by J. M. D. Coey (Ref. [56]).

If a system of magnetic moments is exposed to a magnetic field $\vec{H}$, they favor alignment with the field. In terms of the magnetization $\vec{M}$, the corresponding energy contribution is

$$E_{\mathrm{Zeeman}} = -\mu_0\int_V \vec{M}(\vec{r})\cdot\vec{H}(\vec{r})\ \mathrm{d}^3r, \tag{2.21}$$

where μ_0 is the vacuum magnetic permeability. In the case of an applied external magnetic field $\vec{H} = \vec{H}_{\mathrm{ext}}$, this is the Zeeman energy. If the magnetic field originates from the magnetic material itself, the expression gains a factor 1/2 to avoid double-counting as each magnetic moment contributes as a field source and as a moment experiencing the field. For two parallel magnetic moments side by side "↑↑", the dipole field of one opposes the orientation of the other. Therefore, the stray field is usually called demagnetization field $\vec{H}_{\mathrm{d}}$ inside the magnetic material. The corresponding energy term is

$$E_{\mathrm{demag}} = -\frac{1}{2}\mu_0\int_V \vec{H}_{\mathrm{d}}(\vec{r})\cdot\vec{M}(\vec{r})\ \mathrm{d}^3r. \tag{2.22}$$

Determining the demagnetization field in large systems is often one of the computationally most expensive aspects of micromagnetic simulations due to the non-local interaction. Several approaches exist for its computation [56, 58] as well as an approximation via reduced effective anisotropy often employed for predominantly perpendicularly magnetized thin film systems. This approximation is introduced in the subsequent discussion of magnetic anisotropy. Before turning to magnetic anisotropy, we discuss one concept for modeling stray fields that is particularly helpful to gain an intuitive understanding: Equivalent distributions of "magnetic charge". This approach employs a representation of the system via equivalent magnetic bulk and surface charges defined as

$$\rho = -\nabla \cdot \vec{M} \quad \text{and} \quad \sigma = \vec{M} \cdot \vec{e}_{\mathrm{n}}, \tag{2.23}$$

respectively, where $\vec{e}_{\mathrm{n}}$ is the surface normal vector. Similar to electrostatics, the resulting magnetic field can then be expressed via [56]

$$\vec{H}_{\mathrm{d}}(\vec{r}) = \frac{1}{4\pi} \left\{ -\int_V \frac{\left(\nabla' \cdot \vec{M}\right)(\vec{r}-\vec{r}')}{|\vec{r}-\vec{r}'|^3} \, \mathrm{d}^3 r' + \int_S \frac{\vec{M} \cdot \vec{e}_{\mathrm{n}} \, (\vec{r}-\vec{r}')}{|\vec{r}-\vec{r}'|^3} \, \mathrm{d}^2 r' \right\}, \tag{2.24}$$

where the first integral is over the volume of the magnetic material and the second one is over its surface. The concept of surface charge penalty is particularly helpful to qualitatively gauge the demagnetization energy of different magnetization configurations such as in Fig. 2.3. To avoid surface charges, it is preferable if the magnetization is aligned along the magnets surface instead of perpendicular to it. This favors flux-closure states as depicted in Fig. 2.3b.

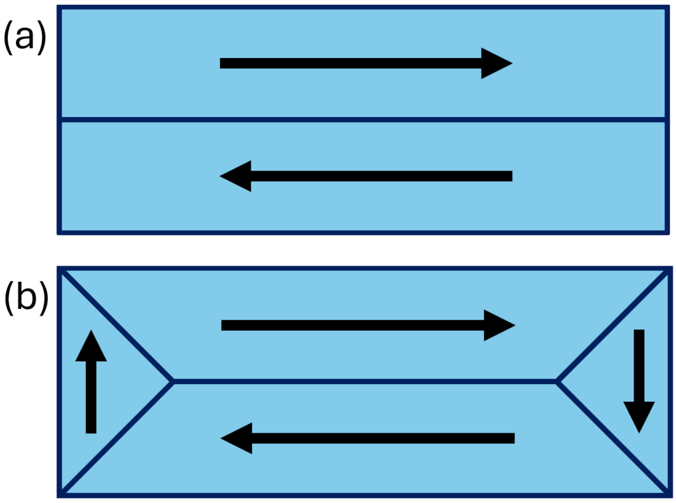

Figure 2.3: Schematic illustration of two different domain structures. Blue-shaded regions indicate magnetic domains, with a black arrow indicating the dominant magnetization direction within each region. The configuration in (a) avoids magnetic surface charges on the long side of the rectangle but still exhibits them on the short side. The flux-closure state in (b) generates less surface charges overall and exhibits lower demagnetization energy.

2.1.2.5 Magnetic Anisotropy

There are several scenarios where the energy of a magnetically ordered system is not invariant under an overall rotation of the magnetization. This magnetic anisotropy can have several origins, including the underlying crystal structure and the geometry (shape) of the magnetic material. Here, uniaxial magnetocrystalline anisotropy is briefly introduced based on the textbook by Rudolf Gross and Achim Marx (Ref. [66]).

Magnetocrystalline anisotropy is linked to the overlap of electron wave functions in atomic lattices. Depending on the crystal structure, the electron wave function can be affected by the interaction of the atomic lattice and the orbital magnetic moment via spin-orbit-coupling leading to different overlaps depending on the alignment of the magnetization with certain symmetry-breaking axes. As a result, some orientations can become energetically favorable (easy axes) while others are energetically penalized (hard axes). In the micromagnetic approximation, such effects are usually modeled phenomenologically by including an additional energy term that depends on the alignment with specific axes. Systems with only one preferred axis exhibit uniaxial anisotropy. The anisotropy direction is usually expressed via a unit vector $\vec{u}$, but parallel and antiparallel orientations are energetically equivalent.

The skyrmion-hosting systems discussed in the thesis exhibit perpendicular magnetic anisotropy (PMA), i.e., the preferred axis of orientation is perpendicular to the extent of the thin film or, phrased differently, along the short direction of the material conventionally labeled "z". The phenomenological energy density for uniaxial anisotropy is usually a power series expansion of $\vec{u} \cdot \vec{m}$ terms [58]

$$E_{\mathrm{anis}}/V = -K_{\mathrm{u1}}(\vec{u} \cdot \vec{m})^2 - K_{\mathrm{u2}}(\vec{u} \cdot \vec{m})^4 + \dots \tag{2.25}$$

that exhibits the correct symmetry, i.e. it includes only even terms since the anisotropy is uniaxial but not unidirectional. Here K_{u1} and K_{u2} are the uniaxial anisotropy constants of first and second order, respectively. Often, only the lowest order term is considered.

Modeling uniaxial anisotropy in this way allows for an efficient approximation of the demagnetization energy of extended thin film systems with PMA. Instead of explicitly modeling the demagnetization energy via Eqn. (2.22), the effect is approximated as a reduction of the PMA strength [67]

$$K_{\mathrm{eff}} = K_{\mathrm{u}} - \frac{1}{2}\mu_0 M_{\mathrm{s}}^2. \tag{2.26}$$

2.1.2.6 Summary of Magnetic Energy Terms

In most real magnetic system, the magnetization configuration arises due to a competition of multiple of the energy terms introduced above. Below, the effects of the different contributions are summarized to facilitate an intuitive understanding of the competition of interactions and resulting magnetic structures.

- Ferromagnetic Exchange: Parallel orientation of all spins is favored independent of the overall orientation of the magnetization. This leads to homogeneous magnetization.

- DMI: Perpendicular orientation of spins is favored leading to spiral states of a fixed chirality and spin canting.
- Zeeman Interaction: Alignment with the applied external magnetic field is favored.
- Stray Field: Minimization of magnetic volume and surface charges is favored. In particular, magnetization perpendicular to the material's surface is penalized, leading to flux-closure states.
- PMA: In thin films with perpendicular magnetic anisotropy, orientation of spins along the anisotropy axes (out-of-plane direction) is favored independent of whether they point in the $+z$ or $-z$ direction.

2.1.3 Magnetization Dynamics: The Landau-Lifshitz-Gilbert Equation

The energy terms discussed above determine the favorable magnetization configuration of a system given the material parameters and external conditions such as applied fields. However, simple energy minimization methods do not address the question of how the magnetization evolves in time. This section phenomenologically motivates the Landau-Lifshitz-Gilbert (LLG) equation [68], inspired by Refs. [68–70].

The LLG equation is a differential equation for the time-dependent magnetization which is typically employed in micromagnetic simulation software [58]. As a starting point for its motivation, we consider a single magnetic moment $\vec{\mu}$ in a field $\vec{H}$, at first without damping effects. In that case, the magnetic moment precesses around the axis determined by $\vec{H}$ due to the acting torque [69, 70]

$$\tau = \mu_0 \vec{\mu} \times \vec{H}. \tag{2.27}$$

Knowing the torque allows us to employ Newton's second law for angular motion

$$\tau = \frac{\mathrm{d}\vec{L}}{\mathrm{d}t} \tag{2.28}$$

using the corresponding angular momentum given by

$$\vec{L} = -\frac{1}{\gamma_{\mathrm{GR}}}\vec{\mu}, \tag{2.29}$$

where γ_{GR} is the gyromagnetic ratio[1]. The corresponding equation of motion is consequently given by

$$\frac{\mathrm{d}\vec{\mu}}{\mathrm{d}t} = -\mu_0 \gamma_{\mathrm{GR}} \vec{\mu} \times \vec{H}. \tag{2.30}$$

However, because we ignored damping effects, this pure precession fails to align the magnetic moment with the field to reach the energy minimum. Therefore, a phenomenological

---

[1] The gyromagnetic ratio γ_{GR} is not to be confused with the effective damping parameter for skyrmions labeled γ, which is introduced in section 2.2.2. The gyromagnetic ratio appears only rarely in this thesis and is explicitly marked as γ_{GR}. Furthermore, the effective skyrmion damping parameter γ should also not to be confused with the Gilbert damping α introduced in this section. The relation between Gilbert damping and the effective skyrmion damping is discussed in section 2.2.3.

damping torque is introduced [68]. Since the magnitude of the magnetic moment is constant, this damping term should be orthogonal to both $\vec{\mu}$ and $\mathrm{d}\vec{\mu}/\mathrm{d}t$. To quantify the strength of this damping torque, the dimensionless Gilbert damping parameter α is introduced, resulting in the equation of motion [68–70]

$$\frac{\mathrm{d}\vec{\mu}}{\mathrm{d}t} = -\mu_0 \gamma_{\mathrm{GR}} \vec{\mu} \times \vec{H} + \frac{\alpha}{|\vec{\mu}|} \vec{\mu} \times \frac{\mathrm{d}\vec{\mu}}{\mathrm{d}t}. \tag{2.31}$$

This is the implicit LLG equation for a single magnetic moment. For the equivalent equation of motion for the magnetization of a material, we need to express all energy terms via an effective field given by the variation of the energy terms

$$\vec{H}_{\mathrm{eff}} := -\frac{1}{\mu_0} \frac{\delta E}{\delta \vec{M}} = \vec{H}_{\mathrm{ex}} + \vec{H}_{\mathrm{anis}} + \vec{H}_{\mathrm{demag}} + \vec{H}_{\mathrm{Zeeman}} + \vec{H}_{\mathrm{DMI}}. \tag{2.32}$$

While the resulting implicit LLG equation for the magnetization [68–70]

$$\frac{\mathrm{d}\vec{M}}{\mathrm{d}t} = -\mu_0 \gamma_{\mathrm{GR}} \vec{M} \times \vec{H}_{\mathrm{eff}} + \frac{\alpha}{M_{\mathrm{S}}} \vec{M} \times \frac{\mathrm{d}\vec{M}}{\mathrm{d}t} \tag{2.33}$$

is easy to interpret via the above motivation, it is converted into the explicit form [58]

$$\frac{\mathrm{d}\vec{M}}{\mathrm{d}t} = -\gamma'_{\mathrm{GR}} \vec{M} \times \vec{H}_{\mathrm{eff}} - \frac{\gamma'_{\mathrm{GR}} \alpha}{M_{\mathrm{S}}} \vec{M} \times \left(\vec{M} \times \vec{H}_{\mathrm{eff}} \right) \tag{2.34}$$

for computational purposes, where $\gamma'_{\mathrm{GR}} := \gamma_{\mathrm{GR}} \mu_0 / (1 + \alpha^2)$. Fig. 2.4 illustrates the directions of the vector expressions at a specific point in space. The explicit LLG equation builds the foundation for the micromagnetic simulations discussed in the next section.

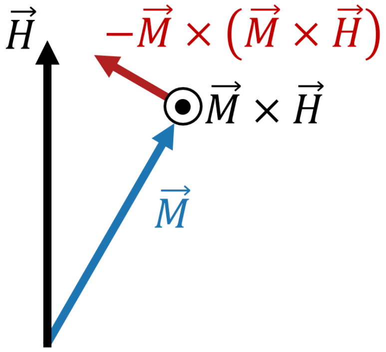

Figure 2.4: Illustration of the directions of the vector expressions occurring in the explicit LLG equation for a specific arrangement of the effective field (here just labeled $\vec{H}$ for simplicity) and the magnetization $\vec{M}$ at a specific position. Arrows indicate only the direction of the vector terms, not their magnitude, and arrows going out of the plane are represented by a dot inside a circle. The labels for the vector expressions are color-coded to match the arrows.

2.1.4 Micromagnetic Simulations

Many magnetic systems of interest are too complex for the LLG equation to be solved analytically. Consequently, micromagnetic simulations, which numerically solve the LLG equation, are a valuable research tool. Owing to their broad applicability, multiple ready-to-use software packages are available [58, 71–73]. While the majority of the simulations performed in this thesis are quasi-particle Thiele model simulations (section 2.2.2), a few micromagnetic simulations are employed to understand effects related to the internal skyrmion structure. The software employed in this thesis is MuMax3, chosen for its efficient GPU implementation, ease of use, and the option to model thermal fluctuations as discussed below.

Micromagnetic simulations operate iteratively, repeating the following two steps until the user-specified exit condition (for instance, a predetermined total runtime) is reached:

1. Determined the effective field $\vec{H}_{\text{eff}}$ for the current magnetization configuration $\vec{M}$.
2. Numerically advance the LLG equation to obtain the new magnetization configuration $\vec{M}$.

The second step is typically performed using higher order Runge-Kutta integrators[2] as they allow for on-the-fly adjustment of the integration time step to balance low numerical errors and fast simulation speeds. However, when simulating a system with thermal fluctuations, it is important to employ an integrator that does not require torque continuity between steps[3]: Thermal fluctuations are modeled using a randomly fluctuating thermal field

$$\vec{B}_{\text{therm}} = c(\mathrm{k_B T}, \mathrm{d}t)\, \vec{\eta}(\text{step}), \tag{2.35}$$

where $\vec{\eta}(\text{step})$ is a random vector from a standard normal distribution changed at every step, and $c(\mathrm{k_B T}, \mathrm{d}t)$ is constant[4] depending on the thermal energy $\mathrm{k_B T}$ and the magnitude of the time step $\mathrm{d}t$. This approach to model thermal fluctuation is conceptually similar to the approach for quasi-particle Thiele model simulations which is discussed in more detail in sections 2.2.3 and 2.2.9.

While the time step, which is the discretization of time, is usually automatically set by the software to match a given tolerance for numerical errors, the cell size, which is the discretization of space, is set by the user. Within a cell, the magnetization is constant. Choosing the right cell size is a crucial decision in setting up micromagnetic simulations: A larger cell size can drastically improve the simulation's performance. However, a too coarse discretization of the system can fail to capture essential effects on short length scales. To gauge the upper limit of the cell size still suitable for reliable simulation, one typically considers the competition of magnetic energy terms that determine the change in magnetization between neighboring cells.

---

[2] MuMax3's default is the Dormand-Prince method RK45 [58, 74].

[3] In that case MuMax3's default is the Heun integrator [58].

[4] For completeness, the constant is given by $c(\mathrm{k_B T}, \mathrm{d}t) := \sqrt{(2\mu_0 \alpha \mathrm{k_B T}) \,/\, (M_\mathrm{s} \gamma'_{\mathrm{GR}} \Delta V \mathrm{d}t)}$, where $\mathrm{k_B}$ the Boltzmann constant, T the temperature, M_s the saturation magnetization, and ΔV the cell volume [58].

First, we consider the competition of ferromagnetic exchange and magnetostatic effects. Below a certain length scale, exchange dominates, the magnetic moments essentially align, and the magnetization is in good approximation constant. Cell sizes sufficiently small compared to this length scale, called the (magnetostatic) exchange length l_{ex}, are therefore considered suitable. It is given by [58]

$$l_{\mathrm{ex}} := \sqrt{\frac{2A_{\mathrm{ex}}}{\mu_0 M_S^2}}\,. \tag{2.36}$$

In addition, the maximum magnetization canting between neighboring cells must be taken into account, in particular when studying systems containing domain walls, because the magnetization is assumed to be slowly varying. General rules of thumb are that the angle between the magnetization in neighboring cells should be significantly below 20 to 30 degrees [58] or, equivalently, a 180° domain wall should consist of at least 7 cells[5]. The important length scale typically considered in this context is

$$l_{\mathrm{DW}} := \sqrt{\frac{A}{K_{\mathrm{u}}}} \tag{2.37}$$

which captures the competition between exchange and anisotropy. It is related to the domain wall width [56].

When simulating thin film multilayer stacks, it is often computationally too expensive to simulate every layer explicitly. One way to overcome the prohibitive computational cost is the effective medium approximation [18], in which all layers of the single-repetition multilayer stack are represented by a single uniform ferromagnetic layer with scaled parameters. The scaling relations follow from the condition that the effective medium parameters yield the same dynamics according to the LLG equation as the real system, i.e.,

$$\frac{\mathrm{d}\vec{M}^*}{\mathrm{d}t} \overset{!}{=} \frac{\mathrm{d}\vec{M}}{\mathrm{d}t}, \tag{2.38}$$

where "*" indicates the value in the effective medium approximation. The scaling relations are derived in the supplementary material of Ref. [18] as

$$\frac{M_{\mathrm{S}}^*}{M_{\mathrm{S}}} = \frac{A_{\mathrm{ex}}^*}{A_{\mathrm{ex}}} = \frac{K^*}{K} = \frac{D^*}{D} = \frac{t_{\mathrm{mag}}}{t_{\mathrm{mag}}^*} = \frac{t_{\mathrm{mag}}}{t_{\mathrm{total}}}, \tag{2.39}$$

where t_{mag} and t_{total} are the thicknesses for the ferromagnetic layer and of all layers, respectively. It is important to check the reliability of the effective medium approximation for a given (large) system via comparison to simulations of the complete multilayer structure, for instance performed in smaller representative test systems. The parameters employed for the micromagnetic simulations in this thesis are either previously determined and tested effective medium parameters or typical parameters for studying general qualitative effects.

---

[5] Author's Mnemonic: "Seven cells must play their role to form a wall from pole to pole."

2.2 Magnetic Skyrmions and Their Quasi-Particle Modeling

While the concept of a skyrmion was originally introduced by Tony Skyrme as a model for baryons [75, 76], his mathematical description later turned out to suit a class of nanometer- to micrometer-sized magnetic textures referred to as magnetic skyrmions[6] [6–10]. These effectively two-dimensional, topologically stabilized magnetic textures exhibit quasi-particle behavior and have been observed in a variety of different systems [9, 77], including materials where they perform thermal diffusion [16, 17, 39]. A variety of external mechanisms to manipulate their dynamics, including electric currents [18–20], magnetic field gradients [21], and temperature gradients [78], as well as their quasi-particle nature, make skyrmions promising for applications in data storage [9, 23, 24] and computing [25–32]. Skyrmion research experienced a significant gain in interest over the past decades, with the yearly number of related publications more than quadrupling between 2010 and 2020 [65], and skyrmions recently even entering the realm of science fiction media [79]. Form a soft matter point of view, skyrmions are particularly interesting because they exhibit behavior that is in many ways similar to colloidal systems[7] [31, 33, 34], but with the benefits of an on-the-fly tunable size [36, 37], the ability to create and annihilate skyrmions [16, 35], the aforementioned variety of dynamics manipulation mechanisms, and good experimental access to the trajectories of micrometer-sized skyrmions via Kerr-microscopy [84].

In this thesis, we mainly focus on the coarse-grained quasi-particle description of skyrmions in the Thiele model [40], where skyrmions are represented as soft two-dimensional discs. While the parameters of the Thiele model can, in principle, be determined from the underlying magnetic structure, the detailed internal structure is often experimentally inaccessible, in particular in the presence of thermal fluctuations. Therefore, we are particularly interested in creating a quantitatively predictive model with parameters determined from experimental skyrmion trajectories only, without any assumptions about the skyrmions' internal magnetic structure or underlying magnetic interactions. The present section starts with an introduction to the internal structure of skyrmions, followed by a more elaborate discussion of the coarse-grained quasi-particle Thiele model where the internal structure is not explicitly modeled. This discussion is mainly structured around the different force terms in the Thiele equation of motion and their impact on skyrmion dynamics. The present section aims to provide the necessary background for performing Thiele model simulations by combining concepts and insights from various sources. The advantages and disadvantages of Thiele model and micromagnetic simulations are then summarized and compared in section 2.2.9.

2.2.1 Internal Skyrmion Structure

In this thesis, we consider effectively two-dimensional chiral Néel-type skyrmions with narrow domain walls. In the following, all building blocks of this statement are explained. A skyrmion is a magnetic texture, i.e., a localized pattern in the magnetization, which

---

[6] In this thesis the adjective "magnetic" is usually dropped as there is no risk of confusion. Only magnetic skyrmions are discussed.

[7] Note that colloids are also employed to research the behavior of effectively two-dimensional systems. For instance, colloids can be geometrically confined between two plates with a distance comparable to the particle diameter [80] or confined by gravity at a water-air interface [81–83].

can move as a whole[8] (soliton property for appropriate excitations) [9]. The skyrmion's internal structure consists of a circular region, the skyrmion core, that exhibits opposite magnetization compared to the surrounding magnetic material. The core is separated from the surrounding magnetic background by a 180° domain wall. Fig. 2.5 depicts two skyrmion structures illustrated in two different styles. Moreover, we predominantly consider micrometer-sized skyrmions in thin film systems, where the magnetic layer only has a thickness of a few nanometers (section 2.4.1). The extent of the skyrmion's magnetic structure is consequently orders of magnitudes larger in the in-plane direction than in the out-of-plane direction, such that any variation of the magnetization in the out-of-plane direction is usually neglected and the skyrmions are considered effectively two-dimensional in excellent approximation.

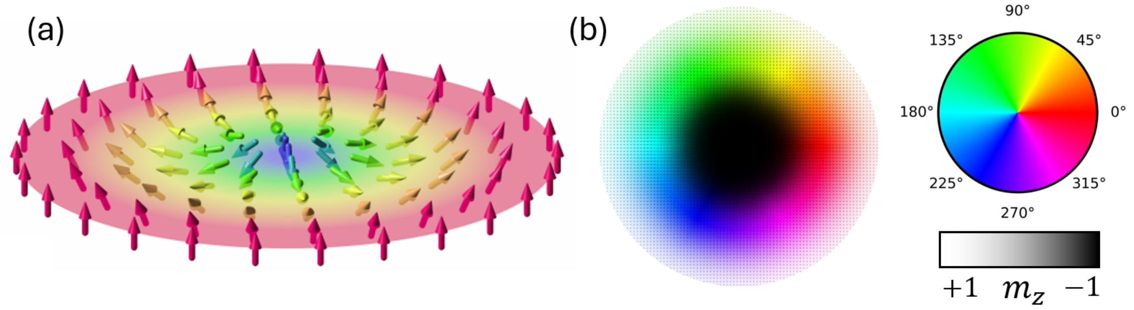

Figure 2.5: Depictions of internal skyrmion structures in two different styles showing a skyrmion with a smaller (a) and a larger (b) core. (a) A skyrmion represented by arrows indicating the spatially-resolved direction of the magnetization. The color code indicates the vertical magnetization with red and blue highlighting the magnetization pointing up and down, respectively. (b) A skyrmion represented by a two-dimensional image in which the spatially-resolved magnetization direction is shown entirely via the color code. The out-of-plane component of the magnetization is depicted using the lightness with white and black corresponding to out-of-the-page and into-the-page orientation, respectively. The hue indicates the polar angle of the in-plane component of the magnetization according to the color wheel on the right. The skyrmions in (a) and (b) have qualitatively the same structure, but the skyrmion in (b) exhibits a larger core compared to the skyrmions overall size. The magnetization at the center of the enclosing domain wall (colored ring in (b)) is pointing outwards everywhere in both structures. Both representations only show one layer of magnetization vectors in the out-of-plane directions as variations of the magnetization in the out-of-plane direction are usually neglected. The representation in (a) is adapted from the original of Karin Everschor-Sitte and Matthias Sitte, which is licensed under Creative Commons Attribution-Share Alike 3.0 Unported (CC BY-SA 3.0).

Even when the general structure of the skyrmion, from the center outwards: core – domain wall – magnetic background oriented opposite to core, is the same, there are different ways

---

[8] Note that the spatially inhomogeneous pinning effects discussed in section 2.2.7 can cause the skyrmion to deform. In addition, thermal fluctuation causes the internal skyrmion structure to fluctuate as well. A quasi-particle description with effective parameters is still applicable, because the skyrmion remains a localized structure despite these small deformations/fluctuations. The introduction here focuses on the case where pinning effects and thermal fluctuation are absent.

to classify skyrmions. The classifications considered here are all related to the skyrmion's domain wall, specifically its type, its chirality, and its width relative to the size of the entire skyrmion [85]. These three properties are discussed below.

Skyrmions are classified as Néel-type or Bloch-type depending on which kind of domain wall is present in the skyrmion. In Néel domain walls, the magnetization only turns in the plane of the wall, as shown in Fig. 2.6. The skyrmions in Fig. 2.5 are Néel-type skyrmions with Fig. 2.6a corresponding to the domain wall on the left in Fig. 2.5a. For the other type of domain walls, Bloch walls, the magnetization would turn perpendicular to the plane of the wall, like a corkscrew. Bloch walls are left beyond the scope of this thesis as the studied skyrmions are Néel-type. The formation of Néel walls is strongly supported by interfacial DMI, which then also sets the chirality of the domain wall and skyrmion, as elaborated on in the following.

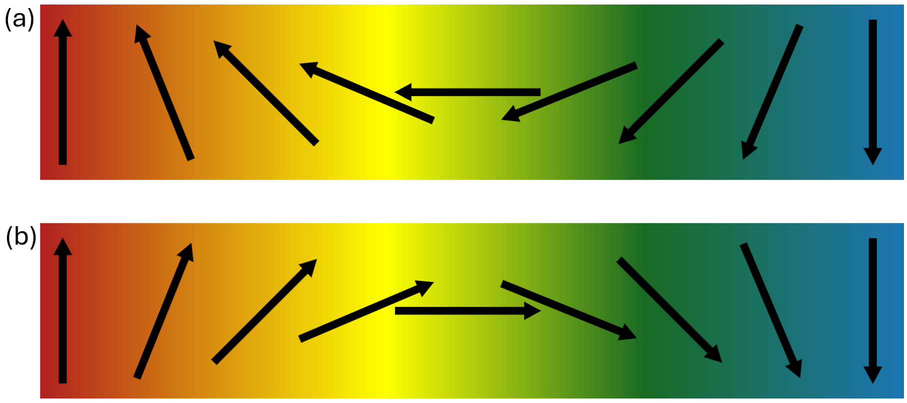

Figure 2.6: Schematic illustration of a left-handed (a) and right-handed (b) Néel domain wall. The arrows indicate the direction of the position-dependent magnetization, and the color code highlights the vertical component of the magnetization as in Fig. 2.5a. Viewed from left to right, the magnetization turns counterclockwise in (a) and clockwise in (b). (a) corresponds the side-view of the domain wall on the left in Fig. 2.5a. The depictions are schematic and are not meant to quantitatively represent the spatial dependence of the vertical magnetization component (compare Fig. 3.11).

Fig. 2.6a and Fig. 2.6b both depict Néel domain walls, but they exhibit different chiralities, i.e., the magnetization turns with a different sense of rotation – counterclockwise (left-handed) in Fig. 2.6a and clockwise (right-handed) in Fig. 2.6b. The chirality of the domain wall translates into the chirality of the skyrmion, with the one shown in Fig. 2.5a being left-handed. In systems with interfacial DMI like the ones studied in this thesis, one chirality is favored. This leads to all skyrmions (with the same core-orientation) exhibiting the same direction of gyrotropic force as discussed in section 2.2.4. An important quantity in this context is the topological winding number [9], which, for skyrmions in two-dimensions, is defined as

$$\mathcal{W} := \frac{1}{4\pi} \int \vec{m} \cdot \left(\frac{\partial \vec{m}}{\partial x} \times \frac{\partial \vec{m}}{\partial y} \right) \mathrm{d}^2 r \tag{2.40}$$

employing the reduced magnetization $\vec{m}$. The skyrmions considered here posses an absolute winding number $|\mathcal{W}| = 1$. To facilitate an intuitive understanding of the winding number and its properties, we consider a one-dimensional cut through the center of the skyrmion in Fig. 2.5, which is shown in Fig. 2.7a. This structure consists of two domain walls of the same chirality (left-handed) and, going from left to right, the magnetization rotates exactly once counterclockwise. This structure has a one-dimensional absolute winding number $|\mathcal{W}| = 1$. However, the similar structure in Fig. 2.7b, which consists of two domain walls of opposite chirality, first rotates 180° in one direction and then 180° in the opposite direction for a total rotation of 0° and a corresponding absolute winding number of $|\mathcal{W}| = 0$. Eqn. (2.40) is the two-dimensional generalization of the winding number concept discussed so far. Its derivation is left beyond the scope of this thesis, as it is only used to highlight the connection between the skyrmion's non-trivial topology and the skyrmion Hall effect in section 2.2.4. Here, we focus on the consequences of a structure having a non-zero winding number instead.

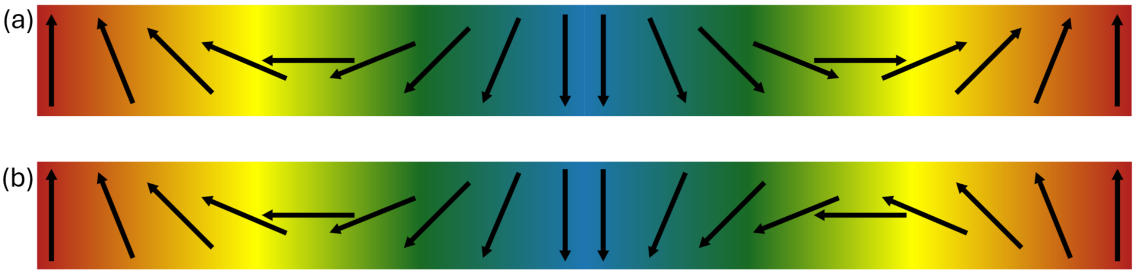

Figure 2.7: Schematics of (a) a one dimensional cut trough the center skyrmion structure in Fig. 2.5 that exhibits two domain walls of the same chirality, and (b) a similar structure consisting of two domain walls of opposite chirality. The left domain wall of both structures is identical to Fig. 2.6a and the same color code is employed. The two structures differ in the chirality of the right domain wall. This schematic is inspired by Ref. [86].

The winding number is often referred to as the topological winding number, because, in a continuous system, the winding number is conserved in the sense that it cannot be changed by performing a continuous transformation. The structure in Fig. 2.7b can be transformed to the trivial ($|\mathcal{W}| = 0$) collinear ferromagnetic mono-domain state via a continuous canting of the magnetization. This statement is not true for the structure in Fig. 2.7a with $|\mathcal{W}| = 1$. However, one must keep in mind that these topological concepts only strictly hold for the continuous case and that real systems are usually discrete, for instance, due to the underlying atomic lattice [9]. Still, the transformation from a nonzero winding number to a topologically trivial state is usually associated with a rather high energy barrier as the transformation requires energetically costly transient states such as a singular magnetization configuration (Bloch point) [87]. Therefore, skyrmions are considered topologically stabilized rather than strictly topologically protected. Under most conditions, in particular the absence of strong external excitations (see chapter 5), the skyrmions studied in this thesis can be considered stable on the time scale of the experimental measurements.

So far, we have only discussed absolute winding numbers. The sign of the winding number depends on the chirality and the orientation of the skyrmion core. Switching the chirality or switching the core orientation each flips the sign of the winding number. This means, that for systems with a fixed chirality dictated by the interfacial DMI, the sign of the winding number can still be flipped by changing the core orientation, which can be achieved by inverting the direction of the applied out-of-plane magnetic field for the systems studied in this thesis. The ability to flip the sign of the winding number is important because it changes the direction of the gyrotropic force (section 2.2.4).

Finally, it is crucial to point out that the skyrmions in the experiments, which are discussed in this thesis, have a very distinct structure from conventional skyrmion schematics such as the ones in Fig. 2.5. The studied skyrmions exhibit a significantly narrower domain wall compared to the size of the entire skyrmion. Such a structure is micromagnetically simulated and shown in chapter 3, Fig. 3.11. The studied skyrmions consist of a huge core enclosed by a very narrow domain wall, reminiscent of the thin soap film enclosing the air in a soap bubble. This limiting case is sometimes referred to as ”bubble skyrmions” [85], however, the same expression is also occasionally employed to refer to skyrmions in systems where both chiralities are stable [9], and the expression is furthermore easily confused with non-chiral magnetic bubbles [88]. For these reasons, the aforementioned terminology is not employed here. Skyrmions with narrow domain walls typically exhibit small skyrmion Hall angles[9] (see the supplementary material of Ref. [85], equation 74), and the width of the domain wall is essential when considering the skyrmion’s interaction with local variations of the magnetic properties (section 2.2.7). This discussion concludes the introduction on the internal skyrmion structure, and we now turn to the coarse-grained quasi-particle Thiele model where this structure’s properties are modeled only implicitly by tuning the parameters of the Thiele equation of motion.

2.2.2 The Thiele Model

The Thiele model for skyrmions [40, 85], is a coarse-grained description of skyrmion dynamics that assumes a rigid internal magnetic structure and treats skyrmions as two-dimensional particles. In principle, the parameters of the Thiele model can be determined from the internal skyrmion structure as the Thiele equation of motion can be derived from the LLG equation under the assumption of a rigid internal skyrmion structure [40, 85]. However, the details of the underlying magnetic structure are often experimentally inaccessible. Moreover, in thermally active systems, which are the primary focus of this thesis, the magnetic structure thermally fluctuates, and a more reliable description should employ effective parameters, for which the effects of thermal fluctuation are averaged out. For these reasons, we are primarily interested in ascertaining the parameters of the Thiele model directly from experimental skyrmion trajectories without any assumptions on the internal skyrmion structure or magnetic interactions. While the development of a fully quantitative quasi-particle modeling of skyrmion dynamics is the goal of chapter 3, here we phenomenologically motivate the Thiele equation of motion and introduce the force terms it entails alongside some other essential concepts.

Thermally active skyrmions have been shown to perform a random motion [16] that is in many ways similar to the Brownian motion of molecules [89]. Systems exhibiting ther-

---

[9] The skyrmion Hall effect is discussed in section 2.2.4.

mal diffusion are typically modeled by the Langevin equation [90] given by

$$m\frac{\mathrm{d}\vec{v}(t)}{\mathrm{d}t} = -\gamma\vec{v}(t) + \vec{F}_{\mathrm{det}} + \vec{F}_{\mathrm{therm}}(t). \tag{2.41}$$

Here, the forces acting on the particle with mass m and velocity $\vec{v}$ consist of a damping force $-\gamma\vec{v}(t)$ which is linear in the velocity with an isotropic scalar damping coefficient γ, a random force $\vec{F}_{\mathrm{therm}}(t)$ modeling thermal fluctuation, and further deterministic forces summarized as $\vec{F}_{\mathrm{det}}$. The latter can include, for instance, effective particle-particle interactions [91, 92]. In many systems, the inertial term $m\ \mathrm{d}\vec{v}(t)/\mathrm{d}t$ is small compared to the damping and the other terms. In these cases, inertial effects are often neglected, and the overdamped Langevin equation [41]

$$0 = -\gamma\vec{v}(t) + \vec{F}_{\mathrm{det}} + \vec{F}_{\mathrm{therm}}(t) \tag{2.42}$$

is employed, which is also referred to as the Brownian dynamics equation of motion. The standard Thiele equation of motion [40] possesses a very similar structure

$$0 = -\gamma\vec{v}(t) - G\vec{z}\times\vec{v}(t) + \vec{F}_{\mathrm{det}} + \vec{F}_{\mathrm{therm}}(t), \tag{2.43}$$

but it includes an additional gyrotropic force (short: gyroforce) term $-G\vec{z}\times\vec{v}(t)$, where $\vec{z}$ is the unit vector in the out-of-plane direction and G is the gyroforce strength. In the Thiele model, the position refers to the position of the skyrmion center. As in the overdamped Langevin equation, the inertial term is neglected here. While skyrmions have been shown to exhibit inertia-like behavior under specific conditions, such as the excitation of internal modes [93] or high-frequency dynamics [94], the experimental skyrmions modeled in this thesis exhibit no significant inertial effects within the experimental resolution. On the studied timescales, the skyrmions respond effectively instantaneously to applied forces and do not show any observable ballistic motion. Therefore, we consider the massless Thiele model introduced above applicable.

In the following sections, the different terms of the Thiele equation are discussed. While, in principle, many different interactions and external motion-inducing mechanisms can be phenomenologically modeled as deterministic forces $\vec{F}_{\mathrm{det}}$, we focus on the following terms due to their relevance for the systems studied in this thesis and for the skyrmion-based computing devices discussed in chapter 6:

- $\vec{F}_{\mathrm{pin}}(\vec{r}) = -\nabla U_{\mathrm{pin}}(\vec{r})$, the position-dependent pinning force due to the spatially inhomogeneous pinning energy landscape $U_{\mathrm{pin}}(\vec{r})$ that arises from the skyrmion's interaction with local variations of the magnetic properties. Pinning effects are unavoidable in state-of-the-art experimental systems.

- $\vec{F}_{\mathrm{SkBd}}(\vec{r})$, the repulsive interaction between the skyrmion and the boundary of the magnetic material.

- $\vec{F}_{\mathrm{SkSk}}(\{\vec{r}\})$, the repulsive interaction between skyrmions, which depends on the positions of all skyrmions in the system $\{\vec{r}\}$.

- $\vec{F}_{\mathrm{current}}\left(\vec{j}(\vec{r})\right)$, the current-induced force acting on the skyrmion, which can inherit a spatial dependence from a spatially inhomogeneous applied current density $\vec{j}(\vec{r})$.

2.2.3 Damping and Thermal Fluctuation

The damping coefficient γ in the Thiele equation (Eqn. (2.43)) quantifies the damping experienced by the skyrmion. This skyrmion damping γ encompasses the system's intrinsic Gilbert damping of the material α but also the damping related to the skyrmion's internal magnetization structure. The latter contribution is conventionally captured by the skyrmion dissipation tensor. Employing a dissipation tensor allows the damping to be anisotropic, which is useful when considering skyrmions subject to targeted deformation as in Ref. [95]. Here, we assume isotropic skyrmions and therefore isotropic damping, i.e., the dissipation tensor is diagonal with the same entry along the diagonal [40, 95]

$$D_{\text{diag}} := D_{xx} = \frac{M_{\text{S}} d}{\gamma_{\text{GR}}} \int \frac{\partial \vec{m}}{\partial x} \cdot \frac{\partial \vec{m}}{\partial x} \, \mathrm{d}^2 r = \frac{M_{\text{S}} d}{\gamma_{\text{GR}}} \int \frac{\partial \vec{m}}{\partial y} \cdot \frac{\partial \vec{m}}{\partial y} \, \mathrm{d}^2 r = D_{yy}. \tag{2.44}$$

Here $\vec{m}$ is the reduced magnetization, γ_{GR} is the gyromagnetic ratio, M_{S} is the saturation magnetization, and d is the thickness of the ferromagnetic layer. The skyrmion damping in the Thiele equation (Eqn. (2.43)) is conventionally related to the intrinsic Gilbert damping α and the diagonal entry of the skyrmion dissipation tensor D_{diag} via [40, 95]

$$\gamma = \alpha D_{\text{diag}}. \tag{2.45}$$

The aim of section 3.2 is to determine the skyrmion damping γ directly from experimental skyrmion trajectories. This has three key benefits over using the above equation. First, the details of the skyrmion's internal magnetization structure are not required. Second, in thermally active systems, the skyrmion's internal magnetic structure thermally fluctuates, which affects the dissipation tensor. For a more reliable description, an effective damping coefficient should be employed, for which the effects of thermal fluctuation are averaged out. This is automatically achieved in the procedure introduced in section 3.2 as it is based on average skyrmion properties. Since we only employ the effective damping coefficient in this thesis, it is just labeled γ. Third, it was recently proposed by Weißenhofer et al. (Ref. [96]) that an additional term is required in Eqn. (2.45) to accurately describe skyrmion dynamics at finite temperatures. Determining the skyrmion damping γ directly from experimental skyrmion trajectories circumvents the need to capture all relevant underlying magnetic contributions to γ.

For thermally active systems, fluctuation and damping are fundamentally linked by the fluctuation-dissipation-theorem [97]. The components of the random force modeling thermal noise, $\vec{F}_{\text{therm}}(t)$, must exhibit the autocorrelation [95, 97]

$$\left\langle F_{\text{therm}}^{(i)}(t) \, F_{\text{therm}}^{(j)}\left(t'\right) \right\rangle = 2 \mathrm{k_B T} \gamma \delta_{ij} \delta\left(t - t'\right) \tag{2.46}$$

to ensure thermal equilibrium, i.e., to ensure that the thermal noise injects energy at the same rate at which it is dissipated by the damping. Here, $i, j \in \{x, y\}$ denote the spatial components, δ_{ij} is the Kronecker delta, $\mathrm{k_B T}$ is the product[10] of the Boltzmann constant k_B and temperature T, and $\delta\left(t - t'\right)$ is the Dirac delta distribution. Angled brackets indicate the average over different realizations of the thermal noise. The implementation of thermal noise in the time-discretized quasi-particle simulations is discussed in section 2.2.9.

---

[10] The thermal energy $\mathrm{k_B T}$ is consistently written in non-italic font to emphasize that, in this thesis, all energy-like quantities are given in multiples of $\mathrm{k_B T}$ and it therefore predominantly takes the role of a unit.

2.2.4 Gyrotropic Force and Skyrmion Hall Effect

The gyrotropic force does not occur in the equation of motion of conventional Brownian dynamics systems and always acts perpendicular to the velocity. It is therefore also called Magnus force, by analogy to the Magnus effect, in which a spinning object moving through a fluid experiences a deflection. Similarly, a skyrmion driven by an external (typically current-induced) force will show a deflection. This effect is called the skyrmion Hall effect [98–100], and the angle between the applied force and the resulting skyrmion velocity is the skyrmion Hall angle θ_{SH}. The skyrmion Hall angle can be related directly to the ratio of the gyroforce strength G and the effective skyrmion damping γ. To derive the relation, we consider a skyrmion subject to a driving force, for instance a current-induced force, which is, without loss of generality, oriented in the positive x-direction $\vec{F}_{\mathrm{drive}} = F_x\vec{x}$. The Thiele equation for this case can be written as

$$-\gamma(v_x\vec{x} + v_y\vec{y}) - G\vec{z} \times (v_x\vec{x} + v_y\vec{y}) + F_x\vec{x} = 0 \tag{2.47}$$

$$-\gamma(v_x\vec{x} + v_y\vec{y}) - G(v_x\vec{y} - v_y\vec{x}) + F_x\vec{x} = 0, \tag{2.48}$$

where $\vec{x}$, $\vec{y}$, $\vec{z}$ are the unit vectors in the respective directions. The equation for the y-component is thus

$$-\gamma v_y - G v_x = 0, \tag{2.49}$$

obtaining the relation

$$\frac{|G|}{\gamma} = \frac{|v_y|}{|v_x|} =: \tan\left(\theta_{\mathrm{SH}}\right) \tag{2.50}$$

This motivates the definition of the relative gyroforce strength

$$G_{\mathrm{rel}} := \frac{G}{\gamma}, \tag{2.51}$$

which can be determined directly from experiments by applying a current-induced force to the skyrmion and measuring the skyrmion Hall angle and the direction of deflection.

Based on the internal magnetization structure of the skyrmion, the gyroforce strength can be expressed as [40, 85]

$$G = \frac{M_{\mathrm{S}}\,d}{\gamma_{\mathrm{GR}}} \int \vec{m} \cdot \left(\frac{\partial \vec{m}}{\partial x} \times \frac{\partial \vec{m}}{\partial y}\right) \mathrm{d}^2 r = \frac{M_{\mathrm{S}}\,d}{\gamma_{\mathrm{GR}}} 4\pi \mathcal{W}, \tag{2.52}$$

where $\vec{m}$ is the reduced magnetization, γ_{GR} is the gyromagnetic ratio, M_{S} is the saturation magnetization, and d is the thickness of the ferromagnetic layer. The integral expression is the same as in the definition of the winding number (Eqn. (2.40)) as indicated by the second equality. This relation motivates the interpretation that the skyrmion Hall effect is a direct consequence of the skyrmion's topologically non-trivial nature. Furthermore, the gyroforce strength inherits the sign of the winding number, which means that its direction is flipped for skyrmions of different chirality or core orientation[11].

---

[11] Note that there exist different conventions considering the signs of the gyroforce term and the gyroforce strength.

Because the gyroforce always acts perpendicular to the skyrmion velocity, it does not contribute to the system's energy, similar to the Lorentz force. It is therefore not expected to impact static equilibrium phenomena [15, 33, 101]. However, it can be crucial for dynamic effects. For instance, dense skyrmion systems with large skyrmion Hall angles have been shown to exhibit an anomalous increase in their diffusion coefficient with increasing density [102, 103]. Finally, it is important to point out that pinning effects typically suppress the skyrmion Hall effect [20, 104], which is captured by employing an effective skyrmion Hall angle θ_{eSH}. The effective skyrmion Hall angle is usually negligible in systems with slow dynamics dominated by pinning [20, 104].

2.2.5 Modified Einstein-Smoluchowski-Relation

To determine the diffusion coefficient D from the trajectory of a particle, one typically considers the time-dependence of the mean squared displacement [89]

$$\langle [\vec{r}\,(t_0 + \Delta t) - \vec{r}\,(t_0)]^2 \rangle = 2d\, D\, \Delta t, \tag{2.53}$$

where $\vec{r}$ is the position at time t, t_0 is the initial time, Δt is the time difference over which the displacement is evaluated, d is the system's spatial dimension, and angled brackets denote the average over trajectory segments of length Δt which corresponds to an average over different realizations of thermal noise. Thus, the diffusion coefficient can be determined by fitting the linear part[12] of the mean squared displacement as a function of the time difference and dividing the slope by $2d$.

In the absence of other forces, in particular in the absence of pinning effects, an analytical expression for the diffusion coefficient D can be derived. Here, the ansatz stated in Ref. [95] is employed, which exploits that the mean squared displacement can be expressed via the velocity autocorrelation. We start with the Thiele equation in the absence of other forces

$$-\gamma \vec{v}(t) - G\vec{z} \times \vec{v}(t) + \vec{F}_{\mathrm{therm}}(t) = 0, \tag{2.54}$$

and employ the shorter notation $\vec{\eta} := \vec{F}_{\mathrm{therm}}$ for readability. In components, we have

$$\begin{aligned} -\gamma v_x + G v_y + \eta_x &= 0 \\ -\gamma v_y - G v_x + \eta_y &= 0, \end{aligned} \tag{2.55}$$

which can be solved for the velocity components by solving the first equation for v_y and inserting it in the second and vice versa for v_x:

$$\begin{aligned} v_x &= \frac{\gamma \eta_x + G \eta_y}{\gamma^2 + G^2} \\ v_y &= \frac{\gamma \eta_y - G \eta_x}{\gamma^2 + G^2} \end{aligned} \tag{2.56}$$

---

[12] Eqn. (2.53) only strictly holds in the long-time limit. In particular, at short time scales pinning effects cause the mean squared displacement to be non-linear. This is not to be confused with the common non-linear (parabola-like) part of the mean squared displacement that particles with significant inertia exhibit at short time scales due to ballistic motion.

Next, we express the velocity autocorrelations in terms of the thermal random force's autocorrelation, because the latter is determined by the fluctuation dissipation theorem (see Eqn. (2.46)). The cross terms $\langle \eta_i(t)\eta_j(t')\rangle$ with $i \neq j$ vanish because of the Kronecker delta in Eqn. (2.46) and we are left with

$$\begin{aligned}\langle v_x(t)v_x(t')\rangle &= \frac{\gamma^2\langle \eta_x(t)\eta_x(t')\rangle + G^2\langle \eta_y(t)\eta_y(t')\rangle}{(\gamma^2+G^2)^2}\\ \langle v_y(t)v_y(t')\rangle &= \frac{\gamma^2\langle \eta_y(t)\eta_y(t')\rangle + G^2\langle \eta_x(t)\eta_x(t')\rangle}{(\gamma^2+G^2)^2}\\ \langle v_x(t)v_y(t')\rangle &= \frac{-\gamma G\left[\langle \eta_x(t)\eta_x(t')\rangle - \langle \eta_y(t)\eta_y(t')\rangle\right]}{(\gamma^2+G^2)^2}.\end{aligned} \tag{2.57}$$

Employing Eqn.(2.46), we immediately get

$$\begin{aligned}\langle v_x(t)v_y(t')\rangle &= 0\\ \langle v_x(t)v_x(t')\rangle &= \langle v_y(t)v_y(t')\rangle\end{aligned} \tag{2.58}$$

with

$$\langle v_x(t)v_x(t')\rangle = \frac{(\gamma^2+G^2)\,2\mathrm{k_B T}\gamma}{(\gamma^2+G^2)^2}\delta(t-t') = \frac{2\mathrm{k_B T}\gamma}{\gamma^2+G^2}\delta(t-t'). \tag{2.59}$$

If we now compare the mean square displacement in x-direction expressed via the above velocity autocorrelation

$$\begin{aligned}\left\langle \Delta x^2(\Delta t)\right\rangle &= \int_0^{\Delta t}\int_0^{\Delta t}\langle v_x(t)v_x(t')\rangle\,\mathrm{d}t\mathrm{d}t'\\ = \int_0^{\Delta t}\int_0^{\Delta t}\frac{2\mathrm{k_B T}\gamma}{\gamma^2+G^2}\delta(t-t')\,\mathrm{d}t\mathrm{d}t' &= 2\frac{\mathrm{k_B T}\gamma}{\gamma^2+G^2}\Delta t\end{aligned} \tag{2.60}$$

to Eqn. (2.53), we obtain the known relation [95, 105]

$$D = \frac{\mathrm{k_B T}\gamma}{\gamma^2+G^2} = \frac{\mathrm{k_B T}}{\gamma(1+G_{\mathrm{rel}}^2)}, \tag{2.61}$$

employing the relative gyroforce strength $G_{\mathrm{rel}} \coloneqq G/\gamma$ the last expression. This is a modified version of the Einstein-Smoluchowski-relation [41, 89] which reduces to its standard form

$$D = \frac{\mathrm{k_B T}}{\gamma} \tag{2.62}$$

for $G_{\mathrm{rel}} = 0$. Note again that this relation only holds for the free diffusion coefficient and not for the pinning-affected one. A way to still leverage this relation in systems with pinning is developed in section 3.2 as a part of this thesis.

2.2.6 Current-Induced Force

Skyrmions can experience a force due to an electrical current applied to the sample [18, 99, 106]. In section 3.3, a method is developed to directly extract the current-induced force acting on the skyrmion from experimental trajectories. This method does not rely on any assumptions about the underlying mechanism that causes the force on the skyrmion. It only assumes that the force is constant for a constant applied current density[13]. While this force originates from current-induced spin torques, spin transport is a vast research field, and a detailed treatment of these effects is intentionally left beyond the scope of this thesis, as it is not required for understanding the research presented in section 3.3. Instead, this section provides a brief conceptual overview of why skyrmions can experience a current-induced force.

If a spin-polarized current flows through a magnetic material, the magnetic moments of the conduction electrons tend to align with the material's local magnetization. Due to conservation of angular momentum, this reorientation gives rise to a (spin-transfer) torque acting on the magnetization [107]. A similar effect occurs for a pure spin current without net charge current that arises when electrons of opposite spins move in opposite directions, thus canceling out the charge transport. One of the most important sources of pure spin current is the spin Hall effect [108]. It describes the phenomenon that, when a charge current is driven through a material with strong spin-orbit coupling, conduction electrons with opposite spins are deflected in opposite transverse directions (Fig. 2.8). This results in a spin current perpendicular to the charge current, which can diffuse into an adjacent magnetic layer [109]. The spin Hall effect is reminiscent of the ordinary Hall effect, as both effects involve a transverse response to a longitudinal current, just that the spin Hall effect generates a transverse spin current instead of a voltage. The resulting torques on the magnetic system are called spin-orbit-torques.

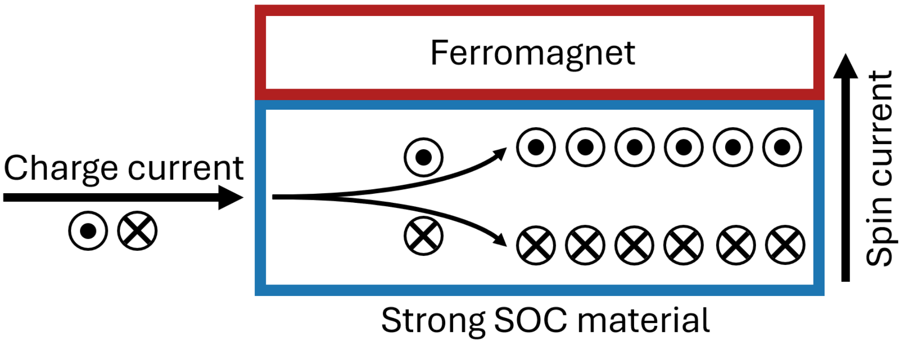

Figure 2.8: Schematic illustration of the spin Hall effect. Conduction electrons are indicated using circles, with spin orientation out of the plane of view and into the plane of view shown with dots and crosses, respectively. Inside the strong spin-orbit-coupling (SOC) material, conduction electrons with opposite spins are deflected in opposite transverse directions due to the spin Hall effect. This creates a transverse spin current which can diffuse into the adjacent ferromagnetic layer. This figure is inspired by Fig. 1a of Ref. [110].

---

[13] In the employed variant of the method, it is also assumed that the direction of the current-induced force is reversed if the direction of current flow is reversed. However, as discussed in section 3.3.1, the method's concept can also be employed using only one direction of applied force and the force-free case. This variant of the method instead assumes that there is no current-induced force before any current is applied, which is fulfilled by causality.

The setup in Fig. 2.8 (magnetic layer adjacent to high spin-orbit-coupling layer) is the same as in Fig. 2.2 that introduced interfacial DMI. This makes employing current-induced spin-orbit-torques particularly attractive for thin film multilayer systems that stabilize skyrmions via interfacial DMI, such as the ones studied in this thesis (see section 2.4.1). For skyrmions, the collective current-induced spin-torques acting on the skyrmion's internal magnetic structure can be described in the Thiele model via an effective force [85] $\vec{F}_{\text{current}}$. If the distribution of current density in the sample is spatially inhomogeneous, the current-induced force acting on the skyrmion inherits a spatial dependence. High applied current densities have been reported to deform skyrmions [20], which alters the skyrmion dissipation tensor and thus the effective damping coefficient γ. Moreover, high current densities can also cause significant Joule heating, locally raising the temperature. For these reasons, the method to ascertain the current-induced force developed in section 3.3.1 employs very low current densities in order to circumvent these effects.

2.2.7 Pinning Effects

In section 2.2.2 it was stated that skyrmion diffusion is fundamentally similar to Brownian dynamics. However, in experimental skyrmion trajectories, such as the ones later shown in chapter 5, Fig. 5.3, the skyrmions' random motion appears distinctly hopping-like [16], in contrast to the expectation for a free particle subject to thermal random noise. The skyrmions remain pinned at a particular position, dwelling there for an extended period of time before moving to the next position, where they remain pinned again. This pinning effect is attributed to the skyrmions' interaction with local variations of the magnetic properties [111]. Several mechanisms have been proposed to cause pinning effects [36, 111], including local variations of anisotropy [112], exchange [113, 114], and DMI [115]. Pinning effects are studied extensively in the later chapters of this thesis, with chapters 3 and 4 employing two different top-down approaches to investigate and model skyrmion pinning.

In chapter 3, pinning is modeled via an effective energy landscape $U_{\text{pin}}(\vec{r})$ in terms of the skyrmion center position $\vec{r}$. This energy landscape is determined via a potential of mean force approach [116, 117]. The potential of mean force is the effective potential that causes the equilibrium skyrmion distribution $\rho(\vec{r})$ (spatial occupation probability density for the skyrmion center) in the system determined by the Boltzmann weight

$$\rho(\vec{r}) \propto \exp\left(\frac{-U_{\text{pin}}(\vec{r})}{\mathrm{k_B T}}\right). \tag{2.63}$$

Consequently, the pinning potential of mean force is given by

$$U_{\text{pin}}(\vec{r}) = -\mathrm{k_B T} \ln\left(\rho(\vec{r})\right). \tag{2.64}$$

In order for this approach to only capture the effects of pinning, it should be applied to a single-skyrmion system or a low-density multi-skyrmion system, where the effects of skyrmion-skyrmion interaction are negligible. The potential of mean force approach is designed to reproduce the time-averaged distribution of skyrmion center positions in the system. It is based solely on the observed skyrmion distribution and does not require any assumptions about the underlying magnetic interactions or the internal skyrmion structure. The pinning energy landscape acts to reduce the skyrmion diffusion coefficient as discussed in section 3.2. In chapter 4, we then go beyond the rigid isotropic structure approximation and study the relation between pinning and skyrmion shape and size. In particular, the role of the skyrmions domain wall is explicitly explored to understand the size-dependence of skyrmion pinning. The implications of chapter 4's results for the quasi-particle modeling of skyrmion dynamics are discussed in section 4.4. In chapter 5, the size-dependence of pinning is then employed to develop a diffusion enhancement mechanism.

2.2.8 Interactions with Other Skyrmions and Material Boundaries

The interactions of skyrmions with each other and with the boundaries of the magnetic material can be key for the design of skyrmion-based devices [24, 31, 32, 118] and the study of the phase behavior of many-skyrmion systems [33, 34]. In the Thiele model, these interactions are represented via interaction potentials that determine the force acting on the skyrmions. Representing the interaction of objects with complex internal structure with effective potentials is a common approach in soft matter physics [91, 92]. For skyrmion-skyrmion interaction, one usually considers two-particle interaction potentials $U_{\mathrm{SkSk}}(r)$ which depend on the distances $r := |\vec{r}_i - \vec{r}_j|$ between each pair of skyrmions i and j in the system. The skyrmion-boundary interaction potential for an infinite straight material boundary $U_{\mathrm{SkBd}}(r)$ depends only on the perpendicular distance to boundary. The latter is also referred to as "r" to simplify discussing the determination of both potentials at the same time, and because of the low risk of confusion. Micromagnetic calculations of the interaction potentials predict purely repulsive potentials [11–14], well-described by an exponential shape for many systems, but exceptions exist [119]. This section discusses the determination of skyrmion interaction potentials directly from experimental skyrmion distributions without any assumptions on the potential's functional form, underlying magnetic interactions, or internal skyrmion structure, based on our publication Ref. [15].

The task of ascertaining the interaction potentials from the experimental skyrmion positions is, in principle, similar to the modeling of pinning discussed in section 2.2.7, which was performed via a potential of mean force approach. The potential of mean force is designed to reproduce the skyrmion distribution in the system. Thus, to determine the skyrmion pair interaction potential, one would employ the pair distribution function. However, there are multiple obstacles to this approach. Most importantly, when considering a system of many interacting skyrmions, especially at high density, the pair-potential of mean force would also implicitly include the interactions of all other particles. Therefore, the resulting pair potential would not accurately represent the pure two-particle interaction and would not necessarily reproduce the skyrmion distribution. A solution for this problem would be to employ a system of only two skyrmions; however, it is difficult to determine the pair distribution function at short distances for two free particles that are expected to strongly repel each other at close range. In addition, pinning effects are still present in the system and will impact the pair distribution function. To reduce this effect, a denser many-skyrmion system is favorable as the skyrmion distribution in the system will be determined predominantly by the skyrmion-skyrmion interaction, given it is sufficiently strong (at close range) to dominate over pinning effects. A way to overcome these obstacles is to employ a many-skyrmion system and correct the potential of mean force such that the resulting potential reflects the pure pair-potential. This is done using the iterative Boltzmann inversion (IBI) method [120], where the initial potential given by the potential of mean force is iteratively updated until convergence. The potential at step $i+1$ is updated based on the ratio between the previous simulated distribution function at $g_i(r)$ and the experimental distribution function $g(r)$ via[14] [120]

$$V_{i+1}(r) = V_i(r) + \alpha_{\mathrm{IBI}} \mathrm{k_B T} \ln \frac{g_i(r)}{g(r)} \tag{2.65}$$

with

$$V_0(r) = -\mathrm{k_B T} \ln g(r), \tag{2.66}$$

where the dimensionless parameter $\alpha_{\mathrm{IBI}} \in (0,1]$ regulates the overall magnitude of the changes in the potential within one updating step [120]. Larger values of α_{IBI} lead to faster convergence but can also cause oscillation around the correct potential. The distribution functions $g(r)$ relevant for skyrmion-skyrmion and skyrmion-boundary interaction are defined below after introducing the experimental system. This section only aims to outline the procedure to determine the potentials; the full experimental details, including material stack composition, skyrmion tracking procedure, and measurement conditions, are given in our publication Ref. [15].

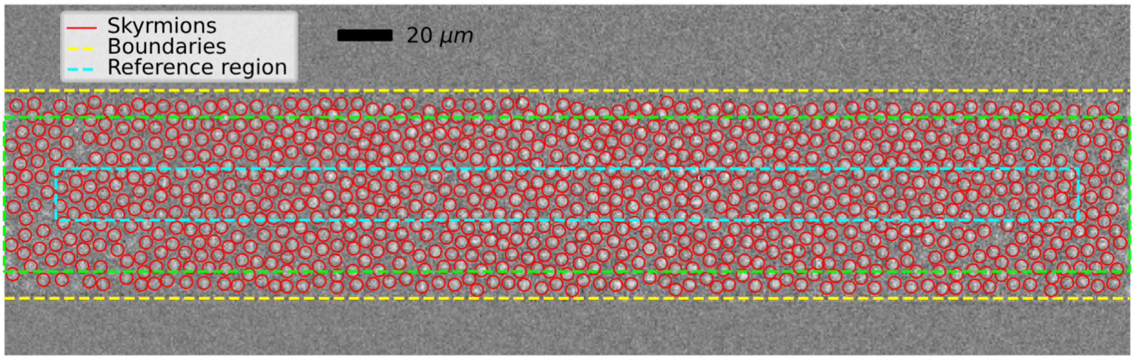

Figure 2.9: Kerr microscopy image of an exemplary experimental skyrmion configuration. Red circles highlight skyrmions (bright dots). The two yellow dashed lines indicate the boundaries of the magnetic material, which horizontally extends far beyond the field of view. For the determination of the skyrmion-skyrmion interaction potential, skyrmions within the region enclosed by cyan dashed lines are employed as reference particles, and all skyrmions within the region enclosed by the green dashed lines are counted as neighbors for the reference particles. This figure is taken from our publication Ref. [15].

The experimental system (Fig.2.9) is designed such that the skyrmion-skyrmion and skyrmion-boundary potential can be determined simultaneously. The skyrmions are confined to a rectangular stripe that is significantly longer than the field of view, such that the skyrmion-boundary potential can be assumed to depend on the perpendicular distance from the boundaries (yellow lines) alone. The skyrmions are imaged via time-resolved Kerr microscopy, and the skyrmion center positions are determined via the tracky python

---

[14] The potentials are labeled V instead of U here to be consistent with Ref. [15].

package [121] (see section 2.4.2). For the skyrmion-skyrmion interaction, only skyrmions in the region enclosed by the cyan dashed lines are considered, within which the distribution function is expected to be largely unaffected by the skyrmion-boundary interaction.

The distribution function $g(r)$ relevant for the skyrmion-skyrmion interaction is the discretized radial distribution function. The discretized radial distribution function represents the dimensionless[15] particle density within a shell of width Δr located at a distance r from a reference particle, averaged over all reference particles. It is given by[16]

$$g(r) = \frac{1}{\rho N} \frac{1}{2\pi r \Delta r} \sum_{i \neq j} \left[\theta\left(r_{ij} - r\right) - \theta\left(r_{ij} - r - \Delta r\right)\right], \tag{2.67}$$

where ρ is the skyrmion area density in the region enclosed by the green dashed lines (reference particles), N is the number of skyrmions in the region enclosed by the cyan dashed lines (all particles considered as neighbors), and θ indicates the Heaviside step function. The sum is over all pairs of particles i within the cyan dashed lines and particles j within the green dashed lines for which $i \neq j$, and r_{ij} is the distance between particles i and j. Analogously, one can define the discretized boundary distribution function for a homogeneous straight boundary as

$$g_{\mathrm{Bnd}}(r) = \frac{1}{\rho} \frac{1}{L \Delta r} \sum_{i} \left[\theta\left(r_i - r\right) - \theta\left(r_i - r - \Delta r\right)\right], \tag{2.68}$$

where L is the length of the boundary and r_i is the perpendicular distance of particle i to the boundary. For the IBI protocol, a system with the same geometry and number of skyrmions as in the experiment is simulated with periodic boundary conditions in the horizontal direction. For each step, both interaction potentials are calculated via Eqn. (2.65) up to the first minimum of the distribution function[17], with the full simulation details given in Ref. [15].

Fig. 2.10 shows the resulting simulated distribution functions after 500 iterations at $\alpha_{\mathrm{IBI}} = 0.2$ alongside the experimental ones. The experimental boundary distribution function suffers from significantly less statistics compared to the radial distribution function, and is therefore more prone to the impact of pinning effects. The reduced statistics arises because every skyrmion contributes only once per Kerr video frame to the average in Eqn. (2.68), in contrast to the radial distribution function. In addition, there is a small peak in Fig. 2.10b around 7.5 µm that is likely caused by pinning effects, and does not reflect the effect of the skyrmion-boundary interaction. Therefore, a boundary distribution function smoothed via a running average over eight neighboring bins in each direction (dotted black line in Fig. 2.10b) is employed for the IBI procedure.

---

[15] It is normalized to converge to 1 at long distances for systems without long-range order.

[16] Note that the IBI update scheme (Eqn. (2.65)) does not converge well when $g(r)$ has very sharp peaks and deep troughs. Therefore, the density is chosen sufficiently low such that the system does not form a lattice structure. As discussed above, higher densities are favorable to mitigate the impact of pinning; thus, the ideal density for this procedure is determined by the competition of these two effects.

[17] The first peak corresponds to the nearest neighbor distance for the radial distribution function and first layer distance for the boundary distribution function.

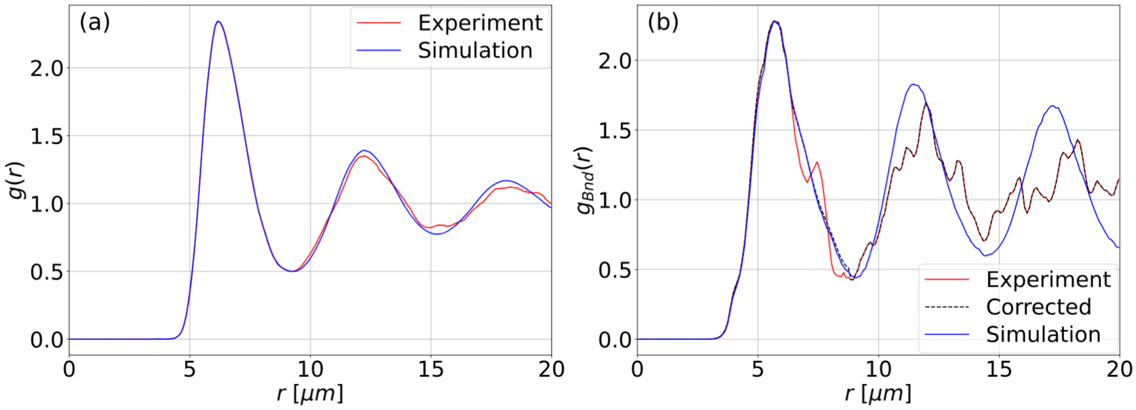

Figure 2.10: Comparison of the experimental distribution functions and the simulated distribution functions after 500 IBI iterations at $\alpha_{\mathrm{IBI}} = 0.2$. (a) and (b) show the radial distribution functions and boundary distribution functions, respectively, with experimental results shown in red and the final simulated distribution functions in blue. (b) additionally shows the smoothed boundary distribution function used in the IBI procedure as a dashed black curve. The bin width is $\Delta r = 0.1\,\mu\mathrm{m}$ for all functions. This figure is taken from our publication Ref. [15].

In future research, the statistics of the experimental boundary distribution function could be improved by employing a larger field of view. The IBI method reproduces both distribution functions very well up to the first minimum and, for the radial distribution function in Fig. 2.10a, to a good extent beyond this region.

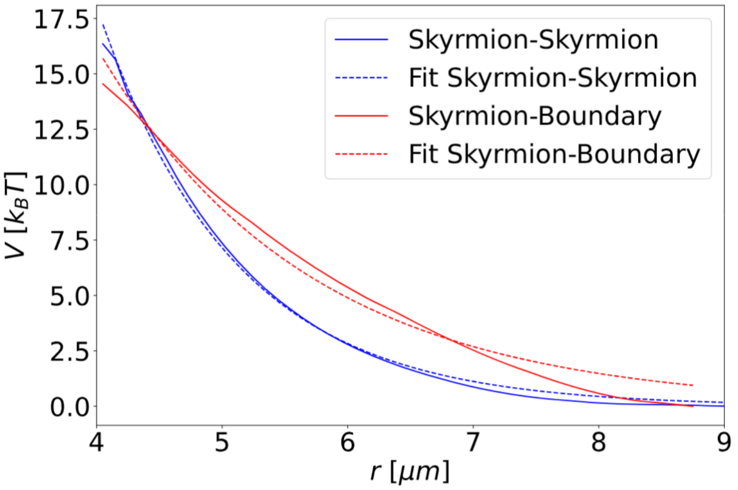

Figure 2.11: Skyrmion-skyrmion (blue solid curve) and skyrmion-boundary (red solid curve) interaction potentials after 500 IBI iterations at $\alpha_{\mathrm{IBI}} = 0.2$. The dashed lines show exponential fits $V(r) = a\exp(-r/b)$. The fit values are $a_{\mathrm{SkSk}} = 735.1\,\mathrm{k_B T}$ and $b_{\mathrm{SkSk}} = 1.079\,\mu\mathrm{m}$ for the skyrmion-skyrmion interaction, and $a_{\mathrm{SkBd}} = 176.7\,\mathrm{k_B T}$ and $b_{\mathrm{SkBd}} = 1.673\,\mu\mathrm{m}$ for the skyrmion-boundary interaction. This figure is taken from our publication Ref. [15].

The resulting final interaction potentials shown in Fig. 2.11 are fully repulsive and well approximated by exponential functions in agreement with micromagnetic predictions [11–14]. Note again that the IBI procedure does not rely on any assumptions about the shape of the potentials and would, in principle, also capture attractive interactions [120]. The resulting potentials depend on the skyrmion size as well as temperature and material properties, and can consequently differ from system to system [122]. Still, the determined potentials serve as a valuable estimate of the interactions even in slightly different systems. Ref. [15] contains further discussions of the IBI method's limits alongside additional verifications of the determined potentials based on comparisons of structural properties.

2.2.9 Quasi-Particle Simulations and Comparison to Micromagnetics

The quasi-particle skyrmion simulations employed in this thesis solve the Thiele equation of motion (Eqn. (2.43)) numerically for every skyrmion in the system. This essentially amounts to Brownian dynamics simulations [123, 124]. However, gyrotropic force, pinning effects, and position-dependent current-induced force do not appear in conventional Brownian dynamics systems, and are therefore not implemented in standard simulation software [125, 126]. For this reason, a custom C++ implementation is employed, which was originally developed by [redacted] [127] and extended and reworked by me to suit the studied systems. The explicit Euler method [128]

$$\vec{r}_i(t+\Delta t) = \vec{r}_i(t) + \vec{v}_i(t)\Delta t \tag{2.69}$$

is employed, where a small discrete time step Δt is chosen to minimize numerical errors. Typically $\Delta t = 10^{-5}\,\tau_{\mathrm{sim}}$, where τ_{sim} is the simulation time unit (see section 3.2). The next position $\vec{r}_i(t+\Delta t)$ for each skyrmion i is determined based on the velocity at the current time step $\vec{v}_i(t)$. The latter is in turn determined based on the system configuration at the current time step via the Thiele equation of motion Eqn. (2.43). Importantly, the autocorrelation of the thermal random force Eqn. (2.46) must be adapted for discretized time [125]

$$\left\langle F^{(i)}_{\mathrm{therm}}(t)\, F^{(j)}_{\mathrm{therm}}(t')\right\rangle = \frac{2\mathrm{k_B T}\gamma}{\Delta t}\delta_{ij}\delta_{tt'}, \tag{2.70}$$

where i and j refer to the spatial components. Moreover, while thermal random forces are typically assumed to be Gaussian distributed, uniform noise can produce consistent results at a significantly reduced computational cost if the boundaries of the uniform distribution are chosen such that it exhibits the same mean and variance as the target Gaussian distribution [129].

The differences in favorable application scenarios for quasi-particle and micromagnetic (section 2.1.4) simulation methods arise mainly because of two properties: access to the skyrmion's internal magnetic structure and computational cost. Micromagnetic simulations can capture changes in the skyrmion's magnetic structure, such as deformation or internal excitations, which are fundamentally inaccessible to Thiele model simulations as the skyrmions' internal structure not explicitly modeled. This trade-off comes with the upside of significantly faster computation time, with simulation speeds close to real time for many experimental systems as discussed in section 3.2.2. One of the most important benefits of Thiele model simulations for the studied micrometer-sized systems, is that the computation speed does not depend on the overall scale of the system – a nanometer-sized system of nanometer-sized skyrmions requires the same computation power as a micrometer-sized system of micrometer-sized skyrmions. For the computational efficiency of Thiele model simulations, the number of skyrmions plays a role, but the individual size of the skyrmions does not. In contrast, the computation speed of micromagnetic simulations is strongly impacted by the required number of cells, and the maximum cell size is limited, for instance, by the domain wall width (section 2.1.4). Consequently, for skyrmions such as the one studied in this thesis, where the radius is in the micrometer range but the domain wall width is only a few nanometers (section 3.3.3), micromagnetic simulations of dynamics come with a prohibitive computational cost. This limitation could be somewhat mitigated by multi-scale micromagnetic modeling approaches that model the skyrmion domain wall in more detail than the skyrmion core and surrounding material, but even then, the computation speed is unlikely to be comparable to the quasi-particle Thiele model simulations.

2.3 Unconventional Computing using Skyrmions

Skyrmions are considered promising for a variety of device applications in data storage [9, 23, 24] and computing [25–32] due to their quasi-particles properties [9, 40], the existence of several dynamics manipulation mechanisms [18–21, 78], and their thermally activated dynamics [16, 29]. In this thesis, we focus on two unconventional computing approaches, Brownian computing [28, 51, 52] and reservoir computing [45–49]. In particular, the development of a skyrmion-based Brownian reservoir computer is the central content of chapter 6. Since section 6.1 introduces our device concept by identifying the steps of its operation with the general operation steps of a reservoir computer, and section 6.4 is entirely dedicated to understanding the Brownian computing aspects of our device, the present introduction is intentionally kept brief. This introduction is based on our review/perspective publication Ref. [28].

2.3.1 Brownian Computing

Central to the Brownian computing paradigm is the broad idea of exploiting the random dynamics of a physical system for the benefit of a computer architecture. It is inspired by noise-exploiting mechanisms in biological processes, such as molecular machines driven by Brownian motion [130, 131]. The Brownian computing concept stated in this way is very general, as the benefits provided by incorporating Brownian computing aspects into a computer architecture depend strongly on the chosen architecture. This is best illustrated with a few examples for different computer architectures, for which the operating principles and role of thermal diffusion are outlined below.

For devices that are intended to be operated at room temperature anyway, one obvious target benefit would be to directly harness thermal energy from the environment for ultra-low-power computing. Therefore, the idea of a Brownian token-based computer [51, 52] is to exploit thermal random motion as a propagation mechanism for signal carriers. In Brownian token-based circuits, computations are performed as the signal carriers, called ”tokens” in this context, find their way through a network of computational paths. I.e., inputs are encoded via the tokens' initial positions, and their final positions after traversing the circuit correspond to the output. Due to the second law of thermodynamics, computations cannot be performed based on equilibrium thermal random motion alone. Therefore, the circuits contain some actively powered elements that encode the logic by setting passing rules for the tokens. Typically, employing thermal randomness in a computer architecture comes with a trade-off. In the case of Brownian token-based computing, the downside is a non-deterministic computation time. Section 5.4 provides an outlook on the application of diffusion enhancement mechanisms, such as the one explored in chapter 5, to significantly extend the range of viable application scenarios of Brownian token-based computing.

Brownian computing aspects can also take a more supportive role in a computer architecture. For instance, a skyrmion-based Brownian reshuffler device for stochastic computing was developed and experimentally demonstrated [16, 132]. In stochastic computing, numerical values are encoded as the probability of a "1" occurring in random bit-streams. Then, computations are performed by applying bit-wise operations and determining the probability of a "1" in the output bit-stream[18]. For this approach to work, the bit streams must be uncorrelated. A reshuffler device rearranges the sequence of ones and zeros in a bit-stream while leaving the probabilities of a "1" occurring unchanged to decorrelate bit streams. In Refs. [16, 132], this is achieved by encoding bit streams via skyrmions and exploiting the randomness of thermal skyrmion diffusion for decorrelation. For the device developed in chapter 6, the benefit provided by thermal activity is yet of a different nature again, as discussed in section 6.4.

2.3.2 Reservoir Computing

Feeding input data into an artificial neural network can be viewed as a complex non-linear transformation of the input data into the network's high-dimensional feature space. Similarly, applying a manipulation to a physical system, the information encoded in that manipulation is transformed into the physical system's high-dimensional state space by means of the system's often complex, non-linear response to the manipulation. This similarity motivates the concept of physical[19] reservoir computing [45–49]. A reservoir computer can therefore be interpreted as an artificial neural network in which most of the network is replaced by a physical system, called the "reservoir" [45–49].

The general operating principle of a reservoir computer is illustrated in Fig. 2.12. Input data is fed into the reservoir by encoding it as a manipulation to the system. As the system responds to the manipulation, the encoded input information is translated into the system's high-dimensional state space. Information about the system's response

---

[18] Example: Multiplication can be realized by bit-wise application of the AND operation on two bit streams, each encoding a number between 0 and 1 as the probability of a "1" occurring in the bit-stream. This works because a "1" occurs in the resulting bit stream only when, at that point in the bit-sequences, both bit-streams contain a "1". This happens with a probability that is the product of the individual bit-streams "1"-probabilities. Thus, the resulting bit-stream encodes the product of the numbers encoded in the two input bit-streams.

[19] The adjective "physical" is dropped in this thesis, as we only consider reservoir computers where the reservoir is a physical system, and a distinction from pure software approaches is therefore unnecessary.

to the manipulation can be ascertained by measuring a experimental observables. Then, the input is classified based on these observables. The operating concept of a reservoir computer is that, by processing the data through the reservoir, a complex non-linear classification problem in terms of the input data is reduced to a much simpler classification problem based on the measured observables. Then, a simple classifier can be trained, for instance, based on labeled training data. Crucially, the reservoir itself does not need to be trained, and the same reservoir is often suitable for multiple tasks, such that training costs are minimal compared to artificial neural networks. The performance of the reservoir computing approach depends strongly on how well the reservoir's dynamics is compatible with the classification problem at hand, and how well the chosen experimental observables characterize the essential aspects of the system's response. While task-agnostic metrics to gauge a reservoir's performance, like the balance between non-linearity and memory capacity, have been brought forward for the case of time-dependent manipulations [133], understanding the physics behind why a specific reservoir computer works can be crucial for the development of improved devices. Therefore, section 6.3 is dedicated to interpreting the optimized parameters of the simple classifier by taking into account the system's underlying physics.

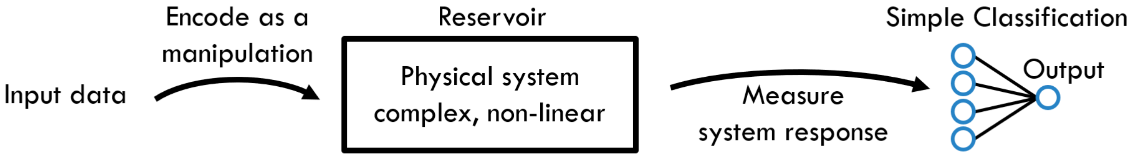

Figure 2.12: Illustration of reservoir computing's operating principle. The input data is encoded as a manipulation to the reservoir. Consequently, the input is translated into the reservoir's high-dimensional state space as the system responds to the manipulation. This response is then measured in terms of a few characteristic experimental observables. Then a simple classification method is performed on the, again lower-dimensional, collection of experimental observables to generate the entire reservoir computer's output. In Fig. 6.1, the operating principle of the Brownian reservoir computer developed in chapter 6 is explained alongside this general illustration.

2.4 Experimental Methods Overview

As stated at the beginning of this chapter, my contributions to the results presented in this thesis are of a purely theoretical nature. While I occasionally helped designing experimental system setups, I did not perform any measurements or sample fabrication. The experimental physicists of [redacted]'s group, who conducted the experiments, are credited at the beginning of the corresponding chapters and in the dedicated contribution sections in the appendix (section A.1) throughout this thesis. For these reasons, this section aims to provide only a brief overview of the required experimental methods with a focus on information necessary for understanding and interpreting the shown experimental data.

2.4.1 Sample Structure

The samples that host the skyrmions discussed in this thesis are magnetic thin-film multilayer stacks. Their structure is (from bottom to top) Ta/$Co_{20}Fe_{60}B_{20}$/Ta/MgO/Ta, where the precise thicknesses of the layers vary for different projects but are always in the nanometer-range except for the thinner Ta interlayer. The following explanation of the purpose of the different layers is based on the supplementary material of our publication Ref. [39]. The top Ta-layer, that prevents oxidation of the lower layers, is replaced by HfO_2 for some projects. The latter material is transparent to the visible light used in the Kerr microscopy discussed below and thus produces increased contrast. The bottom Ta layer has a twofold purpose as it generates sufficient DMI in the ferromagnetic amorphous CoFeB-layer to stabilize skyrmions and provides a significant spin-Hall-effect to enable skyrmion motion due to current-induced spin-orbit-torques. Finally, the purpose of the MgO-layer is to enhance the perpendicular magnetic anisotropy, which can be further tuned using the thin Ta dusting layer between the CoFeB and MgO.

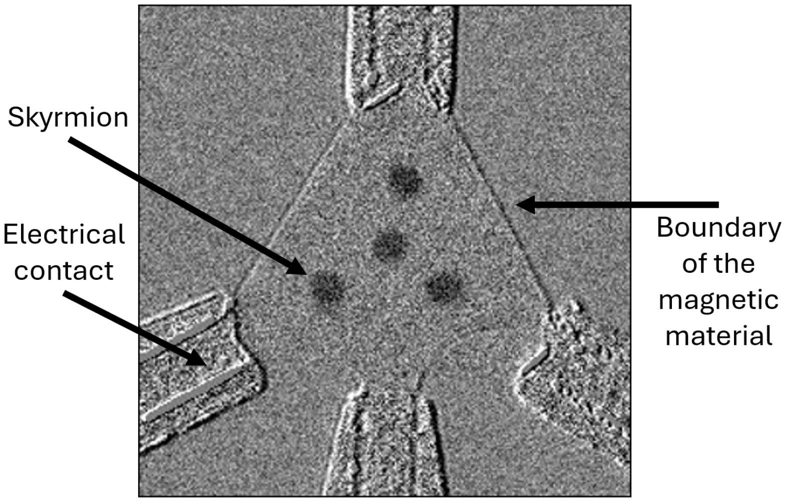

Figure 2.13: Exemplary background-subtracted Kerr microscopy image of four skyrmions (dark dots) confined in a triangular structure with four contacts, one at each corner of the confinement and an additional one at the bottom center. The brightness indicates the out-of-plane magnetization at each pixel relative to a background image of the fully-saturated out-of-plane magnetized system. The side length of the equilateral triangle is 40 µm. Underneath the visible parts of the contacts, there are channels too thin for the skyrmions to enter easily due to repulsion from the boundaries of the magnetic material (see also Fig. 6.2). Thereby, the skyrmions are prevented from moving under the contacts where they would not be visible while still providing a large interface between the contact and the skyrmion-hosting material. This figure is taken from the supplementary material of our publication Ref. [31].

Throughout this thesis, the direction along the stacked layers will be referred to as the z-direction (out-of-plane). The extension of the samples in the xy-plane (in-plane direction), as well as the regions that are observed using microscopy, are on the micrometer scale. Therefore, the skyrmion system is in very good approximation two-dimensional. Structures can be patterned on the samples by removing the surrounding magnetic material using electron beam lithography. The purpose of such structures can, for instance, be to confine skyrmions to a particular region or to provide a channel that is too narrow for skyrmions to enter but that can be used to place electrical contact pads around and on top of the channels. These concepts are shown in Fig. 2.13.

2.4.2 Imaging and Tracking

In the experiments discussed in this thesis, skyrmions are imaged using magneto-optical Kerr effect microscopy [84]. The Kerr effect describes the change of intensity and polarization of light as it is reflected from a magnetic surface. In the discussed experiments, Kerr microscopy is used to identify the positions (and sometimes shapes) of skyrmions in the system. To this purpose, the polar Kerr microscopy configuration [134] is employed, which can provide the spatially-resolved relative magnitude of the out-of-plane magnetization component. Consequently, skyrmion cores appear as dots of opposite out-of-plane magnetization (and thus brightness in Fig. 2.13) compared to the surrounding. The wavelength of the employed visible light fundamentally limits the spatial resolution of Kerr microscopy. The skyrmions' domain walls cannot be resolved directly, but their position may still be estimated as discussed in section 4.1. The Kerr microscopy images shown in the thesis are background-subtracted, i.e., the brightness in the resulting image (Fig. 2.13) indicates the out-of-plane magnetization at each pixel relative to a background image of the fully-saturated out-of-plane magnetized system. Background-subtraction is performed to isolate the magnetic information from other sources of intensity variation, such as surface reflectivity variations due to sample topography or dust. Slight misalignment of the background image can cause structural properties, such as the boundaries of the magnetic material, to be visible in the resulting images. In Fig. 2.13 the boundaries of the magnetic material (the two top lines of the triangle) and the placement of gold contacts (structures at the corners and center of the bottom side of the triangle) are visible.

Most of the analysis in this thesis is based on the time-resolved skyrmion positions, which requires assigning a center position to each skyrmion (”tracking”) in each Kerr microscopy video frame. This step is done by fitting Gaussians to the peaks in the brightness distribution. For the quasi-one-dimensional single-skyrmion systems in chapter 3, the one-dimensional skyrmion trajectory can be obtained by, for every frame, fitting the Gaussian-smoothed intensity accumulated along the direction perpendicular to the skyrmion motion with a Gaussian. The center of that Gaussian is then employed as the skyrmion position, and its standard deviation as a measure for the skyrmion size. For two-dimensional systems studied in chapters 4 and 5, the tracking is performed predominantly using the trackpy python package [121], which fits two-dimensional Gaussians to the peaks in the brightness distribution. The package allows for specifying thresholds for the peak's extent and total intensity as well as the minimum separation of distinct peaks. Trackpy furthermore provides the radius of gyration and eccentricity of the brightness distributions as measures for size and shape, respectively. Specialized machine-learning-based software for skyrmion detection (Ref. [135]) was published after the main research presented in chapters 4 and 5, Ref. [36] and Ref. [37] respectively, was completed.

For systems containing more than a single skyrmion, converting the skyrmion positions in each frame of a Kerr microscopy video into multiple distinct trajectories (”linking”) is non-trivial. While this is not required to determine the skyrmion distribution in the system, it is necessary to obtain the diffusion coefficient from the mean squared displacement as discussed in section 2.2.5. The trackpy package [121] includes a linking algorithm, which works by minimizing the sum of all squared distances traveled by the skyrmions from one frame to the next. It should be noted that this algorithm tends to underestimate the diffusion[20]. However, whenever the diffusion of multi-skyrmion systems is studied in this thesis, we are predominantly interested in relative changes in the diffusion coefficient.

---

[20] As an illustrative example, if two close skyrmions were to switch positions within one frame, the algorithm would just exchange their labels, and the resulting trajectories would report no distance traveled within this frame for both skyrmions.

3. Conversion of Time and Current-Induced Force

Thiele model [40] simulations are a valuable tool to study skyrmion systems as their heavily coarse-grained nature allows for predictions on the large experimentally relevant time and length scales. These scales are inaccessible to conventional atomistic or micromagnetic simulations [10, 111] due to their prohibitive computational cost. While Thiele model simulations have been very successful in quantitatively describing the statics of experimental skyrmion systems [15, 33, 42, 43], the study of skyrmion dynamics has so far been limited to qualitative results only [38, 42, 43]. In this chapter, we overcome this limitation. We develop and experimentally demonstrate methods to ascertain the two key missing parameters required to calibrate the experimental and simulation time scales and current-induced forces. To this purpose, we study the spatially resolved pinning energetics of a confined quasi-one-dimensional skyrmion system and determine the system's complete, high-resolution potential energy landscape.

After introducing the parameters required for quantitative Thiele model predictions alongside existing determination methods, this chapter consists of two major sections: The first one deals with determining the conversion between simulation time and real experimental time. We first discuss the design of the experimental setup based on simulations and then introduce two methods to determine the conversion, each with its own trade-offs and favorable application scenarios. In the second major section of this chapter, we develop a method to determine the conversion between the applied current density to the system and the total current-induced force acting on the skyrmion. This method is first explained along simulation data, and then applied to experiments. Finally, the results are compared to analytical predictions using the 360°-domain wall model for skyrmions [85].

Most of the contents of this chapter are published in our publication

- Maarten A. Brems, Tobias Sparmann, Simon M. Fröhlich, Leonie-C. Dany, Jan Rothörl, Fabian Kammerbauer, Elizabeth M. Jefremovas, Oded Farago, Mathias Kläui, and Peter Virnau, ”Realizing Quantitative Quasiparticle Modeling of Skyrmion Dynamics in Arbitrary Potentials”, *Physical Review Letters* **134**, 046701 (2025) (Ref. [39]).

In addition, the results of sections 3.2.3 and 3.2.4 are currently planned to be published as

- Simon M. Fröhlich, Tobias Sparmann, Maarten A. Brems, Jan Rothörl, Fabian Kammerbauer, Klaus Raab, Sachin Krishnia, Mathias Kläui, and Peter Virnau, "Real-Time Simulation of Skyrmion Dynamics in 2D Spatially-Dependent Pinning Potential Landscapes", *in preparation* (2025) (Ref. [44]).

The present chapter is based on these works. Additional results regarding the flow behavior of skyrmions are employed in section 3.2.1 to discuss the boundary conditions at the edges of the magnetic material. These results are published in our publication

- Klaus Raab, Maurice Schmitt, Maarten A. Brems, Jan Rothörl, Fabian Kammerbauer, Sachin Krishnia, Mathias Kläui, and Peter Virnau, "Skyrmion flow in periodically modulated channels", *Physical Review E* **110**, L042601 (2024) (Ref. [38]).

The experiments discussed in this chapter were performed without my participation; I contributed through method development, simulation, experiment conceptualization, analysis, interpretation and discussion[1].

3.1 Parameters for Quantitative Thiele Modelling

Our goal is to obtain all parameters of the Thiele equation of motion [40] directly from experiment without the need for any assumptions on skyrmion's internal structure or the underlying magnetic interactions. The Thiele equation of motion including the relevant terms for skyrmion-based computing [16, 28, 29, 31, 132, 136] and storage devices [9, 23, 24] is given by

$$-\gamma\vec{v} - G_{\mathrm{rel}}\gamma\vec{z}\times\vec{v} + \vec{F}_{\mathrm{therm}} + \vec{F}_{\mathrm{pin}}(\vec{r}) + \vec{F}_{\mathrm{SkSk}}(\{\vec{r}\}) + \vec{F}_{\mathrm{SkBd}}(\vec{r}) + \vec{F}_{\mathrm{current}}(\vec{r}) = 0 \tag{3.1}$$

where $\vec{r}$ and $\vec{v}$ are the skyrmion center position and velocity respectively, $\{\vec{r}\}$ represents the positions of all skyrmions. The relative gyrotropic force strength G_{rel} can be determined from the effective skyrmion Hall angle θ_{eSH} via $|G_{\mathrm{rel}}| = \tan(\theta_{\mathrm{eSH}})$. The effective skyrmion Hall angle is usually negligible in systems where the slow dynamics is dominated by pinning [20, 104]. At sufficiently strong current-induced forces, it can be determined as the angle between the directions of current flow and skyrmion motion [20, 99, 100]. The thermal random force $\vec{F}_{\mathrm{therm}}$ is usually assumed to be Gaussian white noise. Its strength is determined by the effective damping parameter[2] γ and the temperature via

---

[1] The experiments were conducted predominantly by [redacted] with the help of [redacted] without my involvement. I developed the method for matching current-induced forces (section 3.3) and the approach to match time scales based on the skyrmion diffusion coefficient (section 3.2.2). For these parts, I performed the experiment conceptualization, the computer simulations, and the data analysis except the tracking and the determination of the diffusion coefficient and skyrmion size. The approach to match time scales based on transition times was originally developed by [redacted] and [redacted] in another system and adapted to the studied confined system by me. The experiments considering the flow behavior of skyrmions have been predominantly conducted by [redacted] without my participation and analyzed by [redacted] with my help. I performed the simulations of electrical current flow. The appendix section A.1.1 provides a detailed description of my contributions to the research presented in this chapter.

[2] The skyrmion damping γ entails both the system's intrinsic Gilbert damping as well as effects related to the skyrmion's internal magnetic structure. While the latter thermally fluctuates, the effective skyrmion damping coefficient describes the average damping experienced by the skyrmion. The methods based on time-averaged properties introduced in this chapter automatically provide the effective skyrmion damping. Section 2.2.3 provides a detailed discussion on skyrmion damping.

the fluctuation-dissipation-theorem [97]. Spatially inhomogeneous material growth introduces regions to the sample that are more energetically favorable for the skyrmion than others due to local variations of the magnetic properties. Consequently, skyrmions appear to be "pinned" at certain positions for extended periods of time. The position-dependent pinning force $\vec{F}_{\text{pin}}(\vec{r})$ to model these effects can be determined from the experimentally ascertained potential of mean force as discussed in the next section. The interaction force between different skyrmions $\vec{F}_{\text{SkSk}}(\{\vec{r}\})$ and between skyrmions and the boundaries of the magnetic material $\vec{F}_{\text{SkBd}}(\vec{r})$ can be determined using iterative Boltzmann intervention as demonstrated in our publication Ref. [15]. This only leaves the effective damping parameter γ and the current-induced force $\vec{F}_{\text{current}}(\vec{r})$ depending on an applied current density profile to be determined in this chapter.

The above equation also reveals why, so far, only qualitative predictions of dynamics could be made as the damping parameter and the velocities in response to acting forces only appear as a product. Consequently, the damping parameter sets the time scale of dynamics. In standard simulation units, where unit length is set to 1 µm, the effective damping $\gamma_{\text{sim}} = 1$, and the product of the Boltzmann constant and temperature[3] $\mathrm{k_B T_{sim}} = 1$, we obtain all time-like quantities in the simulation time unit

$$\tau_{\text{sim}} = \gamma \cdot \left(1\,\mu\text{m}^2/\mathrm{k_B T}\right). \tag{3.2}$$

This relation can be derived by noticing that the diffusion coefficient (without loss of generality at $G_{\text{rel}} = 0$ and $\vec{F}_{\text{pin}}(\vec{r}) = 0\ \forall \vec{r}$) given by the Einstein-Smoluchowski-relation [41, 89] $D = \mathrm{k_B T}/\gamma$ in real units must match the diffusion coefficient converted from simulation units $D = 1\,\mu\text{m}^2/\tau_{\text{sim}}$. For these reasons, the effective damping parameter is key for quantitative modeling of skyrmion dynamics. In the following, we discuss two different methods to determine it from experimental data. In section 3.3, we then develop a method to ascertain the current-induced forces to complete the set of parameters for quantitative Thiele model simulations.

3.2 Time Scale Conversion and Damping Parameter

This section aims to determine the conversion from simulation time to real (experimental) time or, equivalently, the effective skyrmion damping parameter. Since damping affects all dynamic processes, the evident approach is to match a dynamic process to experimental data, such as thermal diffusion or current-induced dynamics. However, straightforward relations such as the modified Einstein-Smoluchowski-relation [41, 89, 95, 105] for the skyrmion diffusion coefficient (derivation in section 2.2.5)

$$D^{\text{free}} = \mathrm{k_B T}/\left(\gamma\left(1 + G_{\text{rel}}^2\right)\right) \tag{3.3}$$

or the relation for the velocity under applied current $\vec{v} = \vec{F}_{\text{current}}/\gamma$ only hold in the absence of pinning effects. As pinning effects are unavoidable in state-of-the-art systems,

---

[3] The thermal energy $\mathrm{k_B T}$ is consistently written in non-italic font to emphasize that all energy-like quantities are given in multiples of $\mathrm{k_B T}$ and it therefore predominantly takes the role of a unit in this thesis.

two methods are presented in this section to incorporate pinning effects in determining the effective skyrmion damping[4]. To obtain good statistics for studying the effects of pinning, we confine skyrmions in narrow channels by limiting the magnetic material. Thereby, we make our systems effectively one-dimensional. The details of the experiment design based on simulation studies are discussed in the following section.

3.2.1 Experiment Design and Experimental Setup

Designing the experimental setup requires estimating at which channel widths the skyrmion dynamics will be in good approximation one-dimensional. This approximation will be employed in the analysis and the simulation of skyrmions in narrow wires in the remainder of this chapter. Therefore, we employ two-dimensional computer simulations of confined skyrmions to gauge the accuracy of this approximation.

Skyrmions are simulated in periodic channels with different widths and no pinning. We employ the slope of the mean squared displacement as a measure for the effective dimension of the dynamics exploiting the relation $\langle [x(t_0+\Delta t) - x(t_0)]^2 \rangle = 2d \cdot D \cdot \Delta t$, where $x(t)$ is the position at time t, t_0 is the initial time, Δt is the time difference over which the displacement is evaluated, $\langle \cdot \rangle$ denotes the average over all segments of length Δt, d is the dimension, and D is the diffusion coefficient [89]. In the general case of a non-zero skyrmion Hall angle, the latter is given by $1/\left(\gamma\left(1+G_{\mathrm{rel}}^2\right)\right)$ at $\mathrm{k_B T_{sim}} = 1$ and $\gamma_{\mathrm{sim}} = 1$, see Eqn. (3.3). It is to note here, that pinning effects have been shown to strongly suppress the skyrmion Hall effect for the low skyrmion velocities occurring in the pure diffusion and current-induced creep regimes studied in this chapter [20, 137]. Moreover, even without pinning-induced suppression, the skyrmion Hall angle in the systems we investigate can be estimated to be small, and we focus on the regime $0 \leq G_{\mathrm{rel}} \lesssim 0.25$ for designing experimental systems [15, 20, 42]. For the simulations, we employ the skyrmion-boundary interactions determined in our publication Ref. [15], which features the same material composition and similar-sized skyrmions as the following experiments. The experiments employ a $\mathrm{Ta(5)/Co_{20}Fe_{60}B_{20}(0.9)/Ta(0.08)/MgO(2)/Ta(5)}$ multilayer stack. The respective thicknesses of the layers in nanometers is given in parenthesis and the elemental ratio is indicated by the subscripts.

Each point in Fig. 3.1 represents the mean value for the effective $d/\left(\gamma\left(1+G_{\mathrm{rel}}^2\right)\right)$ over at least 10 simulations of 100 trajectories with a length of $10^4\,\tau_{\mathrm{sim}}$, with the error given by the standard error of mean. The simulations have been performed using an Euler integrator with a time step of $\Delta t = 10^{-5}\,\tau_{\mathrm{sim}}$ and the trajectories have been sampled every $0.1\,\tau_{\mathrm{sim}}$. Based on the dependencies depicted in Fig. 3.1, we chose a channel width of 5 µm for the system studied in this section and 7 µm in section 3.3, both deep in the effective one-dimensional regime to account for the case of smaller skyrmions than in Ref. [15]. For the method presented in this section, these considerations are particularly important as we determine the experimental and simulated diffusion coefficients from the

---

[4] At sufficiently large applied current densities, the current-induced force dominates over pinning effects such that the relation $\vec{v} = \vec{F}_{\mathrm{current}}/\gamma$ holds again. However, large applied current densities also induce a deformation of the skyrmion profile [20], affecting the skyrmion dissipation tensor, potentially not being captured by the Thiele model, and consequently also affecting the effective damping [95].

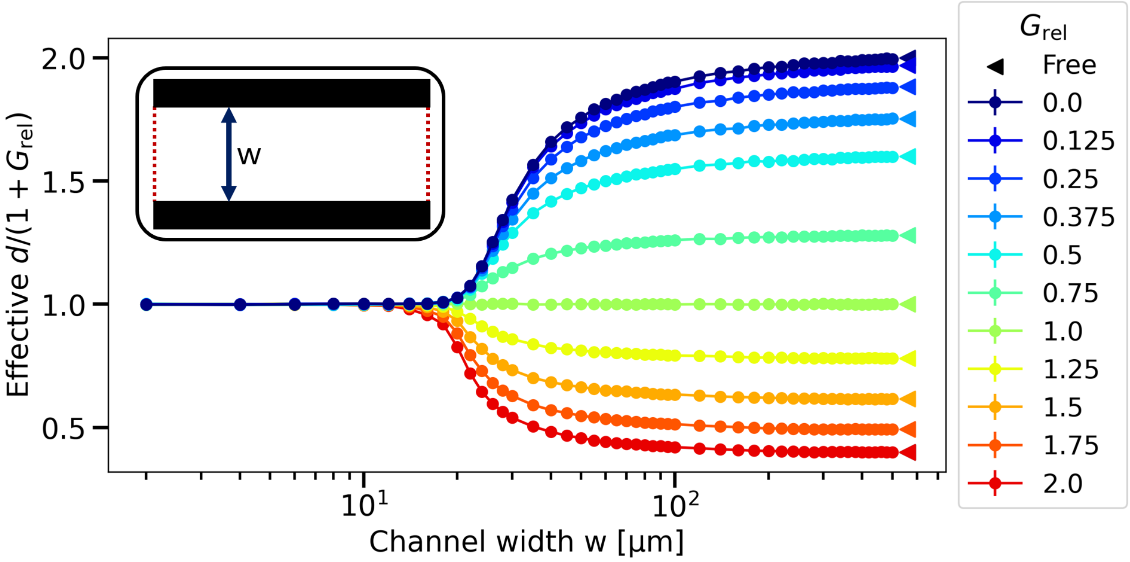

Figure 3.1: The effective $d/\left(\gamma\left(1+G_{\text{rel}}^2\right)\right)$ of skyrmions with different relative gyroforce strengths as a function of the width of the confining channel. The errors estimated by the standard error of mean are smaller than the point markers and solid lines act as a guide to the eye. Triangular markers indicate the values given by the modified Einstein-Smoluchowski-relation that is valid in the no-confinement case. The inset shows a schematic of the channel, with the channel width indicated by a blue double-headed arrow and the connected periodic boundaries marked via dotted red lines. This figure is adapted from the supplementary material of our publication Ref. [39].

slope of the one-dimensional mean squared displacement. In addition, the simulations will be performed in one dimension (instead of modeling the boundaries of the magnetic material as in this section) since pinning will be modeled as a one-dimensional spatially inhomogeneous energy landscape. As a side note, Fig. 3.1 also reveals that for $G_{\text{rel}} > 1$ the effective $d/\left(\gamma\left(1+G_{\text{rel}}^2\right)\right)$ increases due to the confinement. Consequently, the diffusion coefficient increases with confinement, similar to the recently studied anomalous increase in diffusivity with increasing particle density in odd-diffusive systems including skyrmions [102, 103]. For $G_{\text{rel}} = 1$ the effective $d/\left(\gamma\left(1+G_{\text{rel}}^2\right)\right)$ is independent of the confinement.

For the experimental setup, a ring-shaped structure with an inner radius of 12.5 µm and a width of 5 µm is patterned using electron-beam lithography (Fig. 3.2 center). Employing a ring-shaped structure creates periodic boundary conditions for the one-dimensional skyrmion dynamics.

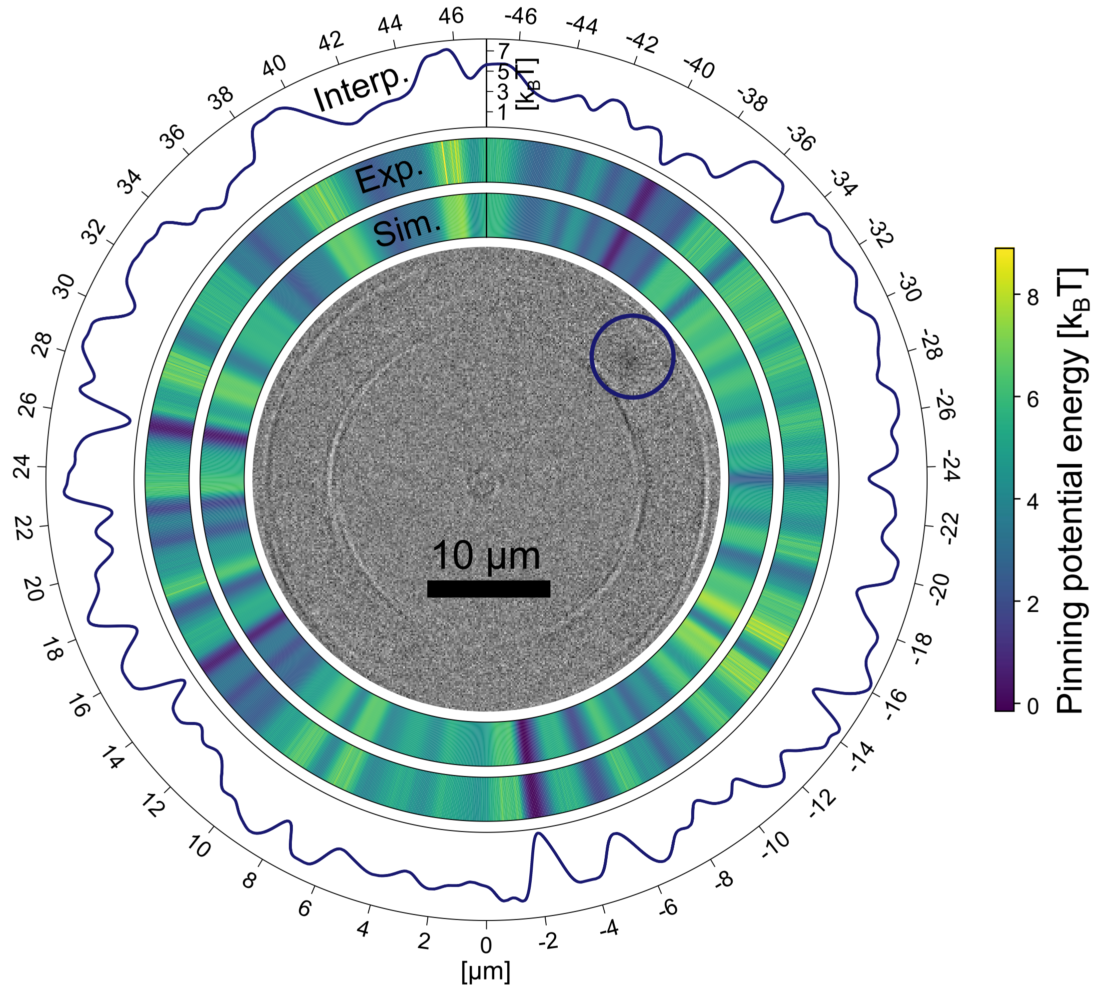

Figure 3.2: Central image: Kerr microscopy image of a single skyrmion (dark spot highlighted by a blue circle) confined to a ring with an inner radius of 12.5 µm and a width of 5 µm. The two surrounding heatmaps show the one-dimensional pinning energy landscapes determined from experiment (outer) and recovered from simulation (inner). The outermost plot depicts the Gaussian RBFN fit of the experimental pinning energy landscape that is employed in the simulation. Fig. 3.5 contains a more detailed depiction of this curve as well as the two heatmaps. The outside axis labels refer to the distance along the ring in micrometers. This figure is taken from our publication Ref. [39].

In general, curvature can impact diffusive behavior depending on the boundary conditions at the edges of the channel [138]. Therefore, we investigate the boundary conditions in our systems by studying the flow of skyrmions trough an 80 µm wide channel (Fig. 3.3a) patterned on a similar multilayer stack $\mathrm{Ta}(5)/\mathrm{Co}_{20}\mathrm{Fe}_{60}\mathrm{B}_{20}(0.95)/\mathrm{Ta}(0.09)/\mathrm{MgO}(2)/\mathrm{Ta}(5)$. Flow behavior is an excellent test for boundary conditions at the channel edges as they greatly impact the velocity profile resolved in the direction perpendicular to the channel. No- or partial-slip boundary conditions reduce the velocity close to the channel edges compared to the center of the channel. We drive the skyrmions via a current-induced force by applying a current density of $5.7 \times 10^7\ \mathrm{A/m^2}$ along the wire. Fig. 3.3b shows the velocity profile across the channel. We observe no significant velocity reduction close to the channel edges and therefore conclude “slip” boundaries conditions. Under these conditions, we assume the one-dimensional approximation for the ring-shaped structure in Fig. 3.2 to be justified. As a consistency check for this analysis method, we study structured channel edges as shown in Fig. 3.3c. Inside and close to the triangular modulation we observed a reduced average velocity, and the system consequently exhibits partial slip boundary characteristics (Fig. 3.3d). This effect can be explained by the low relative current density in these regions shown in the COMSOL Multiphysics [73] simulation in Fig. 3.4 as well as the fact that skyrmions reentering the central region of the channel will obstruct the flow at the entry points. Note that here only the bottom 5 nm tantalum layer is simulated and that we are only interested in the relative magnitude of the spatially resolved current density.

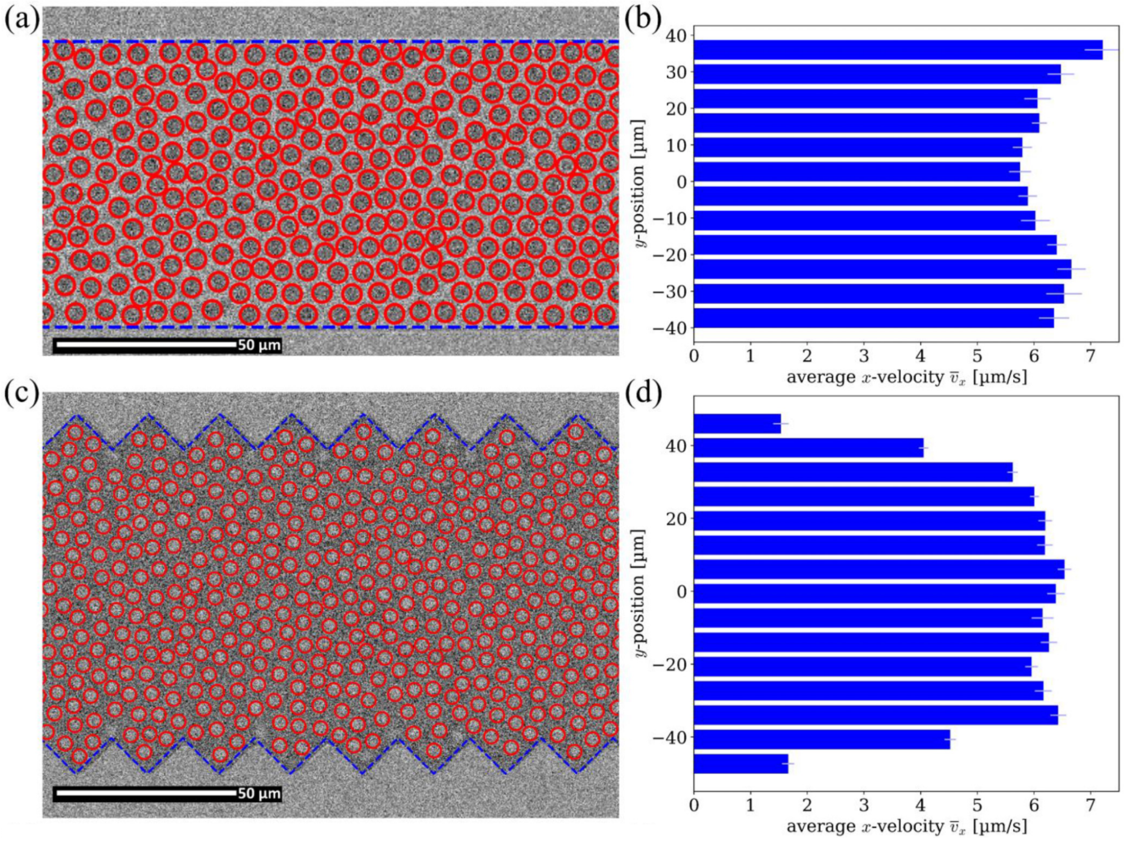

Figure 3.3: (a,c) Kerr microscopy images of exemplary skyrmion configurations in channels without and with structuring of the channel edges, respectively. (b,d) Corresponding distributions of average x-velocities. Here, x and y refer to the directions along the channel and perpendicular to it, respectively. Lines at the tips of the histogram bars represent errors. This figure is adapted from our publication Ref. [38].

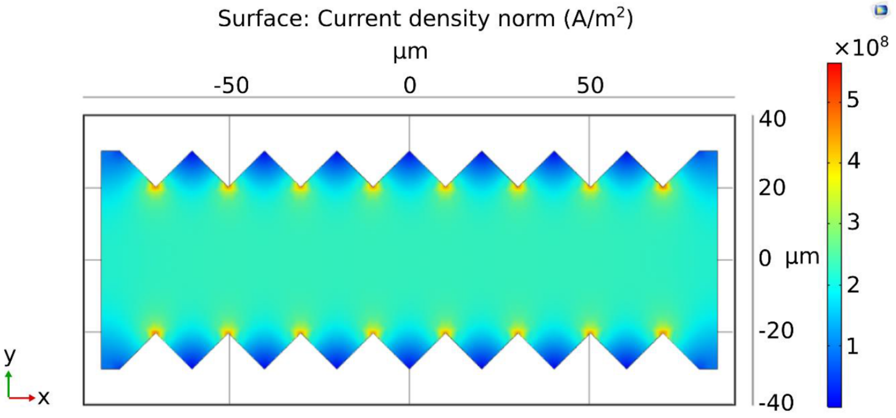

Figure 3.4: Exemplary simulation of the current density distribution in a channel with structured edges. The current density inside the triangular modulation of the edge is significantly smaller than the current density in the center of the channel. The simulation details are provided in appendix section A.2.1. This figure is adapted from the supplementary material of our publication Ref. [38].

3.2.2 Lifson-Jackson Method to Ascertain the Free Diffusion

In this section, we develop an approach to determine the effective skyrmion damping and, thus, the time conversion by combining the modified Einstein-Smoluchowski-relation (Eqn. (3.3)), the Lifson-Jackson framework [139] and a radial basis function network fit of the pinning energy landscape [140]. With this approach, we overcome the challenge that Eqn. (3.3) is valid only for the free diffusion coefficient that is not directly accessible experimentally. In experiments, only the pinning-affected diffusion coefficient can be measured as pinning is unavoidable in state-of-the-art systems.

Our strategy is thus to determine the pinning energy landscape at a sufficiently high resolution to use it reliably in simulations. Then, we obtain the ratio between the pinning-affected diffusion coefficient D^{pin} the free one D^{pin} by observing the reduction of diffusivity due to pinning and use it to estimate the free experimental diffusion coefficient. In periodic systems, this ratio has an analytic form given by the Lifson-Jackson-formula [139, 141]

$$\frac{D^{\text{pin}}}{D^{\text{free}}} = \frac{1}{\left\langle \exp\left(-\frac{U_{\text{pin}}(x)}{\text{k}_{\text{B}}\text{T}}\right)\right\rangle \cdot \left\langle \exp\left(\frac{U_{\text{pin}}(x)}{\text{k}_{\text{B}}\text{T}}\right)\right\rangle} \leq 1 \tag{3.4}$$

where the averages are taken over one unit cell of the potential. The constant $D^{\text{pin}}/D^{\text{free}}$ is thus a functional of $U_{\text{pin}}(x)/\text{k}_{\text{B}}\text{T}$ alone. While the Lifson-Jackson-formalism is typically applied to potentials that have a simple form inside one unit cell, it is applicable to an arbitrary energy landscape provided that the system is subject to periodic boundary conditions. Due to the periodicity of the ring-system, numerically solving the formula for a fit of the experimentally determined U_{pin} provides an alternative approach to determining the Lifson-Jackson-functional $D^{\text{pin}}/D^{\text{free}}$ from simulation. The limitations of this approach are discussed at the end of this section in the context of the properties of the experimental system.

We let the skyrmion thermally explore the entire system for more than 7 hours at $(322.0 \pm 0.2)\,\mathrm{K}$. An external out-of-plane magnetic field is applied to stabilize the skyrmion. The system is imaged using Kerr microscopy at 16 frames per second; a snapshot is shown in Fig. 3.2 (center). The one-dimensional skyrmion trajectory is then obtained by, for every frame, fitting the Gaussian-smoothed intensity accumulated along the radial direction with a Gaussian. The center of that Gaussian is employed as the skyrmion position, and its standard deviation as a measure for the skyrmion size. To accelerate the tracking, this can be performed in a two-step process with iteratively increasing spatial resolution in the vicinity of the approximate skyrmion position. We have verified that this tracking method is consistent with tracking using the trackpy python package [121] but it provides the added benefit that collapsing the data onto one dimension increases the resolution and reliability of the tracking such that the final resolution is 0.001 radians per bin (0.015 µm per bin). Similar to trackpy, the skyrmion center position can be determined with an accuracy higher than the optical resolution of the microscope (1 pixel = 0.1291 µm with the employed lens) as a large number of pixels is taken into account.

From the trajectory, we determine the time-averaged skyrmion distribution $\rho(x)$ to then determine the pinning energy landscape as the potential of mean force

$$U_{\mathrm{pin}}(x) = -\mathrm{k_B T} \ln\left(\rho(x)\right). \tag{3.5}$$

Due to our measurement's good statistics and spatial resolution, we can determine the pinning energy landscape at a bin width of 1/16 µm (outer heatmap in Fig. 3.2 and dark blue curve in Fig. 3.5). Even at this resolution, which is several times higher than in previous experiments [36, 37], no bin remained unsampled. This first complete map of an entire sample's spatially resolved pinning energy also shows that our sample is free of any strong repulsive energy barriers caused by very deep pinning sites that prevent skyrmion passage within reasonable measurement time.

To employ the potential in simulation and in numerical evaluation of the Lifson-Jackson formula, we fit the potential of mean force using a Gaussian radial basis function network (RBFN) [140] implemented in the localreg python package [142] (outermost curve in Fig. 3.2 and red curve in Fig. 3.5). RBFNs fit the data as a weighted sum of fixed basis functions (in our case, a Gaussian with a fixed standard deviation), the center positions of which are determined by k-means clustering. While the weights are determined locally, the standard deviation hyperparameter is trained from multiple iterations of the RBFN fit on all datapoints. This training is, in principle, non-deterministic, but we found the resulting RBFN fits to be consistent in the sense that their deviations are sufficiently small not to significantly impact the simulation results. The clustering and the hyperparameter training are part of the localreg package. Here, we employ an average basis function density of 2.5 basis functions per µm. Even though there were no unsampled bins in this particular experiment, we have found the Gaussian RBFN to deal with missing bins much more reliably compared to other purely local fit methods, such as local polynomial regression [143].

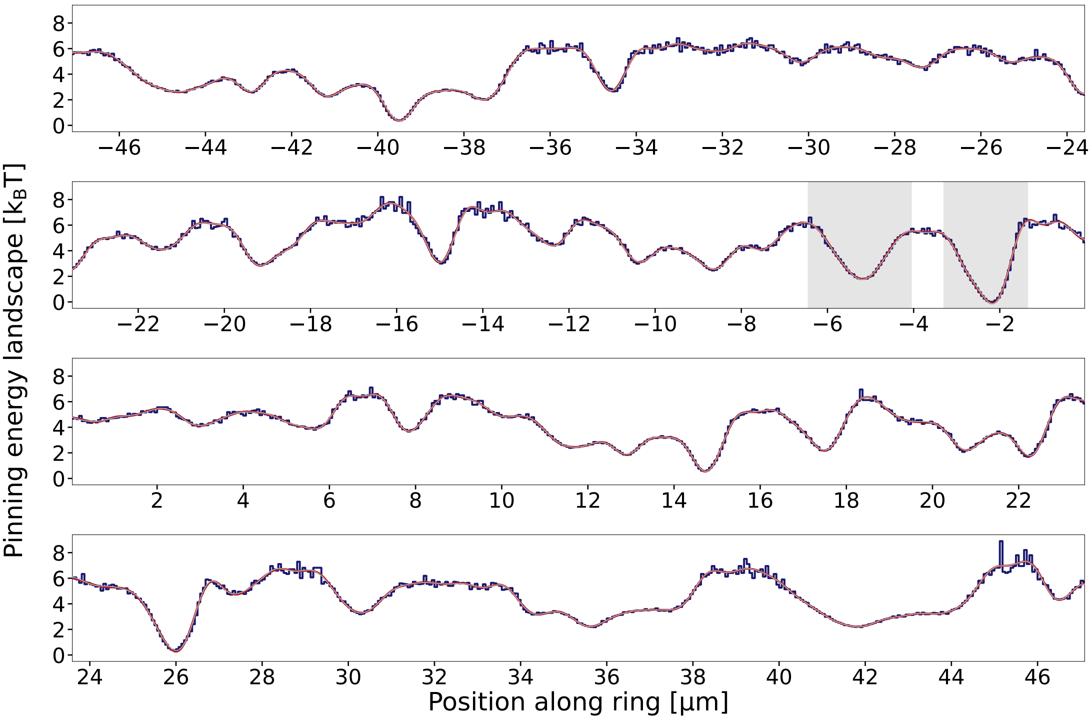

Figure 3.5: Detailed experimental pinning energy landscape (blue) obtained from the experimental skyrmion distribution in the ring at a bin width of 1/16 µm. For the simulations, this data is fitted using a Gaussian RBFN (red). The thin light blue curve (always on top of the red curve) depicts the results of applying the same analysis method to the simulation data, recovering the RBFN fitted experimental pinning energy landscape excellently within reasonable simulation time. The shaded areas highlight the regions assigned to the pair of pinning sites employed in the transition time method in section 3.2.3. This figure is adapted from our publication Ref. [39].

To numerically estimate $D^{\text{pin}}/D^{\text{free}}$ using the RBFN fitted pinning energy landscape, we employ the mean and standard error of the mean over 10 simulations of 100 trajectories for $10^5\,\tau_{\text{sim}}$. Therein, we employ the Euler integrator with a time step of $\mathrm{d}t = 10^{-5}\,\tau_{\text{sim}}$, sample the trajectories every $0.1\,\tau_{\text{sim}}$ and set the spatial resolution of the tabulated pinning energy landscape in the simulation to 1/64 µm. We obtain the simulated estimate of $D^{\text{pin}}/D^{\text{free}} = (0.124 \pm 0.001)$. This is in reasonable agreement with the numerical determination of the Lifson-Jackson functional (Eqn. (3.4)) $D^{\text{pin}}/D^{\text{free}} = 0.119$ obtained via numerically integrating the exponentials in the denominator based on the RBFN fit of the energy landscape. Appendix section A.2.2 discusses a coarse estimate of the uncertainty of this value.

One must also note here that, since the entire systems' energy landscape is used in the Lifson-Jackson-formula, it strictly speaking only holds for diffusion coefficients determined at times much larger than the characteristic diffusion time over the entire ring such that the entire energy landscape's structure is reflected in the reduction of the diffusion coefficient. Consequently, for shorter trajectories on shorter timescales, it is most reliable to determine $D^{\mathrm{pin}}/D^{\mathrm{free}}$ from simulations where experimental and simulated pinning-affected diffusion constants can both be determined on the same length scales. Experimentally, the maximum length of a continuous measurement was limited, since preventing artifacts due to sample drift requires periodically capturing new, fully magnetically saturated background images for the background-subtracted Kerr video. For the determination of the pinning energy landscape several trajectories covering the complete system multiple times with a total measurement duration of more than 7 hours have been combined. For the determination of the diffusion coefficient, however, a reliable mean squared displacement from a continuous trajectory on length scales larger than the ring circumference could not be obtained. Still, the Lifson-Jackson formula is in good agreement with the simulation results for the measurement presented in this section. This agreement can be understood in the sense that averaging the reduction of diffusivity over several trajectory segments spanning the entire system does still reflect the entire systems' pinning energy landscape. The experimental diffusion coefficient is determined from a 30-minute uninterrupted trajectory which includes a maximum directed travel distance of 1.9 ring circumferences. Similar to section 3.2.1, the diffusion coefficient was determined from the slope of the mean squared displacement (dimension $d = 1$). The mean squared displacement is determined up to a maximum time difference of 75 s and fitted with a linear function from 10 s onward. Here, the analysis was performed on three equal parts of the experimental trajectory and the diffusion coefficient and its error are determined via the mean and standard error of mean as $D^{\mathrm{pin}}_{\mathrm{exp}} = (3.76 \pm 0.74)\,\mathrm{\mu m^2/s}$. The simulated diffusion coefficient was determined on similar length scales (similar maximum mean squared displacement). Another formal limitation of the Lifson-Jackson-approach is that the energy gaps between neighboring local minima and maxima are not much greater than $\mathrm{k_B T}$ [139, 141] which essentially coincides with the condition that we have significant thermal diffusion across the entire ring and the skyrmion is not, for instance, stuck inside a single pinning site for major parts of the measurement duration. Such effects do not occur in our measurements.

The experimental diffusion coefficient $D^{\mathrm{pin}}_{\mathrm{exp}} = (3.76 \pm 0.74)\,\mathrm{\mu m^2/s}$ together with the simulated value for $D^{\mathrm{pin}}/D^{\mathrm{free}} = 0.124$ allow us to estimate the effective damping. Assuming $G_{\mathrm{rel}} \approx 0$, Eqn. (3.3) yields a damping of $\gamma = (0.033 \pm 0.006)\,(\mathrm{k_B T/\mu m})/(\mathrm{\mu m/s})$ or equivalently the time conversion $\tau_{\mathrm{sim}} = (0.033 \pm 0.006)\,\mathrm{s}$ using Eqn. (3.2). Apart from completing the set of Thiele model parameters relevant to most device concepts, this value also allows us to estimate the speed of our simulations compared to real time. For instance, using a more efficient Heun integrator with a time step of $10^{-4}\,\tau_{\mathrm{sim}}$, a simulation of 100 non-interacting particles can be run in real time on a single CPU core resulting in an effective simulation speed of 100 s of combined trajectory length per second of run time. This benchmark was performed by [redacted]. With sufficient hardware, also more complicated interacting systems can be simulated for typical experiment durations of minutes to hours within reasonable computation time. As a consistency check and to demonstrate that within reasonable simulation time we can surpass experimental statistics, we also apply the same procedure for obtaining the pinning energy landscape from experimental data to the simulated trajectories and show that we can fully recover the input potential (inner heatmap in Fig. 3.2 and thin light blue curve in Fig. 3.5).

The main advantage of this method is its simplicity in the sense that it requires only a few assumptions and parameter choices. While the Lifson-Jackson formula as stated in Eqn. (3.4) is only valid in one dimension, the Lifson-Jackson functional $D^{\mathrm{pin}}/D^{\mathrm{free}}$ could still be determined via simulations in a two-dimensional system. However, this requires a well-sampled, high-resolution pinning energy landscape of the entire sample or at least an extended region, which is hard to achieve in large two-dimensional systems without geometrical confinement. Therefore, an alternative method to determine the time conversion based on only a few well-sampled pinning sites is introduced in the next section.

3.2.3 Transition Time Method

This section outlines an alternative approach to determine the time scale conversion. In this section, the method is adapted and applied to the studied effectively one-dimensional system to directly compare the two methods and their results in the same system, which has not been done before. Therefore, the experimental and simulation data used here is the same as in the previous section.

The idea behind the method is to match a dynamic process between Thiele model simulation and experiment. However, instead of matching the long-time diffusion process as in the previous section, we now consider the transition across an energy barrier separating two pinning sites and match the distribution of transition times. The advantage of this method is that only a smaller region of the system needs to be well sampled compared to the previous approach. In principle, it suffices if two pinning sites and the dominant transition path between them is well sampled.[5] Consequently, this method has great potential for application in large two-dimensional systems where experimentally ascertaining a complete map of the system's pinning energy landscape would require impractically long measurement durations. This section aims to outline the transition time method and show that it provides consistent results with the Lifson-Jackson functional method for the studied system. The trade-offs of the two methods are compared at the end of this section.

The processes under consideration are transitions between two neighboring pinning sites separated by an energy barrier. We estimate the time scale conversion by comparing the distribution of transition times from one site to the other between experiment and simulation. To ensure the robustness of this method, we require several properties for the pair of pinning sites. First, the transition must be sampled sufficiently in the experiment so that the distributions of transition times can be reliably compared. Here, we require at least about 200 transitions in each direction. Second, the energy barrier must be sufficiently large such that the time constant of the exponential part of the transition time distribution is significantly (here at least one order of magnitude) larger than the time-resolution of the microscope (0.0625 s). Thereby, we ensure that contributions from unresolved multi-transitions[6] are low. Finally, both pinning sites should be well-definable

---

[5] Of course, data on the transitions for multiple pairs of pinning sites enhances the methods reliability. Moreover, certain conditions must be met by the pairs of pinning sites and the measurement statistics for the method to work well as elaborated in this section.

[6] Unresolved multi-transitions refer to processes like "Left → Right → Left → Right" that are identified as "Left → Right" due to the time resolution of the microscope.

from the potential of mean force in the sense that another sufficiently high energy barrier separates them from the surrounding system and that they have no complex internal structure like another double-well in the potential. Thereby, we ensure that "the skyrmion being inside either of the two pinning sites" is a well-defined state that does not drastically depend on the precise boundaries of the region assigned to each pinning site.

For the system studied here, only one pair of pinning sites fulfills all the above conditions. The regions assigned to these pinning sites are indicated by the shaded areas in Fig. 3.5. Ideally, one would like to perform the following analysis for several pinning site pairs and average over all estimates for the time scale conversion factor. In extended two-dimensional systems that contain more pinning sites in total, which can be simultaneously sampled by multiple skyrmions at a low density as shown in section 5.2, we generally find more suitable pinning site pairs [44]. Section 3.2.4 discusses the advantages of the transition time method for two-dimensional systems and suggests an approach for dealing with unsampled regions (missing bins) in the energy landscape that are typically much more prominent in two-dimensional systems.

We start tracking the transition time from the left pinning site to the right pinning site when the skyrmion enters the left pinning site either from the left (negative position) of the left pinning site or from the right pinning site. Thus, if the skyrmion leaves the pinning site to the left (outside the pinning site pair) and at a later point in time reenters the pinning site, the transition time is reset[7]. The time is stopped when the skyrmion enters the region assigned to the right pinning site. The transition time from right to left is determined accordingly. Since there is a non-zero distance between the pinning sites, a lower bound exists for the transition time, and the total distribution exhibits a peak at a low but non-zero transition time. For large transition times, the estimated probability is zero due to the finite duration of the experiments and simulations. Here, we consider only the well-sampled region in between these regimes where the transition time distribution can be well-described by a falling exponential (see simulation curves in Figs. 3.6b,d). Since the observed skyrmion trajectory is discrete, so are the dwell times with a discretization given by the microscopy video's frame rate and the simulation's write-out frequency. To avoid possible artifacts due to binning, we perform an unbinned negative log-likelihood fit using the python package iminuit [144, 145]. The normalized discrete fit function for the transition time distributions is chosen as

$$P(t) = \frac{1}{N} e^{-t/T} \,\text{with}\, N = \sum_{t=t_{\min}}^{t_{\max}} e^{-t/T} = \frac{e^{-t_{\max}/T} - e^{(1-t_{\min})/T}}{1 - e^{1/T}}, \tag{3.6}$$

where $t_{\min}$ and $t_{\max}$ refer to the minimum and maximum frames in between which the distribution is considered, respectively , and the time constant T is later employed to determine the time scale conversion. "Frames" refer to experimental microscopy video frames and simulation write-outs. We simulate 100 trajectories for $10^6\,\tau_{\text{sim}}$ and sample the trajectory every $2\,\tau_{\text{sim}}$ at identical parameters as in the previous section. To have similar contributions from unsampled multi-processes in both experiment and simulation, the simulation write-out frequency is chosen such that the real-time length of one frame

---

[7] The time is not reset when entering the region between the pinning sites.

is comparable between experiment and simulation. Thus, in general, and in particular, for two-dimensional systems, the choice of write-out frequency is to be seen as iterative and self-consistent in the sense that the time scale conversion is determined for a given write-out frequency, and then using this conversion, the write-out frequency is adjusted. This procedure is then repeated until convergence.

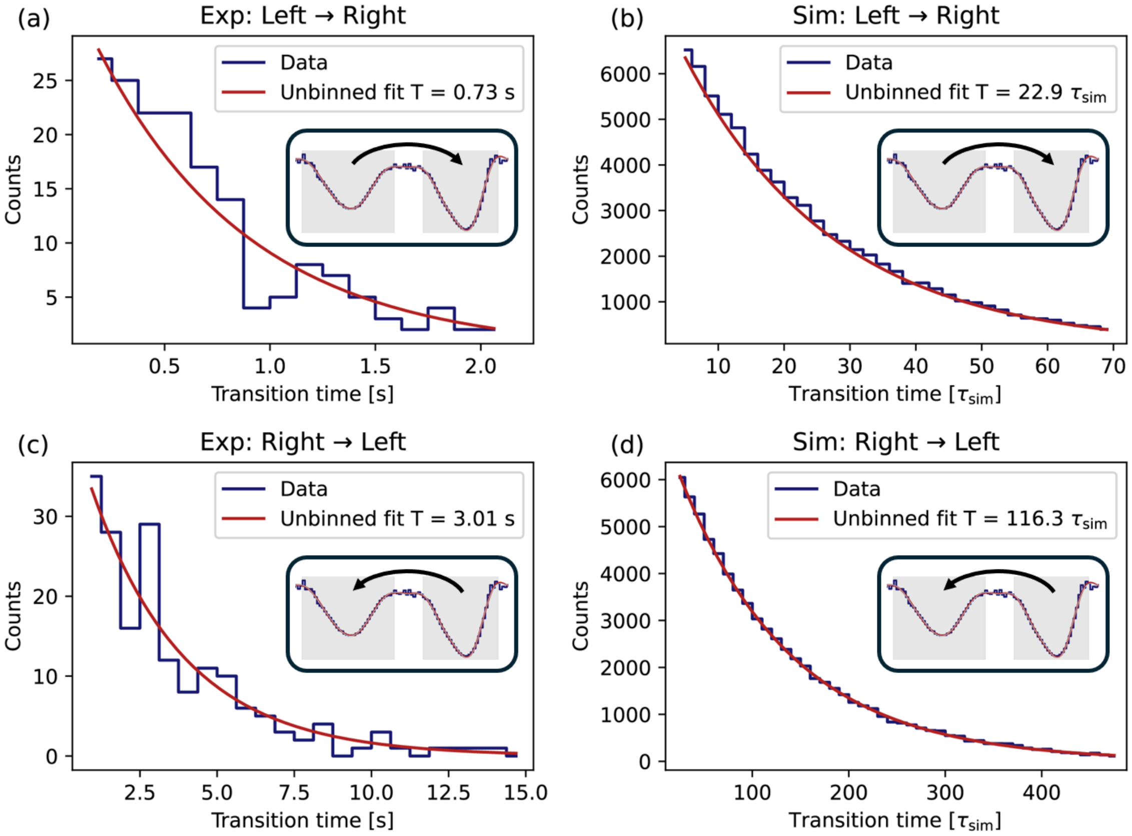

Figure 3.6: Transition rate distributions for the transition from the left to the right pinning site (a,b) and from the right to the left (c,d). The regions assigned to these pinning sites are shaded in Fig. 3.5 and reproduced in the insets alongside an arrow indicating the transition direction. The blue histogram shows the distribution obtained from experiment (a,c) or simulation (b,d), whereas the red curve is the fit to the unbinned data in the same range of transition times according to Eqn. (3.6). Here, the fit has been multiplied with the normalization such that the data can be given in counts instead of probability to highlight the difference in statistics between experiment and simulation.

Fig. 3.6 shows the unbinned fits alongside the binned distributions of the transition time distributions from the left pinning site to the right pinning site (a,b) and vice versa (c,d) for experiment (a,c) and simulation (b,d). The exponential fit describes the distributions excellently for the simulation and quite well for the experiment despite the low statistics. The ratio between the time constants for each process serves as an estimate of the time scale conversion factor. The mean value of $\tau_{\mathrm{sim}} = 0.029\,\mathrm{s}$ is in good agreement with the value from the Lifson-Jackson functional method $\tau_{\mathrm{sim}} = (0.033 \pm 0.006)\,\mathrm{s}$. The error of the mean[8] based on the error propagation of the fit uncertainties is 0.002 s. However, this error estimate does not take into account errors introduced by exposure effects in the microscopy. Exposure effects refer here to the key difference between microscopy video frames and simulation write-outs: When a microscopy image is taken, the brightness distribution is averaged over the exposure time (1 experimental frame), which is similar to averaging over the skyrmion trajectory during this time. In contrast, for the simulation, one write-out per simulation frame corresponds to the instantaneous position of the skyrmion at that time. Similarly, exposure effects also impact the potential of mean force determined from the experimental trajectory. A thorough investigation of the impact of exposure effects is the subject of future research beyond the scope of this thesis.

3.2.4 Method Comparison and Outlook on Treating Unsampled Regions

The key steps for the two methods to determine the time scale conversion between experiment and simulation are summarized below.

Diffusion-based method (section 3.2.2):	Transition time method (section 3.2.3):
1. Start from high-resolution pinning energy landscape	1. Start from well-sampled pinning site pairs
2. Determine $D^{\text{pin}}/D^{\text{free}}$	2. Select suitable pinning site pairs
3. Obtain effective damping γ from Einstein-Smoluchowski-relation	3. Match transition times between experiment and simulation
4. Calculate the time conversion	4. Calculate the time conversion

Compared to the diffusion-based Lifson-Jackson functional method, the transition time method is less straightforward in the sense that more parameters must be carefully analyzed, such as the region assigned to a pinning site, the simulation write-out frequency and the conditions to include a pinning cluster into the analysis. In principle however, the transition time method has one key advantage: Only considering dynamics within a pinning site pair circumvents the diffusion-based method's requirement of a well-sampled energy landscape everywhere, opening up applicability for large two-dimensional systems. In large two-dimensional systems, unsampled regions are much more prominent within reasonable measurement time[9]. However, to simulate such systems, a complete pinning energy landscape without undefined regions is required. Fig. 3.7 depicts a schematic excerpt of a two-dimensional pinning energy landscape containing containing pinning site pairs with sampled transition path between them, but also extended unsampled regions (white space). The following paragraph provides an outlook on a method for treating unsampled regions that combines ideas from both of the discussed methods.

---

[8] The values for "Left → Right" and "Right → Left" are $\tau_{\text{sim}} = (0.032 \pm 0.003)\,\text{s}$ and $\tau_{\text{sim}} = (0.026 \pm 0.002)\,\text{s}$, respectively.

[9] Of course, the number of empty bins in the skyrmion distribution depends on the bin size. The discussion assumes a small bin size suitable for simulation with minimal discretization artefacts.

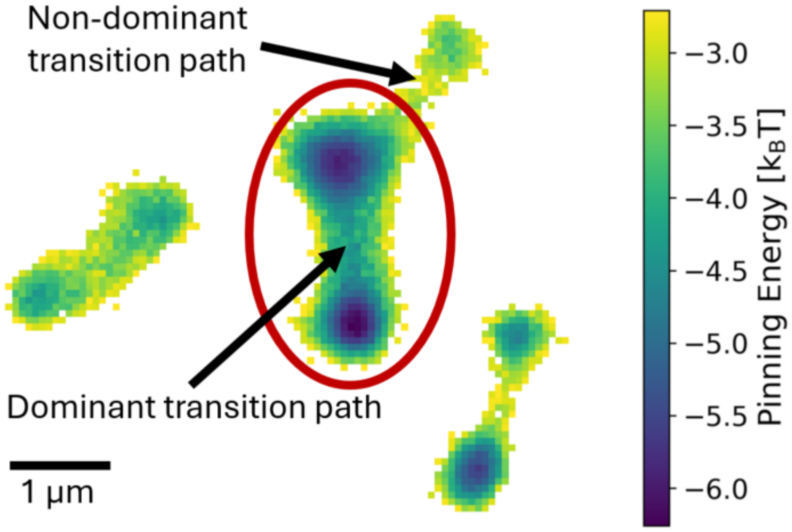

Figure 3.7: Schematic depiction of pinning site pairs in a two-dimensional pinning energy landscape. The white areas correspond to unsampled regions. The pinning site pair encircled in red exhibits a second sampled but non-dominant transition path to another pinning site.

The above summary of the two methods' key steps reveals that the starting point of the diffusion-based method is precisely what we are looking for: a high-resolution pinning energy landscape without significant unsampled regions, i.e., unsampled regions that cannot easily be interpolated. In addition, the final step of the methods is, of course, identical. This motivates the idea to approximate unsampled regions by applying the diffusion-based method in reverse, once the time conversion has been determined using the transition time method. The crude approximation employed in the suggested procedure is assigning the same average energy level to all unsampled regions. However, for most aspects of the skyrmion dynamics in the system, the location, arrangement, and shape of the pinning sites are likely much more relevant than the details of the energy landscape within the rarely visited, experimentally unsampled regions. The aim of the approach presented here is to, on average, accurately present the energy barriers for leaving the dominant pinning sites in the sample. The steps of the procedure, continuing after the last step of the transition time method, are given below.

5. From the time conversion calculate the effective damping γ
6. From γ determine D^{free} and experimentally measure D^{pin} to calculate the experimental $D^{\text{pin}}/D^{\text{free}}$
7. Vary the energy level of the unsampled regions in simulation iteratively until it the system approximately exhibits the experimental $D^{\text{pin}}/D^{\text{free}}$

While a full demonstration of this procedure in a two-dimensional system is beyond the scope of this outlook, we plan to publish Ref. [44], which shows that this procedure allows for the quantitative prediction of the density dependence of skyrmion diffusion, which is in excellent agreement with experimental results.

Finally, it is important to note that, due to the transition rate method's general focus on dynamics on shorter time scales, it is more prone to be impacted by the limited experimental time-resolution as well as exposure effects. One possible way to address these effects would be to employ a higher framerate in the experimental setup. Still, the results in the previous sections show very good agreement between both methods. Thereby, we have demonstrated two distinct methods to ascertain the time scale conversion, enabling quantitative predictions of skyrmion dynamics.

3.3 Conversion for Current-Induced Force

The final phenomenon that must be modeled for quantitative simulations of skyrmion devices such as the ones discussed in chapter 6 is current-induced motion of skyrmions [18, 20, 99, 146, 147]. The missing key conversion here is the relation between the current density applied to the system and the force acting on the skyrmion in the Thiele model. In this section, we develop a method to ascertain the total force acting on a skyrmion in response to current-induced spin-torques directly from experiments.

One evident approach would be to drive a skyrmion into the viscous flow regime where the current-induced force dominates over pinning forces and thermal fluctuation. In that case, it follows from Eqn. (3.1) that $\vec{v} = \vec{F}_{\text{current}}/\gamma$, consequently providing the force for known effective damping. The major drawback of this approach is that reaching the viscous flow regime requires high current densities ($> 10^{11}$ A/m^2) [20]. At high current densities, the skyrmion structure is deformed [20], and consequently, the skyrmion dissipation tensor changes and deformations can occur that cannot be described within the Thiele model [40, 85]. However, the effective damping depends on the dissipation tensor [40, 95], and the values obtained by the methods from the previous section no longer apply.

To circumvent the issue of current-induced changes of the skyrmion's internal structure, we focus on the ultra-low current density regime (order 10^6 A/m^2) and develop a method to determine the force on the skyrmion directly, even without knowledge of the effective damping. Apart from these benefits, the regime where current-induced effects, pinning, thermal dynamics, and skyrmion interactions all compete on similar energy scales is very important for unconventional computing approaches like skyrmion-based reservoir computing [28, 31, 32, 43, 132], as discussed in section 6.1. In the upcoming section, we develop the force determination method and demonstrate it in simulation. Then, a suitable experimental system is designed. In the subsequent sections, the experimental data is evaluated and the results are compared to analytical predictions based on the 360°-domain wall model for skyrmions [85].

3.3.1 Developed Method and Demonstration in Simulation

The key idea behind this method is that even current-induced forces that do not sufficiently dominate over pinning effects to deterministically displace the skyrmion, will still bias the skyrmion distribution in the system. As in the previous section, we will again consider a single skyrmion confined to a narrow channel such that the system can be treated as effectively one-dimensional. Thereby, the analysis is simplified, and the required measurement time is significantly reduced. Since the current-induced force only depends on the current density that the skyrmion experiences, the results translate directly to extended two-dimensional systems. In one dimension, the probability density $\rho(x)$ to observe the skyrmion at a position x is then given by the Boltzmann weight

$$\rho(x) \propto \exp\left(-\frac{U(x)}{\mathrm{k_B T}}\right) \tag{3.7}$$

where $U(x)$ is the effective energy landscape, $\mathrm{k_B}$ the Boltzmann constant and T the temperature. As before, we will ascertain the effective energy landscape via the potential of mean force (PMF) $PMF(x) := -\ln(\rho(x)) \cdot \mathrm{k_B T} + \mathrm{const} = U(x) + \mathrm{const}$. Clearly, applying a constant current-induced force F will bias this skyrmion distribution compared to the case where it is determined by the pinning potential U_{pin} alone. As the total deterministic force acting on the skyrmion must equal the sum of the pinning force and the current-induced force, the PMF will be affected as

$$PMF^{\rightarrow}(x) = U_{\mathrm{pin}}(x) - x \cdot F \tag{3.8}$$

for current to the right[10] (positive direction) and for current to the left as

$$PMF^{\leftarrow}(x) = U_{\mathrm{pin}}(x) + x \cdot F \tag{3.9}$$

since $\pm F = -\nabla(\mp x \cdot F)$ for constant F. The behavior of the PMF under reversion of current direction, allows us to infer the pure pinning energy landscape

$$U_{\mathrm{pin}}(x) = \frac{1}{2}\left(PMF^{\leftarrow}(x) + PMF^{\rightarrow}(x)\right) \tag{3.10}$$

and achieve our goal to obtain the pure current-induced force as the slope of the force-bias

$$x \cdot F = \frac{1}{2}\left(PMF^{\leftarrow}(x) - PMF^{\rightarrow}(x)\right). \tag{3.11}$$

Alternatively, one can directly measure $U_{\mathrm{pin}}(x)$ from the distribution at no applied current. Then, it suffices to measure the biased distribution for only one direction of current flow. In principle, this method variant would reduce the experimental effort as $U_{\mathrm{pin}}(x)$ only needs to be measured once. However, the benefit of using both directions of applied current (or determining $U_{\mathrm{pin}}(x)$ before every measurement) is that the result is less-affected by any changes in the pinning energy landscape between measurements. Moreover, it provides a better signal-to-noise ratio as the effect of the current on the sum of the PMFs is twice as large. A detailed comparison and discussion of the pinning energy landscapes for all measurements is given in the final section of this chapter. We decided to measure both directions of applied current as the effect of the current-induced force is more prominent that way.

---

[10] Whether the current-induced force acting on the skyrmion acts along the direction of electrical current or opposite to it depends on the signs of the effective spin-Hall-angle and the skyrmion's topological charge (Eqn. (3.12)). In this chapter we are only interested in the conversion factor between the absolute current density and the force. The explanations and discussions in this chapter are phrased assuming the current-induced force acts along the direction of the current.

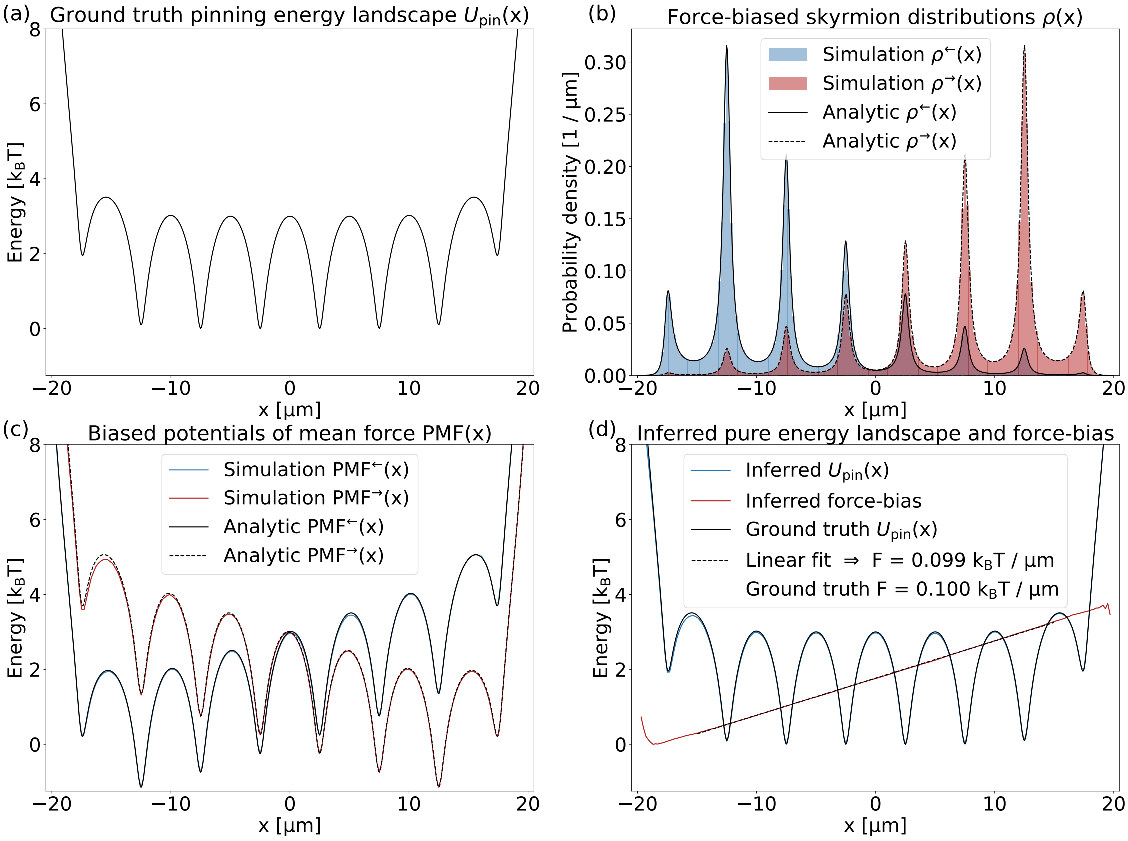

Figure 3.8: Step-by-step illustration of the developed method for simulation data. (a) Ground truth potential. (b) Biased skyrmion distributions for a constant force of $F = 0.1\,(\mathrm{k_B T/\mu m})$ applied to the left (blue) and right (red). (c) The resulting biased PMFs. Black (dashed) lines indicate the analytic solutions in parts (b) and (c). (d) The inferred pure pinning energy landscape (blue) alongside the ground truth potential (solid black) and the inferred pure force-bias (red). The slope of the linear fit (dashed black line) of the central region of the force-bias recovers the constant force excellently as $F = 0.099\,(\mathrm{k_B T/\mu m})$. This figure is taken from the supplementary material of our publication Ref. [39].

The method is illustrated in Fig. 3.8 on simulation data where the ground truth pinning energy landscape and the applied force are known and we aim to recover it. For the pinning energy landscape, we employ $U_{\text{pin}}\,(x) = \mathrm{k_B T} \cdot \ln(1 + \varepsilon \cdot \cos(2\pi \mathrm{x}/\lambda))$ as a test potential to study diffusion in non-flat energy landscapes inspired by Ref. [141] (Fig. 3.8a). For the pinning to roughly resemble the characteristics of real skyrmion pinning in our system as measured in the previous sections, we choose $\varepsilon = \tanh(3/2)$ and $\lambda = 5\,\mu\mathrm{m}$. In addition, the skyrmion-boundary interaction potential from our publication Ref. [15] was used to model the wire's ends (the boundaries of the magnetic material). Here, there is no need for $U_{\text{pin}}\,(x)$ to be periodic or possess any specific structure or symmetry at all except that energy barriers must be frequently traversable in reasonable measurement/sampling time. The potential was only chosen to have a simple shape to improve the visibility of the force-induced biases to the PMFs. The strength of the applied force is set to

$F = 0.1\,(\mathrm{k_B T/\mu m})$ and we simulate 200 trajectories for $5 \cdot 10^9$ steps sampled every 10^4 steps at otherwise identical parameters as in the previous section. Fig. 3.8b depicts the strongly biased skyrmion distributions and the analytic solutions using Eqn. (3.7). From the biased PMFs in Fig. 3.8c we isolate the inferred pinning energy landscape and applied force, which exhibit excellent agreement with ground truth values (Fig. 3.8d).

3.3.2 Experiment Design and Analysis of Experimental Data

Compared to the simulations, we experimentally face the challenge that contacts are required to apply currents. Consequently, we must address two challenges in the design of the experiment: First, the skyrmions must be prevented from moving beneath the contacts where they cannot be observed using Kerr microscopy. Second, in achieving this, skyrmions should not be exposed to strong local current density maxima that may cause the skyrmions to annihilate either by local Joule heating or by pushing the skyrmion too strongly into the boundary of the magnetic material. The second point is further discussed in section 6.1 as it is also highly relevant for designing skyrmion-based Brownian reservoir computers. With these challenges in mind, the designed system geometry shown in Fig. 3.9 and simulated the current flow in the system. The inset of Fig. 3.9 shows a narrow channel with funnel-like ends that prevent the skyrmion from moving near/under the contacts that are placed around and on top of even thinner extension channels due to skyrmion-boundary repulsion [15]. Fig. 3.9 also depicts a COMSOL Multiphysics [73] simulation of the current flow. These contacts for our experimental setups typically consist of 5 nm of chromium and 100 nm of gold on top and are created around and on top of parts of the skyrmion-hosting material to allow current flow through the stack and in particular the bottom tantalum layer causing spin-orbit torques acting on the skyrmion.[11] Note that here only the bottom 5 nm tantalum layer and the surrounding chromium layer are simulated and that we are only interested in the relative magnitude of the spatially resolved current density. We observe strong current density maxima only at the far end of the funnels and therefore expect the skyrmion stability to be unaffected at least at the low overall current densities applied in these experiments.

The experimental system based on these design considerations is depicted in Fig. 3.10a. The channel (without the funnels) is 40 µm long and 7 µm wide and the sample is the same $\mathrm{Ta(5)/Co_{20}Fe_{60}B_{20}(0.9)/Ta(0.08)/MgO(2)/Ta(5)}$ multilayer stack as in the previous sections. The measurements have been performed on two separate devices (called A and B in the following) on the same sample with nominally identical geometries to demonstrate that we indeed isolate the effect of applied current from pinning effects which differ for different regions of the sample. The skyrmion trajectory is imaged at (313.5 ± 0.2) K for device A and (310.4 ± 0.2) K for device B for at least 2 hours for each applied current density. An external out-of-plane magnetic field is applied to stabilize the skyrmions and to tune the skyrmion size. Similar to the ring-shaped structure, the skyrmion position is tracked by summing up the intensity perpendicular to the channel and fitting a Gaussian to the local peak in the resulting one-dimensional intensity distribution.

---

[11] The full experimental details are given in our publication Ref. [39]

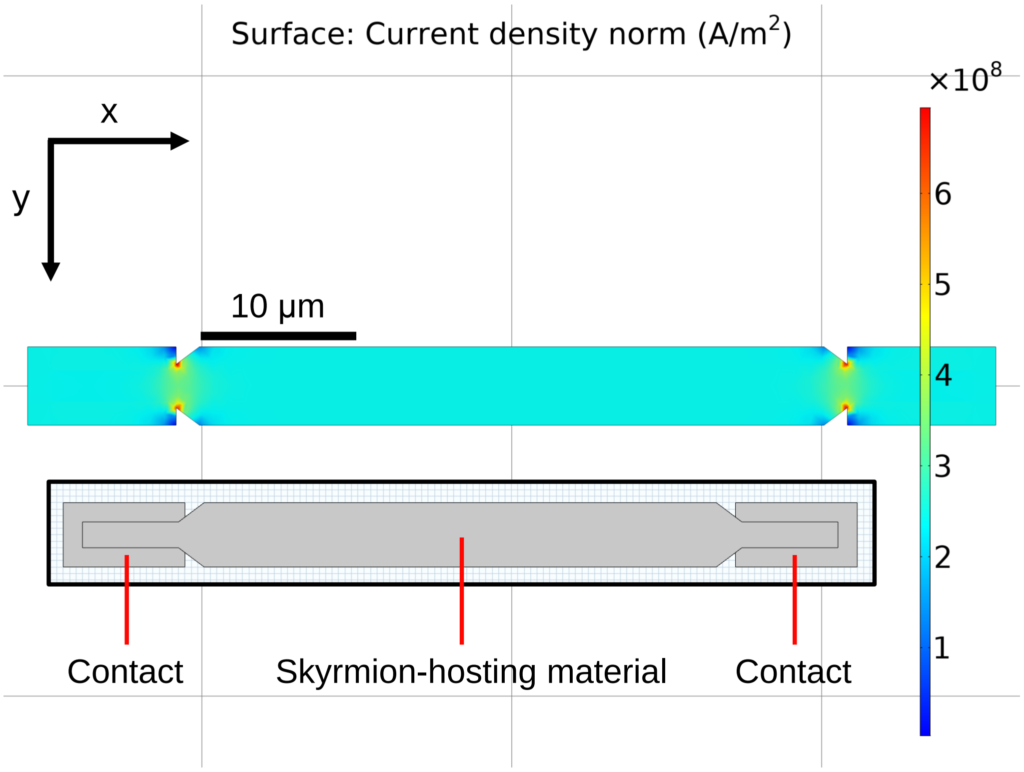

Figure 3.9: Current density distribution in the designed system simulated using COMSOL Multiphysics [73]. The inset shows the geometry of the narrow channel with funnel-like ends leading to thinner extensions with the contacts placed around them. The simulation details are provided in appendix section A.2.1.

Figs. 3.10b-d exemplarily show the steps for the force determination applied to the measurements for a current density of 2.14×10^6 A/m^2. These steps are the experimental equivalents of Figs. 3.8b-d. Here, the current density is determined from the total applied current taking into account the total Ta cross section of the device, as the Ta layers are predominantly responsible for the systems conductivity. While compared to the simulated test system with much more statistics (Fig. 3.8d) the force-bias in Fig. 3.10d exhibits more noise, it still shows excellent linearity in the well-sampled central region of the channel. Thereby, the force acting on the skyrmion can be reliably determined. Several additional measurements at different current densities allow us to determine the relation between applied current density and current-induced force on the skyrmion (Fig. 3.10e).

In Fig. 3.10e, the device used for the measurement is indicated by the color of the points. Since a constant current density is applied, the total force acting on the skyrmion depends on the skyrmion size. Therefore, in addition to the original data points (gray in Fig. 3.10e) we show points adjusted for small deviations of the average skyrmion size in the experiments. This adjustment has been performed by scaling the resulting forces by the individual measurement's average skyrmion size relative to the median average skyrmion size of all measurements for all current densities. As a measure of size, we employ the standard deviation of the Gaussian fit to the brightness profile used for tracking.

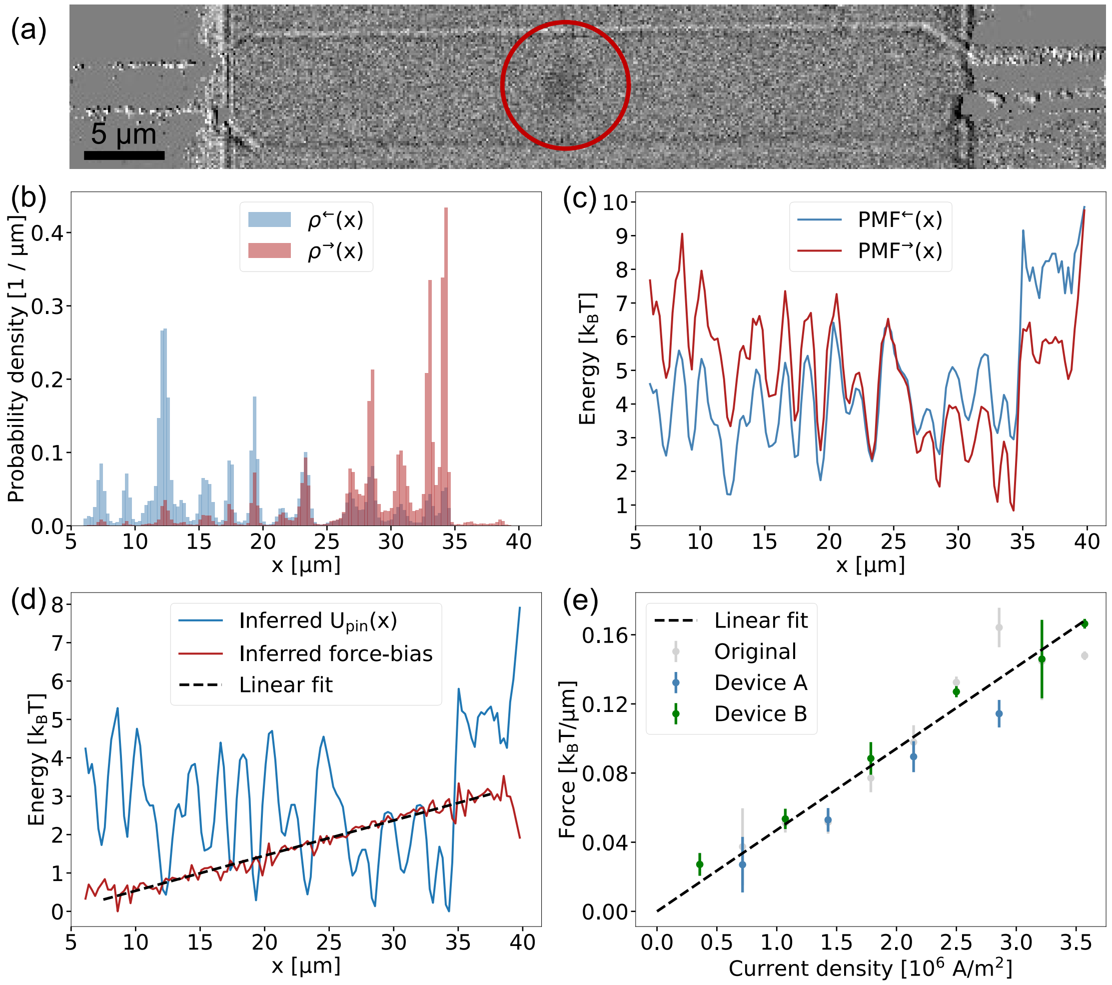

Figure 3.10: Experimental determination of current-induced forces. (a) Kerr microscopy image of a 40 µm × 7 µm channel with funnel-like ends containing a single skyrmion (dark spot highlighted by a red circle). The design is according to Fig. 3.9; contacts are placed at both ends of the wire. (b-d) Exemplary application of the method to experimental data for a current density of 2.14×10^6 A/m^2. (b) The experimental biased skyrmion distributions for current applied to the left (blue) and to the right (red). (c) The resulting biased PMFs. (d) The inferred pinning energy landscape (blue) and the inferred pure force-bias (red). The latter exhibits exhibits good linearity in the channel's central region and the linear fit's slope (dashed line) can be well identified with the force on the skyrmion. (e) The strength of the current-induced force at different current densities. The data points and their errors are estimated by splitting the trajectory into three parts and employing the mean and standard error of mean of the slopes of the force-biases, respectively. Measurements on the two different devices of nominally the same geometry on the same sample are indicated by the color of the data points. These points are adjusted to correct for deviations of the skyrmion size; the original points are given in grey. The relationship is well described by a linear fit function (dashed line, fitted to the adjusted points) with slope $m_F = (4.71 \pm 0.10) \times 10^{-8}$ ($\mathrm{k_B T/\mu m}$)/($\mathrm{A/m^2}$). This figure is adapted from our publication Ref. [39].

The linear relationship between skyrmion radius (or an approximately equivalent measure since here we only consider relative effects between skyrmions of different sizes) and force acting at a constant current density is supported by the analytical calculations in the next section. The isolated pinning potentials as well as the distributions of skyrmion sizes and deformations of all the measurements are compared in the final section of this chapter.

All size-adjusted forces as a function of current density can be well-described by a linear relation (Fig. 3.10e) with a slope of $m_F = (4.71 \pm 0.10) \times 10^{-8}\,(\mathrm{k_B T/\mu m})/(\mathrm{A/m^2})$. The consistency between the measurements on different devices highlights the robustness of our method: It isolates the effects of the energy landscape that are intrinsic to a device from the current induced force that only depends on the material properties and resulting skyrmion structure. These results will be compared to analytical predictions in the next section.

The range of applicability of the method is set by the ability to isolate the force bias: For very low applied forces, the noise of the force bias will hinder reliable determination of its small slope and respectively prohibitively large measurement statistics are required. However, we consider this regime not particularly interesting as this also means that the applied current density is insufficient to significantly alter the skyrmion distribution in the system. This is required for device applications such as Brownian reservoir computing (see chapter 6). For large applied forces, only a small region of the sample will be well-sampled within reasonable measurement time, consequently limiting the region for robust determination of the force bias. In between these limits, our method provides an accurate estimate of the current-induced force, circumventing the issue of current-induced skyrmion deformation. Consequently, our method provides not only a good description within the rigid particle model's validity range, but also a very good starting point for interpolation to other current regimes, even as a first-order prediction for regimes prone to skyrmion deformation.

3.3.3 Comparison to 360°-Domain Wall Model Prediction

In this section, we provide an additional layer of validation for the determined conversion factor between applied current density and total force acting on the skyrmion of $m_F = (4.71 \pm 0.10) \times 10^{-8}\,(\mathrm{k_B T/\mu m})/(\mathrm{A/m^2})$. However, no previous experimental measurements of such a conversion are available. Therefore, we compare our result to an estimate using the analytical 360°-domain wall model by Büttner et al. [85]. As the name suggests, this model for isolated skyrmions assumes a fully circular symmetric domain wall profile and a homogeneous magnetization profile in the out-of-plane direction. However, due to thermal fluctuation and pinning effects, the skyrmion's enclosing domain wall is not circular symmetric most of the time. Therefore, we employ this model as a coarse estimate only to gauge the order of magnitude of the current-induced forces.

Note that that we operate in SI units and, therefore, compared to Ref. [85], all force-like quantities must be multiplied by a factor $M_s d/\gamma_{\mathrm{GR}}$, where M_s is the saturation magnetization, γ_{GR} is the gyromagnetic ratio, and d is the thickness of the ferromagnetic layer. Within the 360°-domain wall model, the current-induced force acting on the skyrmion due to spin-orbit torques (equation 71 of the supplementary material of Ref. [85]) for one stack-repetition is given by

$$F(j) = \frac{\hbar \pi \theta_{\mathrm{SpH}}^{\mathrm{eff}} N}{2e} \Delta I_D(R/\Delta) j \tag{3.12}$$

where j is the current density in the heavy metal, $\hbar$ is the reduced Planck constant, e is the electron charge, $N = 1$ is the skyrmion's topological charge, $\theta_{\mathrm{SpH}}^{\mathrm{eff}}$ is the effective spin-Hall-angle, R and Δ are the skyrmion radius and domain wall width respectively. In the supplementary material of Ref. [85] (see sections S2.4 and S11.3) the function $I_D(R/\Delta)$ is shown to be well-approximated as $I_D(R/\Delta) \approx \pi R/\Delta + (1/2)\mathrm{exp}(-R/\Delta)$.

Since we cannot resolve the domain wall width Δ by Kerr microscopy, we employ micromagnetic simulations to estimate the skyrmion profile and thereby R/Δ in our system. While the dynamics of micrometer-sized skyrmions is inaccessible to micromagnetic simulations due to their prohibitive computational cost, the equilibration of a static skyrmion profile is possible. The chosen parameters to model our experimental system as an effective single material layer have been determined in previous work [95] for Ta(5)/$\mathrm{Co_{20}Fe_{60}B_{20}}$(1)/Ta(0.08)/MgO(2)/Ta(5) system very similar to the one studied here: A $4096 \times 4096 \times 0.6\,\mathrm{nm}^3$ sample is simulated at a cell size of $2 \times 2 \times 0.6\,\mathrm{nm}^3$. Periodic boundary conditions are employed to mimic an extended system. The system size is chosen to be sufficiently large such that the skyrmion does not interact with its periodic images. The material has a saturation magnetization of $M_{\mathrm{s}} = 0.98\,\mathrm{MA/m}$, an exchange stiffness of $A_{\mathrm{ex}} = 2.46\,\mathrm{pJ/m}$, a perpendicular magnetic anisotropy strength of $K_{\mathrm{u}} = 0.64\,\mathrm{MJ/m}^3$ (note that in Ref. [95] there is a typo considering this parameter) and an interfacial Dzyaloshinskii-Moriya interaction strength of $D = 98.5\,\mathrm{\mu J/m}^2$. The skyrmion is stabilized by applying an external out-of-plane magnetic field of 0.2 mT. The simulations have been performed using the MuMax3 software [58] by starting with an initial guessed skyrmion configuration with a large domain wall width and minimizing the total energy using MuMax3's build-in steepest conjugate gradient method.

The magnetization profile in Fig. 3.11a demonstrates that skyrmions in our system possess a very narrow domain wall compared to the large homogeneously magnetized skyrmion core. By fitting the normalized out-of-plane magnetization m_z as a function of distance d from the skyrmion center (here along the 3 o'clock direction in Fig. 3.11a) with a

$$m_z(d) = \tanh((d - R)/\Delta) \tag{3.13}$$

domain wall shape [85], we obtain a domain wall width of $\Delta \approx 6.2\,\mathrm{nm}$ and a skyrmion radius of $R \approx 744.5\,\mathrm{nm}$ resulting in $R/\Delta \approx 119.2$. The simulation data and the fit are shown in Fig. 3.11b. Under these conditions (and also for skyrmions of almost twice the radius as in the above experiments), we can safely neglect the falling exponential term in $I_D(R/\Delta)$ and further approximate $I_D(R/\Delta) \approx \pi R/\Delta$ for R $\gg \Delta$. Thus, for the conversion factor between the applied current density and the force on the skyrmion, we obtain

$$m_F = \frac{\hbar \pi^2 \theta_{\mathrm{SpH}}^{\mathrm{eff}} R}{2e} = 10.6 \times 10^{-8}\,(\mathrm{k_B T/\mu m})/(\mathrm{A/m^2}) \tag{3.14}$$

where we experimentally estimated $R = (1.29 \pm 0.26)\,\mu\text{m}$ as the skyrmion radius in our system[12]. We coarsely estimate the effective spin-Hall-angle $\theta^{\text{eff}}_{\text{SpH}} = 0.11$ based on measurements in a similar system [148], and we employ the sample temperature of device A for the unit conversion to $(\text{k}_\text{B}\text{T}/\mu\text{m})/(\text{A}/\text{m}^2)$. This estimate is less than a factor 3 larger than the experimentally determined value, and, given the coarse nature of the 360°-domain wall model prediction, we gauge the values to be in very good agreement.

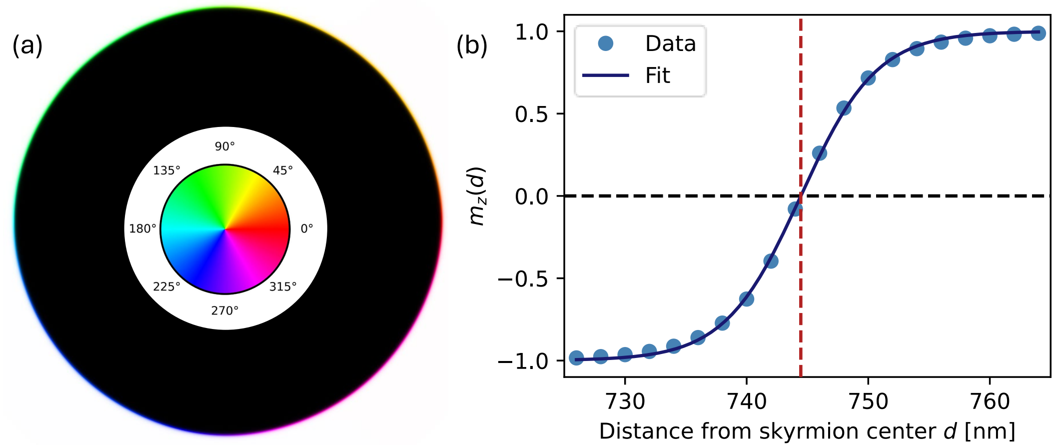

Figure 3.11: (a) Micromagnetically simulated skyrmion magnetization profile. The out-of-plane component of the magnetization is depicted using the lightness with white and black corresponding to magnetization fully out-of-the-page and into-the-page orientation, respectively. The hue indicates the polar angle of the in-plane component of the magnetization according to the color wheel in the center (i.e., red corresponds to an orientation to the right; the magnetization at the enclosing domain wall (colored ring) is turning outwards everywhere). Note that the entire central region (core) of the skyrmion is homogeneously magnetized into the page (black), even though this space is used to show the color wheel for the in-plane component. (b) Normalized out-of-plane magnetization m_z as a function of distance d from the skyrmion center (along the 3 o'clock direction in (a)) fitted by the domain wall profile $m_z(d) = \tanh((d-R)/\Delta)$. The red dashed vertical line indicates the skyrmion radius determined by the fit and the dashed black line acts as a guide to the eye at $m_z = 0$.

3.3.4 Comparison of Pinning Potentials and Skyrmion Sizes

In this section, we compare the isolated pinning potentials that are determined from different measurements at different current densities in Fig. 3.10e. These measurements were performed on two devices (A,B) on the same sample. Therefore, we expect the pinning potentials in Figs. 3.12a,d to be consistent for a single device but distinct between

---

[12] Note that here the skyrmion size is not the standard deviation of the Gaussian fit to the brightness distribution in the Kerr microscopy image. This measure, while well-suited for judging relative skyrmion sizes, does not represent the distance to the domain wall. Instead, the skyrmion radius here was estimated as the approximate radius of the region enclosed by the boundary where the Kerr intensity intersects the mean of the average intensities in the central region of the skyrmion and in the ferromagnetic surrounding.

the two devices. At the same time, we also check for current-induced deformations of the skyrmion by quantifying the distribution of skyrmion sizes in the direction along the channel (Figs. 3.12b,e) and perpendicular to it (Figs. 3.12c,f). As a measure for the size in each microscopy video frame, we employ the standard deviation of the Gaussian fit to the accumulated intensity, where the intensity has been accumulated in the direction perpendicular to the wire to determine the size along the wire and vice versa. We observe that the pinning potentials are in excellent agreement as long as the average skyrmion sizes are close. In two cases, included in Figs. 3.12a,b, the skyrmions are larger. While the dominant characteristics of the pinning potentials still agree, some differences can be observed in the details.

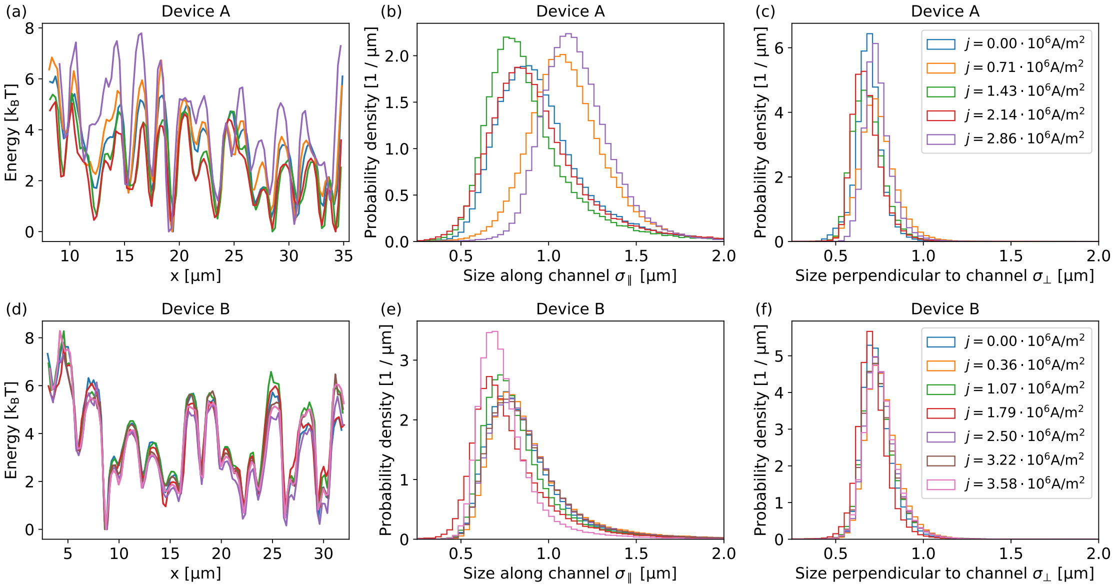

Figure 3.12: Comparison of the isolated pinning potentials (a,d), skyrmion sizes in the direction parallel to the channel (b,e), and skyrmion sizes in the direction perpendicular to the channel (c,f). The applied current densities for each measurement are given in (c,f) and the curve coloring applies to the entire row. The top and bottom rows correspond to devices A and B, respectively. This figure is adapted from the supplementary material of our publication Ref. [39].

The general size-dependence of skyrmion pinning is investigated rigorously in the next chapter. Here, it is important to note that our method to determine current-induced forces works as long as the pinning remains approximately constant throughout the measurement (for one current density). Differences in the potential between measurements are not expected to change the results as the effects of current and pinning are isolated, which is supported by the excellent agreement of the determined forces in Fig. 3.12e even for different devices. The skyrmion size does, however, affect the total force acting on the skyrmion in response to a constant applied current density, which is why we correct for size effects in Fig. 3.10e.

Regarding the shape of the skyrmion, we observe no correlation between skyrmion elongation and applied current. Instead, Figs. 3.12b,c show that the perpendicular extension remains comparable even for the measurements where the size along the channel is larger. Consequently, the skyrmions are slightly elongated in these cases. We attribute this effect to a limitation of the perpendicular extent due to the confinement.

4. Size-Dependent Skyrmion Pinning

Understanding pinning effects is essential for investigating skyrmion dynamics and the design of skyrmion-based devices. Pinning effects are unavoidable in state-of-the art systems but their spatially inhomogeneous nature can drastically impact the system's behavior. By studying a single thermally diffusing skyrmion confined to a small region, we reveal a strong dependence of pinning on the skyrmion's size. By considering not only the skyrmion center position but also the estimated position of the domain wall that encloses the skyrmion core, we identify pinning of the domain wall as the dominant contribution to the pinning rather than pinning of the homogeneously magnetized core. This result is supported by measurements of magnetic stripe domains, where the domain walls are evidently pinned at the same positions as the skyrmion's domain wall. Micromagnetic simulations are employed to demonstrate how size-dependent pinning can occur as a direct consequence of pinning the skyrmion's domain wall, thereby linking these two observations. Since the skyrmion size can be tuned via an applied out-of-plane magnetic field, size-dependent pinning provides a mechanism to alter the pinning effects experienced by a skyrmion.

This chapter aims to explain the mechanism that causes size-dependent skyrmion pinning and demonstrate this mechanism using micromagnetic simulations. The first two sections introduce experimental measurements of skyrmions subject to pinning effects at different out-of-plane fields that tune the skyrmion size. The first section reveals a strong relationship between the position where the skyrmion is pinned and the skyrmion size. The second section considers the positions of the skyrmions' domain walls as well as the arrangements of stripe domains in the same system. Taken together, the results imply that pinning of the skyrmion domain wall is the dominant pinning effect in the system. Then, we employ micromagnetic simulations to connect the results of the previous sections and demonstrate how pinning of the skyrmion domain wall can cause size-dependent skyrmion pinning. The final section discusses the implications of these findings for the dynamics and quasi-particle modeling of skyrmions.

Most of the contents of this chapter are published in our publication

- Raphael Gruber, Jakub Zázvorka, Maarten A. Brems, Davi R. Rodrigues, Takaaki Dohi, Nico Kerber, Boris Seng, Mehran Vafaee, Karin Everschor-Sitte, Peter Virnau, Mathias Kläui, “Skyrmion pinning energetics in thin film systems”, *Nature Communications* **13**, 3144 (2022) (Ref. [36])

and the present chapter is based on this work. The experiments discussed in this chapter were performed without my participation; I contributed through simulation, conceptualization, analysis, interpretation and discussion[1].

4.1 Observation of Size-Dependent Pinning

To investigate the size-dependence of pinning, we study the diffusion of a single skyrmion confined to a circular structure with a diameter of 17 µm patterned via electron beam lithography on a $\mathrm{Ta}(5)/\mathrm{Co}_{20}\mathrm{Fe}_{60}\mathrm{B}_{20}(0.9)/\mathrm{Ta}(0.08)/\mathrm{MgO}(2)/\mathrm{Ta}(5)$ stack. The small confinement lets us ascertain the detailed spatial distribution of the skyrmion's position. The average skyrmion size is tuned via an out-of-plane (OOP) magnetic field.

For this purpose, the skyrmions are imaged at 16 frames per second over 10 minutes for each value of the OOP field. The skyrmion center position is tracked by fitting the intensity distribution with a two-dimensional Gaussian via the trackpy python package [121]. As a quantifier for the skyrmion size, we employ the radius of gyration of the fitted intensity profile, which is also calculated using trackpy. While in this chapter, only the spatial skyrmion distribution $\rho(\vec{r})$ is considered, results translate directly to the pinning energy landscape determined by the potential of mean force ansatz $U_{\mathrm{pin}}(\vec{r}) = -\mathrm{k_B T} \ln(\rho(\vec{r}))$ as done in the previous chapter.

All measurements are performed on the same region of the sample. Here, negative OOP field values correspond to a field applied into the plane, and the magnetization direction of the skyrmion core is out of the plane, while the magnetization direction of the surrounding is into the plane. Therefore, the average skyrmion size increases with increasing OOP field. This means the average skyrmion size increases as the absolute OOP field applied opposite to the direction of skyrmion core magnetization decreases. Measurements of the spatial skyrmion distribution are performed for applied OOP fields between −43 µT and −31 µT, increasing in 2 µT steps. The skyrmion occurrences of all measurements combined are shown in Fig. 4.1a; Figs. 4.1b-e show the spatial skyrmion distribution and the distribution of skyrmion sizes[2] for four interesting cases of applied OOP field. Comparing these four cases, small changes in average skyrmion size by about 5-8% result in significant changes in the spatial skyrmion distribution, demonstrating a strong size-dependence of the pinning. Moreover, if we color code individual skyrmion center positions in the combined data of all measurement with the instantaneous skyrmion size (Fig. 4.1a), we observe a strong correlation between the skyrmion's size and where it is pinned.

---

[1] The experiments were conducted predominantly by [redacted] without my involvement. The skyrmion center distributions were analyzed by [redacted] and me in equal contribution. [redacted] analyzed the positions of the skyrmion domain walls. All computer simulations were performed and analyzed by me. I conceptualized the experiment studying stripe domain arrangements to support the hypothesis of domain wall pinning as the origin of the size-dependence of skyrmion pinning. The appendix section A.1.2 provides a detailed description of my contributions to the research presented in this chapter.

[2] Note that the skyrmion size is stochastically distributed due to thermal fluctuation even in the absence of pinning.

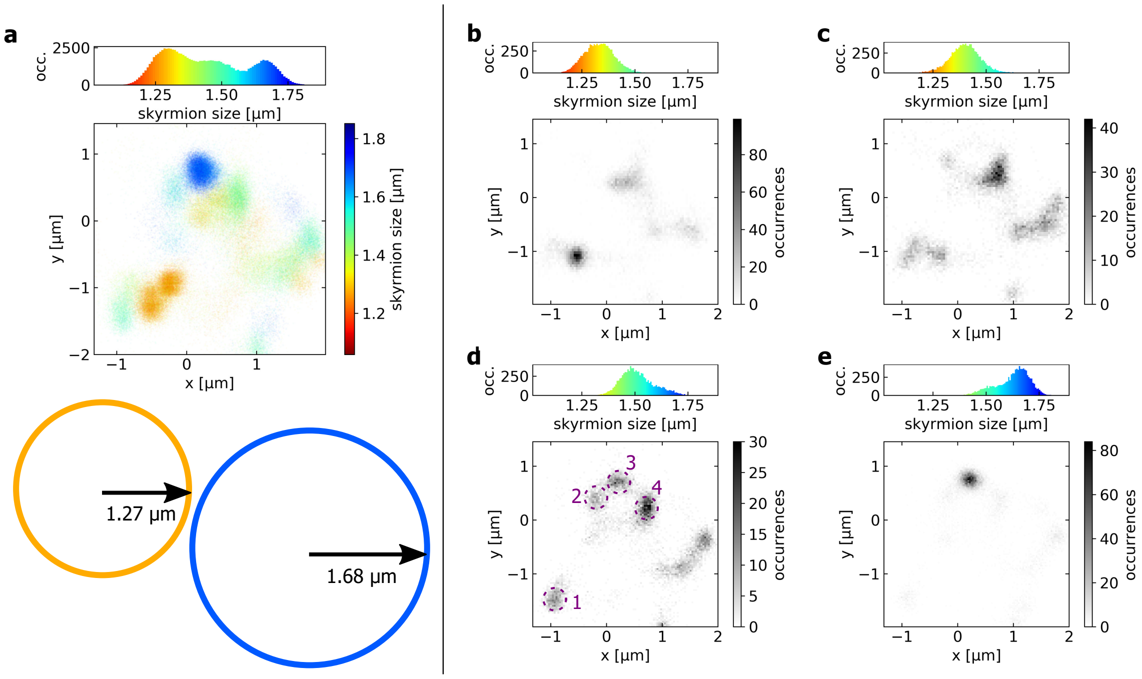

Figure 4.1: Spatial distributions of skyrmion center occurrences and their relation to the skyrmion size. (a) Combined data of all at different OOP fields that tune the average skyrmion size: Each detected skyrmion occurrence is indicated by a scatter plot point at the coordinate of the tracked skyrmion center. The colors represent the skyrmion size, and the color bar next to (a) applies to the skyrmion size distributions at the top of all panels. In (a), the color intensity of the scatter plot indicates the probability density of observing a skyrmion at a particular position. The colored circles on the bottom are consistently sized schematics to visualize the skyrmion sizes compared to each other and the spatially resolved occurrence maps. The color bar that quantifies the skyrmion size also applies to these schematics. (b-e) Histograms of the skyrmion center positions and skyrmion size distributions for four different measurements at applied OOP fields of $-39\,\mu$T (b), $-37\,\mu$T (c), $-35\,\mu$T (d), $-33\,\mu$T (e). The investigated region of the sample is the same in all panels. In (d), four predominant pinning sites are highlighted by dashed violet circles and labeled with integers 1-4. This figure is taken from our publication Ref. [36].

It is to be noted here that the different accumulation points of skyrmion center observations in Fig. 4.1a are separated by distances smaller than or comparable to the skyrmion diameter as indicated by the two colored circles drawn below the plot. This already serves as a first indication that the interaction between the pinning sites and the homogeneously magnetized skyrmion core is unlikely to be the cause of the size-dependence. To elaborate more on this argument: We have seen in the micromagnetic simulation of a skyrmion profile (Fig. 3.11a) for parameters chosen to represent a similar system in section 3.3.3, that the skyrmions we consider consist of a large homogeneously magnetized core enclosed by a very narrow domain wall. In Fig. 4.1d, four different skyrmion center position accumulation points (pinning sites) are marked by dashed violet circles. Since pinning sites 2,3 and 4 occur at distances from each other that are smaller than the expected extent of the homogeneous region of the skyrmion, it is implausible that the origin of the interaction that determines the pinning stems directly from these accumulation points as they all interact with the same local magnetization configuration inside the skyrmion.

To summarize this section, we observe a twofold size-dependence of skyrmion pinning: On the one hand, when setting the average skyrmion size via an applied OOP field, we observe drastic changes in the spatial skyrmion center distribution on scales smaller than or similar to the skyrmion diameter. These changes translate to an altered effective pinning energy landscape in the Thiele model, as it is introduced in the previous chapter. On the other hand, we observe a strong correlation between the position where the skyrmion is pinned and the skyrmion's instantaneous size. The following two sections reveal the underlying mechanism that acts as the origin of the observed size-dependence of skyrmion pinning.

4.2 Pinning of the Skyrmion Domain Wall

To learn more about the dominant pinning mechanism in the studied system, we go beyond the rigid particle approximation and consider the shape of the skyrmion. We analyze how the shape of the skyrmion is affected by the position where the skyrmion center is pinned. For this analysis, we chose the measurement at $-35\,\mu\mathrm{T}$ (Fig. 4.1d) since there are four well-sampled distinct pinning sites present in this measurement (violet dashed circles labeled with integers 1 to 4). The estimated position of the domain wall is determined as the contour where the Kerr intensity profile intersects the mean value between the skyrmion core and the surrounding. To average out noise effects and obtain a sharp estimate for this contour, the intensity profile is first averaged over all skyrmions pinned at each of the four pinning sites (four colored intensity distributions in Fig. 4.2a). Due to the small range of center coordinates considered, we assume that the variations in the skyrmion profile are small, and the estimated position of the domain wall is preserved in the averaging process. For each pinning site, we take into account at least 350 skyrmion observations.

The central plot in Fig. 4.2a shows that while the skyrmion center coordinates all differ, large sections of the estimated domain walls overlap for the skyrmions binned at sites 2-4. Appendix section A.3.1 discusses a second example of this behavior in the measurement at $-37\,\mu\mathrm{T}$ (Fig. 4.1c). We interpret this behavior as an indication that the dominant pinning effects in the system occur at the domain wall of the skyrmion and not at the skyrmion core. To support this hypothesis, we study the arrangement of stripe domains in the same region of the sample created by tuning the OOP field and the nucleation process. Since stripe domains are also enclosed by domain walls, pinning of the domain wall would imply that the contours of the stripes coincide with the previously estimated skyrmion domain walls. Indeed, Fig. 4.2b reveals that for four different arbitrary nucleations of stripe domains, we observe significant overlaps between the stripe domains' contours and the skyrmion contours from Fig. 4.2a.

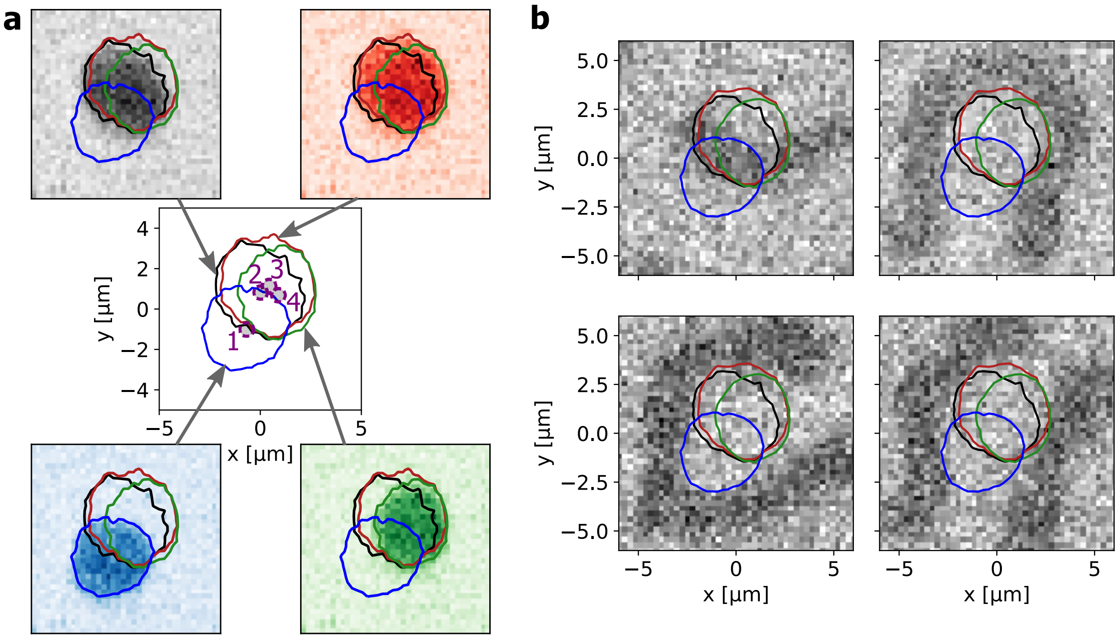

Figure 4.2: (a) For the four labeled pinning sites in Fig. 4.1d, the estimated average domain wall position of all skyrmions pinned at each specific site is determined. The central plot shows the positions of the skyrmion center coordinates associated with each pinning site as dashed violet circles filled with grey shading. The surrounding colored plots show the averaged Kerr intensity distributions for skyrmions with center coordinates assigned to sites 1 (blue), 2 (black), 3 (red), and 4 (green). The contours of these distributions are plotted in the respective colors at consistent positions in every plot in this figure. (b) Kerr microscopy images of arbitrary stripe domain configurations observed in the same region of the sample. The domain walls of the stripe domains match the skyrmion contours determined in (a) in large sections. In the Kerr intensity images, darker color corresponds to magnetization pointing out of the plane, while lighter color corresponds to magnetization pointing into the plane. This figure is taken from our publication Ref. [36].

In the next section, we link the two observations of size-dependent pinning and predominant pinning at the domain wall and demonstrate the suggested mechanism qualitatively using micromagnetic simulations.

4.3 Origin of the Size-Dependence

In this section, we first propose a simple mechanism to describe how pinning of the skyrmion domain wall can introduce size-dependent pinning of the skyrmion center and then demonstrate that mechanism in simulation. The basic idea is illustrated in a one-dimensional schematic in Fig. 4.3: The most favorable position for the skyrmion depends on the commensurability of the spacing of the domain walls and the spacing of the domain wall pinning sites. When the skyrmion size changes, so does the spacing of the domain walls. Consequently, a position commensurate previously may now be unfavorable, and a new position may become favorable. The actual two-dimensional situation is more complicated as more than two points of the domain wall contribute. Therefore, simulations are employed to demonstrate the mechanism in two dimensions.

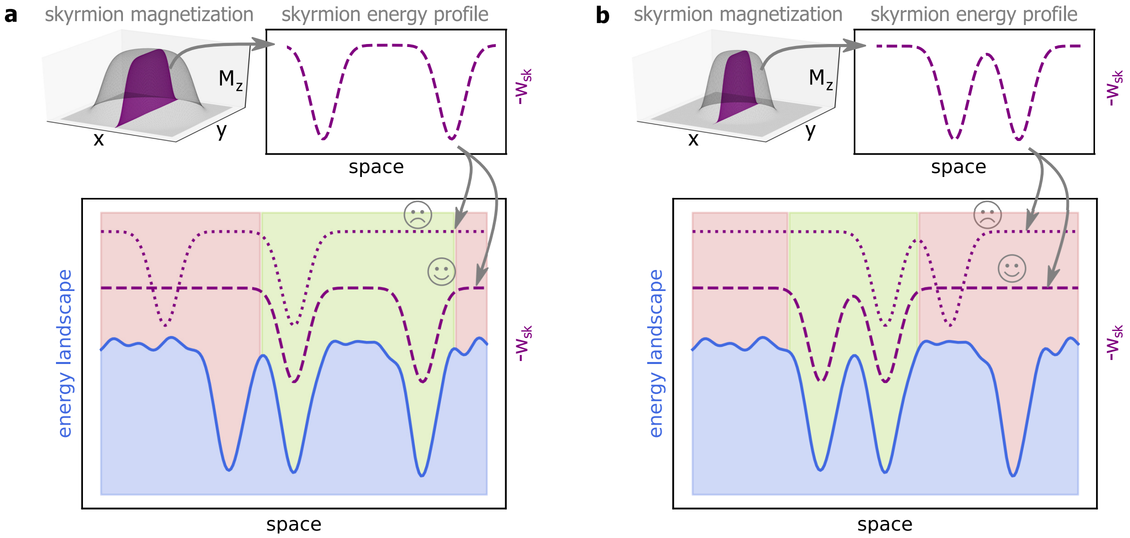

Figure 4.3: Schematic relation between domain wall pinning and size-dependent skyrmion center pinning. Note that in this figure, the pinning energy landscape (blue) refers to pinning effects acting on the domain wall and not on the skyrmion center as in most figures showing pinning effects in this thesis. Domain wall pinning effects could arise for instance due to a locally weakened anisotropy or exchange interaction. As an indicator showing the skyrmion domain wall positions, we employ the cross-section of the negative energy density of the skyrmion magnetization profile W_{sk} with respect to the weakened interaction (violet dashed lines). Neglecting thermal fluctuations, this energy is constant in the homogeneous skyrmion core and higher at the domain wall that deviates from colinear alignment. Even for a constant energy landscape, the favorable position differs for large (a) and small (b) skyrmions due to the commensurability between the spacing of the domain walls and the pinning sites. None of the curves in this schematic are not meant to reflect accurate proportions, and the negative energy density is plotted to illustrate better how the domains “fit” in the pinning sites. This figure is taken from our publication Ref. [36].

In the Thiele model (Eqn. (3.1)), skyrmions are described in terms of their center position alone; their size only appears implicitly, and the domain wall itself is not explicitly modeled. Possible future extension paths to incorporate size-dependent pinning and/or domain wall pinning into a particle-based description are discussed in the next section. Here, we turn to micromagnetic simulations where the entire skyrmion structure is explicitly simulated. However, due to the high computational cost of micromagnetic simulations compared to Thiele model simulations, simulating the diffusive dynamics of micrometer-sized skyrmions over sufficiently long durations to determine the skyrmion distribution in the system is infeasible. Therefore, we study a nanometer-sized test system, limit ourselves to studying qualitative effects only, and discuss the difference to the micrometer-sized case at the end of the section.

Similar to the experiment, we consider a single skyrmion exhibiting thermally activated diffusion. The simulations are performed using the MuMax3 simulation software [58]. Note that the exact parameters of the simulated system are not essential for the qualitative effects investigated here. We employ typical nano-scale sample parameters[3] based on Refs. [149, 150] and simulate a $128 \times 128 \times 1\,\mathrm{nm}^3$ system with open boundary conditions. We employ a cell size of $1 \times 1 \times 1\,\mathrm{nm}^3$. The material has a saturation magnetization of $M_\mathrm{s} = 1\,\mathrm{MA/m}$, a Gilbert damping of $\alpha = 0.01$, an exchange stiffness of $A_\mathrm{ex} = 15\,\mathrm{pJ/m}$, and an interfacial Dzyaloshinskii-Moriya interaction strength of $D = 3.22\,\mathrm{mJ/m}^2$. For performance reasons, the demagnetization energy is accounted for as a reduction of the effective perpendicular magnetic anisotropy strength $K_\mathrm{eff} = K_\mathrm{u} - 0.5 \cdot \mu_0 M_\mathrm{s}^2$ with $K_\mathrm{u} = 1.1\,\mathrm{MJ/m}^3$, which has been shown to be a good approximation for considering an infinite thin film and explicitly calculating the demagnetization field [67].

We include three domain wall pinning sites in our system as a minimalistic system setup to demonstrate the connection between domain wall pinning and size-dependent skyrmion pinning. These $4 \times 10\,\mathrm{nm}^2$ rectangular pinning sites are shown as red boxes in Figs. 4.4a,b. Exemplarily, the effective anisotropy within these regions is lowered to 20%, such that they act energetically favorably for the domain wall that exhibits lower alignment with the anisotropy axis than the skyrmion core. The spacing of the regions was chosen to be similar to the average diameter of the smallest simulated skyrmions. Appendix Fig. A.6 schematically depicts possible skyrmion arrangements alongside a discussion of their energetic favorability in appendix section A.3.2. As in the experiments, we tune the skyrmion size by applying an OOP field of either $0.15\,\mathrm{T}$ (smaller skyrmions) or $0.05\,\mathrm{T}$ (larger skyrmions). We then evolve the system according to the finite temperature ($T = 100\,\mathrm{K}$) Landau-Lifschitz-Gilbert equation for $60\,\mu\mathrm{s}$ for each OOP field. The magnetization configuration is sampled every $1\,\mathrm{ns}$. To stay as close as possible to the experimental procedure, the magnetization configuration is converted into the skyrmion's trajectory by using trackpy [121] on grayscale images, in which every pixel represents the specific cell's OOP magnetization.

Fig. 4.4 shows a strong size-dependence of the pinning that arises evidently from the commensurability between the skyrmion size and the spacing of the domain wall pinning sites. While small skyrmions (Fig. 4.4a) can fit in between the pinning sites, the most favorable positions for larger skyrmions (Fig. 4.4b) are above or below all pinning sites to achieve maximum overlap between the regions of reduced effective anisotropy and the domain wall. Exemplary simulating snapshots illustrating these arrangements are shown and discussed in appendix section A.3.2.

---

[3] I am grateful to Davi R. Rodrigues for pointing me towards these parameters.

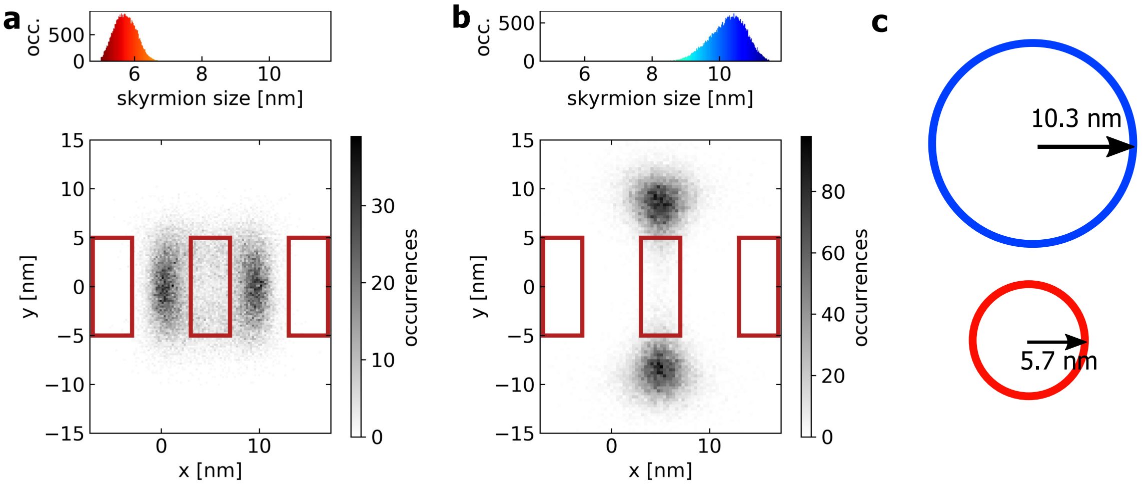

Figure 4.4: Demonstration of size-dependent skyrmion center pinning in micromagnetic simulation. The histograms of skyrmion center positions differ strongly for small (a) and large (b) skyrmions. Red rectangles indicate regions with reduced effective anisotropy favorable for the domain wall. (c) Circles indicating the average skyrmion size are scaled accurately with the distribution plots and are colored according to the skyrmion size distributions in (a) and (b). This figure is taken from our publication Ref. [36].

The main difference between the employed nanometer-sized skyrmion structure (Fig. A.5) and the structure of the studied micrometer-sized skyrmion (like Fig. 3.11a) is that the relative domain wall width is much smaller in the latter case. Therefore, we expect the same mechanism to apply at the microscale. In real experimental systems, in contrast to the minimalist simulation setup, more domain wall pinning sites determine the favorable positions for the skyrmion center. From both differences, we expect the distribution of micrometer-sized skyrmion to be more strongly peaked than in the simulations. This is confirmed by comparing the accumulation regions' extent relative to the skyrmion size between Fig. 4.1 and Fig. 4.4.

4.4 Implications for Skyrmion Dynamics and Modeling

The previous sections have revealed a size-dependence of skyrmion pinning occurring evidently due to dominant pinning effects at the skyrmion's domain wall. This effect opens up a variety of research paths for skyrmion dynamics and its modeling. Since in this thesis, we are predominantly interested in the skyrmions' quasi-particle properties and modeling, the terms related to “pinning” still always refer to the effective pinning of skyrmion center that causes accumulation points in trajectories. This effect is modeled via effective potential energy landscapes obtained by the potential of mean force ansatz as in the previous chapter. When the pinning of the domain wall is discussed, this will be stated clearly. In that spirit, the predominant perspective employed in the subsequent chapters is that the pinning energy landscape changes as the average skyrmion size changes. The advantage of this description is that skyrmions can still be represented as particles via their center coordinate. It is rooted in the fact that the pinning energy landscape, the current-induced force, the effective damping, and the interaction potentials that together describe skyrmion dynamics in the Thiele model are all determined for a specific constant average skyrmion size. In the determination of these parameters, thermal fluctuations of the skyrmion size (and shape) are averaged out. Therefore, we expect a model based on these parameters to describe average skyrmion behavior well. Consequently, this kind of modeling cannot describe changes in instantaneous skyrmion size due to thermal fluctuation on a fundamental level as skyrmion deformations are not captured by the Thiele model [40]. While changes in average skyrmion size can be described by adjusting the above parameters, continuous changes during a simulation are challenging as for the pinning, small changes in skyrmion size have strong effects that make meaningful interpolation between experimentally ascertained energy landscapes difficult. This thesis focuses on systems where the average skyrmion size is kept constant. A fundamental way to address these limitations would be to employ a coarse-grained model for the domain wall and explicitly model the pinning of the domain wall, which is beyond the scope of this thesis.

This chapter's results turn the ability to tune the average skyrmion size via an OOP magnetic field into a mechanism to manipulate skyrmion pinning. Such a mechanism is highly valuable for skyrmion-based devices as it, in principle, allows for the weakening or strengthening of specific pinning sites. However, this is a strongly localized effect since the dominant origin of the pinning effect, the pinning of the domain wall, is still present. Size changes only affect how the domain wall pinning impacts favorable positions of the skyrmion center. On larger scales, we expect the skyrmions' dynamical properties, like the pinning-induced reduction of diffusivity explored in section 3.2.2, to be rather similar even for differently sized skyrmions. Therefore, in the next chapter, we employ this chapter's results to develop a method to tune the effects of pinning on skyrmion dynamics, even on large scales.

5. Enhancing Diffusion via Oscillating Magnetic Fields

The ability to tune, and particularly increase, skyrmion diffusion is extremely valuable for both applications in Brownian computing [28–32, 51, 52] and for fundamental investigations of skyrmion behavior [34]. The conventional approach to enhance diffusive random motion, for instance in a colloidal system, would be via a temperature increase. However, for skyrmion systems, temperature changes also affect the underlying magnetic properties of the sample and may consequently lead to undesired and complex additional effects [16, 151]. In this chapter, we demonstrate a constant-temperature increase in skyrmion diffusivity by more than two orders of magnitude by applying an oscillating out-of-plane magnetic field that tunes the skyrmion size. We apply a fully deterministic excitation to increase random motion at a constant temperature, unlike the procedure based on randomly oriented current pulses proposed previously [29].

The chapter starts with a discussion of the experimental observation of the diffusion enhancement effect. While size-dependent pinning due to pinning of the skyrmion domain wall is not incorporated in the Thiele model, we argue in the next section that on average, on time scales significantly longer than the oscillation period, the oscillating field acts to reduce the effective pinning experienced by the skyrmions. We support this approach by investigating multiple characteristics of the skyrmion dynamics and comparing them to measurements at static field values. The next sections then discuss the limitations of modeling the effect as an effective reduction of pinning and provide an outlook on a possible interpretation of the system's behavior in the context of flashing potentials [152–156]. The latter section also includes suggested further (experimental) investigations to enable a better understanding of the underlying mechanism and verifications of the modeling developed in this chapter. The final section of this chapter outlines applications of diffusion enhancement mechanisms in Brownian computers [29, 30, 32, 157] and fundamental physics research [34].

Most of the results presented in this chapter are published in our publication

- Raphael Gruber, Maarten A. Brems, Jan Rothörl, Tobias Sparmann, Maurice Schmitt, Iryna Kononenko, Fabian Kammerbauer, Maria-Andromach Syskaki, Oded Farago, Peter Virnau, and Mathias Kläui, "300-Times-Increased Diffusive Skyrmion Dynamics and Effective Pinning Reduction by Periodic Field Excitation", *Advanced Materials* **35**, 2208922 (2023) (Ref. [37])

and the present chapter is based on this work. The outlook on applications (section 5.4) is based on our publications

- Maarten A. Brems, Mathias Kläui and Peter Virnau, ”Circuits and excitations to enable Brownian token-based computing with skyrmions”, *Applied Physics Letters* **119**, 132405 (2021) (Ref. [29])

and

- Raphael Gruber, Jan Rothörl, Simon M. Fröhlich, Maarten A. Brems, Fabian Kammerbauer, Maria-A. Syskaki, Elizabeth M. Jefremovas, Sachin Krishnia, Asle Sudbø, Peter Virnau, and Mathias Kläui, ”Real-time observation of topological defect dynamics mediating two-dimensional skyrmion lattice melting”, *Nature Nanotechnology*, in press (2025) (Ref. [34]).

The experiments discussed in this chapter were performed without my participation; I contributed through analysis, interpretation, discussion, simulation, and modeling[1].

5.1 Observation of Enhanced Diffusion

In the previous chapter, we established pinning of the skyrmion domain wall as the dominant pinning effect. This motivates the approach to use a change of the skyrmion size, and consequently of the domain wall configuration, as a depinning mechanism. We demonstrated in the previous chapter that a change in skyrmion size due to a different applied out-of-plane magnetic field locally affects the favorable positions due to pinning. However, assuming randomly distributed domain wall pinning sites due to local variations of the magnetic properties, we do not expect the non-local effects of pinning, such as the pinning-induced reduction of diffusivity, to drastically change for different skyrmion sizes. In this chapter, we explore the idea that skyrmion diffusivity may be increased by periodically depinning the skyrmion using periodic size changes.

We study skyrmion diffusion in a $\mathrm{Ta}(4)/\mathrm{Co}_{20}\mathrm{Fe}_{60}\mathrm{B}_{20}(0.85)/\mathrm{Ta}(0.08)/\mathrm{MgO}(2)/\mathrm{HfO}_2(4)$ multilayer stack. Layer thicknesses are given in nanometers in parentheses. The skyrmions can freely explore the continuous film without any geometrical confinement. A low skyrmion density (Fig. 5.1b) is chosen to minimize skyrmion-skyrmion interaction effects. An out-of-plane magnetic field (30 µT) sets the average skyrmion size. We apply an additional out-of-plane magnetic field that sinusoidally oscillates with frequency f and peak-to-peak amplitude A. In the following, we analyze skyrmion diffusion and stability depending on these parameters. The system is imaged using Kerr effect microscopy at 16 frames per second and converted to individual skyrmion trajectories using the trackpy python package [121] by locally fitting two-dimensional Gaussians to the Kerr microscopy brightness distribution. From the trajectories, diffusion coefficients are determined as in section 3.2.1

---

[1] The experiments were conducted predominantly by [redacted] without my involvement and mainly analyzed in equal contribution. I predominantly contributed to the interpretation of the non-monotonic diffusion enhancement, the discussions on the Thiele model description of the observed effects and its application in Brownian Computing as well as the suggested future research based on chapter 3. The appendix section A.1.3 provides a detailed description of my contributions to the research presented in this chapter.

by fitting the two-dimensional mean squared displacement for 3 to 5 videos of one-minute length for each amplitude-frequency-pair in Fig. 5.1a. The plotted values and error bars are given by the mean and standard error of the mean of the values for each video. All measurements were performed in the same region of the sample. The full experimental details, including the nucleation procedure, are given in our publication Ref. [37].

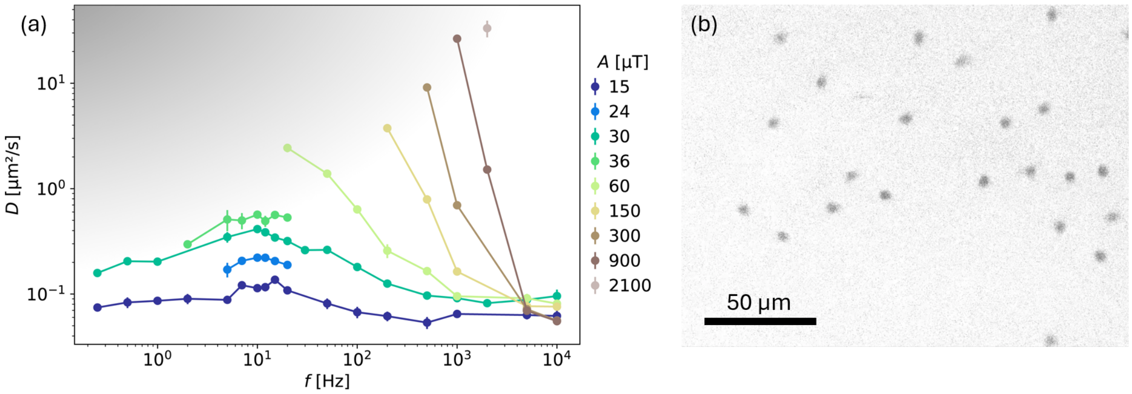

Figure 5.1: (a) Dependence of the skyrmion diffusion coefficient D on the field oscillation frequency f and peak-to-peak amplitude A. Colored solid lines act as a guide to the eye for measurements at the same amplitude. For certain frequency-amplitude-combinations, the skyrmions start annihilating, and a reliable diffusion coefficient cannot be determined. This inaccessible region of the parameter space is roughly indicated by the gray-shaded region in the upper left corner of the plot. (b) Exemplary Kerr microscopy snapshot of a low-density skyrmion (dark dots) system from the measurements in (a). This figure is adapted from our publication Ref. [37].

Fig. 5.1a shows the dependence of the skyrmion diffusion coefficient on the parameters of the field excitation[2]. Interestingly, we observe a non-monotonic frequency dependence with a peak around $(20 \pm 2)\,\mathrm{Hz}$. Likely, for very low frequencies, the depinning effect is too infrequent to significantly affect the thermal diffusion and, for very high frequencies, it is too fast for the skyrmions to adjust. Section 5.3 provides an outlook on an interpretation of this behavior in the context of flashing potentials. The diffusion coefficients appear to approach the unexcited case for very low and high frequencies[3]. We observe a maximum increase by a factor of around 330 between the excited and unexcited cases. Such a constant-temperature increase in diffusivity can be key for the viability and

---

[2] In the spirit of Ref. [30] and for convenience, a procedure that increases diffusivity at constant temperature, such as the oscillating out-of-plane magnetic field discussed here, is referred to as an “excitation.” Consequently, we distinguish the (several) excited diffusion coefficients and the (one) unexcited diffusion coefficient at identical static fields and pinning. This terminology aims to distinguish the absence of external stimulation (unexcited diffusion) from the absence of pinning (free diffusion), which is particularly relevant for the following sections.

[3] The entire measurement series was performed over the course of two days. Diffusion measurements are particularly sensitive to small variations in the experimental conditions (for instance in the alignment of fields and the presence of small field gradients) as demonstrated in section 3.3. In addition, the samples can exhibit minor aging effects already over the course of days. We attribute deviations of the diffusion values for very low and high frequencies between different measurement series (different amplitudes) to these reasons.

speed of Brownian computing approaches as discussed in sections 5.4 and 6.4. The maximum diffusion that can be well-observed experimentally is limited by the time resolution of the microscope. In addition, for low frequencies, we find maximum field amplitudes above which the skyrmions start to annihilate, indicated by the grey-shaded region in Fig. 5.1a. Here, we focus on the stable regime that is most relevant for the quasi-particle modeling of skyrmions and the skyrmion-based computing approaches presented in this thesis. Notably, the skyrmions remain stable for high frequencies even if the oscillating field transiently passes field values at which the skyrmions are unstable in the static case (Fig. 5.2).

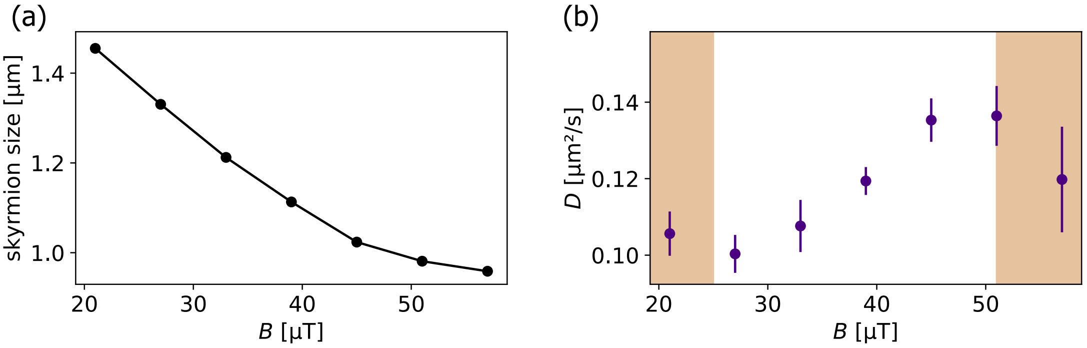

Figure 5.2: Experimental dependence of the average skyrmion size (a) and diffusion coefficient (b) on the static applied out-of-plane magnetic field (no excitation) measured in the same system as Fig. 5.1. Here, the skyrmion size is quantified as the radius of gyration of the Gaussian fit to the brightness distribution as in chapter 4. The mean and standard error of the mean (smaller than the data points in (a)) are shown. The orange-shaded regions in (b) indicate fields at which the skyrmions are unstable. Above about 63 µT, the skyrmions annihilate on the time scale of several seconds with faster annihilation at higher fields (smaller skyrmions). For low fields, the skyrmions start to elongate and turn into stripe domains. This figure is adapted from the supplementary material of our publication Ref. [37].

As first step, we can rule out the size-dependence of the diffusion coefficient as the sole source of the increased diffusion: In general, since the out-of-plane magnetic field tunes the skyrmion size (Fig. 5.2a) and the diffusion coefficient depends on the size [40, 85], the diffusion coefficient inherits a dependence on the applied field (Fig. 5.2b). This is true even in the absence of pinning. Therefore, one might argue that the observed effect stems from an increase in the average diffusion coefficient due to a combination of the oscillating skyrmion size and a non-linearity in the field-size- or size-diffusion-relations. So, the diffusion would only be increased because of the field-dependence of the diffusion coefficient (Fig. 5.2b) and not because of depinning effects. To address this argument, we can compare, for instance, the measured diffusion coefficient at a static field of 45 µT with a measurement where the total field oscillates around 30 µT with a peak-to-peak amplitude of 24 µT (at 10 Hz) such that the oscillating field in the latter case remains below the static field in the former case. If the diffusion enhancement effect were only to stem from averaging the field-dependence of the diffusion coefficient shown in Fig. 5.2b, the case with excitation around the lower field value would yield a lower diffusion coefficient compared to the unexcited case at the higher static field value. Even though the oscillating field never exceeds the static field, we observe a diffusion coefficient of $D = (0.222 \pm 0.011)\,\mu\text{m}^2/\text{s}$ with excitation, which is higher than the diffusion coefficient in the unexcited case $D = (0.135 \pm 0.005)\,\mu\text{m}^2/\text{s}$. Therefore, the diffusion enhancement effect observed in this chapter cannot be explained solely by the size-dependence of the diffusion coefficient and we need to take into account local depinning effects.

5.2 Effective Pinning Reduction and Thiele Modeling

This section discusses pathways for incorporating the diffusion enhancement effect into the quasi-particle Thiele modeling for skyrmions. After reviewing possible approaches to modeling the underlying effect, we focus on describing the average skyrmion behavior on time scales much larger than the field oscillation period. In particular, we compare multiple aspects of the skyrmions' dynamics to support modeling as an effective reduction of pinning.

While this reduction of the effective pinning was brought forward in our publication Ref. [37], it is important to note that the methods and results discussed in section 3.2 had not been developed yet at that point in time. While the analysis performed in the following is sound, the results of section 3.2 indicate that an effective reduction of pinning alone may likely be insufficient to explain the observed 330 times increase in diffusion coefficient: Modeling the effect of the excitation as a reduction of pinning alone cannot explain an increase of diffusivity beyond the free diffusion expected in a flat energy landscape. For the confined quasi-one-dimensional system of Ref. [39], the determined relative increases between pinned and free diffusion amount to a factor of around 8. While it is possible that the system studied in this section simply exhibits an orders of magnitude stronger pinning due to variations in the material stack and fabrication process, additional research is required to determine whether the studied diffusion enhancement method can surpass free diffusion or not. For this reason, the next section provides an outlook on an interpretation of the diffusion enhancement effect in the context of flashing potentials that goes beyond an effective reduction of pinning as well as suggestions for further research. In this section, we only focus on effective pinning in the excited system.

We propose that on long time scales compared to the oscillation frequency, the excitation, on average, acts to reduce the effective pinning experienced by the skyrmion. In particular, we argue that the excited system behaves qualitatively more similar to the expected free diffusion case. Figs. 5.3a,c show the distribution of skyrmion occurrences in the system during a fixed time intervals without and with excitation, respectively. In the excited case corresponding to the highest point in Fig. 5.1a, the distribution is significantly more homogeneous, and much less space remains unsampled (white areas). Figs. 5.3b,d depict two sets of exemplary trajectories from the same measurements. The diffusion appears less hopping-like on the same time scale but a different length scale due to the higher diffusion coefficient.

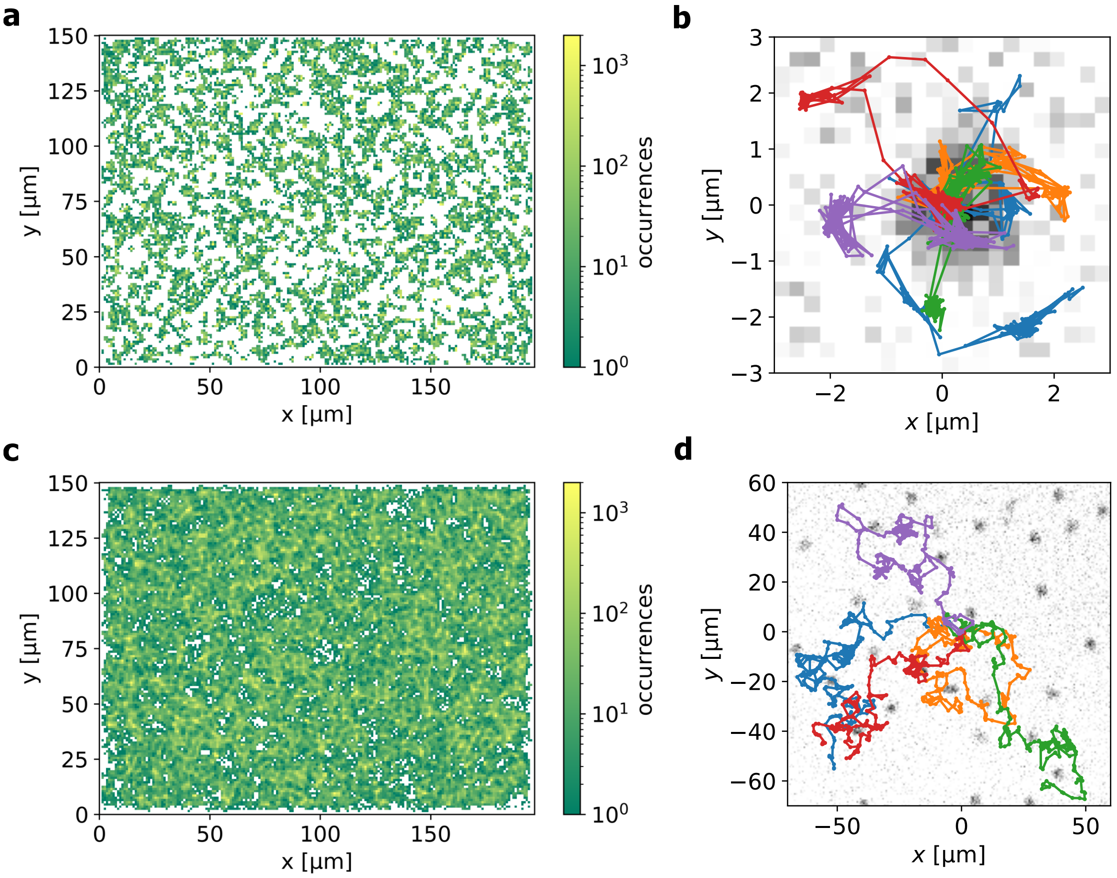

Figure 5.3: (a,c) Spatial distributions of skyrmion occurrences during 10-minute measurements at a static field of 30 µT without and with excitation, respectively. The excitation parameters correspond to the highest point in Fig. 5.1 with a frequency of $f = 2\,\mathrm{kHz}$ and a peak-to-peak amplitude of $A = 2100\,\mu\mathrm{T}$. The histograms employ $1 \times 1\,\mu\mathrm{m}^2$ bins. (b,d) Exemplary 10-minute trajectories for the same measurements. Different colors correspond to different skyrmion trajectories shifted to all start at the same origin. The backgrounds depict single grayscale Kerr microscopy snapshots containing a skyrmion at the start of its trajectory. Due to the higher diffusion coefficient, the trajectories with excitation in (d) explore a larger region of the sample during the same time compared to the unexcited case in (b). This figure is taken from our publication Ref. [37].

Next, we consider the effective pinning energy landscapes determined from the skyrmion distributions via the potential of mean force approach. Here, the parameters are the same as in Fig. 5.3a,c but all data is used. Compared to the unexcited case (Fig. 5.4a), the energy landscape with applied excitation (Fig. 5.4b) is significantly shallower with less steep energy barriers, leading to a reduction of pinning effects overall. Note that these energy landscapes are for comparison purposes only, as $1 \times 1\,\mu\mathrm{m}^2$ bins correspond to an insufficient resolution for a reliable simulation of the system[4].

---

[4] Also note that in contrast to the effectively one-dimensional system studied in section 3.2, unsampled bins exist even when using all available data. These bins have been set to 1 occurrence as 0 occurrences lead

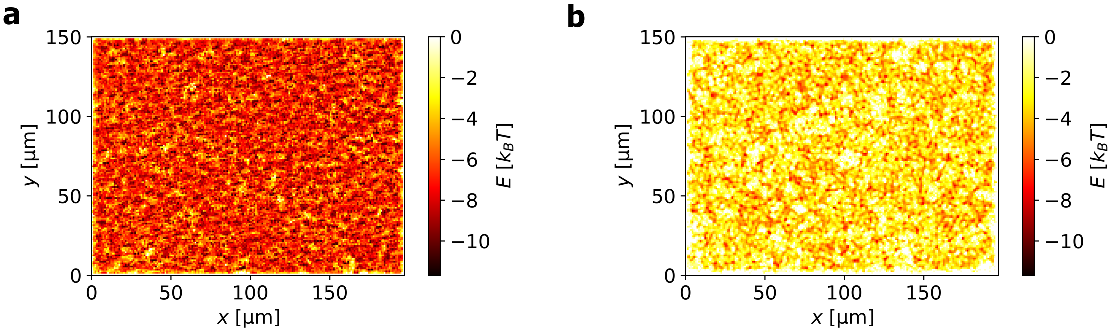

Figure 5.4: Effective pinning energy landscapes determined from the skyrmion distribution without (a) and with excitation (b) via the potential of mean force approach. The parameters of the static field and excitation are the same as in Figs. 5.3a,c. The energy landscape in the exited case is significantly shallower, with less steep energy barriers. This figure is taken from the supplementary material of our publication Ref. [37].

As a final comparison tool, we consider the distribution of skyrmion displacements during a fixed time interval to compare the exited and unexcited systems' behavior to the expectation for free diffusion. This measure was chosen as the instantaneous velocity is experimentally inaccessible. In classical free diffusion, each component of the displacement is expected to be Gaussian distributed, and the absolute two-dimensional displacement consequently follows a Rayleigh distribution (the two-dimensional equivalent of the Maxwell-Boltzmann distribution):

$$p(\Delta x) \sim \Delta x e^{-\frac{\Delta x^2}{2\sigma^2}} \tag{5.1}$$

Figs. 5.5a,c show the displacement distributions over a time interval of 2 s for the unexcited and excited cases. The field and excitation parameters are the same as in the previous two figures. In both cases, a single Gaussian is insufficient to describe the entire distribution. We find an additional peak around zero displacement (regime A) in both cases, which we identify with the small displacements within a pinning site. The remaining part of the distribution (regime B) we interpret as the motion outside of pinning sites or leaving pinning sites. We expect both contributions to exhibit random motion and find that the overall distribution can be well-fitted by a sum of two Gaussians. The purpose of fitting the distributions in Fig. 5.5 is only to compare our expectations to experimental observation. We limit ourselves to a qualitative comparison of the excited and unexcited cases. In the excited case, regime A contributes significantly less to the total distribution, and therefore, the total distribution is more akin to the single Gaussian expectation for the free diffusion limit[5]. Note that the shape of the distribution depends on the time interval, i.e., for very long time intervals, the distributions are expected to approach single Gaussians independently of the presence or absence of excitation. The 2 s time interval

---

to an unphysical infinite repulsive potential in the analysis. This approach is fine for visualization purposes but inaccurate for simulations. At higher resolutions, unsampled bins are more prominent, limiting the maximum resolution. Our planned publication Ref. [44] provides a procedure to overcome these obstacles.

[5] The small net motion that shifts regime B towards negative values in Fig. 5.5c is attributed to a slight magnetic field gradient.

was chosen such that both contributions (regime A and B) are well-observable to compare the excited and unexcited case qualitatively. Next, we consider the two-dimensional absolute displacement distributions shown in Fig. 5.5b,d. Since pinned skyrmions appear in regime A for both the x- and y-displacement, we expect the two-dimensional absolute displacement distribution to follow a sum of two Rayleigh distributions, which we employ as a fit function. Again, the system resembles the expectation for free diffusion more closely in the excited case. In the corresponding distribution, we observe a small addition peak around displacements of around 4 µm which is identified with the characteristic distance between neighboring pinning sites.

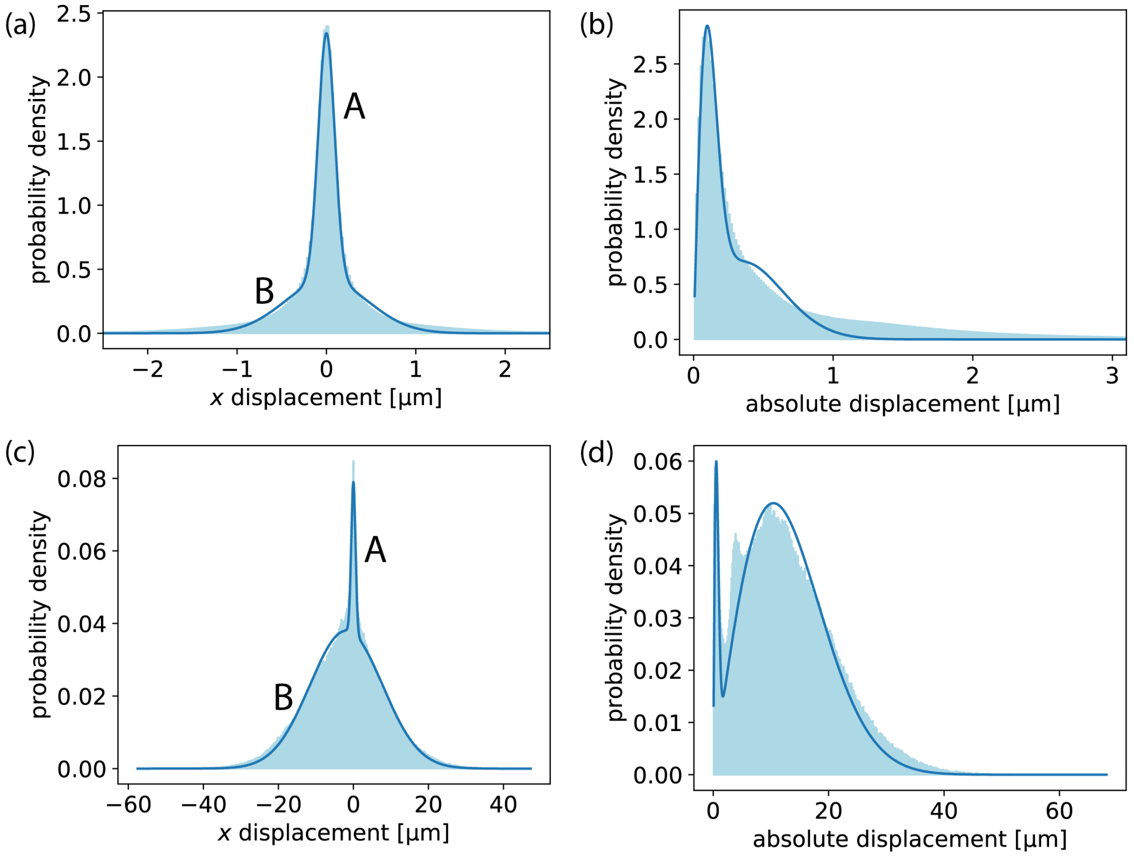

Figure 5.5: Skyrmion displacement distributions (light blue) during a time interval of 2 s without (a,b) and with excitation (c,d). The excitation and static field parameters are the same as in the previous two figures. The distributions of displacements in the x-direction (a,c) are fitted with a sum of two Gaussians (blue line) reflecting two regimes labeled as A and B. The peak around zero displacement (regime A) is identified with movements within a pinning site. The wider distribution (regime B) is attributed to motion outside or leaving pinning sites. The distribution of y-displacements is not shown here, but it exhibits very similar behavior. The distributions of two-dimensional absolute displacements (b,d) are fitted with a sum of two Rayleigh distributions. This figure is adapted from our publication Ref. [37] and its supplementary material.

In this section, we investigated multiple aspects of skyrmion dynamics, based on which we argued that on time scales much longer than the oscillation period, the excitation's average effect is to effectively reduce the pinning experienced by the skyrmion. These observations support the modeling of the effect via an average effective pinning energy landscape. Modeling via an averaged energy landscape alone fundamentally cannot capture a diffusion enhancement beyond the free diffusion coefficient. Therefore, the next section provides an outlook on an interpretation of the system's behavior based on flashing potentials as well as suggestions for further research.

5.3 Outlook on Similarities to Flashing Potentials

The key result of the previous chapter was that the favorable skyrmion positions in the sample change as the skyrmion size changes because the dominant pinning effects occur at the skyrmion's domain wall. As in chapter 3, we can express the favorable and unfavorable skyrmion positions as a spatially inhomogeneous pinning energy landscape for the skyrmion center position, which can be determined as the potential of mean force from a well-sampled skyrmion distribution[6]. In this description, the changes in the skyrmion size enforce changes in the energy landscape, and the oscillating field consequently cycles through various energy landscapes. This concept is very reminiscent of flashing potentials such as the flashing Brownian ratchets used to model molecular motors [152, 154–156]. This section therefore provides an outlook on a possible interpretation of the diffusion enhancement mechanism in the context of flashing potentials.

A conventional Brownian ratchet is a two-state flashing potential, where one state is an asymmetric ratchet potential, and the other state is a flat potential (Fig. 5.6a). By periodically switching between the two states, a thermally diffusing particle inside the Brownian ratchet will experience directed motion depending on the ratchet potential's parameters and flashing frequency [152, 154, 156]. In the ratchet state, the particle is likely close to the energy minimum. Upon switching to the flat state, it performs isotropic thermal diffusion. However, due to the ratchet potential's asymmetry, the particle is more likely to be found in a region where, upon switching back to the ratchet state, it will experience a force to the right (in Fig. 5.6a). This generates an average deterministic drift to the right, thus converting isotropic random motion into directed motion. While conventional Brownian ratchets aim to generate deterministic drift, a similar setup (Fig. 5.6b) can enhance diffusive motion, given the right barrier potential shape and flashing frequency, since the particle moves towards an adjacent minimum upon switching states. Appendix section A.4.1 contains illustrative simulations showing the frequency-dependence of the diffusion enhancement using the toy model displayed in Fig. 5.6b. Similar to the frequency-dependence of the presented diffusion enhancement mechanism, a significant diffusion enhancement occurs only within the right frequency range: For too high frequencies, there is insufficient time for the particle to move to the potential minimum. For too low frequencies, the additional traveled distance due to the switching process contributes little to the total mean squared displacement. While, the flashing potential in Fig. 5.6b is designed such that the minima

---

[6] Low skyrmion densities are chosen such that skyrmion interaction is minimal. Skyrmion interaction can lead to artifacts in the potential of mean force that do not stem from pinning.

of one state and the maxima of the other state align and vice versa, the skyrmion pinning potentials are random. Despite this difference, it is still plausible to expect that, occasionally, the skyrmion will experience local switching between favorable and unfavorable pinning energy landscapes, such as schematically illustrated in Fig. 5.6c.

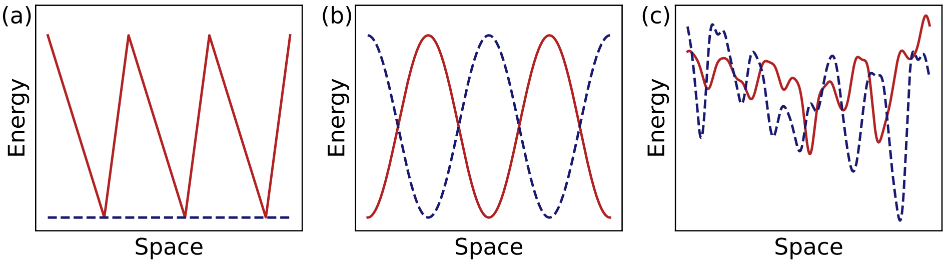

Figure 5.6: Schematic illustrations of different flashing potential configurations. Two distinct states are shown as solid red and dashed blue lines, respectively. (a) A conventional two-state asymmetrical flashing Brownian ratchet that can convert random motion into directed motion to the right. (b) A two-state symmetrical flashing potential that can enhance diffusive motion. (c) Schematic of two skyrmion pinning potentials that is locally similar to (b) in the sense that favorable positions in one state correspond to unfavorable positions in the other state.

Appendix section A.4.1 discusses further key differences between flashing potentials and the presented diffusion enhancement approach[7]. While the flashing potential interpretation provided in this outlook shares some key features with the experimental behavior and may provide some intuition for this kind of systems, it is unclear if this model is well-suited for a reliable and predictive description of the diffusion enhancement mechanism. Such a description requires significant further research beyond the scope of this thesis. Suggested directions for such future research as well as the challenges that must be overcome are discussed in the following.

One important step is to employ the method of section 3.2.3 to a system in which the diffusion enhancement effect is also measured to determine whether it surpasses free diffusion or not. Beyond that, a promising next step would be to explore controlled systems akin to flashing potential systems. As in the previous chapter, we face the challenge that the Thiele model fundamentally does not capture the pinning of the skyrmion domain wall as it describes skyrmions via their center position. We argued before that size-dependent pinning can be modeled by employing a different pinning energy landscape for each average skyrmion size[8]. Consequently, one could propose modeling the field oscillation by employing a different energy landscape for each field value (or groups of field values in the case of a continuous sinusoidal oscillation. Therein, the spatial skyrmion distributions must be measured for the static field configurations to determine the energy landscapes as

---

[7] For instance, the systems mentioned above are two-state flashing potentials. In contrast, continuous size changes mean that the skyrmion likely experiences many different pinning energy landscapes.

[8] In thermally active systems that exhibit pinning, the skyrmion size fluctuates and is position dependent as seen in Fig. 4.1. Therefore, one pinning energy landscape for the skyrmion center is assigned to one average skyrmion size.

the potentials of mean force. However, for many of the measurements shown in Fig. 5.1a, the oscillating field reaches values at which the skyrmions are unstable in the static case. Therefore, this approach could only describe a small subset of all the practical excitation parameters. Instead, in a future experiment, one could switch between two field values and thus two average skyrmion sizes only[9], i.e., using a square wave instead of a sine wave pattern. Therein, the field values would be chosen such that skyrmions are stable at a static field as well. Using static fields, the effective pinning energy landscapes at these two size configurations are determined from the skyrmion distribution. Given sufficient experimental statistics to reliably use the energy landscape in simulation and to apply the method from section 3.2.3 to determine the time-conversion, quantitative simulation of the flashing potential model could be compared to the experiment. In addition, one could compare the excited diffusion to the free diffusion, which can be estimated from the time-conversion and the pinning-affected diffusion coefficient at constant size using Eqns. 3.2 and 3.3. Finally, this analysis would also enable an experimental investigation of the effect of skyrmion size on the free diffusion coefficient by determining the latter for both skyrmion sizes.

5.4 Outlook on Application Scenarios

This section provides an outlook on two classes of application scenarios for the diffusion enhancement mechanism brought forward in this chapter. The first one is to use it as a means of driving a phase transition, essentially as a substitute for tuning random motion via temperature. This is particularly valuable as temperature changes also strongly affect the material parameters, which makes temperature effects on random motion hard to isolate for skyrmion systems [16, 151]. The second application scenario is skyrmion-based Brownian computing [28–32, 51, 52]. This computing approach leverages random motion to benefit a certain computing architecture. Therefore, a mechanism to tune random motion can be key to improving Brownian computers and extending their viable application scenarios [29, 30, 32, 157]. While Brownian reservoir computing [45–49] is the central topic of the next chapter, and section 6.4 discusses the application of diffusion tuning mechanisms to such devices, this section focuses on Brownian token-based computing [29, 51, 52]. For these application scenarios, it is essential to verify that the diffusion enhancement mechanism remains reliable in both dense skyrmion systems and geometrically confined systems, such as narrow channels. This is shown in appendix section A.4.2.

For the first part of the application outlook, we consider the use of the diffusion enhancement to melt a hexatic skyrmion lattice state into a liquid state. The full experimental and analysis details omitted in the following short outlook are given in our publication Ref. [34]. The transition is driven via a stepwise increase of the excitation amplitude at a constant frequency (Fig. 5.7a). Consequently, the diffusion coefficient increases with time. Fig 5.7b shows the time-evolution of the exponent η_6 of the orientational correlation function G_6. The steep and large increase in η_6 across the critical value of 1/4 indicates the transition between the hexatic and liquid regime. Note that in these measurements,

---

[9] For the flashing potential model to be accurate, it is assumed here that the field-induced size change happens significantly faster than the typical time scale of skyrmion motion.

the skyrmions are enclosed in finite hexagonal geometrical confinements[10] (Fig. 5.7c,d). We demonstrate that the diffusion enhancement mechanism can drive a transition between two states characterized by distinct ordering.

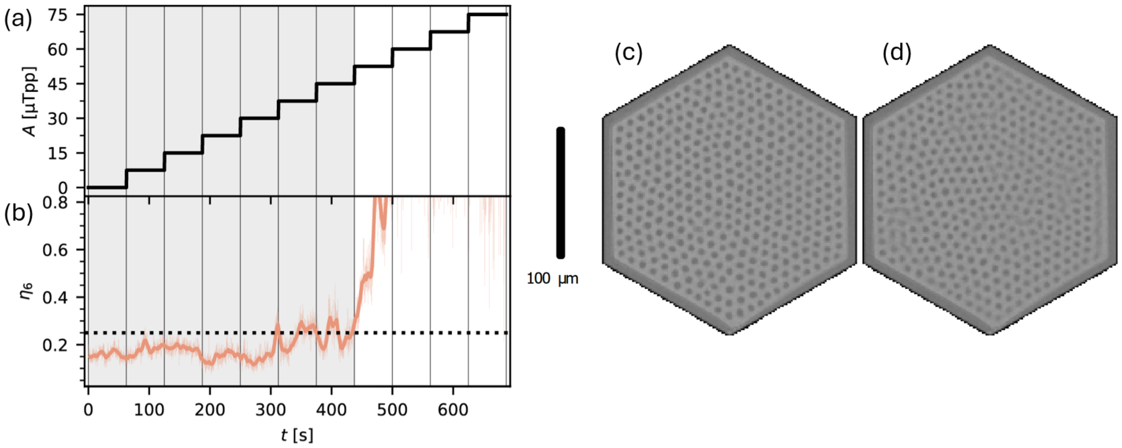

Figure 5.7: Melting of a hexatic lattice state using an oscillating magnetic field at constant frequency. (a) Stepwise increase of the peak-to-peak amplitude A of the oscillation over time. (b) Time evolution of the exponent η_6 of the orientational correlation function G_6. The solid line represents the rolling mean over 6.25 s, and the dotted horizontal line marks the critical exponent of 1/4. The gray-shaded and white areas in (a) and (b) are characterized as hexatic lattice states and unordered liquids, respectively. (c,d) Kerr microscopy images of the system averaged over 5 s determined at $t = 75$ s (c) and $t = 575$ s (d). The smeared-out contrast indicates the increased diffusivity in (d). This figure is adapted from the extended data figures of our publication Ref. [34].

For the second part of the application outlook, we briefly turn to Brownian token-based computing using skyrmions [17, 29, 51, 52]. This paragraph aims to provide a short illustration of the value of external diffusion enhancement in this unconventional computing architecture. For an extended study of Brownian token-based computing using skyrmions and the benefits of external diffusion enhancement methods, I refer to our publication Ref. [29], my master's thesis Ref. [157] and our international patent Ref. [30]. Brownian token-based logic circuits consist of a network of computational paths that is explored by randomly moving signal carriers, called "tokens". The inputs correspond to the tokens' starting positions, and their final positions after traversing the circuit determine the output. The circuits aim to be highly energy efficient since thermal random motion is leveraged for the motion of the tokens. Their downside is that the computation duration is non-deterministic due to the randomness involved in exploring the circuit network. In our publication Ref. [157], we have developed a skyrmion-suitable Half-Adder circuit and brought forward the benefits of conditional application of a diffusion enhancement

---

[10] Phase transitions are defined in the thermodynamic limit where systems approach infinite size. In our small system which is subject to significant finite-size-effects, we still observe a change in the ordering which we associate with a transition between two differently ordered states akin to a hexatic and liquid phase.

method. ”Conditional application” here means only using an external diffusion enhancement mechanism in the randomly occurring cases, where computations are exceptionally slow. Thereby, the circuits remain highly energy efficient on average, but still allow them to be used for time-sensitive tasks, significantly extending the range of viable application scenarios of Brownian token-based computers.

The fundamental idea behind the Brownian computing paradigm, to leverage (thermal) random motion for the benefit of a computing architecture, can be extremely valuable to developing low-power unconventional computing devices. While this short outlook has discussed the potency of diffusion enhancement mechanisms in Brownian token-based computing, the next chapter is entirely dedicated to Brownian reservoir computing using skyrmions. At the end of the next chapter, in section 6.4, we will turn again to the application of diffusion enhancement mechanisms to such devices and the benefits entailed.

6. Brownian Reservoir Computing using Magnetic Skyrmions

Reservoir computing is a computing paradigm that leverages the complex non-linear behavior of a physical system to map a complicated problem to a much simpler linear problem [45–49]. Therein, the physical system, the reservoir, itself does not need to be trained, yielding fast learning at a low computational cost. In addition, reservoir computers can provide high energy efficiency and/or very fast operation depending on the reservoir's intrinsic physical properties. Skyrmion systems are very promising candidates due to the skyrmions' non-linear interactions and electrical manipulability [28]. For these reasons, several theoretical concepts for skyrmion-based reservoir computing have been proposed [25–28, 50]. However, experimental realizations had previously remained elusive, amongst other reasons, because of difficult-to-control pinning effects [25, 26]. In this chapter, we combine the reservoir and Brownian computing [28–30, 51, 52] paradigms and exploit the skyrmions' thermal random motion to overcome these obstacles. We develop and experimentally demonstrate a proof-of-concept Brownian reservoir computer that exploits the effects of spatially inhomogeneous electrical current on a geometrically confined skyrmion performing thermal diffusion. In addition, our design entails an automatic reset mechanism due to the confinement at no additional energy cost.

This chapter starts with an introduction to our device design and the underlying operating principles. The following section then demonstrates that our minimal proof-of-concept device suffices to realize all two-input Boolean logic gate operations, including the not linearly separable XOR gate. Access to the skyrmion trajectory during operation via Kerr microscopy then allows us to understand the trained weights for the linear read-out in the context of the competing interactions in the system. Based on these results, the role of thermal effects in the device's operation is discussed, including their necessity for sufficiently mitigating the effects of pinning for reliable operation. The final section provides an outlook on extension paths based on the presented device design and further use cases. In particular, we realize 3-input logic operations as well as hand gesture recognition using time-dependent inputs, demonstrating that even a minimal skyrmion-based reservoir can be competitive for real-life applications.

The present chapter is based on multiple of our research activities: Most of the contents of this chapter concerning our proof-of-concept device are published in our publication

- Klaus Raab, Maarten A. Brems, Grischa Beneke, Takaaki Dohi, Jan Rothörl, Fabian Kammerbauer, Johan H. Mentik, M. Kläui, ”Brownian reservoir computing realized using geometrically confined skyrmion dynamics”, *Nature Communications* **13**, 6982 (2022) (Ref. [31])

The introduction to reservoir and Brownian computing for the comparison of the general operating principles to our specific device design is based on our review/perspective publication

- Oscar Lee, Robin Msiska, Maarten A. Brems, Mathias Kläui, Hidekazu Kurebayashi, Karin Everschor-Sitte, ”Perspective on unconventional computing using magnetic skyrmions”, *Applied Physics Letters* **122**, 260501 (2023) (Ref. [28]),

to which I contributed section “III. Skyrmion-Based Reservoir and Brownian Computing”, and our scientific outreach publication

- Maarten A. Brems, Klaus Raab, Peter Virnau, Mathias Kläui, ”Brownscher Reservoir-Computer mit Skyrmionen”, *Physik in unserer Zeit* **54**, 60-61 (2023) (Ref. [53]).

We first introduced the use of artificially enhanced diffusion in Brownian computing in our international patent

- Maarten A. Brems, Mathias Kläui, Peter Virnau, ”Information Processing Apparatus”, *International Patent disclosure*, WO2022200504A1 (2022) (Ref. [30])

which was initially developed as a part of my master’s thesis, but to which statements on the explicit application to the kind of devices discussed here were added during the rebuttal stage as a part of my PhD (starting on page 20, line 3 in Ref. [30]). The outlook on the use of time-dependent inputs for gesture recognition is based on our publication

- Grischa Beneke, Thomas B. Winkler, Klaus Raab, Maarten A. Brems, Fabian Kammerbauer, Pascal Gerhards, Klaus Knobloch, Sachin Krishnia, Johan H. Mentink, Mathias Kläui, ”Gesture recognition with Brownian reservoir computing using geometrically confined skyrmion dynamics”, *Nature Communications* **15**, 8103 (2024) (Ref. [32]).

The experiments discussed in this chapter were performed without my participation; I mainly contributed through device developed and optimization, analysis, simulation, interpretation, and discussion[1].

---

[1] The experiments were conducted predominantly by [redacted] and [redacted] without my involvement. I trained the read-out for 2- and 3-input operations and analyzed the device’s performance. [redacted] evaluated the video data with my consultative participation based on that analysis. I interpreted the trained weights to understand the effects of device imperfections as well as the role of thermal diffusion. The appendix section A.1.4 provides a detailed description of my contributions to the research presented in this chapter.

6.1 Operating Principles and Device Design

The goals of this section are to explain the operating principles of our proof-of-concept skyrmion-based Brownian reservoir computer and to illustrate the design process of such a device. In particular, this section aims to establish a correspondence between the general features of a reservoir computer and the specific device studied here, as the design choices are discussed step by step. The studied type of reservoir computing, which uses a physical system as the reservoir, is often referred to as physical reservoir computing to distinguish it from pure software approaches [47–49]. This additional distinction is omitted for simplicity, as only physical reservoir computing is discussed in this thesis. Moreover, the following explanation is phrased with a classification task in mind for ease of understanding and because logic operations can be viewed as a classification of input configurations into the categories "True" or "False".

A reservoir computer can be viewed as an artificial neural network in which most of the network is replaced by a physical system, called the "reservoir" [45–49]. The reservoir should exhibit complex non-linear behavior, typically arising due to a competition of interactions, such that it acts similarly to the replaced part of the artificial neural network in the sense that it reduces a complex non-linear classification problem to a simpler linear one. In particular, reservoir computers exploit that the input data, when encoded as a manipulation of the physical system, is effectively transformed into the system's high-dimensional state space as the system responds to the manipulation. Measuring system's response in terms of a few characteristic observables then produces the reservoir's output, which is lower-dimensional again. The resulting simpler classification problem based on the reservoir output can then be solved, for instance, by a single linear read-out layer. The general operation of a reservoir computer is illustrated in Fig. 6.1a. After the input data passes the reservoir, it should be reliably classifiable based on a linear function of the reservoir's outputs. In this process, the input data is encoded as a manipulation applied to the system and thereby translated to the system's response. Information about the system's response is then read out by performing a measurement in the system. The measured values constitute the output of the reservoir and consequently the input of the linear read-out. Based on labeled training data, the weights of the read-out layer are trained to match the desired classification task. After each operation, the system must be reset to a state that exhibits a reproducible response to the manipulation. "Reproducible" does not necessarily mean "deterministically identical", as we demonstrate with our device. The state only needs to be similar enough such that the reservoir computer works on new data it was not trained on.

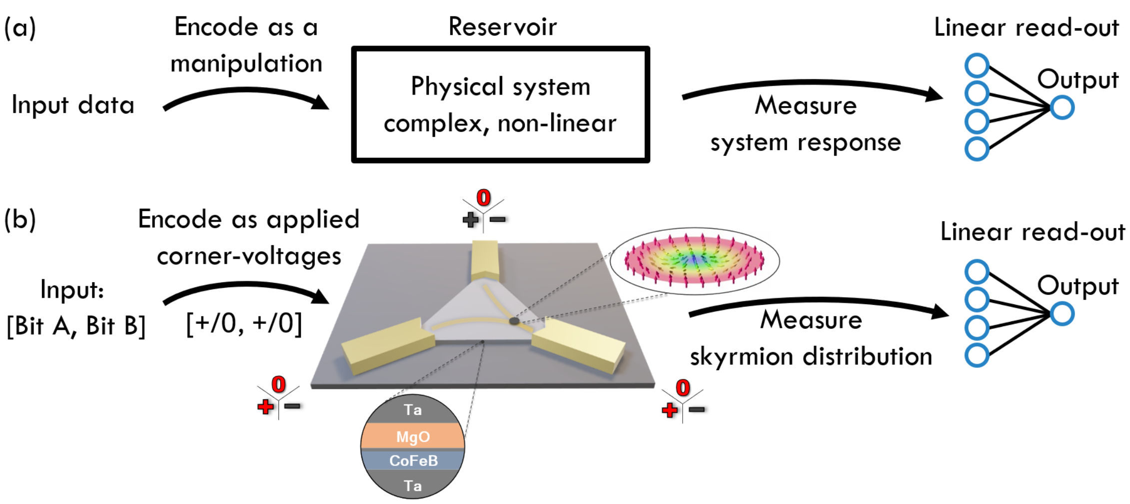

Figure 6.1: Schematic illustration of the operating principles of a general reservoir computer (a) and our device (b). The input data, in our case two bits, is encoded as voltages at the bottom contacts (yellow) as zero or constant positive voltage (options highlighted in red) for “0” and “1” bits, respectively. The system responds to this manipulation in the form of a bias to the skyrmion (grey dot) motion. This response is measured by locally sampling the time-averaged skyrmion distribution in the system, as elaborated in the next section. These measured values are fed into a linear read-out layer. Based on labeled training data, the weights of this layer are trained such that the output of the reservoir computer reflects a chosen Boolean logic operation as discussed in detail in the next section. The insets show a schematic skyrmion structure (upper right) and the stack structure (lower left). The central schematic of our skyrmion-based reservoir is adapted from our publication Ref. [31]. The inset skyrmion structure in that central schematic is adapted from the original of Karin Everschor-Sitte and Matthias Sitte, which is licensed under Creative Commons Attribution-Share Alike 3.0 Unported (CC BY-SA 3.0).

An essential consequence of this design is that only the single read-out-layer must be trained, resulting in fast training requiring little training data. In addition, the same reservoir can be used for various classification tasks by only changing the weights of the read-out layer. The key challenge is usually finding a suitable reservoir for the desired tasks and understanding what makes it suitable [28]. Therefore, we design a skyrmion-based reservoir computer in which we have excellent time-resolved access to the system's state via Kerr microscopy. This allows us to understand how the reservoir acts to enable the classification and interpret the trained weights of the linear read-out in section 6.3.

As a goal for our proof-of-concept device, we chose performing all two-input Boolean logic operations and some three-input operations, all using the same reservoir. We focus on two-input operations first, allowing for an understanding of all essential operation principles. Section 6.5 then provides an outlook on three-input operations. Consequently, the input data for our reservoir computer is a pair of bits. Fig. 6.1b illustrates the operation of our device as a specific realization of the general operation principles in Fig. 6.1a. The design process of our device is discussed in the following. A sensible first step in designing a reservoir computer is choosing which aspects of the system's behavior should be leveraged for the operation. This choice then limits the options for input encoding and the read-out measurement. Here, we chose the current-induced dynamics of a single skyrmion in a geometrically confined system. Specifically, we aim to encode the inputs via current-induced forces [20, 39, 99, 100], which compete with the repulsive forces from the confinement's boundaries [15] and pinning effects [36, 39]. The key advantage of the confinement is that, after the current is turned off, the boundary-repulsion [15] pushes the skyrmion back to the central region of the system. Thereby, our device provides an automatic reset mechanism at no additional energy cost. The competition of the forces determines the favorable positions for the skyrmion. Pinning effects are unavoidable in state-of-the-art systems and can significantly impair a device's performance or even render it completely inoperable. Therefore, we employ skyrmions performing thermally activated random diffusion. Section 6.4 explains the necessity of thermal diffusion and its impact on the device's operation in detail. For now, we only need to consider that, due to the thermal random motion, we need to measure the time-averaged skyrmion distribution instead of just the skyrmion's position at a specific point in time. The former serves as a reproducible system response required for reservoir computing. Exploiting random motion for the benefit of a computing architecture is the central concept of the Brownian computing paradigm [28, 51, 52]. Hence, we refer to our device as a Brownian reservoir computer.

A triangular confinement is chosen for this minimalistic proof-of-concept device as the three corners seem natural locations for three contacts that can encode up to three values as voltages. While, in principle, one could apply voltages of different continuous magnitudes, we limit ourselves to either a constant positive/negative voltage or ground. The device's design is illustrated in a COMSOL Multiphysics simulation in Fig. 6.2. The skyrmion-hosting material is patterned with extrusions at the corners of the triangles for the contacts to be applied around and on top of. Another advantage of the triangular shape is that the acute angles of the triangle, combined with the boundary repulsion, prevent the skyrmion from going near/under the contacts. The same effect prevents the skyrmions from annihilating at the current density hot spots (see Fig. 6.2) at reasonable current densities. Annihilation at these spots is observed experimentally when applying very high current densities. Note that the simulation in Fig. 6.2 employs the same parameters and approximations as in section 3.3.2, i.e., only the magnetic material's bottom tantalum layer and the contacts' chromium layer are simulated. We are only interested in the relative magnitudes of the current densities and not the absolute values to understand, for instance, the likely annihilation points due to strong current-induced force and/or local Joule heating.

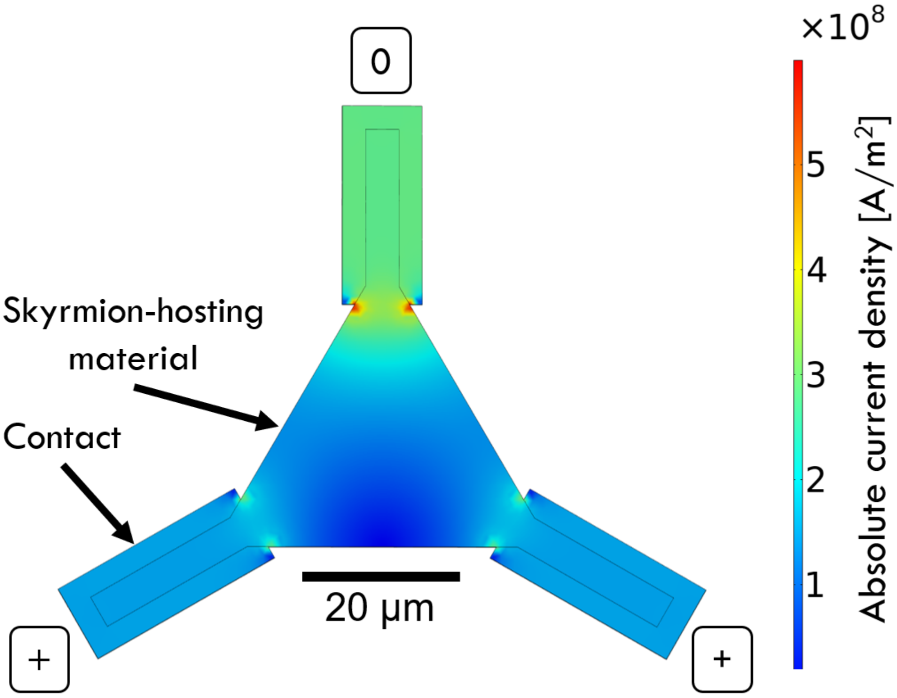

Figure 6.2: Schematic device design and absolute current density distribution simulated using COMSOL Multiphysics [73]. The triangular skyrmion-hosting material is designed to have rectangular extrusions at the corners. The "0", and "+" signs indicate ground, and a constant positive voltage applied at the outermost edge, respectively. The predicted current-density hot spots at the corners coincide with experimentally observed probable skyrmion annihilation positions at very high current voltages (higher than those required for the reservoir computer's operation). The simulation details are provided in appendix section A.5.1.

Fig. 6.3 shows exemplary Kerr microscopy snapshots of an experimental skyrmion system similar to the design in Fig. 6.2. The full experimental details are provided in our publication Ref. [31] and its "Methods" section in particular. We observe current-induced skyrmion motion starting around 5×10^7 A/m^2 and the magnitude of the voltages is chosen such that the current density[2] is in the range of 1×10^8 A/m^2. Similar to section 3.3.2, the employed current densities are orders of magnitude smaller than what is usually employed in comparable systems, as we only need to bias the diffusive skyrmion motion, similar to section 3.3. It is important to remember that Fig. 6.3 only contains single frame snapshots and that the skyrmion performs thermal random motion for all voltage combinations as indicated by the red arrows in Fig. 6.3e. For the use in Brownian reservoir computing, we employ a constant positive voltage to encode a "1" bit or ground to encode a "0" bit, which are applied to the bottom two contacts while the top contact is fixed at ground (voltage options marked in red in Fig. 6.1b). To make the Brownian reservoir computer work, the

---

[2] Note that the current density is spatially inhomogeneous and increases towards the corner of the triangle and the state values are calculated at the half-width of the triangle at the corner from which the current originates.

final remaining steps are to measure the system's response to the input configuration, feed it into a linear read-out layer, and train its weights such that the device performs the desired operation. These steps are explained in the next section.

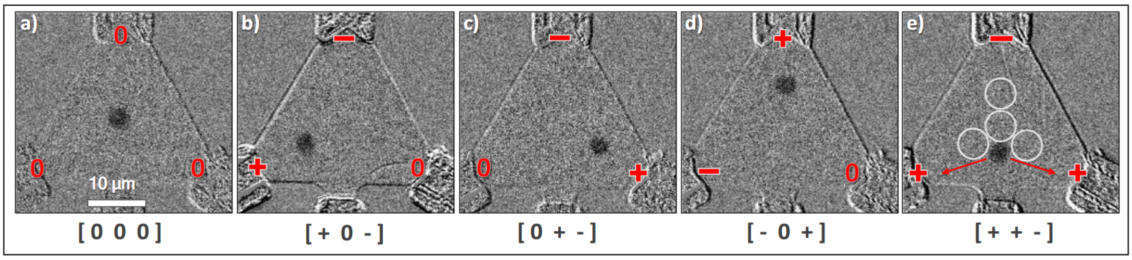

Figure 6.3: Exemplary Kerr-microscopy images of a single skyrmion (dark dot) confined to an equilateral triangle with different voltage configurations. The voltages are applied at the contacts at the corners of the triangle; the additional contact at the bottom center is unused (isolated). The labels at the contacts indicate the voltage configurations. Note that the skyrmion is not fixed at the positions shown in the snapshots. Instead, it performs thermal diffusion biased by the spatially inhomogeneous current-induced force due to the applied voltages, exploring an extended region of the sample as indicated by the arrows in (e). This behavior is studied in detail in section 6.3 and Fig. 6.7. The four white circles in (e) exemplarily indicate the four regions used to sample the skyrmion distribution locally and mimic the magnetic tunnel junction readout discussed in the next section. The circular regions have a radius of 2.2 μm. This figure is taken from our publication Ref. [31].

6.2 Read-Out, Training, and Results for 2-Input Logic Operations

This section is about turning our skyrmion-based reservoir into an actual reservoir computer that can perform Boolean logic operations. To this purpose, we need to measure the system's response to the inputs encoded as voltage configurations. These measurement results act as the input for the linear read-out, in turn providing the output of the logic operation. We have chosen this micrometer-sized skyrmion system for good access to the time-resolved state of the system during operation. This will prove immensely valuable for understanding the trained weights and the role of thermal diffusion in the following sections. However, Kerr microscopy and software-based skyrmion tracking are very impractical for an actual product and infeasible for a scaled-down nanometer-sized device. The latter would likely be the final development goal due to expected lower energy consumption and faster operation, in addition to smaller device dimensions. This research prototype aims to demonstrate and study skyrmion-based Brownian reservoir computing and not to develop a fully optimized device pursuing industrial goals. Still, we want to emulate a read-out mechanism that is favorable for applications and nanometer-sized devices. We chose magnetic tunnel junctions (MTJs) as the read-out device because the tunnel magnetoresistance, which an MTJ measures, depends on the presence of a skyrmion in the region covered by the MTJ [22]. Consequently, the average measured tunnel magnetoresistance depends on the skyrmion occurrence probability within the probed region. Thus, using multiple MTJs at different positions in the system may allow for local sampling of the average skyrmion distribution.

To mimic this kind of read-out, we employ four circular regions in the system indicated by the circles in the schematic Fig. 6.4 and Fig. 6.3(e). The following explanation is based on a minimal emulation of the read-out, which considers only the skyrmion's center position. In this emulation, the skyrmion can only be detected in one region at a time. After that, a more involved read-out emulation is introduced that accounts for the skyrmion size, and the results of both methods are compared. After the input is encoded as the voltage configuration at the corners of the confinement, the system is imaged over a fixed sampling duration. Then, the Kerr video is converted to a skyrmion trajectory using the trackpy python package as in the previous chapter [121]. The number of video frames for which the skyrmion is found in a particular region, divided by the total number of frames, serves as an estimate for the occurrence probability of that respective region P_{region} (see Fig. 6.4). Note that the skyrmion may occur at positions that do not belong to any of the four sampled regions, so when considering only the four local occurrence probabilities P_{left}, P_{right}, P_{middle}, and P_{top}, they do not have to add up to 1.

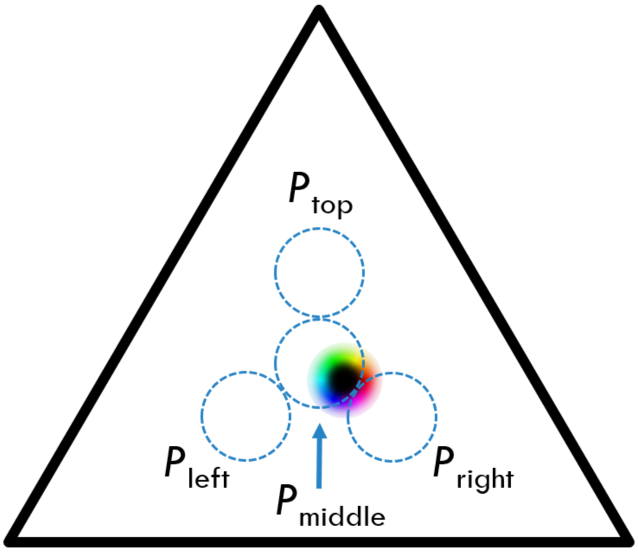

Figure 6.4: Schematic of the emulated MTJ read-out using four circular regions (dashed blue circles). The local occurrence probabilities P_{left}, P_{right}, P_{middle}, and P_{top} serve as the input for the linear read-out and are determined based on the skyrmion position in each Kerr video frame. A colored ring with a black center represents the skyrmion. Note that the width of the domain wall (colored ring) is exaggerated in this schematic, and the experimental skyrmion profile is expected to exhibit a large core and a very narrow domain wall similar to Fig. 3.11a. Using center-based read-out, this skyrmion position only counts as an occurrence of the middle region. In contrast, using overlap-based read-out, it contributes to both P_{middle} and P_{right} with a larger contribution to P_{middle} due to the higher areal overlap with the middle region.

The choice of read-out emulation is particularly relevant for situations as illustrated in Fig. 6.4, where the skyrmion overlaps with two of the read-out regions that mimic MTJs. The center-based read-out discussed so far contributes only to P_{middle}, while the average tunnel magnetoresistance would also be affected within the right region. To address this effect, the training procedure performed in this section and the interpretation of the trained weights in the next section are repeated in appendix section A.5.2 for overlap-based read-out modeling. “Overlap-based read-out modeling” means that fractional occurrences are counted for each frame, depending on the relative overlap between the skyrmion and each region. Thus, the skyrmion can contribute to the local occurrence probabilities of multiple regions, and the contribution is scaled based on the areal overlap of the skyrmion and the region. The results of both methods are compared at the end of this section, with further details provided in appendix section A.5.2.

The local occurrence probabilities of the four regions measure the system’s response for a given input configuration. The output Q of the entire reservoir computer is then determined by the linear read-out function

$$Q = W_{\text{left}}\, P_{\text{left}} + W_{\text{right}}\, P_{\text{right}} + W_{\text{top}}\, P_{\text{top}} + W_{\text{middle}}\, P_{\text{middle}} + W_{\text{intercept}} \tag{6.1}$$

where W_{region} is the weight of the probability P_{region} and $W_{\text{intercept}}$ is an offset. The continuous output Q can then be converted to a binary output based on a threshold value, i.e., mapping all values below the threshold to “0” and above to “1”. The weights are different for each Boolean operation and must be optimized based on labelled training data. Notably, the reservoir itself must not be trained or adjusted for all operations discussed in this chapter. Thereby, the entire training of the reservoir computer reduces to optimizing the above function’s weights. This is done using linear regression via the Scikit-learn python package [158], based on some sets of the four local occurrence probabilities for each input combination. Specifically, the skyrmion is imaged and tracked for a total of 13,000 frames at 16 frames per second for each input combination. This data is then converted into 13 distinct operations of the reservoir computer by determining the local occurrence probabilities for the four regions with a sampling duration of 62.5 s. There are some crucial points to address, considering that the sampling duration sets the time required for a single operation. First, performing a single logic operation in 62.5 s is, of course, not meant to compete with state-of-the-art conventional computing devices with respect to speed or energy consumption. This chapter revolves around successfully demonstrating skyrmion-based Brownian reservoir computing using a minimal proof-of-concept device that facilitates understanding of the relation between the system’s behavior and the computer’s operation. We employ a micrometer-scale device as it provides good access to the system’s time-resolved behavior via Kerr microscopy. The sampling durations required for reliable operation are expected to be much shorter for scaled-down nanometer-sized systems. Moreover, favorable application scenarios for Brownian reservoir computing will likely not be logic operations but more complex classification tasks that are more challenging for conventional computer architectures. Section 6.5 provides an outlook on the use of a similar device for classifying hand gestures [32].

For each input combination, only the first 4 of the 13 sets of local occurrence probabilities are employed to optimize the weights, and the remaining 9 sets are used for testing[3]. The values of the optimized weights for each operation are given in the next section in table 6.1 where they are interpreted in the context of the system's biased effective energy landscapes. Figure 6.5 shows the output of the linear read-out and thus of the entire Brownian reservoir computer, trained for the Boolean operations AND, NAND, OR, NOR, XOR, and XNOR. For each operation and each input combination, the outputs of 13 operations are shown. These correspond to the 13 sets of local occurrence probabilities discussed above. Since the reservoir must not be trained, the same experimental data can be used to demonstrate all six logic operations. The sets used for training and testing are plotted as blue and black curves, respectively. The dashed lines indicate exemplary choices for threshold values for mapping the continuous outputs to binary outputs. Here, they are chosen to be in the middle of the highest value, which should be 0, and the lowest value, which should be 1.

Before discussing the results, it is helpful to briefly review the full operation of our Brownian reservoir computer: The input combinations [A B] $\in$ {[0 0], [0 1], [1 0], [1 1]} are encoded as voltages at the bottom left (A) and right (B) contact of the reservoir, with a “0” bit encoded as ground and a “1” bit encoded as constant positive voltage, and the top contact kept at ground (Fig. 6.1b). For a given input, the reservoir's response to the resulting spatially inhomogeneous current-induced force in competition with pinning effects and boundary repulsion is measured. This is done by estimating the local occurrence probability of the four regions indicated in Fig. 6.4 based on the trajectory of the thermally diffusing skyrmion during a fixed sampling time. These four values serve as the inputs of Eqn. (6.1), the output of which is shown in Fig. 6.5. The weights of Eqn. (6.1) have been trained for each of the logic operations, while the reservoir is always the same.

We observe values close to the correct output for all two-input Boolean logic operations and good separation even on the test set. Particularly noteworthy is the successful demonstration of the not linearly separable XOR functionality. This shows that our minimal proof-of-concept reservoir is already sufficiently complex to perform non-linearly separable tasks. Such tasks are impossible for a conventional single-layer feed-forward perceptron, demonstrating that the reservoir performs complex computational work. Moreover, we demonstrate NAND and NOR, each representing a functionally complete set of logical connectives.

---

[3] We verified that using the 4 sets chronologically measured first does not constitute an outlier in the sense that the device performs much better using these 4 sets for training than random 4 sets. The performance of the Brownian reservoir computer depends on the number of sets used for training, the sampling duration assigned to one operation, as well as the positions, arrangement, and size of the read-out regions. While the impact of the sampling duration is outlined and exemplarily studied using half the measurement duration in section 6.4, an exhaustive study of these parameters is beyond the scope and purpose of this chapter. The parameters are chosen for the purpose of demonstrating and understanding the device operation and not to optimize the device's overall performance with respect to any specific metric.

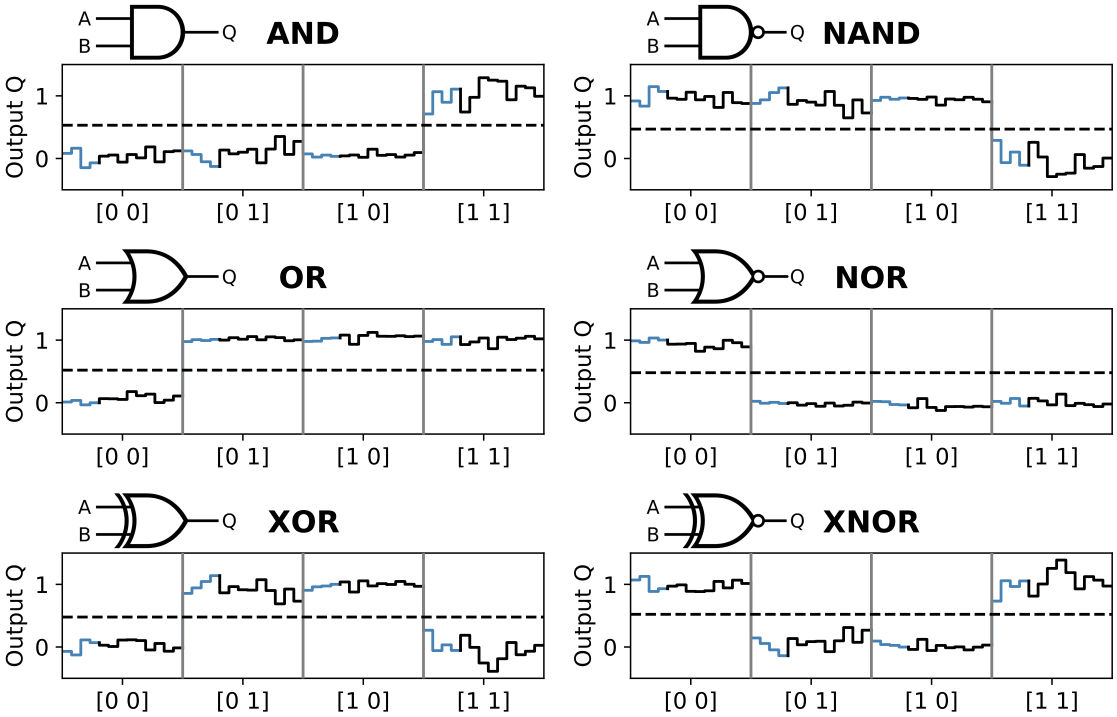

Figure 6.5: Outputs of the linear read-out and thus of the entire Brownian reservoir computer, optimized for different Boolean logic operations. The output Q of the linear read-out (Eqn. (6.1)) for each input [A B] $\in$ {[0 0], [0 1], [1 0], [1 1]} is shown for 13 sets of local skyrmion occurrence probabilities (13 operations of the reservoir computer). Grey vertical lines separate the different inputs. The 4 blue and 9 black sections of the curves indicate the sets used for training and testing, respectively. The dashed horizontal line indicates a possible threshold to map the continuous outputs of the linear read-out to binary outputs. This figure is taken from our publication Ref. [31].

To quantify the performance of the reservoir computer and compare it among different modifications made in the remainder of the chapter, we consider the signal-to-noise ratio (SNR) defined as

$$\mathrm{SNR} := \frac{\langle \mathrm{T} \rangle - \langle \mathrm{F} \rangle}{\sigma_{\mathrm{T}} + \sigma_{\mathrm{F}}}, \tag{6.2}$$

where T and F are the sub-sets of linear read-out outputs Q, for which the corresponding Boolean operation should output True or False, respectively. Angled brackets indicate the mean value of the obtained outputs and $\sigma_{\mathrm{T}}(\sigma_{\mathrm{F}})$ is the standard deviation of the T(F) subset. The data shown in Fig. 6.5 exhibits SNR > 5, averaged over the six logic operations. When using overlap-based read-out instead of center-based read-out, the values do not change significantly (5.49 and 5.55, respectively) even though the optimal weights change. The full results and interpretation for the overlap-based read-out are given in appendix section A.5.2. The SNR predominantly depends on how well distinguishable the responses to the different input combinations are. Since both read-out methods provide good distinguishability, a comparable SNR seems plausible. The optimal weights depend

Operation	W_{left}	W_{right}	W_{top}	W_{middle}	$W_{\text{intercept}}$
AND	1.124	7.497	0.623	1.022	-0.797
NAND	-1.124	-7.497	-0.623	-1.022	1.797
OR	0.272	1.090	-1.403	-2.908	0.942
NOR	-0.272	-1.090	1.403	2.908	0.058
XOR	-0.852	-6.407	-2.027	-3.930	1.739
XNOR	0.852	6.407	2.027	3.930	-0.739

Table 6.1: Optimized weights for the linear read-out (Eqn. (6.1)) corresponding to Fig. 6.5. The weights exhibit the expected sign reversal for the negated operations. However, contrary to the expectation for an ideal device, the weights for the left and right regions are not identical. This table is adapted from the supplementary material of our publication Ref. [31].

on the reservoir's response and on how the response is reflected in the local occurrence probabilities. The next section is dedicated to understanding the trained weights in the context of the system's underlying behavior.

6.3 Interpretation of the Trained Weights

This section aims to understand the optimal weights (table 6.1) for the linear read-out by considering not only the explicitly designed operating principles but also device imperfections such as pinning effects and resistance asymmetries. Dealing with such imperfections that are hard or often even impossible to avoid is essential for designing devices that are not limited to ideal simulation conditions but also work in real experimental environments. Pinning effects in particular may likely be an essential reason why experimental realizations of skyrmion-based reservoir computing remained elusive despite promising theoretical device concepts [25, 26]. We exploit the good access to the time-resolved state of the system during operation, which allows us to go beyond the local occurrence probabilities necessary for the device's operation and take into account the details of the pinning effects present in the system. This section focuses on identifying the challenges related to device imperfections and how they are accounted for in the optimized weights, while the next section establishes thermal activity as the key component that allows for sufficiently mitigating the effects of pinning and enables reliable operation. The optimized weights corresponding to Fig.6.5 are given in table 6.1. As one would expect, the weights for the negated operations (NAND, NOR, and XNOR) are directly related to the weights of their counterparts because negation only switches every "0" output to a "1" output and vice versa. Thus, the weights of these operations are the negatives of the corresponding weights of their operation counterparts, except for the intercepts, which differ by 1. One would also expect the weights for the left and right regions to be identical since the Boolean operations are invariant under an input permutation [A B] to [B A] and since the read-out regions are placed symmetrically around the vertical mirror axis of the triangle. However, this is not the case at all in our device. For all operations, the weights for the right region are multiple times higher than those for the left region. Conversely, the local occurrence probabilities in Fig. 6.6 are significantly higher in the left region at voltage combination

"+0" (left contact positive, right contact ground) than in the right region at "0+". We experimentally identify asymmetries in the resistances between the contacts as the one reason for this. However, pinning effects also contribute to this effect as discussed in the following.

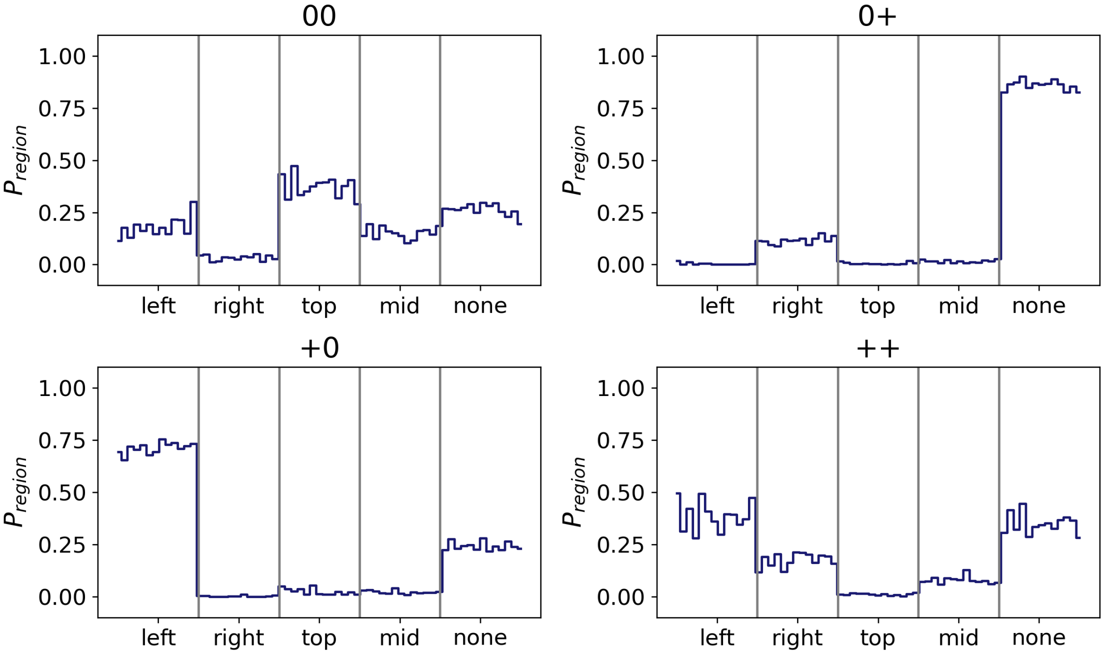

Figure 6.6: Local occurrence probabilities in each region for the different voltage combinations. The probability for the skyrmion to be found in none of the four circular regions indicated in Fig. 6.4 is shown in the "none"-sector of the plots. The labels above each panel correspond to the applied voltage combination, i.e. "+0" corresponds to a constant positive voltage at the bottom left contact and ground at the bottom right contact. Each curve segment for each region corresponds to one of the 13 sets of local skyrmion occurrence probabilities. The values are sorted such that, for instance, the first value in each sector corresponds to the same set, and the probabilities add up to 1. This figure is taken from the supplementary material of our publication Ref. [31].

The spatially resolved skyrmion occurrence distributions for all voltage combinations in Fig. 6.7 reveal a rather strong pinning site just outside the right region (see panel (b)). Because of this pinning site, the probability of finding the skyrmion in none of the regions is much higher for "0+" than for "+0" as seen in Fig. 6.6. This effect also acts to reduce the probability of being in the right region in the for "0+" compared to being in the left region for "+0" in addition to the resistance asymmetry discussed before. When using overlap-based read-out modeling, this effect is much less pronounced since a skyrmion with its center pinned just outside the right region still contributes a significant fractional count to that region, as shown in appendix Fig. A.11b. Independent of the read-out modeling, the device imperfections are automatically adjusted for in the weight optimization. Therefore, as long as the imperfections are not too severe, they do not hinder the device's functionality. Note that this is only true in the presence of thermal random motion, as elaborated in the next section. An important consequence of the above discussion is that the optimal weights are different for different experimental devices. Even if they have nominally identical geometries and material compositions, the devices exhibit pinning and resistance inhomogeneities. Training the weights automatically overcomes reproducibility issues due to variations between devices. The annihilation and renucleation of the skyrmion under equal conditions is not expected to affect the weights because the effective pinning energy landscape remains the same.

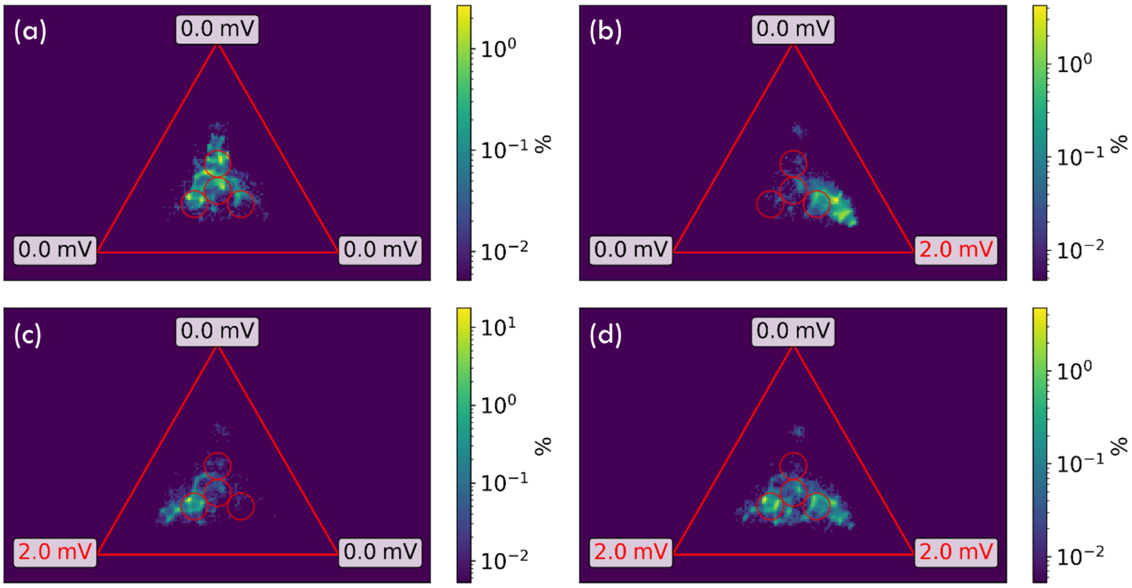

Figure 6.7: Experimental skyrmion occurrence heat maps at different voltage combinations. The applied voltages are shown at the corners of the triangle. At no applied voltages (a), the occurrence distribution is determined predominantly by pinning, and the boundary repulsion prevents the skyrmion from getting close to the edges of the triangle. For non-zero voltages, the spatially inhomogeneous current-induced forces bias the occurrence distribution. However, strong pinning sites can still be identified across different voltage combinations. Red circles indicate the employed read-out regions. This figure is taken from the supplementary material of our publication Ref. [31].

Considerations similar to the points discussed above also allow us to understand differences in the noise of the individual operations. For instance, the OR operation evidently exhibits lower noise in Fig. 6.5 than the other two operations because only the [0 0] input is mapped to the “0”-output, and this is the only combination that exhibits significant occurrence in the top region (Fig. 6.6 and 6.7). Separating this input from the others is significantly easier and, therefore, the output exhibits reduced noise.

6.4 The Role of Thermal Diffusion

The previous section revealed that device imperfections, such as pinning effects, cause behavior drastically different from the expectation for an ideal device. This section addresses the role of thermal diffusion for the device's functionality, or, phrased differently, what makes this reservoir computer a Brownian reservoir computer. The core of the Brownian computing paradigm is to leverage (usually thermal) random motion for the benefit of a specific computer architecture [28–30, 51, 52]. This statement is phrased in a very general manner, as the role of thermal randomness can be very diverse in different computer architectures. For instance, in Brownian token-based computing, it acts as a random propulsion mechanism for signal carriers to explore computational networks [29, 51, 52] as outlined in section 5.4.

To understand the role of thermal activity in our device, we compare its behavior to an otherwise identical setup in which the skyrmion does not perform thermal diffusion. In this system, the quantity manipulated and measured for operation would be the skyrmion position at a specific time instead of the time-averaged skyrmion distribution. Without non-deterministic effects, there is no need to average the system's response. Fig. 6.8 schematically compares the response to the "++" voltage combination for the cases without and with thermal diffusion. Therefore, a deterministically moving skyrmion with an initial position (blue cross in Fig. 6.8a) on the vertical symmetry axis of the confinement (dashed line) will only experience a force acting straight down. In response, the skyrmion moves to the bottom center of the device. This is because the horizontal current-induced forces cancel on the vertical symmetry axis. However, suppose the initial position is not on the vertical symmetry axis (green cross in Fig. 6.8a), for instance, because of pinning effects. In that case, the skyrmion will end up in one of the corners, where the current-induced force is strongest. This is problematic because the response is very hard to distinguish from the response to the "0+" voltage configuration, for which the skyrmion will also end up in the bottom right corner. Moreover, in the presence of pinning, the position the skyrmion returns to after the current is turned off will likely depend on the previous input, since the skyrmion will be pinned at the first position where pinning forces are stronger than the boundary repulsion. Consequently, such effects can violate the condition of reproducible responses. In the case of a diffusing skyrmion, the initial position is randomly distributed, with favorable positions (schematically illustrated as the blue smeared-out triangular region in Fig. 6.8b) determined by the boundary repulsion. However, we measure the time-averaged distribution at active current, not the skyrmion position. The skyrmion will explore the system through thermal diffusion, independent of the initial position before the current was turned on. Given a sufficiently long sampling duration, the average skyrmion distribution at a certain temperature (illustrated as the green elliptical region) is independent of the initial position and determined only by the competition of current-induced forces, boundary repulsion, and pinning. While pinning does drastically affect the exact features of the distribution as seen in Fig. 6.7, the key requirement for reliable operation is only that the distributions are well distinguishable for all input configurations, which is the case for our system (Fig. 6.7). Thus, thermal skyrmion diffusion serves to overcome the obstacles related to pinning effects and the dependence of the system's response on the initial skyrmion position.

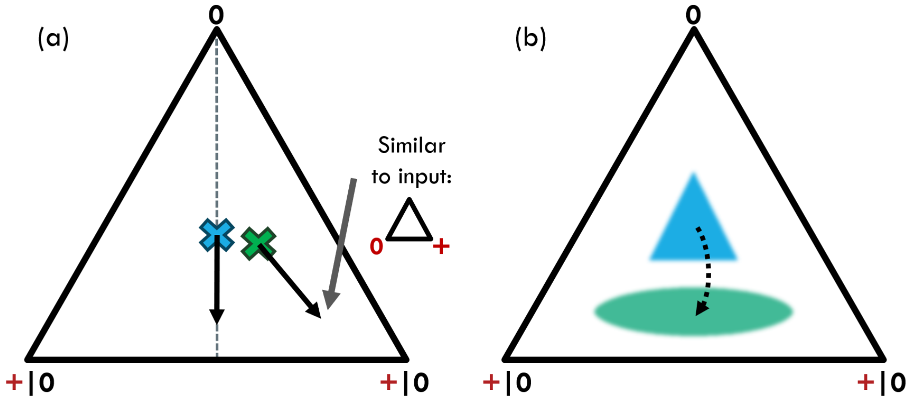

Figure 6.8: Schematic illustration of the reservoir's response to the voltage configuration "++", i.e., a constant positive voltage at both bottom contacts, without (a) and with (b) thermal skyrmion diffusion. At the bottom corners the chosen one of the two voltage options "+" and "0" is highlighted in red. (a) For an initial position on the vertical mirror axis of the triangle (dashed line) indicated by the blue cross, the current induced force (black arrow) acts straight down. In contrast, for an initial position that is offset from the mirror axis, for instance, because of pinning, the current induced force drives the skyrmion into the corner, where its final position is difficult to distinguish from the "0+" input. (b) The initial positions of a skyrmion performing thermal diffusion are randomly distributed, with the details of the distribution determined by the boundary repulsion (and pinning). The blue faded-out triangular region schematically illustrates the distribution. In response to the applied voltages, the skyrmion distribution in the system changes. The resulting distribution (green elliptical region) is independent of the skyrmion's initial position and dependent only on the competition of current-induced force and boundary repulsion (and pinning). The experimental distributions are shown in Fig. 6.7.

An essential consequence of using the skyrmion distribution for the read-out, instead of the skyrmion position, is that the device's performance depends on the duration over which the distribution is sampled. For an infinite sampling duration, the distribution is expected to be completely determined by the competition of forces in the system. Lower sampling durations introduce noise to the estimated skyrmion distribution, making it more difficult to distinguish the reservoir's responses. As an example, Fig. 6.9 shows the equivalent results to Fig. 6.5, but with only half the sampling time used to estimate the local skyrmion occurrence probabilities. The number of training and testing sets is the same. While the reservoir computer still performs well, Fig. 6.9 exhibits a visibly lower signal-to-noise ratio with SNR ≈ 4 compared to SNR > 5 before. While an extensive analysis of the relation between sampling duration and device performance is beyond the scope of this thesis, it is important to discuss the general consequences for applications.

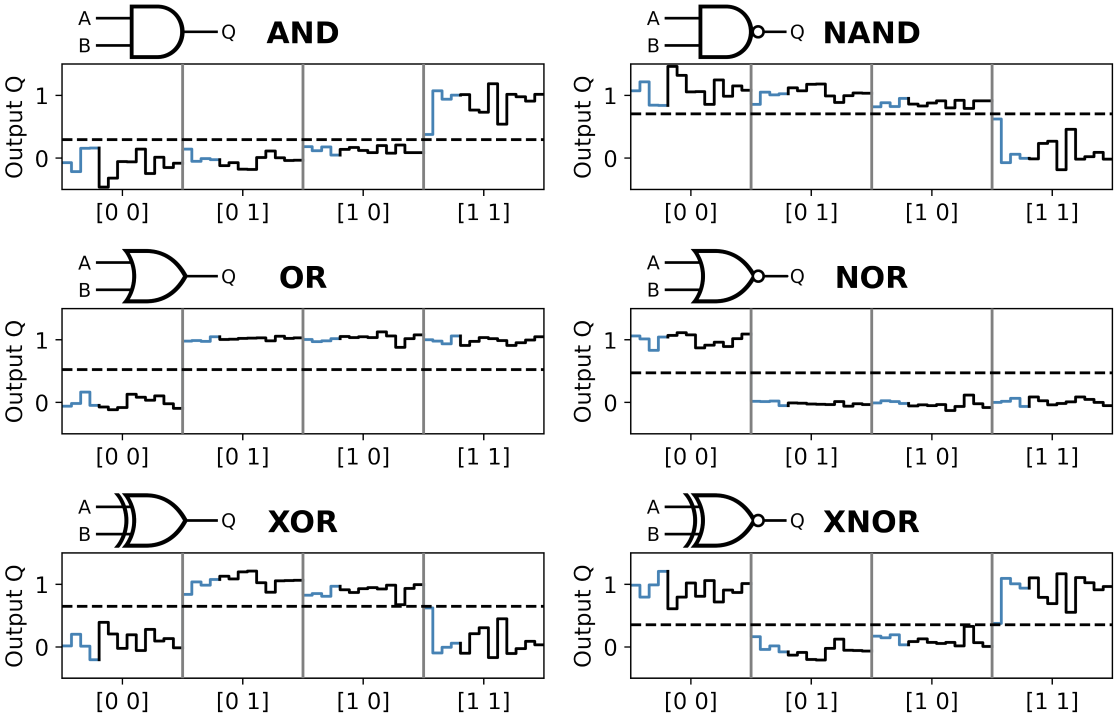

Figure 6.9: Outputs of the linear read-out optimized for different Boolean logic operations. Compared to Fig. 6.5, the sampling duration is halved from 1000 frames to 500 frames, and the output values exhibit a lower signal-to-noise ratio. We still consider 13 device operations, with the first 4 used for training. The dashed thresholds for the mapping to binary values are chosen to be in the middle of the highest output that should be “0” and the lowest value that should be “1”. The right half of the figure shows the corresponding negated operations to the left half. This figure is taken from the supplementary material of our publication Ref. [31].

Reducing the sampling duration allows for a trade-off between device performance and computation speed. The sampling time is the predominant contribution to the required time per operation, but reducing it also reduces the signal-to-noise ratio. Consequently, the same device design can be used for both very reliable but computationally expensive operations, as well as quick but crude estimated results. One can switch between these modes and tune their respective performance by adjusting the sampling duration on the fly. Beyond that, the skyrmion diffusion coefficient plays an important role as well. For low diffusion coefficients, the skyrmion will spend much time in the dominant pinning sites instead of sampling the characteristic features of the effective energy landscape arising due to the competition of interactions. For these reasons, diffusion enhancement mechanisms, such as the one discussed in the previous chapter, can be used to speed up the sampling at the expense of additional energy. Thereby, one can adjust a Brownian reservoir computer’s computation speed and energy efficiency. This general concept to tune the speed-efficiency balance of Brownian computers, as well as the option to use diffusion enhancement on the fly to match circumstance-dependent needs, is the subject of our international patent[4] Ref. [30]. Beyond that, combining this idea with the tunability of the speed-performance-balance via the sampling duration, we could adjust computation speed, energy efficiency, and performance to match the needs of a given application. The resulting versatility and adaptability may make Brownian reservoir computing devices favorable for a broad range of application scenarios. However, it is crucial to keep in mind that this chapter discusses a proof-of-concept device for research purposes, which is far from any kind of industrial product. While the aforementioned properties of Brownian reservoir computing can be valuable in such a context, significant further research is required, in particular to verify that scaled-down nano-scale devices still exhibit the necessary properties for reliable operation.

Beyond their use as an acceleration tool, diffusion enhancement mechanisms are also valuable for tuning the time-scale of the reservoir's dynamics for applications where the manipulation applied to the system is time-dependent. This could save significant preprocessing work otherwise required to match the time-scale of the input-encoding manipulation and the reservoir. The second part of the next section provides an outlook on a skyrmion-based reservoir computer using time-dependent inputs [32].

6.5 Outlook on 3-Input Operations and Time-Dependent Inputs

This section provides an outlook on two extension paths that employ the same fundamental device design presented in this chapter but change the input and read-out mechanisms. The first path uses the device's top contact as a third variable input, thereby allowing the device to perform 3-input operations. The second path employs a time-dependent input signal and measures the time-resolved response of the reservoir [32].

Fig. 6.10 shows exemplary 3-input logic operation using our Brownian reservoir computing device, employing the same sampling duration and amounts of training and test data as in Fig. 6.5. Here, the top contact is used as a third variable input labeled "C". Compared to the two-input case, the average signal-to-noise ratio is reduced, but we still observe good separation and SNR > 3 for these operations. However, we do not expect our device to perform well on any 3-input operation. Most importantly, the voltage combinations "000" and "+++" are identical by design. Therefore, we can fundamentally only perform operations that provide the same output for these input combinations. Moreover, the local skyrmion occurrence probabilities[5] in Fig. 6.11 are well-distinguishable for most voltage configurations, but rather similar for "++0" and "+++". We attribute this effect to the resistance asymmetry and pinning effects discussed in section 6.3, as "0++" is well distinguishable. A possible way to address this obstacle would be to use a different

---

[4] The patent explicitly discusses the present Brownian reservoir computing device starting on page 20, line 3 in Ref. [30]. Note that the patent was initially developed as a part of my master's thesis, but that these statements on the device design introduced in this chapter were added as a part of my PhD.

[5] Note that these probabilities are not directly comparable to the 2-input case because we employ the overlap-based read-out method and a different placement of the read-out regions.

constant voltage at each contact to even out the magnitude of the current-induced force. The good performance in Fig. 6.10 is likely because all operations in Fig. 6.10 map these hard-to-distinguish combinations to the same output. So, while this outlook demonstrates 3-input operations, further research is required to gauge this operating mode's general applicability and robustness.

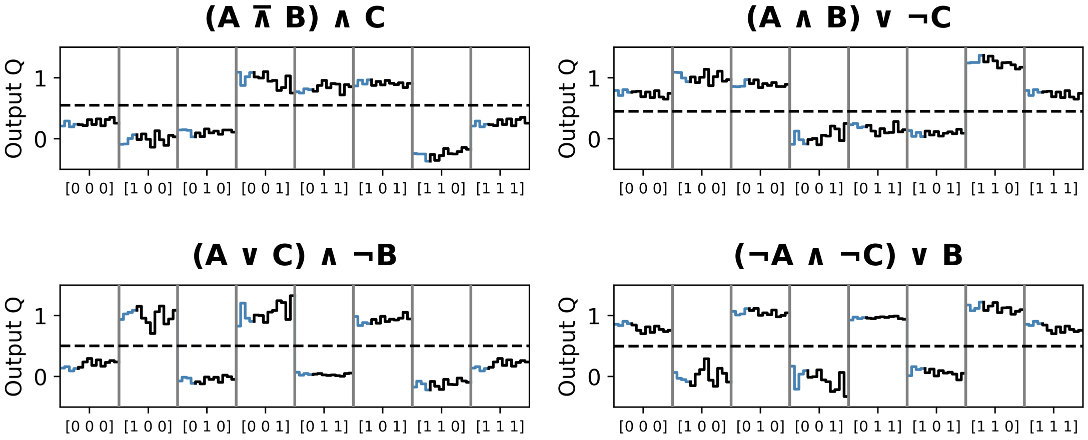

Figure 6.10: Outputs of the linear read-out optimized for exemplary 3-input operations. Similar to Fig. 6.5, the output Q is shown for each input combination [A B C] for 13 sets of local skyrmion occurrence probability. The blue and black segments of the curves indicate training and test data, respectively, and the dashed horizontal line indicates a possible threshold value for mapping the output to binary values. This figure is taken from the supplementary material of our publication Ref. [31].

The second use case for reservoir computing employing a time-dependent input signal, entails a significant deviation from the operating principles discussed so far. Therefore, the remainder of this section only provides a brief outline of this use case based on the task of hand gesture recognition. A complete realization of a skyrmion-based reservoir computing device trained for this purpose is demonstrated in our publication Ref. [32]. The hand gestures considered here are hand motions performed in the air, specifically pushing the hand forward, moving it to the left, and moving it to the right. The basis for the classification task is time-resolved radar data of multiple persons performing these gestures. The data was provided by Infineon Technologies, with which we collaborated for this project. The radar data is Fourier-transformed and reduced to one dimensional time-dependent input data[6]. As illustrated in Fig. 6.12, this input data is encoded as a time-dependent voltage applied between the two bottom contacts. The skyrmion's trajectory is determined by the competition of the spatially inhomogeneous current-induced force, boundary repulsion, pinning effects, and thermal random force. As before, the boundary repulsion acts as an automatic reset mechanism after the operation, and thermal diffusion reduces the impact of pinning effects. Therein, the diffusion is tuned using the mechanism explored in the previous chapter. Unlike for the last device design, the average skyrmion

---

[6] Details of the data processing and experimental setup are purposefully omitted since the focus of this outline is on the operating principles of the reservoir computing device. The full details are given in Ref. [32].

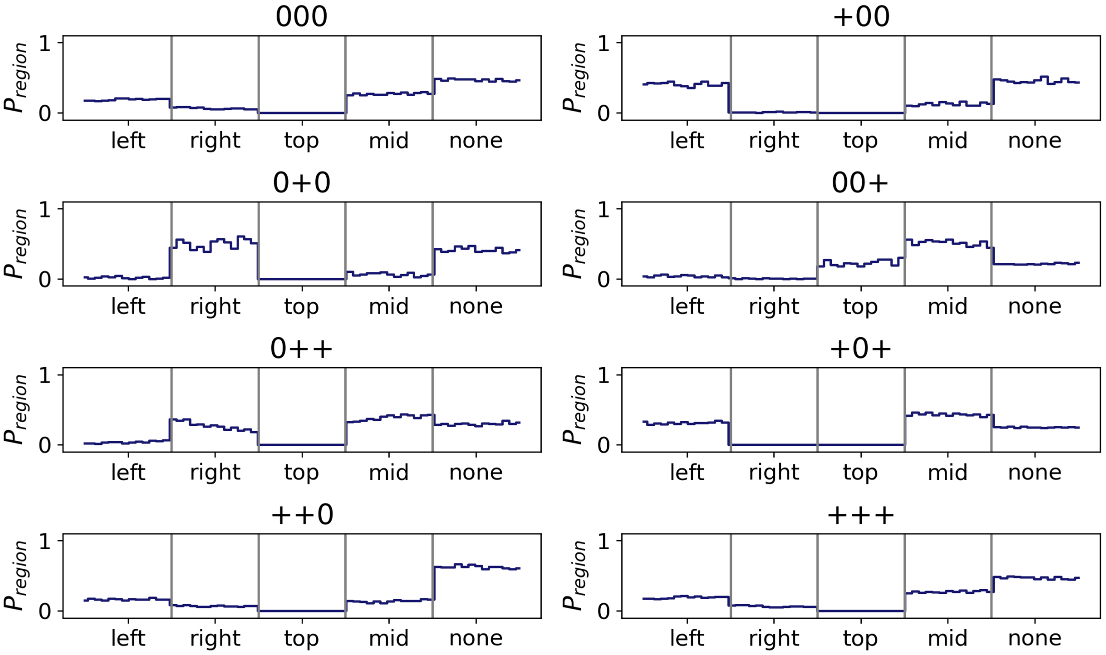

Figure 6.11: Occurrence probabilities in the four read-out regions for all 3-input voltage combinations (“000” and “+++” are the same measurement). Each value for each region corresponds to one of the 13 sets of local skyrmion occurrence probabilities.

distribution is not a good measure for the system’s response due to the time-dependent input. Instead, we employ the time-resolved occurrence of the skyrmion in one or multiple regions of the sample. So, we again emulate the read-out of an MTJ, but in a time-resolved fashion. Then, a linear support vector machine is trained to classify the input data as different hand gestures based on the time-dependent local skyrmion occurrence. While the reservoir’s response is non-deterministic due to the thermal diffusion, it is sufficiently reproducible for reliable operation. We found that employing five read-out regions can surpass state-of-the-art software-based classification methods (explicitly compared for a radial basis function support vector machine) at lower evaluated energy consumption.

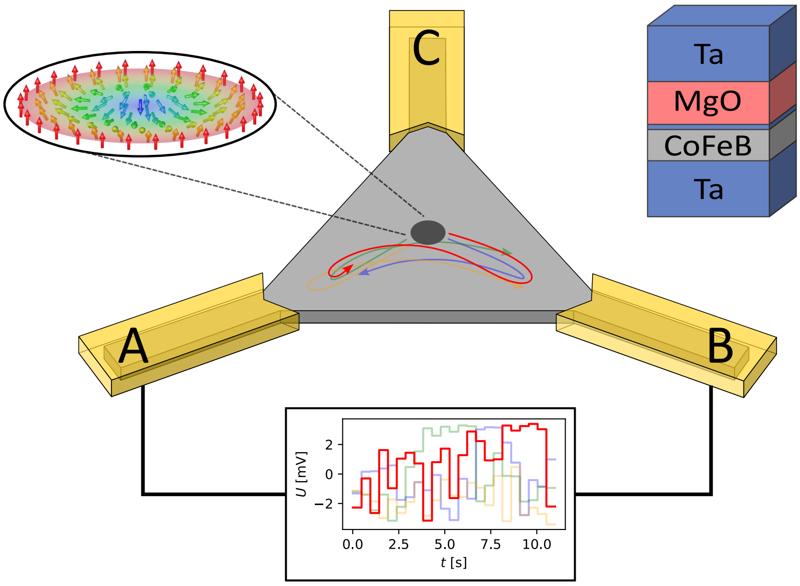

Figure 6.12: Schematic representation of the device's operation using time-dependent inputs. The two bottom contacts (transparent yellow) are connected to a time-dependent voltage that encodes the input. The top contact is isolated (floating). The inset shows four examples of input signals in different colors, one for each gesture type (push, swipe left, swipe right, no gesture). The skyrmion (dark dot) responds to the resulting time-dependent current-induced force, which competes with the other interactions in the system. Colored arrows schematically illustrate possible skyrmion trajectories. The composition of the material stack (grey) hosting the skyrmion is shown in the top right. This figure is taken from our publication Ref. [32].

7. Conclusion and Outlook

In this thesis, we have analyzed the dynamics of magnetic skyrmions to realize quantitative quasi-particle simulations, which are key for quantitative predictions on previously unattainable, experimentally relevant, large time and length scales. Consequently, such simulations are also essential for the in-silico development and optimization of skyrmion-based devices. Central to this thesis has been a top-down approach to the modeling of skyrmion dynamics, which does not rely on any assumptions about the skyrmions' typically experimentally inaccessible internal structure or the underlying magnetic interactions. This approach was pursued in close experimental collaboration, ascertaining the key modeling parameters and essential features of skyrmion behavior directly from experimental observables in the quasi-particle picture. Pinning effects, the interaction with local variations of the skyrmion-hosting material's magnetic properties, can drastically impact skyrmion dynamics [16, 111]. Therefore, they have been studied both within the quasi-particle framework and beyond. Quantitative quasi-particle simulations of skyrmions have previously been limited to predicting static effects only, as a reliable time scale conversion between simulation and experiment had been lacking. This conversion is set by the skyrmion damping coefficient. However, pinning effects break the simple relation between the experimental skyrmion diffusion coefficient and the damping, which would usually follow from the Einstein-Smoluchowski-relation [41, 89]. To overcome this challenge, a quasi-one-dimensional periodic system was designed, which enabled us to assign a high-resolution spatially resolved pinning energy landscape to the system. This was achieved via a potential of mean force approach based on the time-averaged skyrmion distribution [116, 117]. The developed procedure allowed us to isolate the effects of pinning from the intrinsic skyrmion damping and obtain the time scale conversion. A similar method was developed for determining the force on a skyrmion in response to current-induced spin-torques. Applying an external force on skyrmions via spin-torques induced by an electrical current is essential for many skyrmion-based device concepts [9, 23–32]. Our method determines the current-induced force based on the bias it inflicts upon the time-averaged skyrmion distribution. The latter translates to a linear bias in the potential of mean force, which can be isolated from the effects of pinning. This way, the method can resolve forces at current densities orders of magnitude smaller than the ones required for deterministic skyrmion motion [20]. Thereby, it also circumvents any effects of current-induced skyrmion deformation that occur at large current densities [20].

While the employed top-down quasi-particle model for skyrmion dynamics is, by design, in excellent agreement with the experiments, further insights could be gained by comparing the results to a bottom-up approach starting from the skyrmion's estimated internal structure [40], possibly in a simpler test system. Such a study could be used to investigate the effects of thermal fluctuations of the skyrmion structure, which are automatically incorporated via the presented method, but usually neglected in bottom-up approaches. Moreover, for the modeling of current-induced skyrmion motion at high current densities, current-induced skyrmion deformation and especially its effect on the skyrmion damping must be modeled. In addition, several further mechanisms to move skyrmions exist, for instance via temperature gradients [78] or magnetic field gradients [21], which still lack methods to ascertain quantitative quasi-particle descriptions directly from experiments.

We have also observed a strong dependence of pinning effects on the skyrmion size. Consequently, the pinning energy landscape is only accurate for a particular (thermally-averaged) skyrmion size. Changes in the skyrmion size must not only reflect in the pair- and boundary-interaction potentials but also in the description of pinning. By considering the estimated position of the skyrmion's enclosing domain wall, we concluded that pinning at the domain wall is the dominant pinning effect. Micromagnetic simulations were employed to demonstrate the link between these two observations in a minimal test system. A fundamental modeling of the relation between pinning and skyrmion size and shape would require explicitly modeling at least the domain wall, for instance, using a semi-flexible membrane-inspired model.

The size-dependence of pinning was, in addition, employed to develop a diffusion enhancement mechanism. We demonstrated that, by periodically changing the skyrmion size via an oscillating out-of-plane magnetic field, the skyrmion diffusion coefficient can be increased by over two orders of magnitude depending on the amplitude and frequency of the field oscillation. While we argue that this excitation acts to reduce the effective pinning experienced by the skyrmion, it is unclear if modeling the effect by a reduction of pinning alone suffices as an effective model for the diffusion enhancement effect. Such a pure pinning reduction model can fundamentally not capture an increase in the diffusion coefficient beyond the pinning-free value. Therefore, applying the developed method to ascertain the skyrmion damping, and consequently the pinning-free diffusion coefficient, to a system where enhanced diffusion is studied as well, is strongly recommended for future research. Additionally, the application of the diffusion enhancement mechanism holds great potential as a substitute for temperature-based diffusion enhancement. This is particularly valuable, as temperature also affects the skyrmion-hosting material's magnetic properties. Such a use of the method was outlined based on the example of the melting of skyrmion lattices at constant temperature [34]. From an application point of view, on-the-fly tunability of diffusion may be key for competitive realizations of Brownian computing, as discussed for token-based Brownian computing and Brownian reservoir computing.

In the final part of this thesis, we combined the Brownian computing [28, 51, 52] and reservoir computing [45–49] paradigms to develop a skyrmion-based Brownian reservoir computing device. Notably, our proof-of-concept device, consisting of a single thermally active confined skyrmion, already sufficed to realize all two-input Boolean logic operations. This includes the not linearly separable XOR, which is impossible for a conventional single-layer feed-forward perceptron. By analyzing the trained weights of the linear read-out layer and taking into account the time-averaged skyrmion distribution during operation, we have revealed that thermal skyrmion diffusion acts to mitigate the effects of pinning and electrical resistance inhomogeneity. These effects would likely render the device inoperable for a non-thermally-active system. The underlying operating principles of the presented device could be well understood, and the successful use of time-dependent inputs for hand-gesture recognition tasks was outlined. Despite these promising results, the development of a general optimal design procedure for Brownian reservoir computers is still an open research task. Moreover, our research on skyrmion-based Brownian reservoir computing was concluded before the above methods for realizing quantitative quasi-particle simulations were developed. Employing these methods for a systematic, in-silico screening and optimization of potential devices may drastically accelerate development processes and enable a deeper understanding of the devices' underlying operating principles.

Overall, this thesis establishes a foundation for quantitative computer-aided research on skyrmion dynamics, with particular relevance to shaping future applications in unconventional computing. These research fields remain rich with open questions, promising fertile ground for further discoveries.

Acknowledgments

Removed due to data privacy.

A. Appendix

A.1 Detailed Contributions

Since most of the work presented in this thesis was highly collaborative, this section clarifies my own contributions to the different projects and differentiates them from my (in particular experimental) collaborators' contributions. The beginning of each chapter presenting research results features a footnote containing a brief summary of the contributions that refers to one of the following sections for details. With the contributions clarified in this way, the thesis is predominantly written in passive voice or the using the pluralis modestiae for ease of reading.

As a theoretical physicist, my main contributions usually revolved around modeling, simulation, data analysis, interpretation, and conceptualization. While I contributed to experiments in the form of experiment conceptualization and simulation-aided experiment design, I did not perform any experiments in the laboratory or contribute to the fabrication of the samples. The joint publications on which each chapter is based are stated at the beginning of each chapter. In the following sections, I only list collaborators' contributions to our joint research projects that are necessary to differentiate my contributions to the results presented in this thesis from theirs. Therefore, I refer to our publications and my collaborators' theses for details on other contributions concerning, for instance, the details of the sample fabrication.

A.1.1 Contributions to Chapter 3

The detailed contributions were removed due to data privacy but are available from the author upon reasonable request.

A.1.2 Contributions to Chapter 4

The detailed contributions were removed due to data privacy but are available from the author upon reasonable request.

A.1.3 Contributions to Chapter 5

The detailed contributions were removed due to data privacy but are available from the author upon reasonable request.

A.1.4 Contributions to Chapter 6

The detailed contributions were removed due to data privacy but are available from the author upon reasonable request.

This page is intentionally left blank.

A.2 Additions to Chapter 3

A.2.1 Current density simulation details

This section provides further details of the COMSOL Multiphysics [73] simulations in Fig. 3.4 and Fig. 3.9. The aim of the simulations is only to qualitatively compare the relative current density at different positions in the systems. While the exact material and voltage parameters are not relevant for this purpose, the simulation details are provided for completeness.

Only the 5 nm bottom tantalum layer of the skyrmion hosting material and chrome layer of the contacts are simulated with respective electrical conductivities of 7.7×10^6 S/m and 7.9×10^6 S/m. The magnitude of the voltage applied to the outer edge of the contacts is set to 2 mV. Electrical conductivity is enabled between the contacts and structure that represents the skyrmion-hosting material. The simulations were performed using COMSOL's Electic Currents in Shells (ecis) module and the predefined ”Extremely fine” mesh was employed. The mesh structures for Fig. 3.4 and Fig. 3.9 are shown in Fig. A.1 and Fig. A.2, respectively. The systems are placed on non-interacting glass plates.

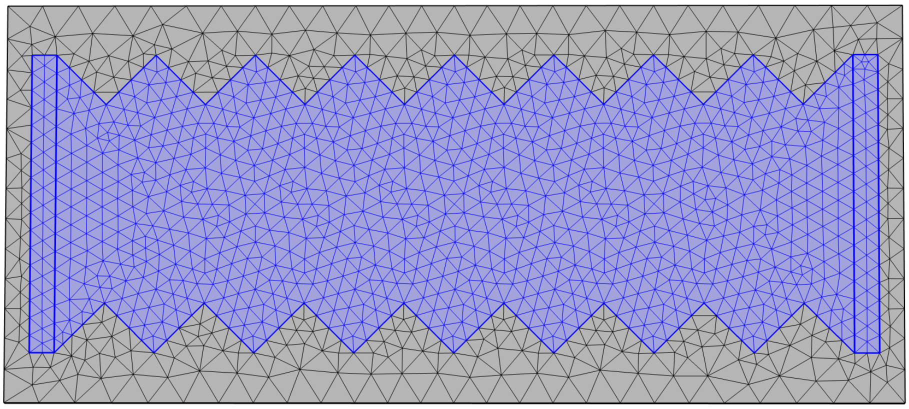

Figure A.1: Mesh employed in the COMSOL Multiphysics [73] simulation of the current density distribution in Fig. 3.4. The conductive region is marked in blue.

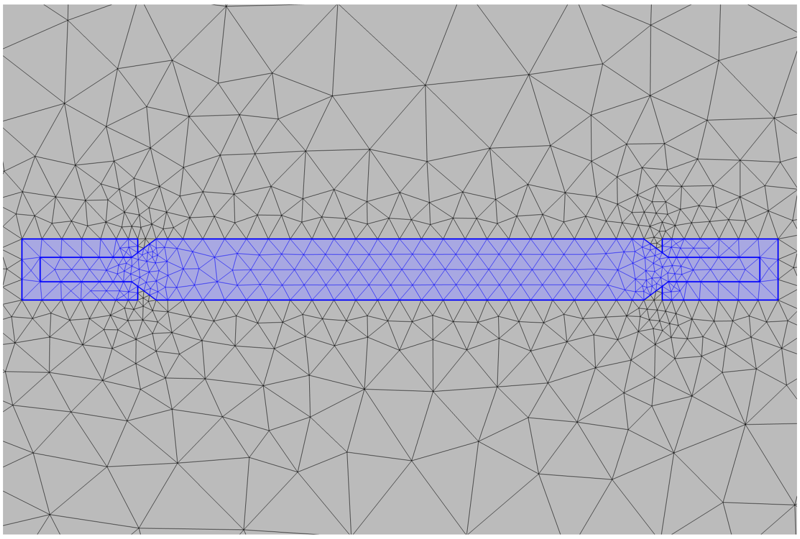

Figure A.2: Mesh employed in the COMSOL Multiphysics [73] simulation of the current density distribution in Fig. 3.9. The conductive region is marked in blue.

A.2.2 Discussion on the Numerical Integration of the LJ Equation

This section aims to coarsely estimate the uncertainty in the determination of via the numerical integration of the exponentials in the denominator of Eqn. (3.4) based on the RBFN fit of the energy landscape. Due to the limited statistics of the underlying skyrmion distribution, we apply the same procedure (potential of mean force, RBFN fit, numerical determination of the Lifson-Jackson functional using the RBFN fit) to random spatial skyrmion distributions generated based on the experimentally observed one. To generate these distributions, the counts in each histogram bin are sampled from a Poisson distribution with the original experimental distribution's value as its mean. The approach serves only as a coarse estimate as it treats all bins, including neighboring ones, as independent. This likely results in an increased local roughness of the resulting energy landscape compared to the experiment, which may lead to an overall lower value for $D^{\mathrm{pin}}/D^{\mathrm{free}}$. To reduce such effects, all RBFN fits use the same hyperparameters (basis function density and standard deviation) that were suitable for the RBFN fit of the original experimental energy landscape and its local roughness. Exemplary plots of the resulting energy landscapes and RBFN fits are shown in Figs. A.3b and A.3a,b alongside the original experimental energy landscape (Fig. A.3a) for comparison. Employing 10 of these random spatial skyrmion distributions, we obtain a standard deviation of 0.002 for $D^{\mathrm{pin}}/D^{\mathrm{free}}$. The mean value of 0.114 is slightly lower compared to the original experimental data.

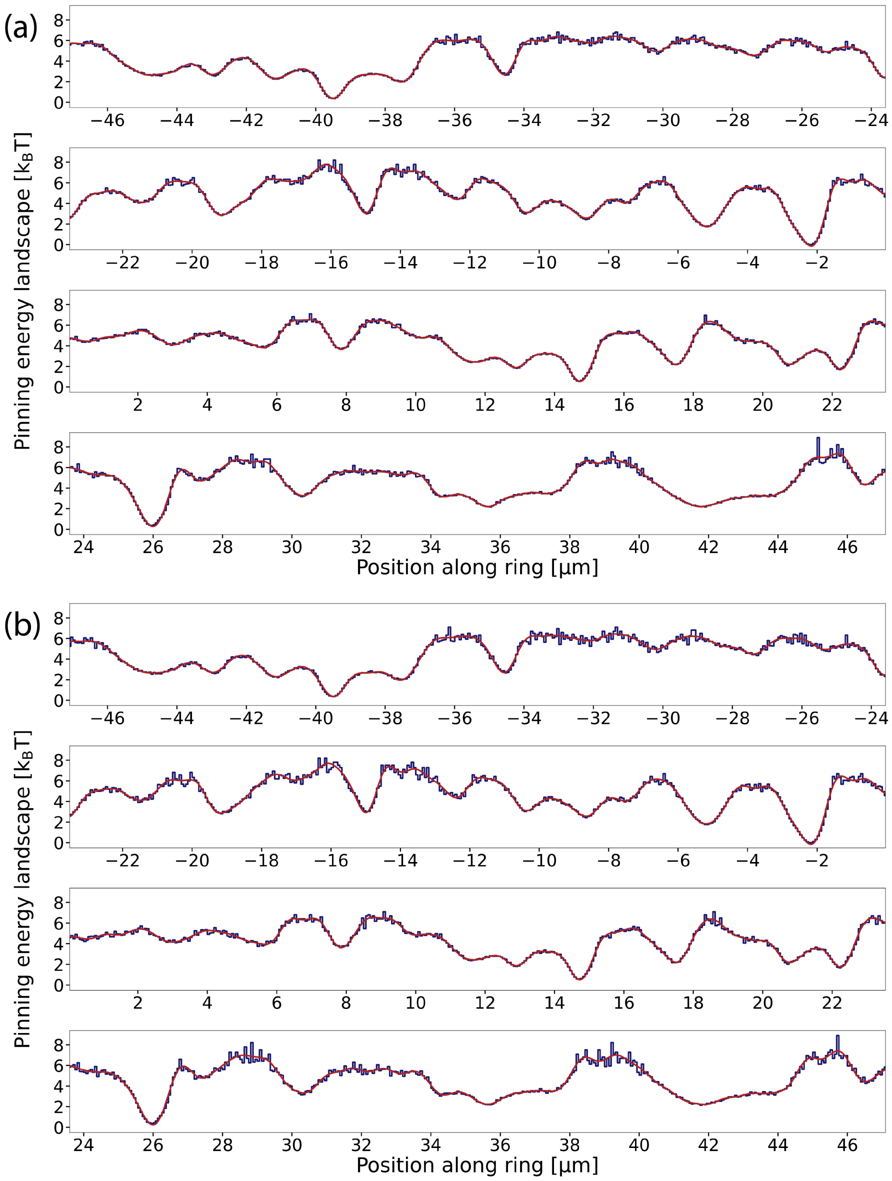

Figure A.3: (a) Original experimental energy landscape (blue) and RBFN fit (red) as in Fig. 3.5 for comparison. (b) First exemplary artificial energy landscape and RBFN fit.

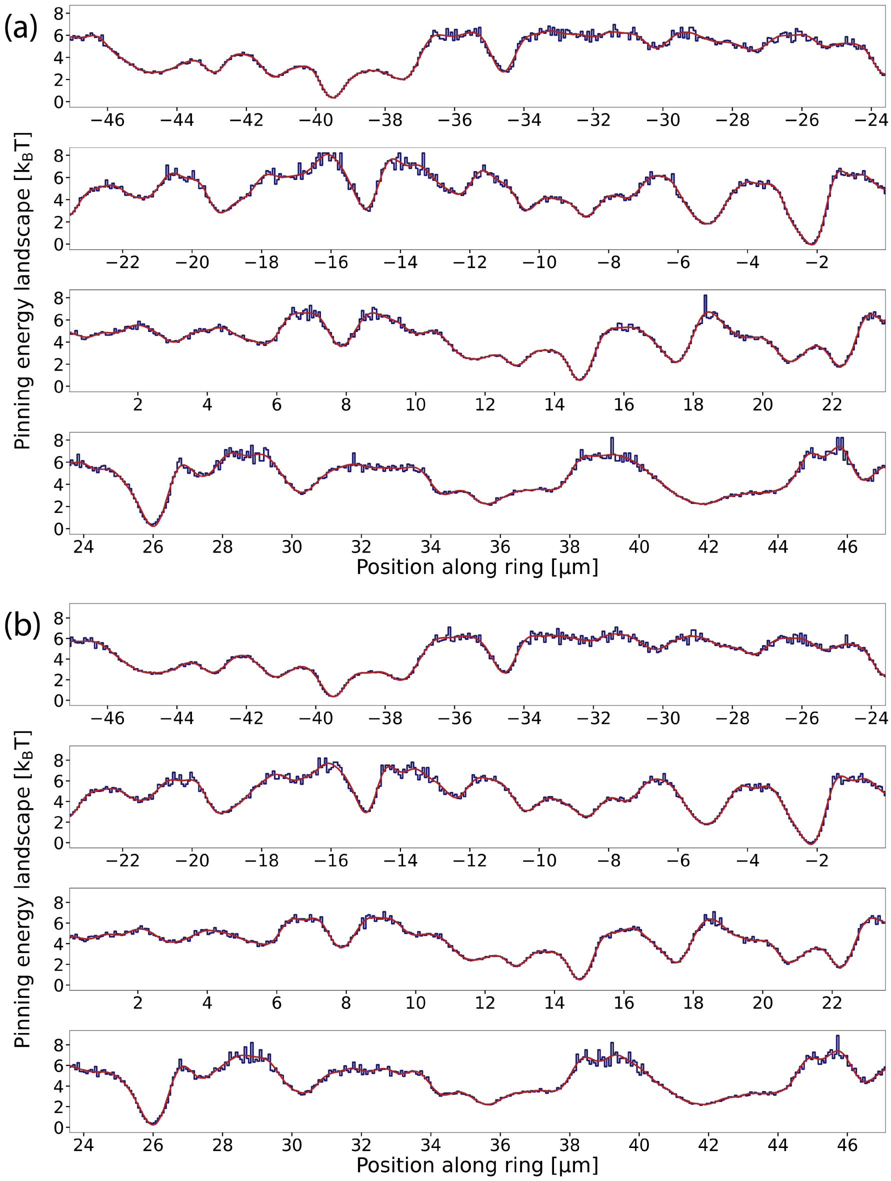

Figure A.4: Second (a) and third (b) exemplary artificial energy landscape (blue) and RBFN fit (red).

A.3 Additions to Chapter 4

A.3.1 Domain Walls of Pinned Skyrmions

To further support the claim in section 4.2 that the dominant contributions to pinning in our systems stem from pinning of the skyrmion domain wall, we study the measurement at an out-of-plane field of $-37\,\mu\mathrm{T}$ more rigorously (Fig. 4.1c but also shown here again). The skyrmion distribution exhibits two skyrmion center accumulation regions in close vicinity, labeled 1A and 1B in Fig. A.5b. The color-coded scatter plot of skyrmion occurrences in Fig. A.5c reveals a significant difference in the instantaneous size of skyrmions pinned at these positions. The estimated domain wall positions in Fig. A.5a for skyrmions with center coordinates at these regions show substantial overlap between the domain walls at the right side of the skyrmions. Here, the domain wall is estimated as explained in section 4.2. This behavior indicates that the dominant pinning effect actually occurs at the domain wall on the right side of the skyrmion and the difference in center position just arises as a consequence of the different skyrmion size.

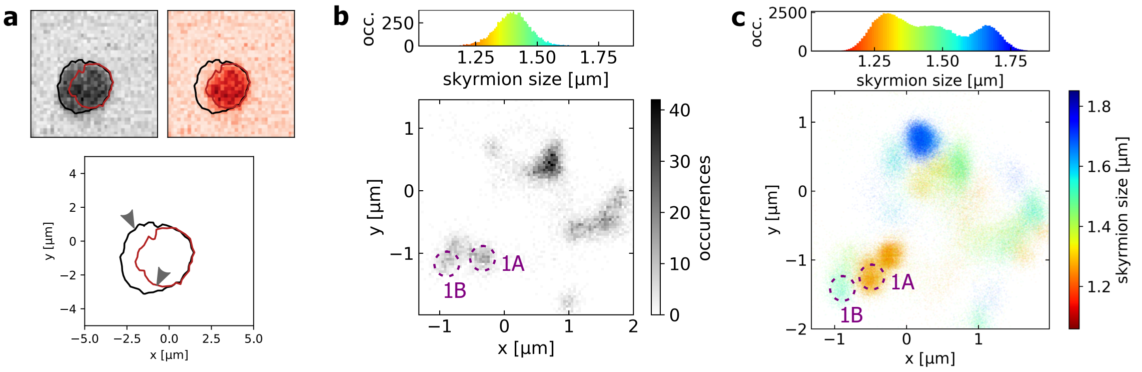

Figure A.5: (a) The top images show the average intensity distributions of skyrmions with center coordinates found at the regions 1A (red) and 1B (black) indicated as dashed violet circles in (b) and (c). The estimated domain walls are depicted by solid lines in the respective colors in the top images and bottom coordinate frame in (a). Panels (b) and (c) are identical to Figs. 4.1c and 4.1a, respectively, but they include labels for the discussed pinning sites 1A and 1B. This figure is taken from the supplementary material of our publication Ref. [36].

A.3.2 Pinned Skyrmions in Micromagnetic Simulation

This section discusses typical skyrmion arrangements in the micromagnetic simulations of section 4.3, where the effective anisotropy is reduced in the red rectangular regions (Fig. A.7). The reduced anisotropy makes these regions favorable for the domain wall that exhibits the lowest alignment with the low anisotropy areas. For the small skyrmion in the schematic Fig. A.6a the obvious favorable position is in between the low anisotropy areas. However, a similar placement for the large skyrmion (Fig. A.6b) provides high overlap between the domain walls and the low anisotropy areas, but the homogeniously magnetized core also covers one of the areas, which is energetically unfavorable. Therefore, one would expect an arrangement below or above the regions as in Fig. A.6c. This intuition is in agreement with the simulation results shown in Fig. A.7.

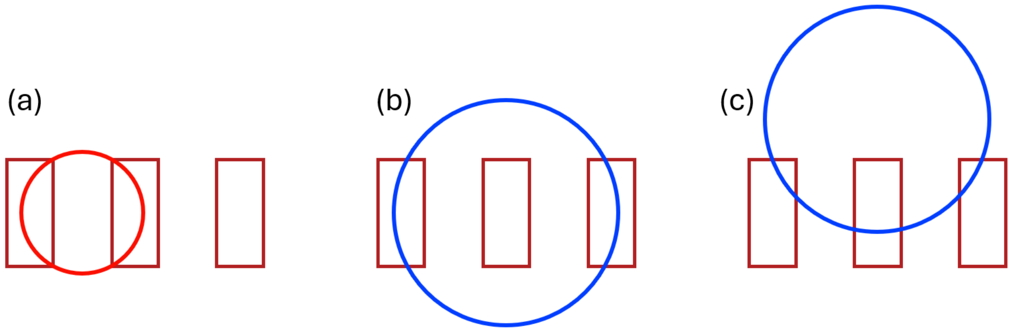

Figure A.6: Schematic illustration of different arrangements of the small (blue circle) and large skyrmion (red circle) with respect to the areas of reduced anisotropy (red rectangles).

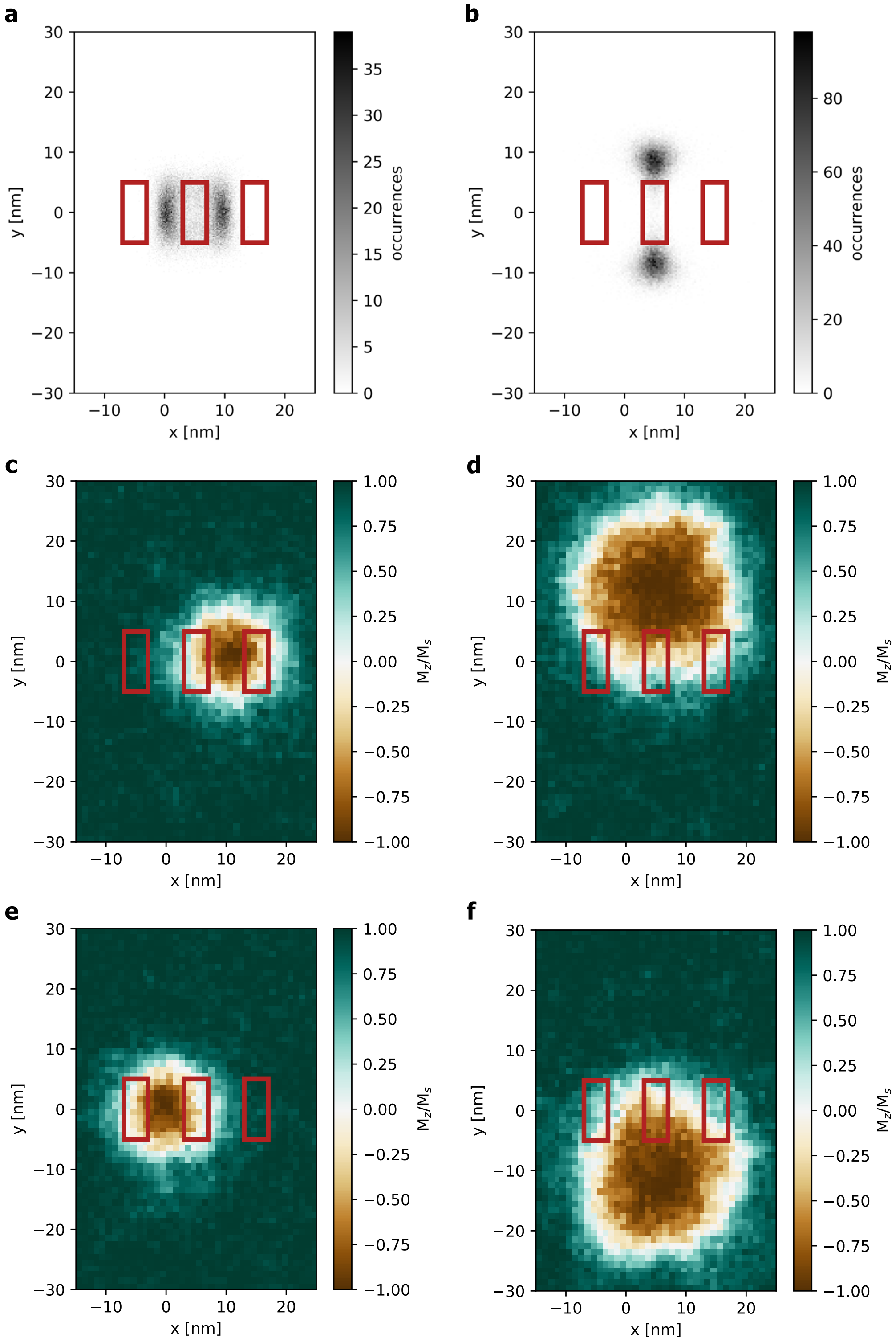

Figure A.7: (a,b) Histograms of the skyrmion center positions for small (a) and large skyrmions (b) as in Fig. 4.4. Exemplary magnetization configurations are shown for small (c,e) and large skyrmions (e,f), where the color indicates the normalized magnetization. This figure is taken from the supplementary material of our publication Ref. [36].

A.4 Additions to Chapter 5

A.4.1 Limitations of the Flashing Potential Interpretation

This section demonstrates the diffusion enhancement mechanism of flashing potentials discussed in section 5.3 via illustrative simulations of a toy model. Furthermore, this section discusses key differences between the diffusion enhancement mechanism of chapter 5 and flashing potentials.

For the simulations, a sine-squared potential toy model $U(x) = A \cdot \sin^2(\frac{2\pi}{\lambda}x)$ is employed. Therein, the parameters $A = 4.7\,\mathrm{k_B T}$ and $\lambda = 4\,\mu\mathrm{m}$ of the potential were chosen to roughly resemble the distance between minima and Lifson-Jackson diffusion reduction factor determined for a quasi-one-dimensional experimental skyrmion system $D^{\mathrm{pin}}/D^{\mathrm{free}} = (0.124 \pm 0.001)$ in section 3.2.2. The latter is $D^{\mathrm{pin}}/D^{\mathrm{free}} \approx 0.115$ for the chosen parameters. The time scale conversion (effective damping parameter) determined in that section is also employed here. In a flashing potential system, the underlying potential (acting similar to how we model pinning energy landscapes), switches periodically between two states. While flashing potentials generally exhibit rich behavior, this section focuses on the non-monotonic frequency dependence of the diffusion coefficient and the high- and low-frequency limits.

The simulation parameters and the diffusion coefficient determination procedure are as described for the determination of the simulation estimate of the Lifson-Jackson diffusion reduction factor in section 3.2.2. The only difference is that Figs. A.8c,d show the mean and standard error of the mean over 3 simulations of 100 trajectories for $10^4\,\tau_{\mathrm{sim}}$.

We first consider the scenario also depicted in Fig. 5.6, where the two potentials are exactly opposite such that the mean potential is flat (Fig. A.8a). Fig. A.8c shows a non-monotonic frequency dependence with a peak at a finite frequency. For very low frequencies, the rare switching between the two potentials has no significant effect compared to the thermal diffusion and the diffusion coefficient approaches the prediction of the Lifson-Jackson equation (Eqn. (3.4)) for either of the two potentials. For very high frequencies, the potential switches too fast for the skyrmion to adjust and it only feels the effect of the mean potential. Therefore, the diffusion coefficient approaches the free diffusion value. In between, there is a maximum where the diffusion coefficient is enhanced compared to both cases. Consequently, it even surpasses free diffusion.

In the scenario, where the two states of the potential do not cancel (Fig. A.8c,d), the diffusion coefficient approaches the Lifson-Jackson prediction for the mean potential in the high frequency case. For the parameters studied here, the maximum diffusion coefficient did not surpass free diffusion. In addition, there are further differences between flashing potentials and the presented diffusion enhancement mechanism for skyrmions, which are discussed in the following.

First, the flashing potential in Fig. 5.6b is designed such that the minima of one state and the maxima of the other state align and vice versa, whereas the skyrmion pinning potentials are random. Second, the systems mentioned above are two-state flashing potentials. In contrast, continuous size changes mean that the skyrmion likely experiences many different pinning energy landscapes. Despite these two differences, it is still plausible to expect that, occasionally, the skyrmion will experience local switching between favorable and unfavorable pinning energy landscapes, such as schematically illustrated in Fig. 5.6c. This local switching may lead to a similar diffusion enhancement mechanism as in the two-state flashing potential discussed before (Fig 5.6b), explaining the non-monotonic frequency dependence. It is important to remember that for the skyrmions, we compare the pinning-affected diffusion at a constant size to the excited diffusion. In research works on flashing potentials, such as in Ref. [153], which discusses an effectively two-dimensional colloidal system subject to a two-state flashing potential working similarly to the schematic in Fig. 5.6b, the excited diffusion is compared to the free diffusion. Since the pinning-affected diffusion coefficient is typically much lower than the free diffusion coefficient (section 3.2.2), we only need a much smaller effect to explain our observations. Moreover, for higher field amplitudes, we expect more drastic changes in the pinning, and therefore, a more pronounced effect of the described local mechanism, leading to a larger diffusion enhancement. In contrast, the system studied in Ref. [153] exhibits almost no amplitude-dependence as the spatial distribution of favorable and unfavorable positions does not change significantly with the excitation amplitude.

Depending on the steepness and spatial arrangement of the flashing potentials, diffusion enhancements as large as experimentally reported in chapter 5 are, in principle, possible. However, the simple arrangements of potentials studied here, which were designed to roughly exhibit similar characteristics to the experimentally determined potential in section 3.2.2, are fare away from the large increases observed experimentally. While flashing potentials exhibit a non-monotonic frequency dependence similar to the one observed for skyrmion diffusion in an oscillating magnetic field, significant additional research is required to gauge the applicability of a flashing potential model. An outlook on suggested approaches for further research is provided in section 5.3.

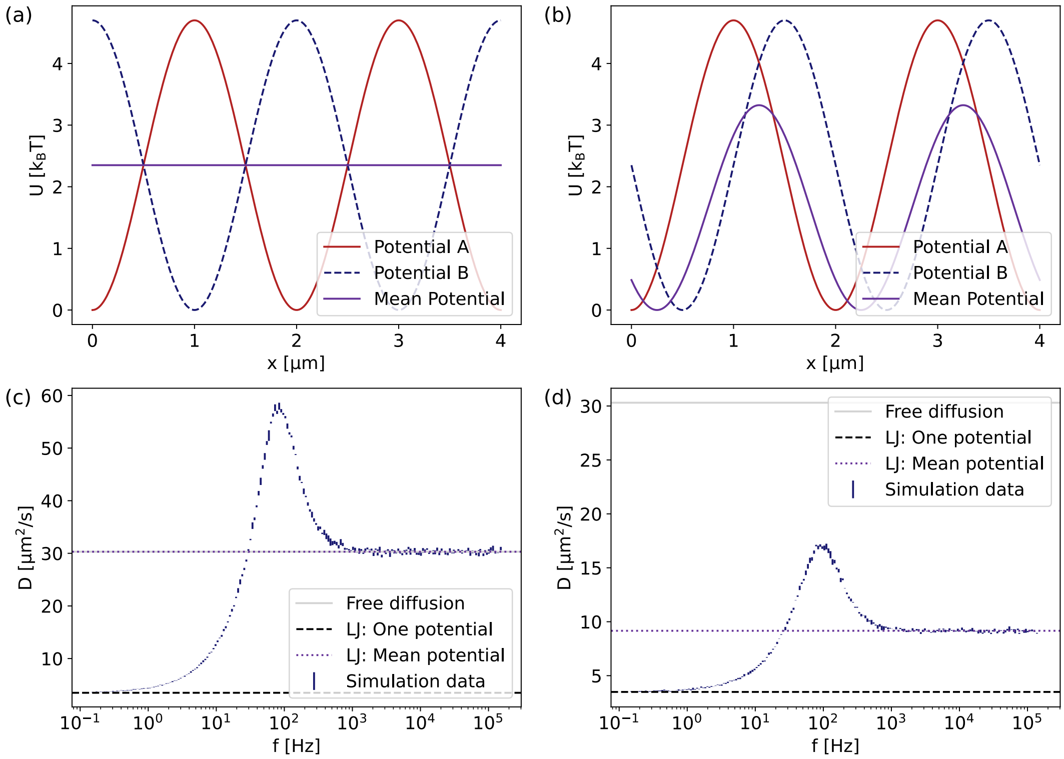

Figure A.8: Two scenarios of flashing potential systems and the resulting frequency-dependence of the diffusion coefficient. In the first scenario (a,c) the two states “Potential A” and “Potential B” cancel such that the mean potential is flat. In the second scenario (b,d), the two potentials do not cancel on average. Panels (c,d) show the mean and standard error of the mean of the diffusion coefficient over 5 simulations consisting of 100 trajectories each as error-bar-markers. The dashed and dotted lines indicate the Lifson-Jackson (LJ) formula prediction for the diffusion coefficient assuming the either of the potentials (A or B) and the mean potential, respectively. The solid gray line depicts the free diffusion coefficient which coincides with the mean potential LJ prediction in the case of canceling potential states (c).

A.4.2 Diffusion Enhancement in Dense and Confined Systems

For applications of the diffusion enhancement mechanism in driving phase transitions [34] and in Brownian computing [29, 30], it is essential to verify that the diffusion enhancement mechanism remains reliable in both dense skyrmion systems and geometrically confined systems, such as narrow channels. This is not obvious since the spatial constraints may lead to skyrmion annihilation as they extend due to the oscillating magnetic field. Figs. A.9a,b show the dependence of the diffusion coefficient on the excitation parameters similar to Fig. 5.1 for a dense skyrmion system and a narrow channel with a width of about 1.8 skyrmion diameters, respectively. In both cases, we observe a significant increase in diffusivity. The experiments were performed in a similar system as studied in the previous sections of this chapter, with the full experimental details given in the supplementary material of our publication Ref. [37].

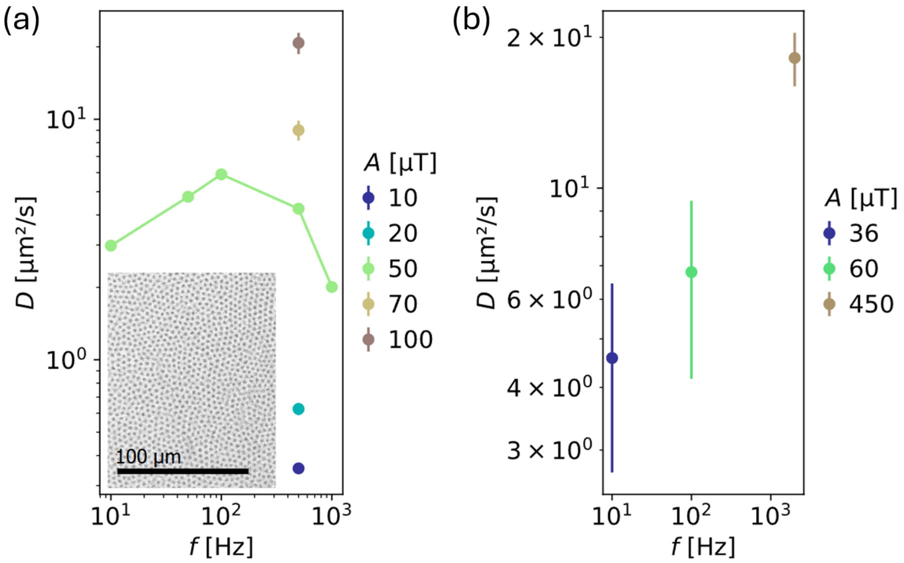

Figure A.9: Dependence of the skyrmion diffusion coefficient D on the frequency f and peak-to-peak amplitude A of the oscillating magnetic field for a dense skyrmion system (a) and a narrow channel (b). The inset in (a) shows a Kerr microscopy snapshot of the system. The gray scale indicates the relative out-of-plane magnetization. In both cases, a significant increase of the static field diffusion coefficients $(0.27 \pm 0.01)\,\mu\text{m}^2/\text{s}$ (a) and $(0.19 \pm 0.03)\,\mu\text{m}^2/\text{s}$ (b) is observed. This figure is adapted from the supplementary material of our publication Ref. [37].

A.5 Additions to Chapter 6

A.5.1 Current density simulation details

This section provides further details of the COMSOL Multiphysics [73] simulation in Fig. 6.2. The aim of the simulation is only to qualitatively compare the relative current density at different positions in the device. While the exact material and voltage parameters are not relevant for this purpose, the simulation details are provided for completeness.

Only the 5 nm bottom tantalum layer of the skyrmion hosting material and chrome layer of the contacts are simulated with respective electrical conductivities of $7.7 \times 10^6\,\text{S/m}$ and $7.9 \times 10^6\,\text{S/m}$. The magnitude of the voltage applied to the outer edge of the contacts is set to 2 mV. Electrical conductivity is enabled between the contacts and structure that represents the skyrmion-hosting material. The simulations were performed using COMSOL's Electic Currents in Shells (ecis) module and the predefined "Extremely fine" mesh was employed (Fig. A.10). The system is placed on a non-interacting glass plate.

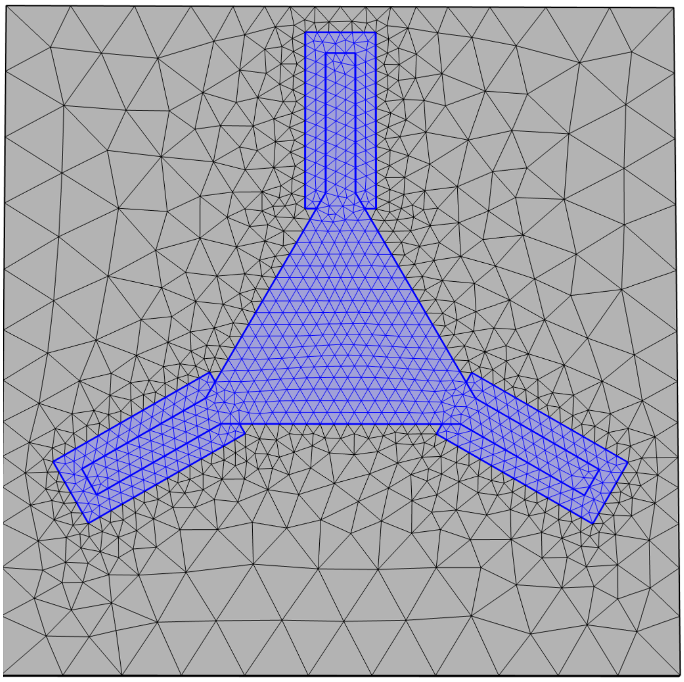

Figure A.10: Mesh employed in the COMSOL Multiphysics [73] simulation of the current density distribution in Fig. 6.2. The conductive region is marked in blue.

A.5.2 Impact of the Read-Out Modeling

In section 6.2, the read-out using magnetic tunnel junctions (MTJs) is modeled by, for every frame of the Kerr video, checking if the skyrmion center is within one of the four circular read-out regions. Based on this procedure, each region's local skyrmion occurrence probability is estimated, which acts similarly to the average tunnel magnetoresistance measured by an MTJ. However, as illustrated in Fig. 6.4, this modeling of MTJ read-out entails a drastic approximation because the skyrmion can only contribute to a single region at a time. Therefore, this section revolves around the training, analysis, and interpretation of the weights using overlap-based read-out modeling. Here, the regions obtain fractional counts for each frame based on the areal overlap of the skyrmion and the read-out region. We assume that the skyrmion is circular and of approximately the same diameter as the read-out regions, such that the areal overlap can be easily calculated based on the skyrmion center and the centers of the read-out regions. With this modeling, the skyrmion can contribute to multiple regions in a single frame. The remaining parts of the training procedure are performed identically to section 6.2, and the optimized weights are given in table A.1. In the following, the results are interpreted in analogy to 6.3. While the patterns in the local occurrence probabilities change (Fig. A.11), the signal-to-noise ratio for the output data at optimized weights (Fig. A.12) remains approximately unchanged, with an SNR of 5.49 and 5.55 for overlap-based and center-based read-out modeling, respectively (Eqn. (6.2)). Fig. A.11 shows good distinguishability for the local occurrence probabilities for both cases. The differences in Fig. A.11 between the two read-out modeling approaches can be well-understood when considering the full spatially resolved skyrmion occurrence

Operation	W_{left}	W_{right}	W_{top}	W_{middle}	$W_{\text{intercept}}$
AND	2.480	9.735	1.595	2.290	-1.287
NAND	-2.480	-9.735	-1.595	-2.290	2.287
OR	0.807	1.915	-1.750	-2.400	0.806
NOR	-0.807	-1.915	1.750	2.400	0.194
XOR	-1.673	-7.820	-3.345	-4.690	2.093
XNOR	1.673	7.820	3.345	4.690	-1.093

Table A.1: Optimized weights for the overlap-based read-out. Of the 13 sets of local skyrmion occurrence probabilities, 4 were used for training. The weights for the center-based read-out are given in table 6.1. This table is adapted from the supplementary material of our publication Ref. [31].

distribution in Fig. 6.7. For instance, there is evidently a strong pinning site just inside the boundary of the right region, which explains a reduction of P_{right} when using overlap-based read-out, which is also reflected in an increase of W_{right} (table A.1). The number of digits given in tables 6.1 and A.1 is only chosen for readability; for the determination of the output, the Scikit-learn standard floating point precision values are employed.

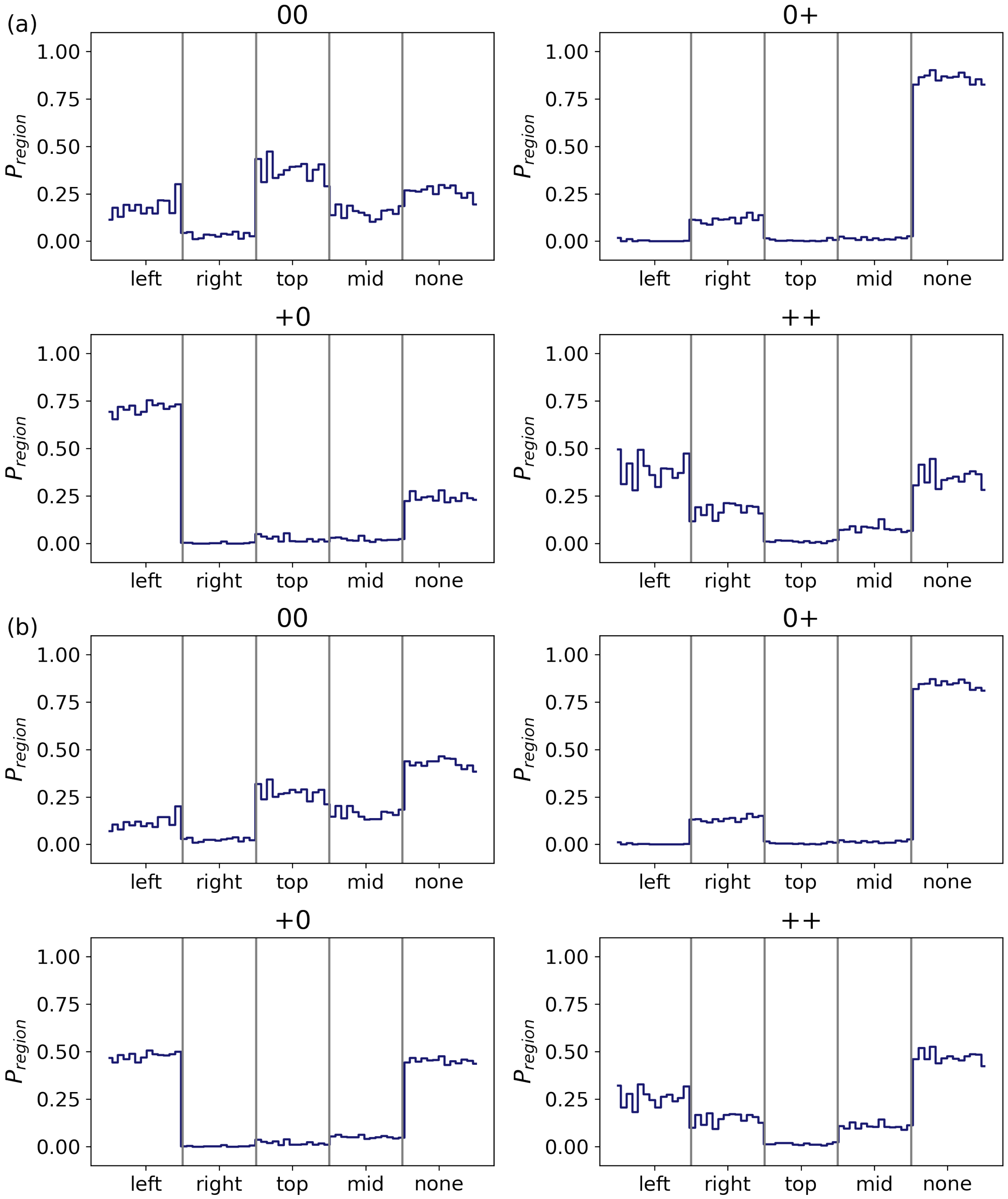

Figure A.11: Comparison of the local occurrence probabilities in the four read-out regions for center-based read-out (a) and overlap-based read-out (b). (a) is identical to Fig. 6.11 and reproduced here for ease of comparison. Each bin in each region corresponds to one of the 13 sets of local skyrmion occurrence probabilities. This figure is taken from the supplementary material of our publication Ref. [31].

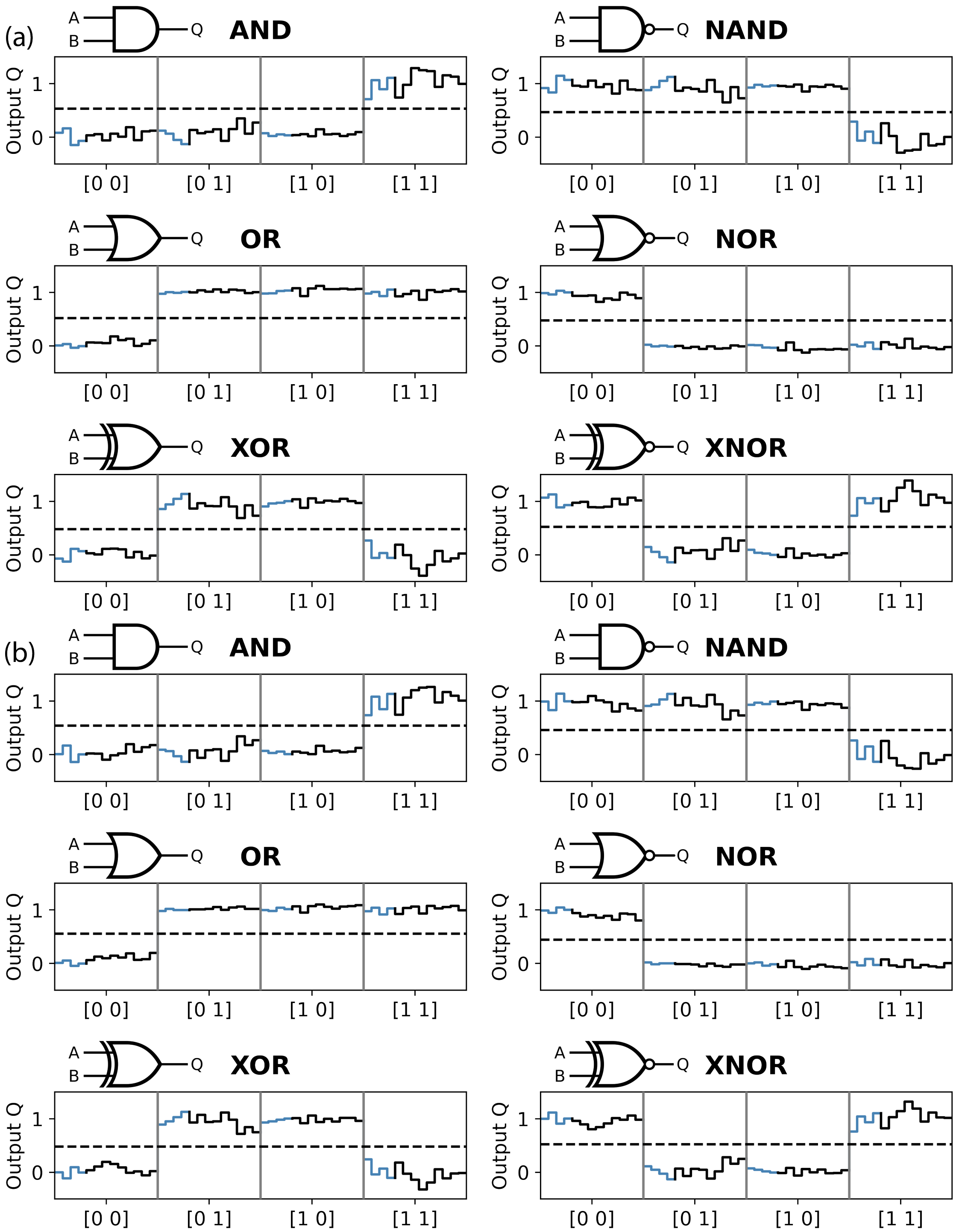

Figure A.12: Comparison of the outputs of the linear read-out optimized for different Boolean logic operations based on the local occurrence probabilities employing center-based (a) or overlap-based (b) read-out modeling. The other parameters are as in Fig. 6.5, which is identical to (a) and reproduced here for easy comparison. This figure is taken from the supplementary material of our publication Ref. [31].

A.6 Biophysics Research

This section discusses side projects in the field of biophysics, on which I worked during the time of my PhD, but which are unrelated to my research on skyrmions. For this reason, these works are not discussed thoroughly. Instead, the associated open-access publications are briefly summarized and then included in full.

The question of how the chemical composition of a protein, the amino acid sequence, determines its 3D structure has been one of the biggest challenges in biophysics for more than half a century. Recently, the artificial intelligence system AlphaFold developed by Google's DeepMind dominated the Critical Assessment of Techniques for Protein Structure Prediction (CASP) [161, 162]. In our publication

- Maarten A. Brems, Robert Runkel, Todd O. Yeates, Peter Virnau, „AlphaFold predicts the most complex protein knot and composite protein knots", *Protein Science* **31**, (8):e4380 (2022) (Ref. [54]),

we analyzed the entire AlphaFold 2 databank available at the time to identify topologically complex proteins containing previously unknown deep knots. In the past two decades, only about 20 different protein families containing knots have been identified [163]. Simulation algorithms often overestimate the knotting probability of proteins, and their folding pathways are usually much more complicated than those of topologically trivial proteins of similar size. These reasons make knotted proteins an excellent test system to gauge AlphaFold's performance on rare and complex folding problems. Within the high-confidence prediction database, we discovered the most topologically complex seven-crossing knot ever found in a protein, as well as composite protein knots. Both predictions have been experimentally verified later [164, 165]. I contributed to this work through the visual inspection of protein topology, the identification of probable homologues, the visualization of proteins and their reduced representations, as well as data analysis and interpretation.

The second publication

- Jan Rothörl, Maarten A. Brems, Tim J. Stevens, Peter Virnau, "Reconstructing diploid 3D chromatin structures from single cell Hi-C data with a polymer-based approach", *Frontiers in Bioinformatics* **3**, 1284484 (2023) (Ref. [55])

concerns the determination of coarse-grained 3D structures of chromatin based on experimental single-cell Hi-C data. We present a simulation protocol to improve the resolution of predicted interphase chromatin structures iteratively. The protocol is based on the association of ambiguous Hi-C contacts that arise for diploid cells, using lower-resolution predictions. Thereby, we overcome the previous limitation to haploid cell data [166] and reach resolutions up to 5000 base pairs per bead. I mainly contributed to this work through method development, in particular concerning the treatment structure chirality.

Received: 6 April 2022 | Revised: 9 June 2022 | Accepted: 11 June 2022
DOI: 10.1002/pro.4380

FULL-LENGTH PAPER

THE PROTEIN SOCIETY WILEY

AlphaFold predicts the most complex protein knot and composite protein knots

Maarten A. Brems[1] | **Robert Runkel**[1] | **Todd O. Yeates**[2,3] | **Peter Virnau**[1]

[1]Department of Physics, Johannes Gutenberg University Mainz, Mainz, Germany

[2]UCLA-DOE Institute for Genomics and Proteomics, University of California Los Angeles, Los Angeles, California, USA

[3]UCLA Department of Chemistry and Biochemistry, University of California Los Angeles, Los Angeles, California, USA

Correspondence
Peter Virnau, Department of Physics, Johannes Gutenberg University Mainz, Staudingerweg 9, Mainz 55128, Germany.
Email: virnau@uni-mainz.de

Funding information
Deutsche Forschungsgemeinschaft, Grant/Award Number: 233630050-TRR 146; TopDyn; Johannes Gutenberg University Mainz

Review Editor: Nir Ben-Tal

Abstract

The computer artificial intelligence system AlphaFold has recently predicted previously unknown three-dimensional structures of thousands of proteins. Focusing on the subset with high-confidence scores, we algorithmically analyze these predictions for cases where the protein backbone exhibits rare topological complexity, that is, knotting. Amongst others, we discovered a 7_1-knot, the most topologically complex knot ever found in a protein, as well several six-crossing composite knots comprised of two methyltransferase or carbonic anhydrase domains, each containing a simple trefoil knot. These deeply embedded composite knots occur evidently by gene duplication and interconnection of knotted dimers. Finally, we report two new five-crossing knots including the first 5_1-knot. Our list of analyzed structures forms the basis for future experimental studies to confirm these novel-knotted topologies and to explore their complex folding mechanisms.

KEYWORDS

AlphaFold, composite knots, protein knots, protein topology

1 | INTRODUCTION

Recently, the artificial intelligence (AI) system AlphaFold developed by Google's DeepMind dominated the Critical Assessment of Techniques for Protein Structure Prediction (CASP) twice.[1] AlphaFold 2, the version under consideration here, is a deep learning system that incorporates training procedures based on the evolutionary, physical, and geometric constraints of protein structures.[2,3] It features iterative refinement of predictions and allows for learning from unlabeled protein sequences using self-distillation and self-estimates of accuracy to directly predict the 3D coordinates of all heavy atoms for a given protein using the primary structure and aligned sequences of homologues.[2,3] AlphaFold 2 has currently predicted several hundred thousand protein structures, most of which are not contained in the Protein Data Bank (PDB),[4,5] which mainly archives experimentally determined structures.[5] Thereby, AlphaFold‘s prediction databank may be of tremendous value, especially for the research of protein phenomena which are infrequent but still of high relevance to understand the intricacies of the underlying mechanisms of protein folding.

A particularly fascinating phenomenon arises for proteins that contain a topological knot in their polypeptide backbone,[6–30] that is, proteins which would not fully disentangle after being pulled from both ends.[6] In the past two decades, only about 20 different protein families

---

Maarten A. Brems and Robert Runkel have contributed equally.

containing knots have been identified.[7] Nevertheless, knotted proteins pose a challenge to protein folding and evolution.[8] Simulation algorithms often overestimate the knotting probability of proteins as the latter is lower than the knotting probability of random chains.[8,12,14,31] Moreover, protein topology is usually similar among homologues, meaning that knotted folds tend to be preserved across proteins closely related in evolution. For these reasons, and owing to the established rarity of knotting among natural proteins, the potential presence of knotted topologies in the vast new database of predicted protein structures is of keen interest. Currently, the most complex knot found in a protein is a single knot with six essential crossings in any projection to a plane[32]; a composite knot has not been observed yet.

We searched the entire AlphaFold 2 databank, including the "Model organism proteomes", "Swiss-Prot" and "Global health proteomes" data sets,[4] for topologically complex proteins containing previously unknown deep knots (which still persist when at least five amino acids [aa] are cut from both ends). We excluded from the analysis those with lower confidence scores (<80) or exceedingly long protein chains (>600 aa), where predicted accuracy and ability to experimentally validate the structures could be limiting. The applied criteria for the survey as well as our knot detection algorithm are discussed in detail in the methods section. Based on this search and visual inspection, we have identified the first 7_1-knot (with at least seven crossings in any projection onto a plane) as well as a likely evolutionary mechanism for generation of $3_1\#3_1$ composite knots, accompanied by several examples. Moreover, we report two new five-crossing knots including the first 5_1-knot in a protein and provide an overview of additional knotted proteins present in the AlphaFold databank (Supporting Information S1).

2 | GENERATION MECHANISM OF COMPOSITE KNOTS

Our survey identified nine cases of composite knots, previously unknown. These are all instances where two essentially independent trefoil knots are present in one longer protein chain. We propose a novel mechanism for generation of such composite knots based on gene duplication and the interconnection of a knotted homodimer. Interestingly, this mechanism resembles a strategy employed for the creation of the first artificial protein knot in which an unknotted dimer was "connected" to form a trefoil.[17] We have observed multiple instances including the methyltransferases and carbonic anhydrases, as discussed below, in which proteins containing

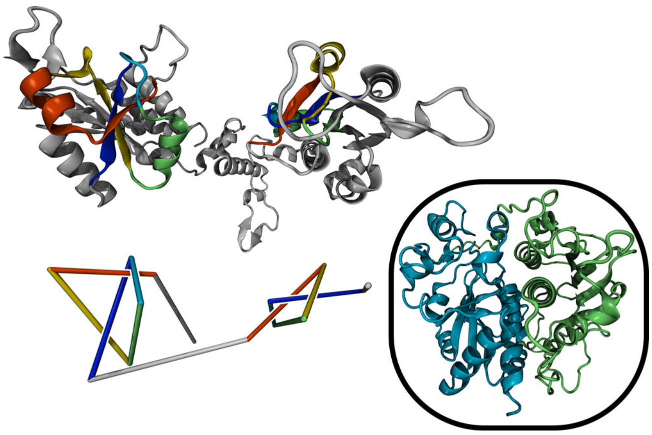

FIGURE 1 3D structure (top) and reduced representation (bottom) of a six-crossing composite knot in protein Q313J9 (methyltransferase). A composite trefoil knot ($3_1\#3_1$) can be identified. Topologically trivial segments are not displayed. Inset: A similar structure is predicted for Methyltransferase A4I142, except the two knotted domains form a more compact arrangement

a composite trefoil knot ($3_1\#3_1$) are homologous to a known knotted homodimer with one trefoil knot in each chain. Figure 1 depicts protein Q313J9, which has been identified as tRNA (guanine-N1-)-methyltransferase, with a length of 425 aa and a knotted core between residues 86 and 360. If not stated otherwise, the protein code refers to the UniProt/AlphaFold identifier[33] and structures are visualized using the Visual Molecular Dynamics (VMD) software.[34] To visualize knots in the protein structures, we employ reduced representations (bottom structures in Figures 1-4), in which the protein is divided into segments such that topology is conserved when the segments are replaced by straight lines connecting their respective start and end points. Methyltransferases are known to usually contain a single trefoil knot[7] per chain and sometimes appear as homodimers. We have observed two variations of this phenomenon: For protein Q313J9 in Figure 1 and a similar methyltransferase Q72DU3, the two main segments containing the trefoil knots appear flexibly connected, whereas predictions for some proteins of similar sequence preserve the presumed original dimer structure more strictly. (See inset of Figure 1.) Examples are the methylases A4I142, Q4DMW6, and Q4D5S2 as well as proteins Q4CYG6, Q4D7N4, and Q381U1. The latter are labeled as uncharacterized but show about 15% sequence identity and 30% matching secondary structure with the methyltransferase pdb:2ha8:A for proteins Q4CYG6 and Q4D7N4 or with the methyltransferase pdb:1v2x:A for protein Q381U1 according to the PBDeFold webserver.[35] Structural alignment and sequence identity discussions based on PDBeFold[35,36] for each group of methyltransferases containing composite knots can be found in the Supporting Information (SI). A

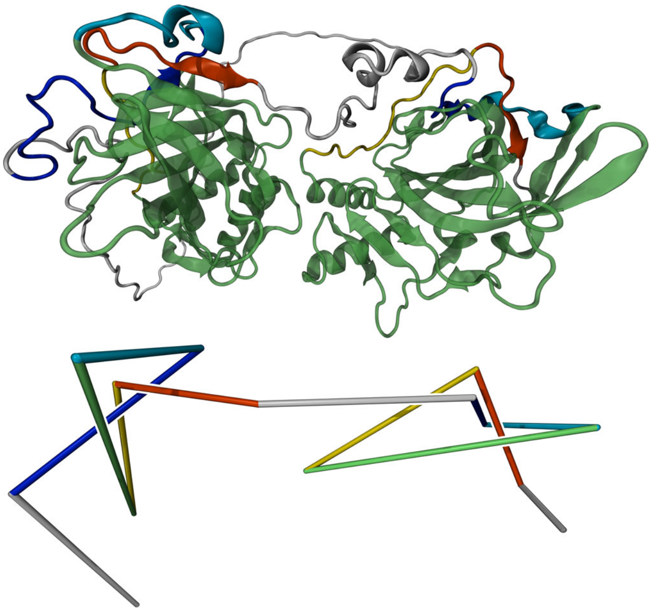

FIGURE 2 3D structure (top) and reduced representation (bottom) of protein P54212 (carbonic anhydrase). A composite trefoil knot ($3_1\#3_1$) can be identified. Topologically trivial segments are not displayed. The large green segments in the top structure are made transparent for a better view of the knotted region

particularly interesting example of the second variant is Carbonic anhydrase P54212 (Figure 2), with a length of 589 aa and a knotted core between residues 198 and 570. Carbonic anhydrases were the first proteins identified as being knotted.[37] Both trefoil knots in methyltransferase Q313J9 and as well as in carbonic anhydrase P54212 have positive chirality. Therefore, the composite trefoil knots can be identified as what is commonly known as a granny knot.[38] The chirality of the composite knots is in agreement with previous results reporting positive chirality for the single trefoil knots in methyltransferases and carbonic anhydrases.[7] We have thereby observed the same phenomenon, a potential mechanism for generation of composite knots, in two distinct protein families and with two structural variations.

3 | FIRST 7_1-KNOT IN A PROTEIN

Figure 3 depicts proteins P73136 and Q9PR55 with lengths of 112 and 89 amino acids, respectively. Both are uncharacterized and no probable homologues could be identified using PDBeFold. However, they have 48% sequence identity and 71% matching secondary structure with respect to each other, which indicates that they are probably homologues. Protein Q9PR55 contains the most complicated knot, a 7_1-knot, known to date with a knotted core between residues 27 and 83. The similar structure of protein P73136 contains a 5_1-knot with a knotted core between residues 45 and 94. Such a pair of homologues where the two proteins possess a different nontrivial topology has not been observed previously. A closer look reveals that the more complex topology of protein Q9PR55 arises from a protein segment that introduces an additional winding (dark blue in Figure 3, right); a 7_1-torus knot is essentially a 5_1-torus knot with one additional winding around the torus. Both knots have positive chirality.

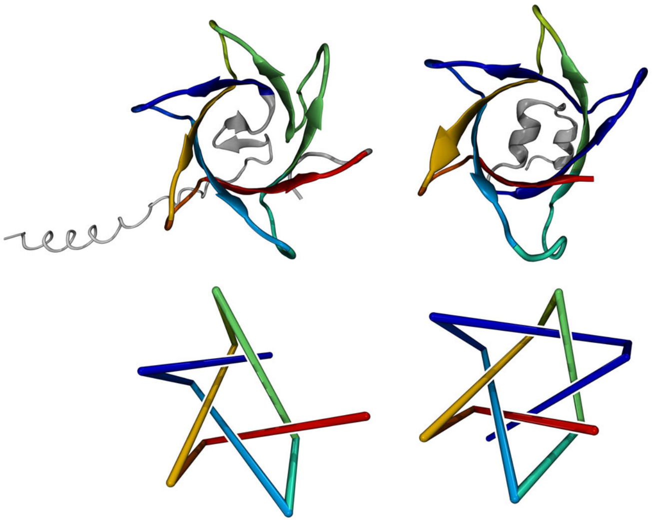

FIGURE 3 Structure and topology of proteins P73136 (left) and Q9PR55 (right). Top: 3D structures predicted by AlphaFold. Bottom: Reduced representations to visualize the 5_1- and 7_1-knots in the left and right structure, respectively. On the right, the dark blue segment introduces an additional winding

4 | NEW 5_1- AND 5_2-KNOTS

We have found two previously unknown knots with five essential crossings, including the first 5_1-knot. Figure 4 (left) depicts protein A0A0K0IQS9 (Bm1115) which contains a 5_1-knot. Its length is 173 aa and its knotted core extends from residue 39 to residue 157. Protein C1GYM9 (Figure 4 right) is uncharacterized, and no probable homologue could be identified using PDBeFold. It contains a 5_2-knot with a knotted core between residues 76 and 391 and its length is 420 aa. Both knots exhibit positive chirality.

5 | TESTS OF ACCURACY

Owing to the novelty of the findings here, validation by independent methods will be important. Ahead of experimental studies, here we applied an orthogonal computational tool, ERRAT,[39] to assess the predicted knotted

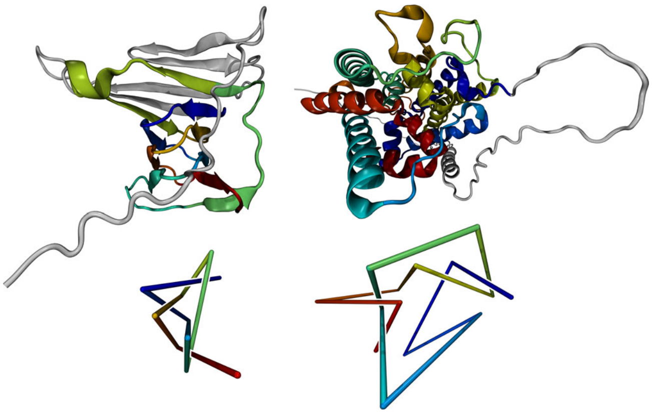

FIGURE 4 Structure and topology of proteins A0A0K0IQS9 (left) and C1GYM9 (right). Top: 3D structures predicted by AlphaFold. Bottom: Reduced representations to visualize the 5_1- and 5_2-knots in the left and right structure, respectively

structures. The ERRAT algorithm evaluates patterns of non-bonded contacts between C, N, and O atoms, and makes a statistical comparison to high resolution structures. By being distinct from metrics employed in AlphaFold (and other prediction methods), it offers an independent assessment. We ran ERRAT[40] on the set of knotted structures discussed above. Discounting occasional extended termini found in some models, all the models tested showed good scores; all cases have >90% of their protein chain falling within (below) the 95% threshold for rejecting unlikely conformations. Our overall assessment was therefore that the predicted structures are correct, at least to a large extent. However, in some cases, local regions of structure appeared potentially problematic. And it is critical to note that minor discrepancies in the path of a protein chain—for example, those that would change an over/under crossing—can change the topology, potentially leading to an incorrect assignment of a knot. With regard to the present study, we note that, for the composite knot Q4D5S2 (and its relatives), the ERRAT program flags a beta strand segment around residues 100–110 as likely to be structurally incorrect (SI, Figure S1). Notably, the passage of the chain in this region is important for the knotted topology. While the AlphaFold program assigns a high degree of confidence to the predicted structure in this region, our independent assessment emphasizes the need for confirmatory experimental studies.

6 | DISCUSSION AND CONCLUSIONS

In conclusion, we have analyzed all predictions for protein 3D structures by the AlphaFold AI system for new topologically complex proteins. Our complete analysis of the data provided by AlphaFold (see SI) reveals several high-confidence proteins containing deep complex knots, which are suitable for experimental verification of their 3D structure. In this data set, we found amongst others a 7_1-knot, the most complex ever discovered in a protein, as well as a new 5_1-knot in a homologue structure and the first instances of composite protein knots. For the latter, we propose an evolutionary mechanism for their creation by gene duplication. As protein topology is an ongoing challenge for protein folding algorithms, it will be important to verify or refute the discussed structure predictions experimentally. One would not only obtain a fine gauge for the capability of AlphaFold AI system to correctly predict the topology of complex proteins, but importantly confirm the multitude of novel protein knots identified here.

7 | METHODS

Mathematically, knots are well-defined in closed three-dimensional curves, and can be categorized according to the minimal number of crossings the curve makes in a projection onto a plane, allowing for any non-breaking manipulations (e.g., smoothing) of the curve. The simplest non-trivial knot is the so-called trefoil knot with three crossings. The figure-eight knot has four crossings, there are two knots with five, three knots with six, and eight distinct knots with seven crossings. In addition, simpler knots can be combined—i.e., formed on separable regions of the same curve—to form composite knots, which are distinct from prime knots; the latter cannot be decomposed into simpler knots. In the present study, topologically non-trivial proteins (i.e., polypeptide backbones that are knotted) have been identified using a classification algorithm based on the Alexander polynomial invariant.[41,42] Note that for a knot to be well-defined, the two ends of the protein must be virtually closed,[41,42] which sometimes leads to ambiguous results and requires additional visual inspection. Employing the algorithm above, we find that the knotting probability (of around 2%) of the AlphaFold database is roughly in accordance with the one from PDB as discussed in the SI.

We limit our detailed, non-algorithmic analysis to proteins which fulfill the following three criteria: First, the average computed confidence score for the predicted structure must be 80 or above. The AlphaFold AI system provides a per-residue estimate of its confidence on a scale from 0 to 100, which is based on the lDDT-Cα metric.[43] Second, the topology of the protein must be more complex than a trefoil (3_1) and figure-eight (4_1) knot, that is, it must contain a knot with at least five essential crossings, which includes any potential composite knots. We exclude combinations of knot types and protein families which are already known, such as 5_2-knots in ubiquitin hydrolases and 6_1-knots in haloacid dehalogenase.[7] Moreover, the knot must be deep in the sense that the topology of the system is invariant under removal of at least 5 aa from both termini. A related measure for the topological robustness of a structure, which we employ in our discussions, is the extend of the knotted core, that is, the smallest region of the protein which still contains the knot. The extend of the knotted core is one of the measures included in the knot matrix representation for proteins introduced by King et al. in Ref. 18 and popularized in further work.[44] Third, the protein must not exceed a length of 600 aa. The final condition was set to mitigate the potential errors in topology assignment that can arise from relatively small structural discrepancies in large structures, in addition to challenges typically associated with experimental studies on very large and potentially flexible protein chains. As established above, correct prediction of protein topology is still an important challenge for modern computer algorithms. Thus, ultimate experimental verification or refutation will highlight the degree to which the AlphaFold AI system can grasp the intricacies of protein folding for highly complex cases. An extensive table of all knotted proteins in AlphaFold's databank, as determined by our algorithm, including all quantitative measures employed in our analysis and filtering can be found in the SI. In the present work, the most interesting proteins that fulfill the conditions above are discussed in detail. In the SI, we also list proteins that fulfilled the computational criteria, but which were set aside as potentially unreliable after visual inspection. The per-residue confidence scores of all proteins depicted in the figures are given in the SI; we observe that no segments which are substantial for the knots possess particularly low confidence. Moreover, we want to acknowledge that we found the 6_3-knot in von Willebrand factor A (identifiers O00534 and Q99KC8), which was also reported in Ref. 45, where AlphaFold predictions for the human proteome were studied, even though it does not satisfy the above conditions stated above due to its length. In the review stage of this manuscript, another paper was published by the same group, which describes a server to determine knots in predicted structures from AlphaFold.[46]

AUTHOR CONTRIBUTIONS

Maarten Alexander Brems: Formal analysis (equal); investigation (supporting); software (equal); visualization (lead); writing – original draft (lead); writing – review and editing (equal). **Robert Runkel:** Formal analysis (equal); investigation (lead); software (equal); writing – review and editing (supporting). **Todd Yeates:** Conceptualization (supporting); methodology (supporting); project administration (supporting); software (equal); supervision (supporting); visualization (supporting); writing – original draft (supporting); writing – review and editing (supporting). **Peter Virnau:** Conceptualization (lead); funding acquisition (lead); methodology (lead); project administration (lead); resources (lead); supervision (lead); writing – review and editing (equal).

ACKNOWLEDGMENTS

We are grateful to the Deutsche Forschungsgemeinschaft (DFG, German Research Foundation) for funding this research: Project number 233630050-TRR 146. The authors gratefully acknowledge computing time granted on the HPC cluster Mogon at Johannes Gutenberg University Mainz. The authors furthermore acknowledge funding from TopDyn. Open Access funding enabled and organized by Projekt DEAL.

CONFLICT OF INTEREST

There is no conflict of interest to declare.

ORCID

Maarten A. Brems https://orcid.org/0000-0002-0210-508X
Todd O. Yeates https://orcid.org/0000-0001-5709-9839
Peter Virnau https://orcid.org/0000-0003-2340-3884

REFERENCES

1. Callaway E. 'It will change everything': DeepMind's AI makes gigantic leap in solving protein structures. Nature. 2020;588:203–204.
2. Jumper J, Evans R, Pritzel A, et al. Highly accurate protein structure prediction with AlphaFold. Nature. 2021;596:583–589.
3. Varadi M, Anyango S, Deshpande M, et al. AlphaFold protein structure database: Massively expanding the structural coverage of protein-sequence space with high-accuracy models. Nucleic Acids Res. 2022;50:D439–D444.
4. Anon AlphaFold Protein Structure Database. Available from: https://alphafold.ebi.ac.uk/
5. wwPDB consortium. Protein data Bank: The single global archive for 3D macromolecular structure data. Nucleic Acids Res. 2019;47:D520–D528.
6. Virnau P, Mallam A, Jackson S. Structures and folding pathways of topologically knotted proteins. J Phys Condens Matter. 2011;23:033101.
7. Jarmolinska AI, Perlinska AP, Runkel R, et al. Proteins' knotty problems. J Mol Biol. 2019;431:244–257.
8. Virnau P, Mirny LA, Kardar M. Intricate knots in proteins: Function and evolution. PLoS Comput Biol. 2006;2:e122.
9. Mansfield ML. Are there knots in proteins? Nat Struct Mol Biol. 1994;1:213–214.
10. Mansfield ML. Fit to be tied. Nat Struct Mol Biol. 1997;4:166–167.
11. Taylor WR. A deeply knotted protein structure and how it might fold. Nature. 2000;406:916–919.

12. Lua RC, Grosberg AY. Statistics of knots, geometry of conformations, and evolution of proteins. PLoS Comput Biol. 2006;2:e45.
13. Yeates TO, Norcross TS, King NP. Knotted and topologically complex proteins as models for studying folding and stability. Curr Opin Chem Biol. 2007;11:595–603.
14. Potestio R, Micheletti C, Orland H. Knotted vs. unknotted proteins: Evidence of knot-promoting loops. PLoS Comput Biol. 2010;6:e1000864.
15. Taylor WR, Lin K. Protein knots: A tangled problem. Nature. 2003;421:25.
16. Kamitori S. A real knot in protein. J Am Chem Soc. 1996;118:8945–8946.
17. King NP, Jacobitz AW, Sawaya MR, Goldschmidt L, Yeates TO. Structure and folding of a designed knotted protein. Proc Natl Acad Sci. 2010;107:20732–20737.
18. King NP, Yeates EO, Yeates TO. Identification of rare slipknots in proteins and their implications for stability and folding. J Mol Biol. 2007;373:153–166.
19. Sriramoju MK, Chen Y, Lee Y-TC, Hsu S-TD. Topologically knotted deubiquitinases exhibit unprecedented mechanostability to withstand the proteolysis by an AAA+ protease. Sci Rep. 2018;8:7076.
20. Ko K-T, Hu I-C, Huang K-F, Lyu P-C, Hsu S-TD. Untying a knotted SPOUT RNA methyltransferase by circular permutation results in a domain-swapped dimer. Structure. 2019;27:1224–1233.e4.
21. Jamroz M, Niemyska W, Rawdon EJ, et al. KnotProt: A database of proteins with knots and slipknots. Nucleic Acids Res. 2015;43:D306–D314.
22. Sulkowska JI, Sulkowski P, Onuchic J. Dodging the crisis of folding proteins with knots. Proc Natl Acad Sci USA. 2009;106:3119–3124.
23. Sulkowska JI, Sulkowski P, Szymczak P, Cieplak M. Stabilizing effect of knots on proteins. Proc Natl Acad Sci USA. 2008;105:19714–19719.
24. Faisca PFN. Knotted proteins: A tangled tale of structural biology. Comp Struct Biotechnol J. 2015;13:459–468.
25. Faisca PFN, Travasso RDM, Charters T, Nunes A, Cieplak M. The folding of knotted proteins: Insights from lattice simulations. Phys Biol. 2010;7:016009.
26. Jackson SE, Suma A, Micheletti C. How to fold intricately: Using theory and experiments to unravel the properties of knotted proteins. Curr Opin Struct Biol. 2017;42:6–14.
27. Mallam AL, Jackson SE. Folding studies on a knotted protein. J Mol Biol. 2005;346:1409–1421.
28. Mallam AL, Jackson SE. Knot formation in newly translated proteins is spontaneous and accelerated by chaperonins. Nat Chem Biol. 2012;8:147–153.
29. Mallam AL, Jackson SE. Probing Nature's knots: The folding pathway of a knotted homodimeric protein. J Mol Biol. 2006;359:1420–1436.
30. Lim NCH, Jackson SE. Molecular knots in biology and chemistry. J. Phys.: Condes. Matter. 2015;27:354101.
31. Wüst T, Reith D, Virnau P. Sequence determines degree of Knottedness in a coarse-grained protein model. Phys Rev Lett. 2015;114:028102.
32. Bölinger D, Sułkowska JI, Hsu H-P, et al. A Stevedore's protein knot. PLoS Comput Biol. 2010;6:e1000731.
33. The UniProt Consortium. UniProt: The universal protein knowledgebase in 2021. Nucleic Acids Res. 2021;49:D480–D489.
34. Humphrey W, Dalke A, Schulten K. VMD: Visual molecular dynamics. J Mol Graph. 1996;14(33–38):27–28.
35. Krissinel E, Henrick K. Secondary-structure matching (SSM), a new tool for fast protein structure alignment in three dimensions. Acta Cryst D. 2004;60:2256–2268.
36. Krissinel E, Henrick K. Multiple alignment of protein structures in three dimensions. In: Berthold MR, Glen RC, Diederichs K, Kohlbacher O, Fischer I, editors. Computational life sciences, Lecture notes in computer science. Berlin, Heidelberg: Springer, 2005; p. 67–78.
37. Richardson JS. β-Sheet topology and the relatedness of proteins. Nature. 1977;268:495–500.
38. Rolfsen D. Knots and links. Berkeley, CA: Publish or Perish, 1976.
39. Colovos C, Yeates TO. Verification of protein structures: Patterns of nonbonded atomic interactions. Protein Sci. 1993;2:1511–1519.
40. Anon SAVESv6.0—Structure Validation Server. Available from: https://saves.mbi.ucla.edu/
41. Virnau P. Detection and visualization of physical knots in macromolecules. Phys Procedia. 2010;6:117–125.
42. Kolesov G, Virnau P, Kardar M, Mirny LA. Protein knot server: Detection of knots in protein structures. Nucleic Acids Res. 2007;35:W425–W428.
43. Mariani V, Biasini M, Barbato A, Schwede T. lDDT: A local superposition-free score for comparing protein structures and models using distance difference tests. Bioinformatics. 2013;29:2722–2728.
44. Sułkowska JI, Rawdon EJ, Millett KC, Onuchic JN, Stasiak A. Conservation of complex knotting and slipknotting patterns in proteins. Proc Natl Acad Sci USA. 2012;109:E1715–E1723.
45. Perlinska AP, Niemyska WH, Gren BA, Rubach P, Sulkowska JI (2022) New 63 knot and other knots in human proteome from AlphaFold predictions: December 30, 2021.474018. Available from: https://doi.org/10.1101/2021.12.30.474018v1
46. Niemyska W, Rubach P, Gren BA, et al. AlphaKnot: Server to analyze entanglement in structures predicted by AlphaFold methods. Nucleic Acids Res.: gkac388. 2022.

SUPPORTING INFORMATION

Additional supporting information can be found online in the Supporting Information section at the end of this article.

How to cite this article: Brems MA, Runkel R, Yeates TO, Virnau P. AlphaFold predicts the most complex protein knot and composite protein knots. Protein Science. 2022;31(8):e4380. https://doi.org/10.1002/pro.4380

Frontiers in Bioinformatics

TYPE Original Research
PUBLISHED 11 December 2023
DOI 10.3389/fbinf.2023.1284484

OPEN ACCESS

EDITED BY
Jianrong Wang,
Michigan State University, United States

REVIEWED BY
Guang Shi,
University of Illinois at Urbana-Champaign, United States
Pavel Kos,
Friedrich Miescher Institute for Biomedical Research (FMI), Switzerland
Tiantian Ye,
Xianghu Laboratory (Zhejiang Laboratory of Agriculture), China

*CORRESPONDENCE
Peter Virnau,
✉ virnau@uni-mainz.de

RECEIVED 28 August 2023
ACCEPTED 24 November 2023
PUBLISHED 11 December 2023

CITATION
Rothörl J, Brems MA, Stevens TJ and Virnau P (2023), Reconstructing diploid 3D chromatin structures from single cell Hi-C data with a polymer-based approach.
Front. Bioinform. 3:1284484.
doi: 10.3389/fbinf.2023.1284484

Reconstructing diploid 3D chromatin structures from single cell Hi-C data with a polymer-based approach

Jan Rothörl[1], Maarten A. Brems[1], Tim J. Stevens[2] and Peter Virnau[1]*

[1]Institute of Physics, Johannes Gutenberg-Universität Mainz, Mainz, Germany, [2]MRC Laboratory of Molecular Biology, Cambridge, United Kingdom

Detailed understanding of the 3D structure of chromatin is a key ingredient to investigate a variety of processes inside the cell. Since direct methods to experimentally ascertain these structures lack the desired spatial fidelity, computational inference methods based on single cell Hi-C data have gained significant interest. Here, we develop a progressive simulation protocol to iteratively improve the resolution of predicted interphase structures by maximum-likelihood association of ambiguous Hi-C contacts using lower-resolution predictions. Compared to state-of-the-art methods, our procedure is not limited to haploid cell data and allows us to reach a resolution of up to 5,000 base pairs per bead. High resolution chromatin models grant access to a multitude of structural phenomena. Exemplarily, we verify the formation of chromosome territories and holes near aggregated chromocenters as well as the inversion of the CpG content for rod photoreceptor cells.

KEYWORDS

chromatin, Hi-C, 3D structure, polymers, diploid cells, interphase, molecular dynamics

1 Introduction

Reconstruction of 3D chromatin conformations is a promising approach to improve our understanding of processes in the cell. While coarse information about the existence of chromosome territories has already been obtained with different methods (Cremer et al., 1993; Cremer and Cremer, 2001; Bolzer et al., 2005; Branco and Pombo, 2006), chromosome conformation capture methods like Hi-C (Lieberman-Aiden et al., 2009) provide more detailed and accurate information about the organization of chromatin. These results can, e.g., be used to improve the understanding of the cell cycle (Naumova et al., 2013), gene regulation (Cremer and Cremer, 2001) and differentiation of cell types (Dixon et al., 2015).

While initially Hi-C was used for bulk data due to the larger amount of accessible contacts (Stefano et al., 2013; Pierro et al., 2016; Stefano et al., 2016; Dudchenko et al., 2017), more recent approaches use single cell Hi-C (Nagano et al., 2013; Flyamer et al., 2017; Nagano et al., 2017; Ramani et al., 2017; Siebert et al., 2017; Stevens et al., 2017; Tan et al., 2018; Oluwadare et al., 2019) to determine chromatin structure as it accounts for cell-to-cell differences (Ramani et al., 2017). Current models may analyze single-cell Hi-C data without creating 3D structures (Flyamer et al., 2017; Ramani et al., 2017; Ing-Simmons et al., 2021; Zhang et al., 2022), reconstruct complete chromatin structures up to a resolution of

20,000 base pairs per bead (bp) (Tan et al., 2018) or lower (Nagano et al., 2013; Nagano et al., 2017; Stevens et al., 2017; Wettermann et al., 2020) or resolve specific regions of chromatin at higher resolutions (Huang et al., 2020). This is done using various approaches like minimization of bead-spring polymer models with simulated annealing (Nagano et al., 2013; Nagano et al., 2017; Stevens et al., 2017), manifold based optimization (Paulsen et al., 2015) or Bayesian inference (Rosenthal et al., 2019).

In this work, we build upon a polymer-based minimization protocol for low-resolution haploid cells (Wettermann et al., 2020), which allows us to resolve 3D structures of diploid cells up to a maximum of 5 kbp resolution. Essentially, the resolution of the model is successively increased by assigning ambiguous Hi-C contacts based on emerging lower resolution structures. Our procedure is tested for consistency of contact lists and chromosome territories. We also re-analyze the spatial distribution of specific parts of DNA like CpG sites (Tan et al., 2018), which play an important role in DNA transcription (Fatemi et al., 2005).

2 Materials and methods

2.1 Polymer-based chromatin model and basic minimization procedure

Individual chromosomes are modeled as coarse-grained bead-spring polymers consisting of spherical beads connected by harmonic springs (Wettermann et al., 2020). One bead represents between 5,000 and 5,000,000 base pairs depending on the chosen resolution. The specific shape for the analyzed cell is enforced with a second harmonic spring potential connecting non-adjacent beads in contact with each other according to experimental single cell Hi-C matrices. Excluded volume required to enforce non-contacts is implemented via a Gaussian potential:

$$V_{\text{Bond/Contact}}(r) = \frac{1}{2}k_{\text{b/c}}\left(r - r_{0,\text{b/c}}\right)^2 \tag{1}$$

$$V_{\text{Gauss}}(r) = \begin{cases} \varepsilon \exp\left(-\frac{1}{2}\left(\frac{r}{\sigma}\right)^2\right) & r < r_{\text{cut}} \\ 0 & r \geq r_{\text{cut}}. \end{cases} \tag{2}$$

Here, r refers to the distance between two beads. $r_{0,\text{b}} = 1$ and $r_{0,\text{c}} = 1.5$ are preferred distances at which bond or contact energy terms are minimal. While these choices are somewhat arbitrary, differences in r_0 ensure that the degeneracy of the ground state of the model is reduced, i.e., each minimization procedure results in a very similar structure. Likewise, final values for k_b and k_c are large (2000) to ensure small variations of bond and contact distances. Excluded volume is characterized by a width σ and a scale ϵ and acts up to a cutoff distance r_{cut} chosen to be around 1 percent of the maximum of the potential to enforce numerical stability during energy minimization. If not mentioned otherwise, all numbers are given in simulation units.

A Molecular Dynamics minimization run starts by placing beads into a small cube of size 10^3. Beads are connected by the bond potential to form individual chromosomes and equilibrated for a few time steps. Afterwards, contact potentials and excluded volume interactions are enforced and gradually increased in five steps by varying k_c and σ, respectively. Throughout this process, intra- and inter-chain bond crossings occur and enable conformational and topological rearrangement of the chromatin structure. Figure 1A provides the complete protocol including parameters and time steps for each phase - potentials are visualized in Figure 2. The final potentials are the same as in our previous work (Wettermann et al., 2020). Intermediate steps are chosen to ensure smooth adjustments from zero to full potentials. Typical 3D structures at different stages of the minimization can be found in Supplementary Figure S2. After a final structure has been created, bond and contact potentials are reset to zero, the structure collapses, and the procedure can start all over again to generate independent conformations. In previous work (Wettermann et al., 2020), we have shown that a similar protocol always leads to similar structures, which fulfill bond and contact requirements and exhibit pronounced chromosome territories. A further verification of this algorithm by using it to reproduce polymer globules (Virnau et al., 2005) is given in Supplementary Material. Note, however, that mirror images of structures may occur in the process as information on the chirality of the whole chromatin structure is not encoded in the contact matrix. In contrast, the relative chirality of individual chromosomes or regions of chromosomes is encoded in the long-range intra-chromosomal and inter-chromosomal contacts in the contact matrix and therefore not arbitrary. Regions lacking these contacts could, however, have ambiguous local chirality leading to a larger uncertainty of the ensemble of different structures. The energy minimization procedure is loosely inspired from methods to generate starting conformations of polymer melts (Auhl et al., 2003). Simulations are performed on GPUs using the general Molecular Dynamics simulation toolkit HOOMD-blue (Anderson et al., 2008; Glaser et al., 2015) with a Langevin thermostat (damping constant $\gamma = 1$, temperature $k_B T = 1$) and a time step of 0.001.

2.2 Mapping of contacts and assignment of ambiguous contacts

In a diploid structure, single cell Hi-C contacts can often not be assigned unambiguously to the individual chromosomes in homologous pairs. In the worst case, four assignments are conceivable corresponding to the four permutations of two chromosome pairs in question. Here, we perform this assignment subsequently by creating energy-minimized structures with increasing resolutions and using these structures for assignment of ambiguous contacts for higher resolution runs. At low resolutions we aim to have around one unambiguous contact per bead. This ensures that the larger scale chromosome geometry and packing is intact, and hence we can estimate for a given contact which permutations of homologous chromosomes are compatible with the emerging structure. A contact which is inconsistent with a low resolution structure is likely also inconsistent at higher resolution even though our procedure in principle allows for this possibility.

Contacts are mapped to simulation beads by determining which beads contain contact sites. If the two partners of a contact are located on the same bead or in beads already connected by a bond-potential, the contact is omitted for the given resolution but can still be relevant for higher resolutions. Duplicate contacts are also

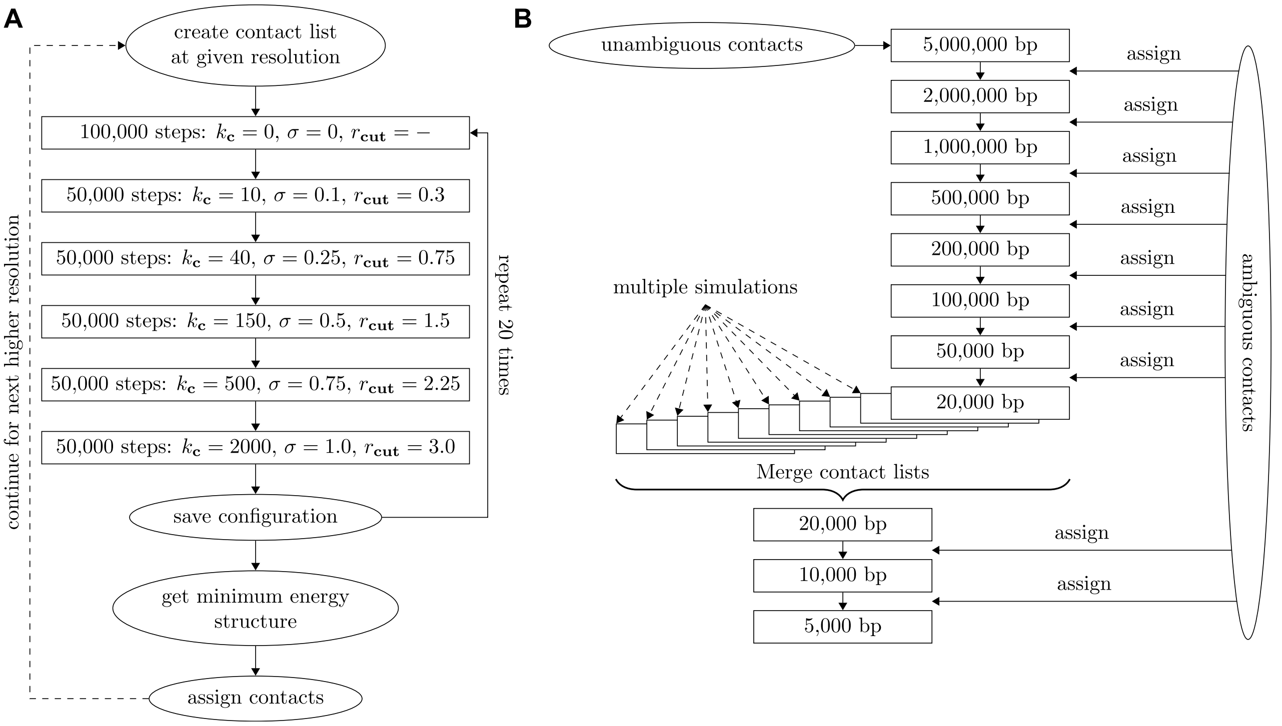

FIGURE 1
(A) Diagram depicting the simulation process at a given resolution including contact assignment and changes of interaction potentials. **(B)** Diagram depicting the contact assignment process with adaptive resolution starting at 5 Mbp. After the first simulation at 20 kbp resolution, contacts from 10 independent runs are merged to get a common contact list.

omitted leading to a fixed contact potential amplitude irrespective of the number of contacts.

We start a first minimization run at a resolution of 5 Mbp resulting in a coarse structure which can be created using only unambiguous contacts. The resolution is then increased up to 20 kbp in eight steps (5M, 2M, 1M, 500k, 200k, 100k, 50k, 20k). After each step, we assign contacts by comparing the distance of all potential contact pairs. This process of contact assignment at increasing resolutions is illustrated in a diagram shown in Figure 1B. A contact is assigned if one assignment option has a distance of less than 3.0 in the minimized structure as the distribution of contract distances decreases significantly for larger values. At the same time the potential contact distances of all other assignment options in the structure need to exceed a value of 5.0 which is incompatible with the distribution of contact distances. If a contact distance becomes larger than 3.0 in the minimized structure, this contact will not be used in the next simulation run (even if it was unambiguous to begin with) and its assignment to specific chromosomes will not be saved. After this run, the contact can, however, be assigned again using the above criteria. This removal option accounts for the uncertainty of the assignment as it allows for correction of assignment and potential Hi-C mapping errors. The reliability of the removal of incorrect assignments was further probed by performing simulations with additional randomly placed contacts (5%) at 100 kbp. In this test, our procedure was able to remove around 90% of the spurious contacts. The distribution of regular and spurious contacts is shown in Supplementary Figure S3.

A resolution of 20 kbp is the highest resolution which can be obtained reliably in a single series of minimization runs, which coincides with the highest resolution in Tan et al. (2018) on which our structures are based. In order to increase resolution further, we merge contact lists from 10 independent minimizations series (each starting at 5 Mbp) to increase the number of contacts: Incompatible contacts which are assigned inconsistently across different runs are discarded as it is not possible to reliably assign them to one specific pair of contact partners. In the case of the cell gm12878_17 (Tan et al., 2018) presented here, e.g., each individual run gave roughly 766,000 contacts. After the merge, a total of 1.01 million contacts were assigned while about 43,000 contact pairs from individual simulations were discarded. Note that these numbers include duplicates at a given resolution and contacts within a bead. The actual number of contacts used for the merged 20 kbp structure is around 499,000. Based on this new contact list, another minimization run is performed at 20 kbp before the resolution is increased further to 10 and finally 5 kbp. The total simulation cycle takes between 2 days and a week on a single GPU depending on the amount of base pairs and contacts and the computational power of the specific GPU used. (In this work we mostly used Nvidia RTX 2070 cards and Nvidia Tesla V100 SXM2 for the higher resolution structures as the latter required more video memory). The concrete protocol should also only serve as a guideline and may need to be adjusted depending on the quality of the available data. Specifically, the initial resolution can be higher if more unambiguous contacts are known. Similarly, the final resolution is limited by the total number

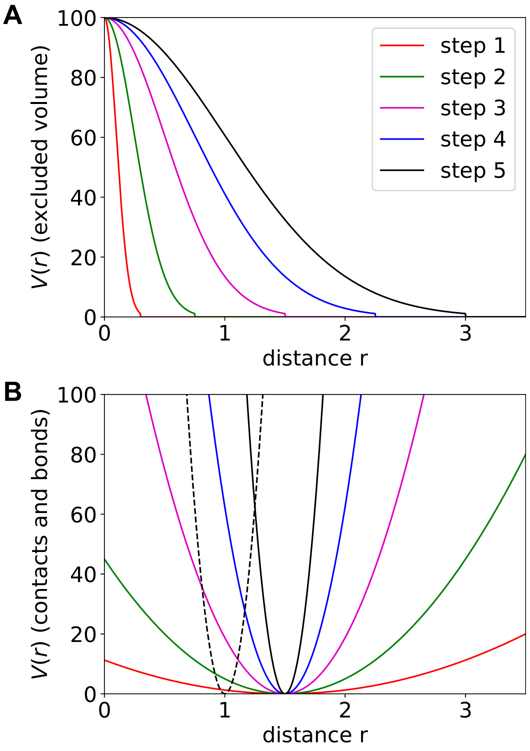

FIGURE 2
Gradually increasing excluded volume **(A)** and contact potentials **(B)** potentials used in the course of the minimization procedure. Potentials drawn in the same color in **(A)** and **(B)** belong to the same step. The excluded volume is increased by increasing the width σ while for the contact potential k_c is increased. The (fixed) bond potential (k_b = 2000) is indicated by a black dotted line in **(B)**.

of contacts. In comparison to our previous studies on haploid cells (Wettermann et al., 2020), here we had to increase the amount of steps in which the interaction potentials were incremented to account for larger cells and higher resolutions to ensure that the simulation program can still thermally equilibrate the conformations appropriately.

2.3 Removal of edge segments without contacts and reflection of mirror images

Typical experimental contact lists contain fairly large parts with only few Hi-C-contacts due to repetitive sequences, so some parts of the chromosomes are not connected to the main structure but form “arms”. These minimization artifacts are located outside the main structure and have different positions in each simulation run. Here, outliers are defined by counting the number of contacts in a 0.5 megabasepair neighborhood of each bead. As suggested by Tan et al. (2018), the 6% of the beads with the lowest number of nearby contacts are removed from the final structures for visualization and analysis purposes. This exclusion could alternatively be performed by removing beads with high RMSD. This approach would lead to a similar result as beads with few contacts are typically less located.

Finally, we need to map mirror-inverted structures onto each other. These mirrored structures occur as information on chirality cannot be deduced from contact lists alone, i.e., a structure and its mirror image are both compatible with the same contact list (Wettermann et al., 2020). As a measure of chirality we use the sign of the triple product of the center of mass positions of the first three chromosomes after translating the entire structure into its total center of mass

$$\mathrm{Chir}\left(\vec{R}^{(1)}, \vec{R}^{(2)}, \vec{R}^{(3)}\right) = \mathrm{sgn}\left(\det\begin{pmatrix} R_x^{(1)} & R_y^{(1)} & R_z^{(1)} \\ R_x^{(2)} & R_y^{(2)} & R_z^{(2)} \\ R_x^{(3)} & R_y^{(3)} & R_z^{(3)} \end{pmatrix}\right), \qquad (3)$$

where sgn is the sign function, det the determinant and $R_j^{(i)}$ the jth component of the center of mass vector of the ith chromosome. In principle, one could also use a singular value decomposition of the same matrix to detect different chiralities. The choice of the first three chromosomes is arbitrary but assuming that the simulated structures have the same chromosome territories at the same place, any choice allows for the same chirality correction. The validity of this assumption has been checked on some samples for 100 kbp and higher resolutions. This result is then used to mirror all structures with Chir = −1 such that all structures have the same chirality.

3 Results

3.1 Cell structures at different resolutions and quality assessment

In the following we visualize our approach and gauge the quality of resulting chromatin structures using an experimental data set for single diploid human cells from Tan et al. (2018). Representative structures at various resolutions are shown in Figure 3. At low resolutions chromosome territories are still not well-developed. Meaningful structures start at a resolution of around 100 kbp (*F*), and exhibit prominent chromosome territories upon increasing the resolution further. The root mean square deviation (RMSD) is employed as a measure for the quality of created structures. Its value between structure j and a structure with mean coordinates is defined as

$$\mathrm{RMSD}_j = \sqrt{\frac{1}{N}\sum_{i=1}^{N}\left(\vec{r_i}(j) - \langle\vec{r_i}\rangle\right)^2}. \qquad (4)$$

High values of the RMSD indicate that structures from different minimization runs (using the same list of contacts) differ significantly and therefore the structures are of low precision. RMSD values for all resolutions are presented in Figure 4. While structures at the coarsest resolution exhibit a rather large RMSD (which in part can be explained by problems arising from our chirality transformation for very coarse structures), the latter drops and stays low up to 100 kbp before rising again due to the reduced number of contacts per bead. Note that the RMSD is given in simulation units and therefore the same RMSD for a higher resolution indicates a smaller relative deviation of the chromatin structure (as beads shrink). The data merge at 20 kbp (which is the highest resolution presented in Tan et al. (2018)) results in a significant drop of the RMSD which enables us to increase resolution further by a factor of two or even four. Overall,

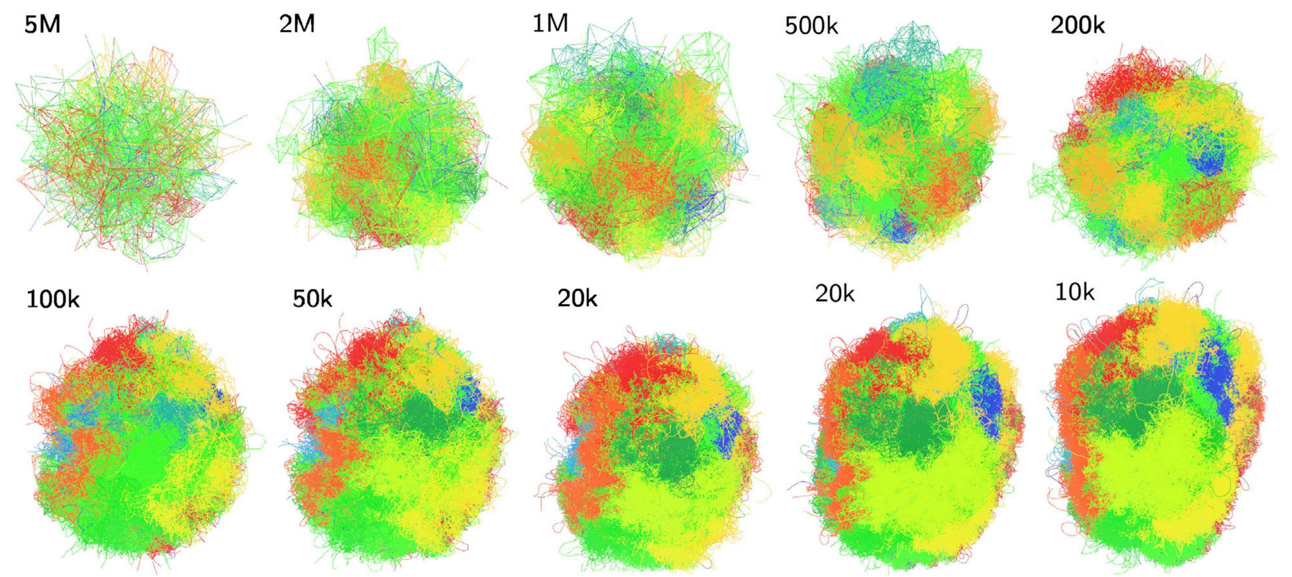

FIGURE 3
Structures of cell gm12878_17 obtained for all resolutions between 5,000,000 and 10,000 bp: The last two structures are using the combined contact list. Structures have been scaled to a similar overall size, rotated and mirrored to allow for a meaningful comparison.

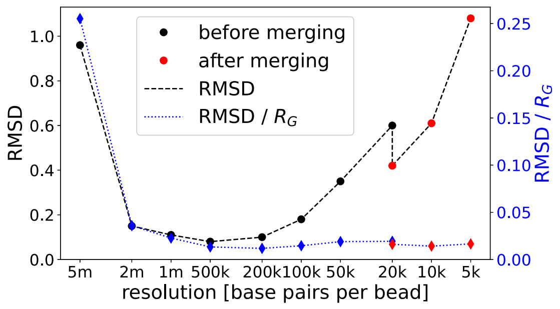

FIGURE 4
Average RMSD values of 20 different structures per resolution obtained from one specific run compared to respective structures with mean coordinates. Lines are added for readability.

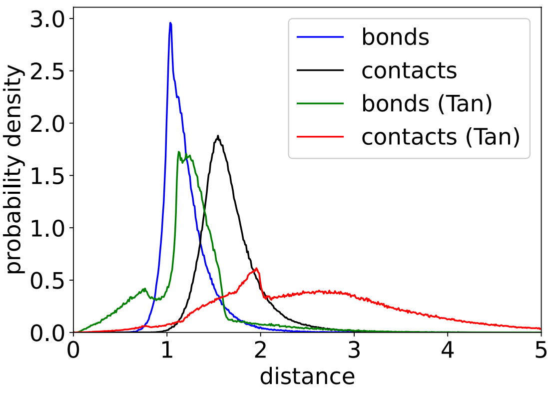

FIGURE 5
Probability density of bond and contact lengths for a 20 kbp structure from our minimization protocol and minimizations performed by Tan et al. (2018).

structures emerging from our procedure yield similar results as the ones provided by Tan et al. (2018). The RMSD of the two 20 kbp structures with the lowest energy resulting from completely independent runs starting at 5 Mbp resolution is 0.96 (after the merge) as opposed to 1.23 in Tan et al. (2018) after correcting for chirality.

Bond and contact length distributions of 3D structures indicate how well simulation results agree with a given list of contacts. A perfect structure would exhibit narrow peaks of these distributions near the potential minima, which are at 1.0 for bonds and at 1.5 for contacts in this work. However, limitations of our model such as potential assignment errors and the incompleteness of the underlying experimental contact matrix as well as potential mapping errors lead to broader distributions with slightly overstretched bonds and contacts as shown in Figure 5. In comparison, results of Tan et al. (2018) show a more complex behavior with several peaks and a somewhat broader distribution.

The final step of the simulation protocol yields structures at a resolution of 5 kbp. One such structure is presented from two perspectives in Figure 6. Chromosome territories are clearly visible for all chromosomes and the overall shape of the 3D structure is rather prolate than spherical and somewhat rougher compared to lower resolution structures, which indicates that the resolution should not be increased further (in agreement with our observations of RMSDs). Further cells from the same data set are displayed in Supplementary Figure S4. In Supplementary Figure S5 we also display a contact matrix based on the final 5 kbp structure shown above. Recorded Hi-C contacts

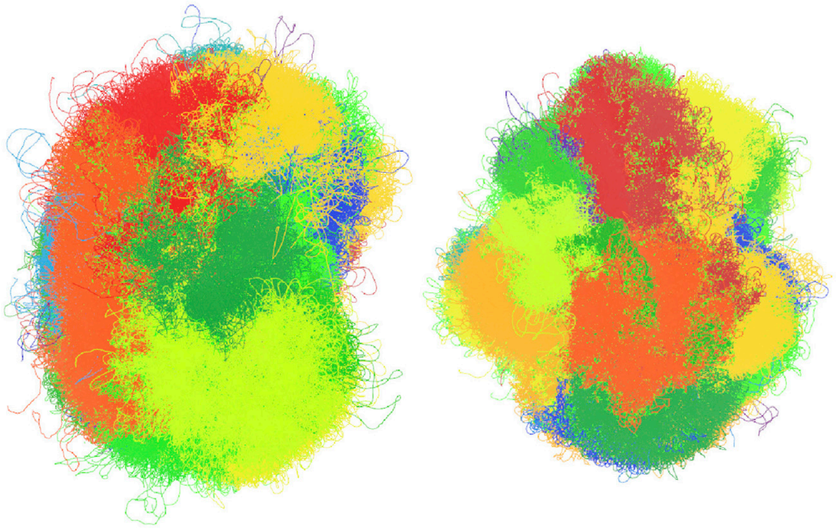

FIGURE 6
Two different perspectives on the chromatin structure of cell gm12878_17 (Tan et al., 2018) at a resolution of 5 kbp. The two images have the same relative size.

roughly account for 1.5% of the close beads pairs observed in the final structure (defined as distances smaller than 3) which lies in the expected range (Stevens et al., 2017).

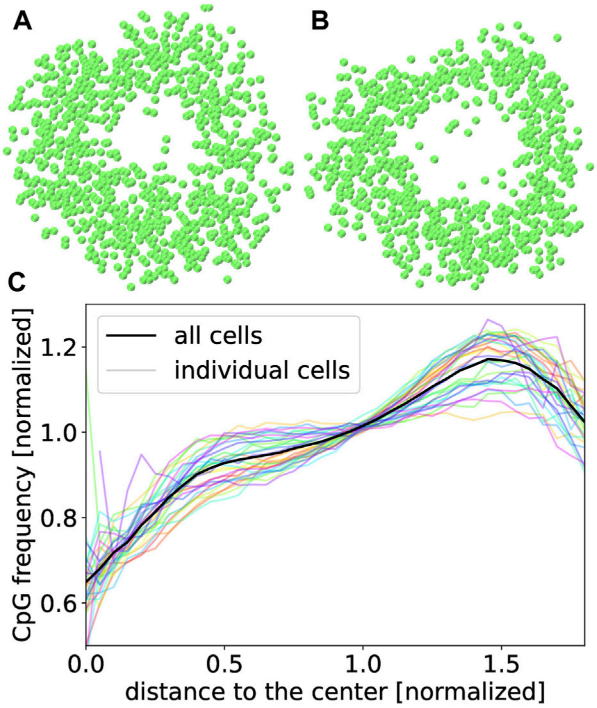

FIGURE 7
Cross-sections through the center of 20 kbp structures of cell 170 from Tan et al. (2019) **(A)** and from this work **(B)**. Both cuts are done along the same plane. **(C)** CpG density averaged over 30 different male young adult rod photoreceptor cells from Tan et al. (2019) at a resolution of 20 kbp. The transparent lines show the CpG density of each individual cell.

3.2 Rod photoreceptor cells

Our procedure was also adapted to rod photoreceptor cells of mice from Tan et al. (2019). As less Hi-C contacts were available for this data set, the protocol was modified to only include resolutions up to 20 kbp and exclude merging of contact lists. Additionally, the lowest simulated resolution was 500 kbp because the set contains a larger fraction of unambiguous contacts.

Resulting 3D structures contain a clearly visible hole for most rod photoreceptor cells as shown in Figure 7. Holes resulting from our procedure (B) tend to be somewhat larger than in structures published by Tan et al. (2019) (A) which can likely be explained by the employment of spherical confinement in (A) while our minimizations were unconstrained.

Another special property of rod photoreceptor cells is the inverted CpG density distribution. While most cells have the highest density of CpG sites near their center, rod photoreceptors are assumed to have the highest value in the periphery (Solovei et al., 2009; Tan et al., 2019). This inversion was found for all 30 cells we have analyzed as shown in Figure 7.

4 Discussion

We developed a computational scheme based on Molecular Dynamics simulations at multiple resolutions and a bead-spring model for DNA which allows for assignment of ambiguous single cell Hi-C contacts applying a structure-based approach. As a result, robust single-cell 3D structures of interphase chromatin in diploid cells could be simulated at resolutions of up to 5,000 base pairs per bead improving upon previously achievable resolutions based on the same data (Tan et al., 2018). Computational effort to recreate 3D structures at a resolution of 20 kbp only amounts to a few hours on a single GPU, while resolutions of 5 kbp can be obtained in a few days. Our model and procedure was verified and assessed on two previously published data sets of diploid cells

(Tan et al., 2018; 2019). We were also able to reproduce prominent structural features such as CpG inversion in photoreceptor cells while maintaining a high level of structural fidelity as indicated by low RMSDs and rather tight bond and contact distributions. In future research, one could test the reliability and potentially extend our approach to even more challenging systems such as tetraploid cells (Sun et al., 2022) or cells exhibiting chromosome alignment.

Data availability statement

Publicly available datasets were analyzed in this study. This data can be found here: https://www.ncbi.nlm.nih.gov/geo/query/acc.cgi?acc=GSE117874 and https://www.ncbi.nlm.nih.gov/geo/query/acc.cgi?acc=GSE121791. The code required to perform the computer simulations presented here is publicly availible on https://gitlab.rlp.net/3d-diploid-chromatin/simulation-code/.

Ethics statement

Ethical approval was not required for the study involving humans in accordance with the local legislation and institutional requirements. Written informed consent to participate in this study was not required from the participants or the participants' legal guardians/next of kin in accordance with the national legislation and the institutional requirements.

Author contributions

JR: Writing–original draft, Data curation, Formal Analysis, Investigation, Methodology, Software, Validation, Visualization, Writing–review and editing. MB: Methodology, Software, Writing–review and editing. TS: Conceptualization, Writing–review and editing. PV: Writing–original draft, Conceptualization, Funding acquisition, Project administration, Resources, Supervision, Writing–review and editing.

Funding

The author(s) declare financial support was received for the research, authorship, and/or publication of this article. This project was funded by the Deutsche Forschungsgemeinschaft (DFG, German Research Foundation)—SFB 1551—Project No. 464588647. The authors also acknowledge funding by the Horizon Europe Project no. 101070290 (NIMFEIA) and from TopDyn. MB is supported by a doctoral scholarship of the Studienstiftung des deutschen Volkes. TJS is supported by the Medical Research Council, as part of United Kingdom Research and Innovation (MC_U105178783).

Conflict of interest

The authors declare that the research was conducted in the absence of any commercial or financial relationships that could be construed as a potential conflict of interest.

Publisher's note

Supplementary material

The Supplementary Material for this article can be found online at: https://www.frontiersin.org/articles/10.3389/fbinf.2023.1284484/full#supplementary-material

References

Anderson, J. A., Lorenz, C. D., and Travesset, A. (2008). General purpose molecular dynamics simulations fully implemented on graphics processing units. *J. Comput. Phys.* 227, 5342–5359. doi:10.1016/j.jcp.2008.01.047

Auhl, R., Everaers, R., Grest, G. S., Kremer, K., and Plimpton, S. J. (2003). Equilibration of long chain polymer melts in computer simulations. *J. Chem. Phys.* 119, 12718–12728. doi:10.1063/1.1628670

Bolzer, A., Kreth, G., Solovei, I., Koehler, D., Saracoglu, K., Fauth, C., et al. (2005). Three-dimensional maps of all chromosomes in human male fibroblast nuclei and prometaphase rosettes. *PLOS Biol.* 3, e157. doi:10.1371/journal.pbio.0030157

Branco, M. R., and Pombo, A. (2006). Intermingling of chromosome territories in interphase suggests role in translocations and transcription-dependent associations. *PLOS Biol.* 4, e138. doi:10.1371/journal.pbio.0040138

Cremer, T., and Cremer, C. (2001). Chromosome territories, nuclear architecture and gene regulation in mammalian cells. *Nat. Rev. Genet.* 2, 292–301. doi:10.1038/35066075

Cremer, T., Kurz, A., Zirbel, R. M., Dietzel, S., Rinke, B., Schröck, E., et al. (1993). Role of chromosome territories in the functional compartmentalization of the cell nucleus. *Cold Spring Harb. Symposia Quantitative Biol.* 58, 777–792. doi:10.1101/SQB.1993.058.01.085

Dixon, J. R., Jung, I., Selvaraj, S., Shen, Y., Antosiewicz-Bourget, J. E., Lee, A. Y., et al. (2015). Chromatin architecture reorganization during stem cell differentiation. *Nature* 518, 331–336. doi:10.1038/nature14222

Dudchenko, O., Batra, S. S., Omer, A. D., Nyquist, S. K., Hoeger, M., Durand, N. C., et al. (2017). *De novo* assembly of the *Aedes aegypti* genome using Hi-C yields chromosome-length scaffolds. *Science* 356, 92–95. doi:10.1126/science.aal3327

Fatemi, M., Pao, M. M., Jeong, S., Gal-Yam, E. N., Egger, G., Weisenberger, D. J., et al. (2005). Footprinting of mammalian promoters: use of a CpG DNA methyltransferase revealing nucleosome positions at a single molecule level. *Nucleic Acids Res.* 33, e176. doi:10.1093/nar/gni180

Flyamer, I. M., Gassler, J., Imakaev, M., Brandão, H. B., Ulianov, S. V., Abdennur, N., et al. (2017). Single-nucleus Hi-C reveals unique chromatin reorganization at oocyte-to-zygote transition. *Nature* 544, 110–114. doi:10.1038/nature21711

Glaser, J., Nguyen, T. D., Anderson, J. A., Lui, P., Spiga, F., Millan, J. A., et al. (2015). Strong scaling of general-purpose molecular dynamics simulations on GPUs. *Comput. Phys. Commun.* 192, 97–107. doi:10.1016/j.cpc.2015.02.028

Huang, K., Li, Y., Shim, A. R., Virk, R. K. A., Agrawal, V., Eshein, A., et al. (2020). Physical and data structure of 3D genome. *Sci. Adv.* 6, eaay4055. doi:10.1126/sciadv.aay4055

Ing-Simmons, E., Vaid, R., Bing, X. Y., Levine, M., Mannervik, M., and Vaquerizas, J. M. (2021). Independence of chromatin conformation and gene regulation during drosophila dorsoventral patterning. *Nat. Genet.* 53, 487–499. doi:10.1038/s41588-021-00799-x

Lieberman-Aiden, E., van Berkum, N. L., Williams, L., Imakaev, M., Ragoczy, T., Telling, A., et al. (2009). Comprehensive mapping of long-range interactions reveals folding principles of the human genome. *Science* 326, 289–293. doi:10.1126/science.1181369

Nagano, T., Lubling, Y., Stevens, T., Schoenfelder, S., Yaffe, E., Dean, W., et al. (2013). Single-cell Hi-C reveals cell-to-cell variability in chromosome structure. *Nature* 502, 59–64. doi:10.1038/nature12593

Nagano, T., Lubling, Y., Várnai, C., Dudley, C., Leung, W., Baran, Y., et al. (2017). Cell-cycle dynamics of chromosomal organization at single-cell resolution. *Nature* 547, 61–67. doi:10.1038/nature23001

Naumova, N., Imakaev, M., Fudenberg, G., Zhan, Y., Lajoie, B. R., Mirny, L. A., et al. (2013). Organization of the mitotic chromosome. *Science* 342, 948–953. doi:10.1126/science.1236083

Oluwadare, O., Highsmith, M., and Cheng, J. (2019). An overview of methods for reconstructing 3-D chromosome and genome structures from Hi-C data. *Biol. Proced. Online* 21, 7. doi:10.1186/s12575-019-0094-0

Paulsen, J., Gramstad, O., and Collas, P. (2015). Manifold based optimization for single-cell 3D genome reconstruction. *PLOS Comput. Biol.* 11, 10043966. doi:10.1371/journal.pcbi.1004396

Pierro, M. D., Zhang, B., Aiden, E. L., Wolynes, P. G., and Onuchic, J. N. (2016). Transferable model for chromosome architecture. *Proc. Natl. Acad. Sci.* 113, 12168–12173. doi:10.1073/pnas.1613607113

Ramani, V., Deng, X., Qiu, R., Gunderson, K. L., Steemers, F. J., Disteche, C. M., et al. (2017). Massively multiplex single-cell Hi-C. *Nat. Methods* 14, 263–266. doi:10.1038/nmeth.4155

Rosenthal, M., Bryner, D., Huffer, F., Evans, S., Srivastava, A., and Neretti, N. (2019). Bayesian estimation of three-dimensional chromosomal structure from single-cell Hi-C data. *J. Comput. Biol.* 26, 1191–1202. doi:10.1089/cmb.2019.0100

Siebert, J. T., Kivel, A. N., Atkinson, L. P., Stevens, T., Laue, E., and Virnau, P. (2017). Are there knots in chromosomes? *Polymers* 9, 317. doi:10.3390/polym9080317

Solovei, I., Kreysing, M., Lanctot, C., Kösem, S., Peichl, L., Cremer, T., et al. (2009). Nuclear architecture of rod photoreceptor cells adapts to vision in mammalian evolution. *Cell* 173, 356–368. doi:10.1016/j.cell.2009.01.052

Stefano, M. D., Paulsen, J., Lien, T. G., Hovig, E., and Micheletti, C. (2016). Hi-C-constrained physical models of human chromosomes recover functionally-related properties of genome organization. *Sci. Rep.* 6, 35985. doi:10.1038/srep35985

Stefano, M. D., Rosa, A., Belcastro, V., di Bernardo, D., and Micheletti, C. (2013). Colocalization of coregulated genes: a steered molecular dynamics study of human chromosome 19. *PLOS Comput. Biol.* 9, 1–13. doi:10.1371/journal.pcbi.1003019

Stevens, T. J., Lando, D., Basu, S., Atkinson, L. P., Cao, Y., Lee, S. F., et al. (2017). 3D structures of individual mammalian genomes studied by single-cell Hi-C. *Nature* 544, 59–64. doi:10.1038/nature21429

Sun, H., Jiao, W.-B., Krause, K., Campoy, J. A., Goel, M., Folz-Donahue, K., et al. (2022). Chromosome-scale and haplotype-resolved genome assembly of a tetraploid potato cultivar. *Nat. Genet.* 54, 342–348. doi:10.1038/s41588-022-01015-0

Tan, L., Xing, D., Chang, C.-H., Li, H., and Xie, X. S. (2018). Three-dimensional genome structures of single diploid human cells. *Science* 361, 924–928. doi:10.1126/science.aat5641

Tan, L., Xing, D., Daley, N., and Xie, X. S. (2019). Three-dimensional genome structures of single sensory neurons in mouse visual and olfactory systems. *Nat. Struct. Mol. Biol.* 26, 297–307. doi:10.1038/s41594-019-0205-2

Virnau, P., Kantor, Y., and Kardar, M. (2005). Knots in globule and coil phases of a model polyethylene. *J. Am. Chem. Soc.* 127, 15102–15106. doi:10.1021/ja052438a

Wettermann, S., Brems, M., Siebert, J. T., Vu, G. T., Stevens, T. J., and Virnau, P. (2020). A minimal Gō-model for rebuilding whole genome structures from haploid single-cell Hi-C data. *Comput. Mater. Sci.* 173, 109178. doi:10.1016/j.commatsci.2019.109178

Zhang, R., Zhou, T., and Ma, J. (2022). Multiscale and integrative single-cell Hi-C analysis with Higashi. *Nat. Biotechnol.* 40, 254–261. doi:10.1038/s41587-021-01034-y

A.7 Anhänge Gemäß Prüfungsordnung

Removed due to data privacy.

This page is intentionally left blank.

Removed due to data privacy.

Removed due to data privacy.

B. References

[1] X. Fang, L. Tao, and Z. Li. “Anchoring AI Capabilities in Market Valuations: The Capability Realization Rate Model and Valuation Misalignment Risk.” *arXiv: 2505.10590* (2025).

[2] B. Cottier, R. Rahman, L. Fattorini, N. Maslej, T. Besiroglu, and D. Owen. “The rising costs of training frontier AI models.” *arXiv: 2405.21015* (2025).

[3] G. E. Moore. “Cramming more components onto integrated circuits, Reprinted from Electronics, volume 38, number 8, April 19, 1965, pp.114 ff.” *IEEE Solid-State Circuits Society Newsletter* 11.3 (2006), 33–35.

[4] M. M. Waldrop. “The chips are down for Moore’s law.” *Nature News* 530.7589 (2016), 144.

[5] J. D. Meindl, Q. Chen, and J. A. Davis. “Limits on Silicon Nanoelectronics for Terascale Integration.” *Science* 293.5537 (2001), 2044–2049.

[6] U. K. Rößler, A. N. Bogdanov, and C. Pfleiderer. “Spontaneous skyrmion ground states in magnetic metals.” *Nature* 442.7104 (2006), 797–801.

[7] S. Mühlbauer, B. Binz, F. Jonietz, C. Pfleiderer, A. Rosch, A. Neubauer, R. Georgii, and P. Böni. “Skyrmion Lattice in a Chiral Magnet.” *Science* 323.5916 (2009), 915–919.

[8] X. Z. Yu, Y. Onose, N. Kanazawa, J. H. Park, J. H. Han, Y. Matsui, N. Nagaosa, and Y. Tokura. “Real-space observation of a two-dimensional skyrmion crystal.” *Nature* 465.7300 (2010), 901–904.

[9] K. Everschor-Sitte, J. Masell, R. M. Reeve, and M. Kläui. “Perspective: Magnetic skyrmions—Overview of recent progress in an active research field.” *Journal of Applied Physics* 124.24 (2018), 240901.

[10] G. Finocchio, F. Büttner, R. Tomasello, M. Carpentieri, and M. Kläui. “Magnetic skyrmions: from fundamental to applications.” *J. Phys. D: Appl. Phys.* 49.42 (2016), 423001.

[11] S.-Z. Lin, C. Reichhardt, C. D. Batista, and A. Saxena. “Particle model for skyrmions in metallic chiral magnets: Dynamics, pinning, and creep.” *Phys. Rev. B* 87.21 (2013), 214419.

[12] A. F. Schäffer, L. Rózsa, J. Berakdar, E. Y. Vedmedenko, and R. Wiesendanger. “Stochastic dynamics and pattern formation of geometrically confined skyrmions.” *Commun Phys* 2.1 (2019), 72.

[13] D. Capic, D. A. Garanin, and E. M. Chudnovsky. “Skyrmion–skyrmion interaction in a magnetic film.” *J. Phys.: Condens. Matter* 32.41 (2020), 415803.

[14] R. Brearton, G. van der Laan, and T. Hesjedal. “Magnetic skyrmion interactions in the micromagnetic framework.” *Phys. Rev. B* 101.13 (2020), 134422.

[15] Y. Ge, J. Rothörl, M. A. Brems, N. Kerber, R. Gruber, T. Dohi, M. Kläui, and P. Virnau. “Constructing coarse-grained skyrmion potentials from experimental data with Iterative Boltzmann Inversion.” *Commun Phys* 6.30 (2023), 1–6.

[16] J. Zázvorka, F. Jakobs, D. Heinze, N. Keil, S. Kromin, S. Jaiswal, K. Litzius, G. Jakob, P. Virnau, D. Pinna, K. Everschor-Sitte, L. Rózsa, A. Donges, U. Nowak, and M. Kläui. “Thermal skyrmion diffusion used in a reshuffler device.” *Nat. Nanotechnol.* 14.7 (2019), 658–661.

[17] Y. Jibiki, M. Goto, E. Tamura, J. Cho, S. Miki, R. Ishikawa, H. Nomura, T. Srivastava, W. Lim, S. Auffret, C. Baraduc, H. Bea, and Y. Suzuki. “Skyrmion Brownian circuit implemented in continuous ferromagnetic thin film.” *Applied Physics Letters* 117.8 (2020), 082402.

[18] S. Woo, K. Litzius, B. Krüger, M.-Y. Im, L. Caretta, K. Richter, M. Mann, A. Krone, R. M. Reeve, M. Weigand, P. Agrawal, I. Lemesh, M.-A. Mawass, P. Fischer, M. Kläui, and G. S. D. Beach. “Observation of room-temperature magnetic skyrmions and their current-driven dynamics in ultrathin metallic ferromagnets.” *Nature Mater* 15.5 (2016), 501–506.

[19] X. Z. Yu, N. Kanazawa, W. Z. Zhang, T. Nagai, T. Hara, K. Kimoto, Y. Matsui, Y. Onose, and Y. Tokura. “Skyrmion flow near room temperature in an ultralow current density.” *Nat Commun* 3.1 (2012), 988.

[20] K. Litzius, J. Leliaert, P. Bassirian, D. Rodrigues, S. Kromin, I. Lemesh, J. Zazvorka, K.-J. Lee, J. Mulkers, N. Kerber, D. Heinze, N. Keil, R. M. Reeve, M. Weigand, B. Van Waeyenberge, G. Schütz, K. Everschor-Sitte, G. S. D. Beach, and M. Kläui. “The role of temperature and drive current in skyrmion dynamics.” *Nat Electron* 3.1 (2020), 30–36.

[21] S. L. Zhang, W. W. Wang, D. M. Burn, H. Peng, H. Berger, A. Bauer, C. Pfleiderer, G. van der Laan, and T. Hesjedal. “Manipulation of skyrmion motion by magnetic field gradients.” *Nat Commun* 9.1 (2018), 2115.

[22] R. Tomasello, M. Ricci, P. Burrascano, V. Puliafito, M. Carpentieri, and G. Finocchio. “Electrical detection of single magnetic skyrmion at room temperature.” *AIP Advances* 7.5 (2017), 056022.

[23] A. Fert, V. Cros, and J. Sampaio. “Skyrmions on the track.” *Nature Nanotech* 8.3 (2013), 152–156.

[24] X. Zhang, G. P. Zhao, H. Fangohr, J. P. Liu, W. X. Xia, J. Xia, and F. J. Morvan. “Skyrmion-skyrmion and skyrmion-edge repulsions in skyrmion-based racetrack memory.” *Sci Rep* 5.1 (2015), 7643.

[25] D. Pinna, G. Bourianoff, and K. Everschor-Sitte. “Reservoir Computing with Random Skyrmion Textures.” *Phys. Rev. Appl.* 14.5 (2020), 054020.

[26] D. Prychynenko, M. Sitte, K. Litzius, B. Krüger, G. Bourianoff, M. Kläui, J. Sinova, and K. Everschor-Sitte. "Magnetic Skyrmion as a Nonlinear Resistive Element: A Potential Building Block for Reservoir Computing." *Phys. Rev. Appl.* 9.1 (2018), 014034.

[27] G. Bourianoff, D. Pinna, M. Sitte, and K. Everschor-Sitte. "Potential implementation of reservoir computing models based on magnetic skyrmions." *AIP Advances* 8.5 (2018), 055602.

[28] O. Lee, R. Msiska, M. A. Brems, M. Kläui, H. Kurebayashi, and K. Everschor-Sitte. "Perspective on unconventional computing using magnetic skyrmions." *Applied Physics Letters* 122.26 (2023), 260501.

[29] M. A. Brems, M. Kläui, and P. Virnau. "Circuits and excitations to enable Brownian token-based computing with skyrmions." *Appl. Phys. Lett.* 119.13 (2021), 132405.

[30] M. A. Brems, M. Kläui, and P. Virnau. "Information processing apparatus." *International Patent: WO2022200504A1* (2022).

[31] K. Raab, M. A. Brems, G. Beneke, T. Dohi, J. Rothörl, F. Kammerbauer, J. H. Mentink, and M. Kläui. "Brownian reservoir computing realized using geometrically confined skyrmion dynamics." *Nat Commun* 13.1 (2022), 6982.

[32] G. Beneke, T. B. Winkler, K. Raab, M. A. Brems, F. Kammerbauer, P. Gerhards, K. Knobloch, S. Krishnia, J. H. Mentink, and M. Kläui. "Gesture recognition with Brownian reservoir computing using geometrically confined skyrmion dynamics." *Nat Commun* 15.1 (2024), 8103.

[33] J. Zázvorka, F. Dittrich, Y. Ge, N. Kerber, K. Raab, T. Winkler, K. Litzius, M. Veis, P. Virnau, and M. Kläui. "Skyrmion Lattice Phases in Thin Film Multilayer." *Advanced Functional Materials* 30.46 (2020), 2004037.

[34] R. Gruber, J. Rothörl, S. M. Fröhlich, M. A. Brems, F. Kammerbauer, M.-A. Syskaki, E. M. Jefremovas, S. Krishnia, A. Sudbø, P. Virnau, and M. Kläui. "Real-time observation of topological defect dynamics mediating two-dimensional skyrmion lattice melting." *Nat. Nanotechnol.* in press (2025).

[35] K. Everschor-Sitte, M. Sitte, T. Valet, A. Abanov, and J. Sinova. "Skyrmion production on demand by homogeneous DC currents." *New J. Phys.* 19.9 (2017), 092001.

[36] R. Gruber, J. Zázvorka, M. A. Brems, D. R. Rodrigues, T. Dohi, N. Kerber, B. Seng, M. Vafaee, K. Everschor-Sitte, P. Virnau, and M. Kläui. "Skyrmion pinning energetics in thin film systems." *Nat Commun* 13.1 (2022), 3144.

[37] R. Gruber, M. A. Brems, J. Rothörl, T. Sparmann, M. Schmitt, I. Kononenko, F. Kammerbauer, M.-A. Syskaki, O. Farago, P. Virnau, and M. Kläui. "300-Times-Increased Diffusive Skyrmion Dynamics and Effective Pinning Reduction by Periodic Field Excitation." *Advanced Materials* 35.17 (2023), 2208922.

[38] K. Raab, M. Schmitt, M. A. Brems, J. Rothörl, F. Kammerbauer, S. Krishnia, M. Kläui, and P. Virnau. "Skyrmion flow in periodically modulated channels." *Phys. Rev. E* 110.4 (2024), L042601.

[39] M. A. Brems, T. Sparmann, S. M. Fröhlich, L.-C. Dany, J. Rothörl, F. Kammerbauer, E. M. Jefremovas, O. Farago, M. Kläui, and P. Virnau. “Realizing Quantitative Quasiparticle Modeling of Skyrmion Dynamics in Arbitrary Potentials.” *Phys. Rev. Lett.* 134.4 (2025), 046701.

[40] A. A. Thiele. “Steady-State Motion of Magnetic Domains.” *Phys. Rev. Lett.* 30.6 (1973), 230–233.

[41] M. von Smoluchowski. “Zur kinetischen Theorie der Brownschen Molekularbewegung und der Suspensionen.” *Annalen der Physik* 326.14 (1906), 756–780.

[42] C. Song, N. Kerber, J. Rothörl, Y. Ge, K. Raab, B. Seng, M. A. Brems, F. Dittrich, R. M. Reeve, J. Wang, Q. Liu, P. Virnau, and M. Kläui. “Commensurability between Element Symmetry and the Number of Skyrmions Governing Skyrmion Diffusion in Confined Geometries.” *Advanced Functional Materials* 31.19 (2021), 2010739.

[43] T. B. Winkler, J. Rothörl, M. A. Brems, G. Beneke, H. Fangohr, and M. Kläui. “Coarse-graining collective skyrmion dynamics in confined geometries.” *Applied Physics Letters* 124.2 (2024), 022403.

[44] S. M. Fröhlich, T. Sparmann, M. A. Brems, J. Rothörl, F. Kammerbauer, K. Raab, S. Krishnia, M. Kläui, and P. Virnau. “Real-Time Simulation of Skyrmion Dynamics in 2D spatially-dependent Pinning Potential Landscapes.” *in preparation* (2025).

[45] H. Jaeger. “The ”echo state” approach to analysing and training recurrent neural networks-with an erratum note’.” *Bonn, Germany: German National Research Center for Information Technology GMD Technical Report* 148 (2001).

[46] W. Maass, T. Natschläger, and H. Markram. “Real-Time Computing Without Stable States: A New Framework for Neural Computation Based on Perturbations.” *Neural Computation* 14.11 (2002), 2531–2560.

[47] K. Nakajima and I. Fischer, eds. *Reservoir Computing: Theory, Physical Implementations, and Applications.* Natural Computing Series. Singapore, 2021.

[48] G. Tanaka, T. Yamane, J. B. Héroux, R. Nakane, N. Kanazawa, S. Takeda, H. Numata, D. Nakano, and A. Hirose. “Recent advances in physical reservoir computing: A review.” *Neural Networks* 115 (2019), 100–123.

[49] K. Nakajima. “Physical reservoir computing—an introductory perspective.” *Jpn. J. Appl. Phys.* 59.6 (2020), 060501.

[50] R. Msiska, J. Love, J. Mulkers, J. Leliaert, and K. Everschor-Sitte. “Audio Classification with Skyrmion Reservoirs.” *Advanced Intelligent Systems* 5.6 (2023), 2200388.

[51] F. Peper, J. Lee, J. Carmona, J. Cortadella, and K. Morita. “Brownian Circuits: Fundamentals.” *J. Emerg. Technol. Comput. Syst.* 9.1 (2013), 3:1–3:24.

[52] J. Lee, F. Peper, S. D. Cotofana, M. Naruse, M. Ohtsu, T. Kawazoe, Y. Takahashi, T. Shimokawa, L. B. Kish, and T. Kubota. “Brownian Circuits: Designs.” *Int. Journ. of Unconventional Computing* 12 (2016), 341–362.

[53] M. A. Brems, K. Raab, P. Virnau, and M. Kläui. “Brownscher Reservoir-Computer mit Skyrmionen.” *Physik in unserer Zeit* 54.2 (2023), 60–61.

[54] M. A. Brems, R. Runkel, T. O. Yeates, and P. Virnau. “AlphaFold predicts the most complex protein knot and composite protein knots.” *Protein Science* 31.8 (2022), e4380.

[55] J. Rothörl, M. A. Brems, T. J. Stevens, and P. Virnau. “Reconstructing diploid 3D chromatin structures from single cell Hi-C data with a polymer-based approach.” *Frontiers in Bioinformatics* 3 (2023).

[56] J. M. D. Coey. *Magnetism and Magnetic Materials.* Cambridge, 2010. ISBN: 978-0-521-81614-4.

[57] A. Einstein and W. J. de Haas. “Experimenteller Nachweis der Ampèreschen Molekularströme.” *Deutsche Physikalische Gesellschaft* 17 (1915), 152–170.

[58] A. Vansteenkiste, J. Leliaert, M. Dvornik, M. Helsen, F. Garcia-Sanchez, and B. Van Waeyenberge. “The design and verification of MuMax3.” *AIP Advances* 4.10 (2014), 107133.

[59] S. Blundell. *Magnetism in Condensed Matter.* 2001. 251 pp. ISBN: 978-0-19-850592-1.

[60] W. Pauli. “The Connection Between Spin and Statistics.” *Phys. Rev.* 58.8 (1940), 716–722.

[61] D. J. Griffiths and D. F. Schroeter. *Introduction to Quantum Mechanics.* 2018. 511 pp. ISBN: 978-1-107-18963-8.

[62] W. Heisenberg. “Zur Theorie des Ferromagnetismus.” *Z. Physik* 49.9 (1928), 619–636.

[63] I. Dzyaloshinsky. “A thermodynamic theory of “weak” ferromagnetism of antiferromagnetics.” *Journal of Physics and Chemistry of Solids* 4.4 (1958), 241–255.

[64] T. Moriya. “Anisotropic Superexchange Interaction and Weak Ferromagnetism.” *Phys. Rev.* 120.1 (1960), 91–98.

[65] R. E. Camley and K. L. Livesey. “Consequences of the Dzyaloshinskii-Moriya interaction.” *Surface Science Reports* 78.3 (2023), 100605.

[66] R. Gross and A. Marx. *Festkörperphysik.* 2022. ISBN: 978-3-11-078239-4.

[67] A. Hubert and R. Schäfer. *Magnetic Domains: The Analysis of Magnetic Microstructures.* 1998. 1182 pp. ISBN: 978-3-540-64108-7.

[68] T. Gilbert. “A phenomenological theory of damping in ferromagnetic materials.” *IEEE Transactions on Magnetics* 40.6 (2004), 3443–3449.

[69] M. Lakshmanan. “The fascinating world of the Landau–Lifshitz–Gilbert equation: an overview.” *Philosophical Transactions of the Royal Society A: Mathematical, Physical and Engineering Sciences* 369.1939 (2011), 1280–1300.

[70] K. Everschor-Sitte. “Current-Induced Dynamics of Chiral Magnetic Structures: Skyrmions, Emergent Electrodynamics and Spin-Transfer Torques.” PhD thesis. 2012.

[71] R. F. L. Evans, W. J. Fan, P. Chureemart, T. A. Ostler, M. O. A. Ellis, and R. W. Chantrell. “Atomistic spin model simulations of magnetic nanomaterials.” *J. Phys.: Condens. Matter* 26.10 (2014), 103202.

[72] *MicroMagnum/MicroMagnum (GitHub).* 2025.

[73] *COMSOL Multiphysics® Ver. 5.5 (Software).* Stockholm, Sweden.

[74] J. R. Dormand and P. J. Prince. "A family of embedded Runge-Kutta formulae." *Journal of Computational and Applied Mathematics* 6.1 (1980), 19–26.

[75] T. H. R. Skyrme and B. F. J. Schonland. "A non-linear theory of strong interactions." *Proceedings of the Royal Society of London. Series A. Mathematical and Physical Sciences* 247.1249 (1997), 260–278.

[76] T. H. R. Skyrme. "A unified field theory of mesons and baryons." *Nuclear Physics* 31 (1962), 556–569.

[77] N. Nagaosa and Y. Tokura. "Topological properties and dynamics of magnetic skyrmions." *Nature Nanotech* 8.12 (2013), 899–911.

[78] E. Raimondo, E. Saugar, J. Barker, D. Rodrigues, A. Giordano, M. Carpentieri, W. Jiang, O. Chubykalo-Fesenko, R. Tomasello, and G. Finocchio. "Temperature-Gradient-Driven Magnetic Skyrmion Motion." *Phys. Rev. Appl.* 18.2 (2022), 024062.

[79] FromSoftware. *Armored Core VI: Fires of Rubicon, Mission objective: Destroy the large skyrmion generators (Software).* 2023.

[80] A. H. Marcus and S. A. Rice. "Observations of First-Order Liquid-to-Hexatic and Hexatic-to-Solid Phase Transitions in a Confined Colloid Suspension." *Phys. Rev. Lett.* 77.12 (1996), 2577–2580.

[81] K. Zahn, R. Lenke, and G. Maret. "Two-Stage Melting of Paramagnetic Colloidal Crystals in Two Dimensions." *Phys. Rev. Lett.* 82.13 (1999), 2721–2724.

[82] N. Hoffmann, C. N. Likos, and H. Löwen. "Microphase structuring in two-dimensional magnetic colloid mixtures." *J. Phys.: Condens. Matter* 18.45 (2006), 10193.

[83] N. Hoffmann, F. Ebert, C. N. Likos, H. Löwen, and G. Maret. "Partial Clustering in Binary Two-Dimensional Colloidal Suspensions." *Phys. Rev. Lett.* 97.7 (2006), 078301.

[84] J. Kerr. "XLIII. On rotation of the plane of polarization by reflection from the pole of a magnet." *The London, Edinburgh, and Dublin Philosophical Magazine and Journal of Science* 3.19 (1877), 321–343.

[85] F. Büttner, I. Lemesh, and G. S. D. Beach. "Theory of isolated magnetic skyrmions: From fundamentals to room temperature applications." *Sci Rep* 8.1 (2018), 4464.

[86] M. Hoffmann, B. Zimmermann, G. P. Müller, D. Schürhoff, N. S. Kiselev, C. Melcher, and S. Blügel. "Antiskyrmions stabilized at interfaces by anisotropic Dzyaloshinskii-Moriya interactions." *Nat Commun* 8.1 (2017), 308.

[87] M. T. Birch, D. Cortés-Ortuño, N. D. Khanh, S. Seki, A. Štefančič, G. Balakrishnan, Y. Tokura, and P. D. Hatton. "Topological defect-mediated skyrmion annihilation in three dimensions." *Commun Phys* 4.1 (2021), 175.

[88] E. A. Giess. "Magnetic Bubble Materials." *Science* 208.4446 (1980), 938–943.

[89] A. Einstein. "Über die von der molekularkinetischen Theorie der Wärme geforderte Bewegung von in ruhenden Flüssigkeiten suspendierten Teilchen." *Annalen der Physik* 322.8 (1905), 549–560.

[90] D. S. Lemons and A. Gythiel. “Paul Langevin’s 1908 paper “On the Theory of Brownian Motion” [“Sur la théorie du mouvement brownien,” C. R. Acad. Sci. (Paris) 146, 530–533 (1908)].” *American Journal of Physics* 65.11 (1997), 1079–1081.

[91] C. N. Likos. “Effective interactions in soft condensed matter physics.” *Physics Reports* 348.4 (2001), 267–439.

[92] M. Paciolla, C. N. Likos, and A. J. Moreno. “Validity of Effective Potentials in Crowded Solutions of Linear and Ring Polymers with Reversible Bonds.” *Macromolecules* 55.7 (2022), 2659–2674.

[93] I. Makhfudz, B. Krüger, and O. Tchernyshyov. “Inertia and Chiral Edge Modes of a Skyrmion Magnetic Bubble.” *Phys. Rev. Lett.* 109.21 (2012), 217201.

[94] F. Büttner, C. Moutafis, M. Schneider, B. Krüger, C. M. Günther, J. Geilhufe, C. v. K. Schmising, J. Mohanty, B. Pfau, S. Schaffert, A. Bisig, M. Foerster, T. Schulz, C. a. F. Vaz, J. H. Franken, H. J. M. Swagten, M. Kläui, and S. Eisebitt. “Dynamics and inertia of skyrmionic spin structures.” *Nature Phys* 11.3 (2015), 225–228.

[95] N. Kerber, M. Weißenhofer, K. Raab, K. Litzius, J. Zázvorka, U. Nowak, and M. Kläui. “Anisotropic Skyrmion Diffusion Controlled by Magnetic-Field-Induced Symmetry Breaking.” *Phys. Rev. Appl.* 15.4 (2021), 044029.

[96] M. Weißenhofer, L. Rózsa, and U. Nowak. “Skyrmion Dynamics at Finite Temperatures: Beyond Thiele’s Equation.” *Phys. Rev. Lett.* 127.4 (2021), 047203.

[97] R. Kubo. “The fluctuation-dissipation theorem.” *Rep. Prog. Phys.* 29.1 (1966), 255.

[98] G. Chen. “Skyrmion Hall effect.” *Nature Phys* 13.2 (2017), 112–113.

[99] K. Litzius, I. Lemesh, B. Krüger, P. Bassirian, L. Caretta, K. Richter, F. Büttner, K. Sato, O. A. Tretiakov, J. Förster, R. M. Reeve, M. Weigand, I. Bykova, H. Stoll, G. Schütz, G. S. D. Beach, and M. Kläui. “Skyrmion Hall effect revealed by direct time-resolved X-ray microscopy.” *Nature Phys* 13.2 (2017), 170–175.

[100] W. Jiang, X. Zhang, G. Yu, W. Zhang, X. Wang, M. Benjamin Jungfleisch, J. E. Pearson, X. Cheng, O. Heinonen, K. L. Wang, Y. Zhou, A. Hoffmann, and S. G. E. te Velthuis. “Direct observation of the skyrmion Hall effect.” *Nature Phys* 13.2 (2017), 162–169.

[101] B. L. Brown, U. C. Täuber, and M. Pleimling. “Effect of the Magnus force on skyrmion relaxation dynamics.” *Phys. Rev. B* 97.2 (2018), 020405.

[102] D. Schick, M. Weißenhofer, L. Rózsa, J. Rothörl, P. Virnau, and U. Nowak. “Two levels of topology in skyrmion lattice dynamics.” *Phys. Rev. Res.* 6.1 (2024), 013097.

[103] E. Kalz, H. D. Vuijk, I. Abdoli, J.-U. Sommer, H. Löwen, and A. Sharma. “Collisions Enhance Self-Diffusion in Odd-Diffusive Systems.” *Phys. Rev. Lett.* 129.9 (2022), 090601.

[104] C. Reichhardt, D. Ray, and C. J. O. Reichhardt. “Collective Transport Properties of Driven Skyrmions with Random Disorder.” *Phys. Rev. Lett.* 114.21 (2015), 217202.

[105] C. Schütte, J. Iwasaki, A. Rosch, and N. Nagaosa. “Inertia, diffusion, and dynamics of a driven skyrmion.” *Phys. Rev. B* 90.17 (2014), 174434.

[106] W. Jiang, P. Upadhyaya, W. Zhang, G. Yu, M. B. Jungfleisch, F. Y. Fradin, J. E. Pearson, Y. Tserkovnyak, K. L. Wang, O. Heinonen, S. G. E. te Velthuis, and A. Hoffmann. “Blowing magnetic skyrmion bubbles.” *Science* 349.6245 (2015), 283–286.

[107] J. C. Slonczewski. “Current-driven excitation of magnetic multilayers.” *Journal of Magnetism and Magnetic Materials* 159.1 (1996), L1–L7.

[108] J. E. Hirsch. “Spin Hall Effect.” *Phys. Rev. Lett.* 83.9 (1999), 1834–1837.

[109] L. Liu, C.-F. Pai, Y. Li, H. W. Tseng, D. C. Ralph, and R. A. Buhrman. “Spin-Torque Switching with the Giant Spin Hall Effect of Tantalum.” *Science* 336.6081 (2012), 555–558.

[110] M.-G. Kang, S. Lee, and B.-G. Park. “Field-free spin-orbit torques switching and its applications.” *npj Spintronics* 3.1 (2025), 8.

[111] C. Reichhardt, C. J. O. Reichhardt, and M. V. Milošević. “Statics and dynamics of skyrmions interacting with disorder and nanostructures.” *Rev. Mod. Phys.* 94.3 (2022), 035005.

[112] J. Iwasaki, M. Mochizuki, and N. Nagaosa. “Universal current-velocity relation of skyrmion motion in chiral magnets.” *Nat Commun* 4.1 (2013), 1463.

[113] Y.-H. Liu and Y.-Q. Li. “A mechanism to pin skyrmions in chiral magnets.” *J. Phys.: Condens. Matter* 25.7 (2013), 076005.

[114] A. Derras-Chouk and E. M. Chudnovsky. “Skyrmions near defects.” *J. Phys.: Condens. Matter* 33.19 (2021), 195802.

[115] C. Navau, N. Del-Valle, and A. Sanchez. “Interaction of isolated skyrmions with point and linear defects.” *Journal of Magnetism and Magnetic Materials* 465 (2018), 709–715.

[116] J. G. Kirkwood. “Statistical Mechanics of Fluid Mixtures.” *J. Chem. Phys.* 3.5 (1935), 300–313.

[117] J.-P. Hansen and I. R. McDonald. *Theory of Simple Liquids: with Applications to Soft Matter*. 2013. 637 pp. ISBN: 978-0-12-387033-9.

[118] J. Müller. “Magnetic skyrmions on a two-lane racetrack.” *New J. Phys.* 19.2 (2017), 025002.

[119] L. Rózsa, A. Deák, E. Simon, R. Yanes, L. Udvardi, L. Szunyogh, and U. Nowak. “Skyrmions with Attractive Interactions in an Ultrathin Magnetic Film.” *Phys. Rev. Lett.* 117.15 (2016), 157205.

[120] D. Reith, M. Pütz, and F. Müller-Plathe. “Deriving effective mesoscale potentials from atomistic simulations.” *J Comput Chem* 24.13 (2003), 1624–1636.

[121] D. B. Allan, T. Caswell, N. C. Keim, C. M. van der Wel, and R. W. Verweij. *soft-matter/trackpy: v0.6.2 (Zenodo)*. Version v0.6.2. 2024.

[122] T. C. Moore, C. R. Iacovella, and C. McCabe. “Derivation of coarse-grained potentials via multistate iterative Boltzmann inversion.” *J. Chem. Phys.* 140.22 (2014), 224104.

[123] B. J. Alder and T. E. Wainwright. “Studies in Molecular Dynamics. I. General Method.” *J. Chem. Phys.* 31.2 (1959), 459–466.

[124] D. Frenkel and B. Smit. *Understanding Molecular Simulation: From Algorithms to Applications.* 2023. 868 pp. ISBN: 978-0-323-91318-8.

[125] J. A. Anderson, J. Glaser, and S. C. Glotzer. “HOOMD-blue: A Python package for high-performance molecular dynamics and hard particle Monte Carlo simulations.” *Computational Materials Science* 173 (2020), 109363.

[126] A. P. Thompson, H. M. Aktulga, R. Berger, D. S. Bolintineanu, W. M. Brown, P. S. Crozier, P. J. in ’t Veld, A. Kohlmeyer, S. G. Moore, T. D. Nguyen, R. Shan, M. J. Stevens, J. Tranchida, C. Trott, and S. J. Plimpton. “LAMMPS - a flexible simulation tool for particle-based materials modeling at the atomic, meso, and continuum scales.” *Computer Physics Communications* 271 (2022), 108171.

[127] J. Rothörl. “Particle-based computer simulations of magnetic skyrmions.” PhD thesis. Johannes Gutenberg-Universität Mainz, 2024.

[128] L. Euler. *Institutionum calculi integralis.* 1768. 560 pp.

[129] B. Dünweg and W. Paul. “Brownian dynamics simulations without gaussian random numbers.” *Int. J. Mod. Phys. C* 02.3 (1991), 817–827.

[130] T. Yanagida. “Fluctuation as a tool of biological molecular machines.” *Biosystems.* Selected Papers presented at the International Conference ”Collective Dynamics: Topics on Competition and Cooperation in the Biosciences 93.1 (2008), 3–7.

[131] P. Reimann. “Brownian motors: noisy transport far from equilibrium.” *Physics Reports* 361.2 (2002), 57–265.

[132] D. Pinna, F. Abreu Araujo, J.-V. Kim, V. Cros, D. Querlioz, P. Bessiere, J. Droulez, and J. Grollier. “Skyrmion Gas Manipulation for Probabilistic Computing.” *Phys. Rev. Appl.* 9.6 (2018), 064018.

[133] J. Love, R. Msiska, J. Mulkers, G. Bourianoff, J. Leliaert, and K. Everschor-Sitte. “Spatial analysis of physical reservoir computers.” *Phys. Rev. Appl.* 20.4 (2023), 044057.

[134] K. Sato and T. Ishibashi. “Fundamentals of Magneto-Optical Spectroscopy.” *Front. Phys.* 10 (2022).

[135] I. Labrie-Boulay, T. B. Winkler, D. Franzen, A. Romanova, H. Fangohr, and M. Kläui. “Machine-learning-based detection of spin structures.” *Phys. Rev. Appl.* 21.1 (2024), 014014.

[136] X. Zhang, M. Ezawa, and Y. Zhou. “Magnetic skyrmion logic gates: conversion, duplication and merging of skyrmions.” *Sci Rep* 5.1 (2015), 9400.

[137] C. Reichhardt and C. J. O. Reichhardt. “Noise fluctuations and drive dependence of the skyrmion Hall effect in disordered systems.” *New J. Phys.* 18.9 (2016), 095005.

[138] N. Ogawa. “Diffusion in a curved tube.” *Physics Letters A* 377.38 (2013), 2465–2471.

[139] S. Lifson and J. L. Jackson. “On the Self-Diffusion of Ions in a Polyelectrolyte Solution.” *J. Chem. Phys.* 36.9 (1962), 2410–2414.

[140] D. Broomhead and D. Lowe. “Radial basis functions, multi-variable functional interpolation and adaptive networks.” *Royal signals and radar establishment malvern (united kingdom)* Rsre-memo-4148 (1988).

[141] M. Sivan and O. Farago. “Probability distribution of Brownian motion in periodic potentials.” *Phys. Rev. E* 98.5 (2018), 052117.

[142] S. Marholm. *sigvaldm/localreg: Multivariate RBF output (Zenodo).* Version 0.5.0. 2022.

[143] A. Savitzky and M. J. E. Golay. “Smoothing and Differentiation of Data by Simplified Least Squares Procedures.” *Anal. Chem.* 36.8 (1964), 1627–1639.

[144] F. James and M. Roos. “Minuit - a system for function minimization and analysis of the parameter errors and correlations.” *Computer Physics Communications* 10.6 (1975), 343–367.

[145] H. Dembinski, P. Ongmongkolkul, C. Deil, H. Schreiner, M. Feickert, C. Burr, J. Watson, F. Rost, A. Pearce, L. Geiger, A. Abdelmotteleb, A. Desai, B. M. Wiedemann, C. Gohlke, J. Sanders, J. Drotleff, J. Eschle, L. Neste, M. E. Gorelli, M. Baak, M. Eliachevitch, and O. Zapata. *scikit-hep/iminuit (Zenodo).* Version v2.30.2. 2024.

[146] A. Fert, N. Reyren, and V. Cros. “Magnetic skyrmions: advances in physics and potential applications.” *Nat Rev Mater* 2.7 (2017), 1–15.

[147] J. Sampaio, V. Cros, S. Rohart, A. Thiaville, and A. Fert. “Nucleation, stability and current-induced motion of isolated magnetic skyrmions in nanostructures.” *Nature Nanotech* 8.11 (2013), 839–844.

[148] R. Lo Conte, E. Martinez, A. Hrabec, A. Lamperti, T. Schulz, L. Nasi, L. Lazzarini, R. Mantovan, F. Maccherozzi, S. S. Dhesi, B. Ocker, C. H. Marrows, T. A. Moore, and M. Kläui. “Role of B diffusion in the interfacial Dzyaloshinskii-Moriya interaction in Ta/Co20Fe60B20/MgO nanowires.” *Phys. Rev. B* 91.1 (2015), 014433.

[149] S. Rohart and A. Thiaville. “Skyrmion confinement in ultrathin film nanostructures in the presence of Dzyaloshinskii-Moriya interaction.” *Phys. Rev. B* 88.18 (2013), 184422.

[150] B. F. McKeever, D. R. Rodrigues, D. Pinna, A. Abanov, J. Sinova, and K. Everschor-Sitte. “Characterizing breathing dynamics of magnetic skyrmions and antiskyrmions within the Hamiltonian formalism.” *Phys. Rev. B* 99.5 (2019), 054430.

[151] Y. Wang, J. Wang, T. Kitamura, H. Hirakata, and T. Shimada. “Exponential Temperature Effects on Skyrmion-Skyrmion Interaction.” *Phys. Rev. Applied* 18.4 (2022), 044024.

[152] R. D. Astumian and M. Bier. “Fluctuation driven ratchets: Molecular motors.” *Phys. Rev. Lett.* 72.11 (1994), 1766–1769.

[153] P. Tierno and M. R. Shaebani. “Enhanced diffusion and anomalous transport of magnetic colloids driven above a two-state flashing potential.” *Soft Matter* 12.14 (2016), 3398–3405.

[154] P. Hänggi. “Artificial Brownian motors: Controlling transport on the nanoscale.” *Rev. Mod. Phys.* 81.1 (2009), 387–442.

[155] F. Jülicher, A. Ajdari, and J. Prost. “Modeling molecular motors.” *Rev. Mod. Phys.* 69.4 (1997), 1269–1282.

[156] S. N. Ethier and J. Lee. “The flashing Brownian ratchet and Parrondo’s paradox.” *Royal Society Open Science* 5.1 (2018), 171685.

[157] M. A. Brems. *Development and Computer Simulation Study of Token-Based Computing Methods Exploiting Thermal and Artificially Induced Diffusion of Magnetic Skyrmions (Master’s thesis).* 2021.

[158] F. Pedregosa, G. Varoquaux, A. Gramfort, V. Michel, B. Thirion, O. Grisel, M. Blondel, P. Prettenhofer, R. Weiss, V. Dubourg, J. Vanderplas, A. Passos, D. Cournapeau, M. Brucher, M. Perrot, E. Duchesnay, and G. Louppe. “Scikit-learn: Machine Learning in Python.” *Journal of Machine Learning Research* 12 (2012).

[159] S. M. Fröhlich. *Coarse grained simulations of magnetic skyrmions (Master’s thesis).* 2024.

[160] T. Sparmann. *Skyrmion pinning energetics and diffusion influenced by externally applied forces (Master’s thesis).* 2024.

[161] J. Jumper, R. Evans, A. Pritzel, T. Green, M. Figurnov, O. Ronneberger, K. Tunyasuvunakool, R. Bates, A. Žídek, A. Potapenko, A. Bridgland, C. Meyer, S. A. A. Kohl, A. J. Ballard, A. Cowie, B. Romera-Paredes, S. Nikolov, R. Jain, J. Adler, T. Back, S. Petersen, D. Reiman, E. Clancy, M. Zielinski, M. Steinegger, M. Pacholska, T. Berghammer, S. Bodenstein, D. Silver, O. Vinyals, A. W. Senior, K. Kavukcuoglu, P. Kohli, and D. Hassabis. “Highly accurate protein structure prediction with AlphaFold.” *Nature* 596.7873 (2021), 583–589.

[162] E. Callaway. “‘It will change everything’: DeepMind’s AI makes gigantic leap in solving protein structures.” *Nature* 588.7837 (2020), 203–204.

[163] A. I. Jarmolinska, A. P. Perlinska, R. Runkel, B. Trefz, H. M. Ginn, P. Virnau, and J. I. Sulkowska. “Proteins’ Knotty Problems.” *Journal of Molecular Biology* 431.2 (2019), 244–257.

[164] M.-F. Hsu, M. K. Sriramoju, C.-H. Lai, Y.-R. Chen, J.-S. Huang, T.-P. Ko, K.-F. Huang, and S.-T. D. Hsu. “Structure, dynamics, and stability of the smallest and most complex 71 protein knot.” *Journal of Biological Chemistry* 300.1 (2024), 105553.

[165] A. P. Perlinska, M. L. Nguyen, S. P. Pilla, E. Staszor, I. Lewandowska, A. Bernat, E. Purta, R. Augustyniak, J. M. Bujnicki, and J. I. Sulkowska. “Are there double knots in proteins? Prediction and in vitro verification based on TrmD-Tm1570 fusion from C. nitroreducens.” *Front. Mol. Biosci.* 10 (2024).

[166] S. Wettermann, M. Brems, J. T. Siebert, G. T. Vu, T. J. Stevens, and P. Virnau. “A minimal Gō-model for rebuilding whole genome structures from haploid single-cell Hi-C data.” *Computational Materials Science* 173 (2020), 109178.

Removed due to data privacy.

Removed due to data privacy.